Relaxation Dynamics of Non-thermal Electrons in a Warm Dense Plasma

Yuanfeng Shi (石元峰)

St. Peter's College

University of Oxford

A thesis submitted for the degree of

Doctor of Philosophy

Michaelmas 2024

Abstract

The relaxation dynamics of non-thermal electrons in warm dense plasmas (WDM) are critical for understanding energy transport and equilibration in extreme environments, such as inertial confinement fusion, planetary interiors, and laser-driven plasmas. WDM exists in a unique regime where quantum effects and strong coupling coexist, challenging the direct application of mature theories applicable to ideal plasma or condensed matter systems. This thesis presents a comprehensive study of non-thermal electron relaxation in WDM, combining experimental, theoretical, and computational approaches to measure electron collision times and probe fundamental interaction mechanisms.

A novel method for measuring collision times was developed by leveraging X-ray Free Electron Laser (XFEL)-driven plasmas and studying non-thermal electron emission spectra as a function of XFEL pulse duration. Theoretical simulations using the `CCFLY` collisional-radiative code revealed that shorter XFEL pulses enhance non-thermal electron features in emission spectra. Electron-electron (e-e) collisions predominantly broaden non-thermal peaks, while electron-ion (e-i) collisions depopulate these peaks, providing a clear distinction between the two mechanisms. These insights validate the experimental approach for probing ultrafast electron dynamics.

State-of-the-art experimental techniques, including single-photon counting (SPC) detectors and advanced clustering and deconvolution algorithms, were employed to capture weak non-thermal signals in XFEL-driven Mn plasmas. The experiment, conducted at the Linac Coherent Light Source (LCLS), utilised XFEL pulses ranging from 5 to 60 femtoseconds to create and observe non-thermal electron relaxation. Non-thermal features in the emission spectra decayed with increasing pulse duration, allowing direct observation of electron thermalisation dynamics. Analysis revealed that e-i collisions dominate relaxation, with a collision rate of approximately 0.1 fs^{-1} (collision time of 10.5 fs). The e-e collision rate was constrained to an upper limit of 8.3 fs^{-1} (collision time $>$ 0.12 fs), providing the first direct measurement of electron collision times in WDM.

This study establishes a robust framework for investigating ultrafast relaxation processes in WDM, bridging the gap between theoretical predictions and experimental validation. By enabling direct observation of electron thermalisation, this work contributes to advancing the understanding of energy transport and fundamental interactions in strongly coupled systems. Future developments, including attosecond XFEL pulses, improved spectroscopic resolution, and machine learning-based data analysis, hold the potential to further refine these methodologies and deepen our understanding of WDM dynamics.

Relaxation Dynamics of Non-thermal Electrons in a Warm Dense Plasma



Yuanfeng Shi (石元峰)

St. Peter's College

University of Oxford

Supervised by:

Prof. Sam M. Vinko and Prof. Justin S. Wark

A thesis submitted for the degree of

Doctor of Philosophy

Michaelmas 2024

to my love 何玮洁

Abstract

The relaxation dynamics of non-thermal electrons in warm dense plasmas (WDM) are critical for understanding energy transport and equilibration in extreme environments, such as inertial confinement fusion, planetary interiors, and laser-driven plasmas. WDM exists in a unique regime where quantum effects and strong coupling coexist, challenging the direct application of mature theories applicable to ideal plasma or condensed matter systems. This thesis presents a comprehensive study of non-thermal electron relaxation in WDM, combining experimental, theoretical, and computational approaches to measure electron collision times and probe fundamental interaction mechanisms.

A novel method for measuring collision times was developed by leveraging X-ray Free Electron Laser (XFEL)-driven plasmas and studying non-thermal electron emission spectra as a function of XFEL pulse duration. Theoretical simulations using the `CCFLY` collisional-radiative code revealed that shorter XFEL pulses enhance non-thermal electron features in emission spectra. Electron-electron (e-e) collisions predominantly broaden non-thermal peaks, while electron-ion (e-i) collisions depopulate these peaks, providing a clear distinction between the two mechanisms. These insights validate the experimental approach for probing ultrafast electron dynamics.

State-of-the-art experimental techniques, including single-photon counting (SPC) detectors and advanced clustering and deconvolution algorithms, were employed to capture weak non-thermal signals in XFEL-driven Mn plasmas. The experiment, conducted at the Linac Coherent Light Source (LCLS), utilised XFEL pulses ranging from 5 to 60 femtoseconds to create and observe non-thermal electron relaxation. Non-thermal features in the emission spectra decayed with increasing pulse duration, allowing direct observation of electron thermalisation dynamics. Analysis revealed that e-i collisions dominate relaxation, with a collision rate of approximately 0.1 fs^{-1} (collision time of 10.5 fs). The e-e collision rate was constrained to an upper limit of 8.3 fs^{-1} (collision time > 0.12 fs), providing the first direct measurement of electron collision times in WDM.

This study establishes a robust framework for investigating ultrafast relaxation processes in WDM, bridging the gap between theoretical predictions and experimental validation. By enabling direct observation of electron thermalisation, this work contributes to advancing the understanding of energy transport and fundamental interactions in strongly coupled

systems. Future developments, including attosecond XFEL pulses, improved spectroscopic resolution, and machine learning-based data analysis, hold the potential to further refine these methodologies and deepen our understanding of WDM dynamics.

Acknowledgements

Doing a PhD at Oxford has been one of the most extraordinary experiences of my life. I would like to take this opportunity to express my gratitude to the many people who have profoundly shaped who I am today.

First and foremost, I wish to thank my supervisors, Sam Vinko and Justin Wark, for their insightful advice on this research and their supportive attitude toward my approach to problems. Learning from experienced researchers is perhaps the most effective way to become an independent researcher, and I firmly believe that your imperceptible influence will be key to my future career.

Numerous people have contributed to this research, each deserving special mention. On the simulation side, I wish to thank Shenyuan Ren (任申元) and Quincy van den Berg for your generous help with atomic kinetics, the Fokker-Planck equation, and the art of `C++` programming, even after leaving the group and becoming extremely busy with new endeavours.

On the experimental side, I am deeply grateful to the incredibly reliable team of Tom Campbell, Tom Gawne, and Alessandro Forte, who participated in four experimental beamtimes with me, leading to exciting scientific discoveries that extended far beyond my research. Thanks to Hae Ja Lee and Bob Nagler for extensive cooperation in various beamtimes and in commissioning the LCLS non-thermal experiment. To Oliver Humphries for valuable discussions on SPC. To Céline Crépisson, Karim Alaa-El-Din, Domenic Peake, and Tom Preston for conducting the LCLS non-thermal experiment. Due to growing international tensions, it has been nearly impossible for Chinese citizens to enter the US for experimental work. Consequently, I had to lead the experiment remotely from Oxford. The LCLS non-thermal experiment would not have succeeded without your dedication.

I also wish to thank Yizhen Wang (王艺臻) for his help in the experimental data analysis.

Finally, to my family: To my parents, Yongkuan Shi (石永宽) and Zheng He (何拯), thank you for your unwavering support of my studies, both emotional and financial.

To my love, Weijie He (何玮洁), for being my guiding star in my darkest days and my pillar of strength in my difficult times. Your unwavering faith in me and selfless support have meant more than words can express.

And to Ying (石英), my little one, who joined our family shortly after the LCLS experiment, bringing both challenges, but more importantly, immeasurable joy, to my life.

Contents

List of Figures viii

List of Abbreviations xi

List of Symbols xv

1 Introduction 1

1.1 Background and Motivation . . . 1
1.2 Relevant Concepts . . . 3
1.3 Thesis Structure . . . 13
1.4 Author Contributions . . . 14

2 Free Electron Relaxation Dynamics 17

2.1 Introduction . . . 17
2.2 Electron Relaxation in Ideal Plasmas . . . 19
2.3 Electron Relaxation in Quantum Plasmas . . . 33
2.4 Summary . . . 43

3 Electron Thermalisation and Collision Time 45

3.1 Introduction . . . 46
3.2 Non-thermal Electrons in XFEL-driven Plasmas . . . 47
3.3 Collisional-radiative Simulation . . . 50
3.4 Feasibility Demonstration . . . 57
3.5 Summary . . . 64

4 Experimental Techniques for Non-thermal Experiments 66

4.1 Introduction . . . 66
4.2 Single-photon Counting Technique . . . 69
4.3 Application of SPC in Non-thermal Experiments . . . 88
4.4 Summary . . . 99

5 Measuring the collision time at the LCLS XFEL Facility **101**

5.1 Introduction 102

5.2 Design of the Experiment 103

5.3 Experimental Results 112

5.4 Inferred Collision Time 120

5.5 Summary 136

6 Conclusions **139**

6.1 Summary 139

6.2 Future Work 141

Appendices

A Transition Rates and Collision Operators **147**

A.1 Transition Rates in Atomic Kinetics 147

A.2 Electron Source Operators 148

A.3 Inelastic Collision Operators 149

References **150**

List of Figures

1.1 Phase Diagram of Plasmas 5
1.2 Operation principle of XFELs 7
1.3 SASE process in XFEL 8
1.4 Peak brightness of some X-ray sources 9
1.5 Picture of the Coulomb logarithm 12
1.6 Breakdown of the Coulomb logarithm 13

2.1 Two body Coulomb Collisions 20
2.2 Classical Coulomb logarithms 30
2.3 Quantum Coulomb logarithms 35
2.4 Breakdown of the modified quantum CL 36
2.5 Mulser CL and terms in the collision operator 37
2.6 Minimal β value at low temperatures 40

3.1 Distribution of thermal and non-thermal electrons 47
3.2 Creating non-thermal electrons using an XFEL 48
3.3 Illustration of photons energies from non-thermal electrons 49
3.4 Evolution of the non-thermal electron distribution 58
3.5 Tailoring non-thermal electron distributions by an XFEL 59
3.6 Effect of the XFEL pulse duration on the emission spectrum 60
3.7 Contribution of e-e collision and e-i collision to $\frac{\partial f}{\partial t}$ 61
3.8 Contribution of e-i and e-e collisions to electron thermalisation. 62
3.9 Collision time from different CL models 63
3.10 Non-thermal features under different e-e collision times 63

4.1 Illustration of a flat crystal spectrometer 67
4.2 Illustration of the single-photon counting technique 69
4.3 Illustration of charge generation in CCD 71
4.4 Charge transfer in CCD 72
4.5 Background subtraction of a pixel detector 73
4.6 Charge spread and clusters 74

4.7 Primary thresholding for SPC . . . 75
4.8 Cluster layouts for SPC . . . 75
4.9 Deconvolution for SPC . . . 81
4.10 Monte Carlo data for SPC . . . 84
4.11 Mimicking charge spread effect in the MC data . . . 84
4.12 Size of clusters under different assumed charge spread radii . . . 85
4.13 Monte Carlo simulation of SPC data with charge spread . . . 85
4.14 Histogram of pixels and clusters in SPC . . . 86
4.15 Reconstruction of spectra in SPC with MC data . . . 87
4.16 RR emission energies from KLM and KMM Auger processes . . . 89
4.17 RR emission energies from PI processes . . . 89
4.18 Diagram of Inverse Compton Scattering . . . 92
4.19 Diagram of Compton Scattering . . . 92
4.20 Energy gain from head-on ICS . . . 94
4.21 Angular geometry of ICS . . . 95
4.22 Combined ICS and XRTS spectrum . . . 96
4.23 Transforming velocity space distribution to distribution with respect to v_x . . . 97
4.24 SPC dual detector set-up . . . 99

5.1 Overall design of the experiment . . . 103
5.2 Diagram of primary RR emission energy for various mid-Z elements . . . 105
5.3 Sketch of the selective spoiling technique through a slotted foil . . . 106
5.4 Sketch of the XLEAP technique . . . 107
5.5 Sketch of XTCAV technique for pulse duration measurement . . . 108
5.6 tSPC photon image . . . 113
5.7 Non-thermal electron Spectrum obtained from the tSPC . . . 114
5.8 Power profiles obtained from SPC . . . 116
5.9 Distribution of the pulse durations . . . 117
5.10 Pulse-duration-grouped spectra from tSPC . . . 118
5.11 Decay of the non-thermal peak with respect to pulse durations from experiment 119
5.12 Comparison between the electron-only mode and the standard mode of `CCFLY` 124
5.13 Effect of the XFEL pulse duration on the Mn emission spectrum . . . 126
5.14 Collisional ionisation rates as a function of energy . . . 127
5.15 Decay of the non-thermal peak with respect to pulse durations from simulation 128
5.16 Mapping collision rates to decay parameters and fitting process . . . 130
5.17 Comparison of fitted and simulated decay curves . . . 131
5.18 Posterior distribution of the relaxation rates . . . 132

5.19 Comparison of MCMC results with the experimental data 133
5.20 Marginalized distributions of collision rates 134
5.21 Conditional distribution of electron-electron collision rate 135

List of Abbreviations

Terminologies

Acronym	Description
AD	Auger decay
ADC	Analog-to-digit converter
ADU	Analog-to-digit unit
AMO	Atomic, molecular and optical (physics)
b-b	Bound-bound (transitions)
b-f	Bound-free (transitions)
f-f	Free-free (transitions)
BBGKY	Bogoliubov-Born-Green-Kirkwood-Yvon (hierarchy)
BC	Burgess and Chidichimo (BC) (model)
BGK	Bhatnagar-Gross-Krook (model)
BUU	Boltzmann-Uehling-Uhlenbeck (equation)
CAM	Clark, Abdallah, and Mann (model)
CCD	Charge-coupled devices
CD	Collisional de-excitation
CE	Collisional excitation
CI	Collisional ionisation
CL	Coulomb logarithm
COM	Centre of mass

Continued on next page

Continued from previous page

Acronym	**Description**
CPA	Chirped pulse amplification
CR	Collisional recombination
DR	Dielectron recombination
DFT	Density functional theory
e-e	Electron-electron (collisions)
e-i	Electron-ion (collisions)
EEHG	Echo-enabled harmonic generation
FWHM	Full width at half maximum
HED	High energy density (science)[1]
ICF	Inertial confinement fusion
ICS	Inverse Compton scattering
IPD	Ionisation potential depression
Linac	Linear accelerator
LFP	Landau-Fokker-Planck (collision operator)
qLFP	Quantum LFP (collision operator)
LRT	Linear response theory
ML	Machine learning
MC	Monte Carlo
MCMC	Markov chain Monte Carlo
QMC	Quantum Monte Carlo
MCF	Magnetic confinement fusion
QED	Quantum electrodynamics
RTA	Relaxation time approximation

Continued on next page

[1] also refers to the end station at EuXFEL with the same name

Continued from previous page

Acronym	**Description**
RIXS	Resonant inelastic X-ray scattering
ROIC	Readout integrated circuit
PE	Photon excitation
PI	Photon-ionisation
PSF	Point spread function
RR	Radiation recombination
SASE	Self amplified spontaneous emission
ESASE	Enhanced SASE
SNR	Signal to noise ratio
SPC	Single-photon counting
tSPC	top SPC
bSPC	back SPC
SpD	Spontaneous decay
StD	Stimulated decay
XES	X-ray emission spectroscopy
XFEL	X-ray free electron laser
XRS	X-ray Raman scattering
XRTS	X-ray Thomson scattering
XLEAP	X-ray laser-enhanced attosecond pulse

Institutions and Facilities

Acronym	Description
DESY	Deutsches Elektronen-Synchrotron
EuXFEL	European XFEL
FERMI	Free Electron Laser Radiation for Multidisciplinary Investigations
FLASH	Free Electron Laser in Hamburg
HED	High Energy Density (an endstation at EuXFEL)
LCLS	Linac Coherent Light Source
MEC	Matter under Extreme Conditions (an endstation at LCLS)
PAL	Pohang Accelerator Laboratory
PSI	Paul Scherrer Institute
SACLA	SPring-8 Angstrom Compact Free Electron Laser
SHINE	Shanghai High Repetition Rate XFEL and Extreme Light Facility
SPring-8	Super Photon ring-8 GeV
SARI	Shanghai Advanced Research Institute
SLAC	Stanford Linear Accelerator Center
SXFEL	Shanghai X-ray Free Electron Laser

Simulation Packages

Acronym	Description
`CCFLY`	Atomic Kinetics Code (C++ version)
`FLYCHK`	Atomic Kinetics Code (Fortran version)
`SCFLY`	Atomic Kinetics Code (Fortran version)

List of Symbols

Physical Quantities and Operators

Notation	Description	Preferred Unit
$\vec{B}$	Magnetic field	T
$\vec{E}$	Electric field	$\mathrm{V \cdot m^{-1}}$
$\vec{e}$	Vector basis	-
$\mathcal{E}$	Spectral emissivity	$\mathrm{erg \cdot s^{-1} \cdot cm^{-3} \cdot Hz^{-1} \cdot Sr^{-1}}$
$\vec{F}$	Force	N
$f[\cdot]$	Distribution function	per unit of $\cdot$
$f[W]$	of energy[2]	$\mathrm{eV^{-1}}$
$f_{v_x}[v_x]$	of v_x [3]	$\mathrm{(m \cdot s^{-1})^{-1}}$
$\mathcal{H}$	Hamiltonian	J
$\vec{j}$	Flux density	
$\vec{j}_q$	Current density	$\mathrm{A \cdot m^{-2}}$
$\vec{j}_Q$	Heat flux density	$\mathrm{W \cdot m^{-2}}$
K	Transition rate for ions	$\mathrm{s^{-1}}$ [4]
K'	Transition rate for free electrons	$\mathrm{m^3 \cdot s^{-1}}$ [5]

Continued on next page

[2] of electron (in 3) or photon (in 4.2)
[3] of electron (in 4.3.2)
[4] as in Eq. 3.3
[5] as in Eq. 3.12

Continued from previous page

Notation	Description	Preferred Unit
l	Length	m
l_{attn}	Attenuation length	Å
l_{d}	Interplanar spacing	Å
l_{dB}	Reduced de Broglie wavelength	Å
l_{u}	Undulator period	cm
l_{w}	Wavelength	Å
m	Mass	kg, g
m_{r}	Reduced mass	kg, g
N	Number (of particles, pixels, ...)	-
N_{det}	Number of pixels on detector	-
$\mathcal{N}$	Degeneracy of state	-
n	Density of state	-
$\hat{\mathcal{O}}$	Operator	
$\hat{\mathcal{O}}_{\mathrm{coll}}$	Collision Operator	
$\hat{\mathcal{O}}_{\mathrm{e}}$	Elastic collision Operator	
$\hat{\mathcal{O}}_{\mathrm{i}}$	Inelastic collision Operator	
$\hat{\mathcal{O}}_{\mathrm{S}}$	Source Operator	
$\vec{p}$	Momentum	$\mathrm{kg \cdot m \cdot s^{-1}}$
q	Charge	$\mathrm{A \cdot s}$

Continued on next page

Continued from previous page

Notation	Description	Preferred Unit
$\vec{r}$	Position vector	m
r	Radius	m
r_{b}	Impact parameter	nm, m
r_{b_0}	Classical distance of closest approach	nm, m
r_{D}	Debye length	nm, m
r_{s}	Charge spread radius	pixel
r_{TF}	Thomas-Fermi screening length	nm, m
r_{WS}	Wigner Seitz radius	nm, m
S	Area, cross-section	cm^2, $\mu\mathrm{m}^2$, m^2
T	Temperature	eV
T_{F}	Fermi temperature	eV
t	Time	fs, s
t_{rlx}	Relaxation time	fs
t_{d}	Decay time	fs
t_{p}	Pulse duration	fs
$t_{\text{e-e}}$	e-e collision time	fs
$t_{\text{e-i}}$	e-i collision time	fs
$u_{\cdot}$	Uncertainty of $\cdot$	Same as $\cdot$
$\mathcal{U}$	Chemical potential	eV
V	Volume	cm^3, m^3
$\vec{v}$	Velocity	$\mathrm{m}\cdot\mathrm{s}^{-1}$, $\mathrm{cm}\cdot\mathrm{s}^{-1}$
$\vec{v}_{\mathrm{r}}$	Relative velocity	$\mathrm{m}\cdot\mathrm{s}^{-1}$, $\mathrm{cm}\cdot\mathrm{s}^{-1}$

Continued on next page

Continued from previous page

Notation	Description	Preferred Unit
W	Energy	eV, J
W_i	Ionisation energy	eV, J
W_kin	Kinetic energy	eV, J
W_pot	Potential energy	eV, J
W_res	Residual energy	eV, J
W_trans	Transition energy	eV, J
x, y, z	Coordinate	m
β	Unitless factor	-
β_coup	Coupling parameter	-
β_esc	Escape factor	-
β_deg	Degeneracy parameter	-
β_f	Fano factor	-
β_L	Lorentz factor	-
β_P	Poisson parameter	-
β_ph	Photon fraction	-
β_px	Fill fraction	-
β_trans	Transmission rate	-
η	Unitless factor	-
θ	Angle	rad
θ_s	Scattering angle	rad
θ_p	Azimuthal scattering angle	rad
κ	Opacity	m^{-1}
$\varkappa$	CR rate coefficient	$\mathrm{m}^4 \cdot \mathrm{s}$

Continued on next page

Continued from previous page

Notation	Description	Preferred Unit
Λ	Argument of CL	-
$\ln[\Lambda]$	CL	-
ν	Collision rate	fs^{-1}
$\nu_{\text{e-e}}$	e-e collision rate	fs^{-1}
$\nu_{\text{e-i}}$	e-i collision rate	fs^{-1}
ξ	Temporary variable	
ρ	Density	$\mathrm{g} \cdot \mathrm{cm}^{-3}$, $\mathrm{kg} \cdot \mathrm{m}^{-3}$
ρ_N	Number density	cm^{-3}
$\varrho[\vec{v}, \vec{r}]$	Distribution function[6]	$\mathrm{cm}^{-3}(\mathrm{m} \cdot \mathrm{s}^{-1})^{-3}$
$\tilde{\varrho}[\vec{p}, \vec{r}]$	Reduced distribution function[7]	-
σ	Transport coefficient	
σ_q	Electrical conductivity	$\mathrm{S} \cdot \mathrm{m}^{-1}$
σ_Q	Thermal conductivity	$\mathrm{W} \cdot \mathrm{m}^{-1} K^{-1}$
Υ	Volume in the phase space	
$\Upsilon_{\vec{p}}$	Volume in the momentum space	$\mathrm{kg}^{-3} \cdot \mathrm{m}^{-3} \cdot \mathrm{s}^{3}$
$\Upsilon_{\vec{r}}$	Volume in the real space	m^{-3}
$\Upsilon_{\vec{v}}$	Volume in the velocity space	$\mathrm{m}^{-3} \cdot \mathrm{s}^{3}$
φ	Angle	
Ψ	Spectral intensity	$\mathrm{erg} \cdot \mathrm{cm}^{-2} \cdot \mathrm{Hz}^{-1} \cdot \mathrm{Sr}^{-1}$
ψ	Wave function	
ω	Angular frequency[8]	s^{-1}
Ω	Solid Angle	Sr

[6] in the phase space

[7] in the momentum phase space

[8] usually used as photon energy $\hbar\omega$ with eV as the preferred unit.

Constants

Notation	Description	Value
$k_{\mathbf{B}}$	Boltzmann constant	1.38×10^{-23} J $\cdot$ K^{-1}
$m_{\mathbf{e}}$	Electron mass	9.11×10^{-31} kg
$q_{\mathbf{e}}$	Elementary charge	1.602×10^{-19} C
$r_{\mathbf{e}}$	Classical electron radius	2.818×10^{-15} m
$v_{\mathbf{c}}$	Speed of light in vacuum	2.998×10^{8} m $\cdot$ s^{-1}
$\varepsilon_{\mathbf{0}}$	Vacuum permittivity	8.854×10^{-12} F $\cdot$ m^{-1}
$\mu_{\mathbf{0}}$	Vacuum permeability	1.2566×10^{-6} H $\cdot$ m^{-1}
$\hbar$	Reduced Planck constant	1.05457×10^{-34} J $\cdot$ s
e	Base of natural logarithm	2.71828
π	Pi	3.14159

Mathematical Functions and Operators

Notation	Description	Notes
$\mathbf{E}[\cdot]$	Expectation of $\cdot$	
Erf$[\cdot]$	Error function	
$\hat{\mathrm{L}}\cdot$	Laplace transform	
$O[\cdot]$	Of the order of $\cdot$, or the Big O notation	
$\boldsymbol{p}[\cdot]$	Probability of $\cdot$	
$\mathbf{Var}[\cdot]$	Variance of $\cdot$	
ln$[\cdot]$	Natural logarithm	
$\delta[\cdot]$	Dirac delta function	

Continued on next page

Continued from previous page

Notation	Description	Notes
$\delta_{\bar{i}\bar{j}}$	Kronecker delta	
$\Gamma[\cdot]$	Gamma function	

Other Notations

Notation	Description	Notes
$\Delta\cdot$	Difference of $\cdot$	
$\otimes$	Convolution	
$\lvert\cdot\rangle$	Quantum state	
$\langle\cdot\rangle$	Average	
$\bar{\cdot}$	Integer / index	$\bar{i}, \bar{j}, \cdots$
$\underline{\cdot}$	Integer / index	$\underline{i}, \underline{j}$ [9]
$\overrightarrow{\overrightarrow{\mathbb{1}}}$	Unit tensor	
$:$	Double dot product	
$[\cdots]$	Quantity described by $\cdots$	
$\#[\cdots]$	Number of $\cdots$	

[9] Einstein summation applies when $\bar{i}$ appears with $\underline{i}$: $\sum_{\bar{i}} a_{\bar{i}} b_{\bar{i}} = a_{\bar{i}} b_{\underline{i}}$.

All equilibrium systems are similar, but each non-equilibrium system is non-equilibrium in its own way.

— Leo Tolstoy (Parody)

1 Introduction

Contents

1.1 Background and Motivation **1**
1.2 Relevant Concepts **3**
1.2.1 Warm Dense Matter 3
1.2.2 X-ray Free Electron Lasers (XFELs) 6
1.2.3 Electron Collision Dynamics 10
1.3 Thesis Structure **13**
1.4 Author Contributions **14**

1.1 Background and Motivation

In recent years, there has been an acceleration in the study of high energy density (HED) physics, driven by advances in experimental facilities and diagnostic techniques. HED physics studies matter under extreme conditions of pressure, temperature, and density. It typically deals with matter when the energy density exceeds about $1 \times 10^{11}\,\mathrm{J \cdot m^{-3}}$, or pressures above 1 megabar, where the kinetic energy of the particle is sufficient to overcome its intrinsic structural and electronic integrity. Due to these extreme conditions, the matter is predominantly in the plasma state, where atoms are partially or fully ionised, and the interplay of free electrons and ions, as well as the behaviour of free electrons themselves, plays a crucial role in determining the properties of the plasma.

These plasmas are common in astrophysical environments, planetary cores, and nuclear fusion experiments. In astrophysics, HED plasmas exist in stellar interiors, supernovae, and neutron stars [1, 2]. In planetary science, they are crucial for understanding gas giant planets and planetary formation [3]. In nuclear fusion research, both inertial confinement fusion (ICF) and magnetic confinement fusion (MCF) rely on the understanding of HED plasmas to achieve fusion conditions [4–6]. The study of HED thus underpins a broad range of research, such as the design of ICF systems [7, 8], laboratory astrophysics [9], materials properties under extreme conditions [10], planetary interior modelling [11], and much else [12].

Plasmas of various regimes can be classified by their density and temperature. Generally speaking, plasmas with high temperature and low density behave like an ideal gas and are known as classical plasmas, where the thermal energy dominates over the Coulomb interaction energy. At the other extreme, systems with lower temperatures and higher densities are more similar to solid metals, falling outside the HED regime and becoming a topic of condensed matter physics (for example, the study of liquid metals [13]).

Between these two extremes sits warm dense matter (WDM, also known as warm dense plasma), where neither classical plasma physics nor standard condensed matter approaches is fully applicable. In this regime, the thermal (kinetic) energy of electrons is comparable to both the Fermi energy ($W_{\mathrm{kin}} \sim W_{\mathrm{F}}$) and the potential energy ($W_{\mathrm{kin}} \sim W_{\mathrm{pot}}$). As a result, the electron-electron (e-e) and electron-ion (e-i) interactions become many-body events, and both quantum effects and strong coupling must be considered simultaneously, making WDM theoretically challenging to describe.

The advent of X-ray free electron lasers (XFELs) has opened up new opportunities in the study of WDM. XFELs are capable of generating high-intensity radiation exceeding $1 \times 10^{19}\,\mathrm{W/cm^2}$ with fully-tunable X-ray wavelengths, and have proven capable of creating matter under extreme conditions of temperature, pressure, and density [14–17]. More importantly, owing to their narrow bandwidth and tunable wavelength, XFELs are also excellent tools for probing and diagnosing WDM. X-ray diffraction (XRD) enables direct measurement of atomic structure and phase transitions in WDM [18–22]. The coherent X-ray pulses allow for single-shot diffraction patterns, providing temporal resolution of structural dynamics. Using split-and-delay techniques, XFEL pulses can be separated into pump and probe beams with precisely controlled delays [23], enabling time-resolved measurements of electronic and structural dynamics with femtosecond resolution. X-ray Thomson scattering (XRTS) provides direct measurements of electron temperature, density, and ionisation state through analysis of elastic and inelastic scattering features [24–26]. Additionally, X-ray emission spectroscopy (XES) offers element-specific information about the electronic structure and chemical environment changes in WDM [27].

This thesis focuses on understanding the properties of WDM at the level of electron collisional dynamics. The collisional interactions of charged particles serve as the principal mechanism governing a host of relaxation and equilibration processes in plasma systems [28, 29]. For weakly coupled systems, e-e and electron-ion e-i interactions are most commonly described as binary interactions, assuming cumulative small-angle collisions dominate over hard Coulomb collisions with large deflection angle. With this assumption, the interaction is typically described in terms of a Coulomb logarithm (CL) $\mathrm{Ln}\,[\Lambda]$, where Λ is the ratio of maximum to minimum impact parameters [30]. However, in the WDM regime, this assumption is known to break down due to the many-body interaction nature, requiring either modifications to models within the CL framework, or novel approaches altogether.

1.2 Relevant Concepts

The work presented in this thesis involves the modelling of WDM as well as its interaction with XFELs. This section introduces the key physical concepts and theoretical frameworks necessary for understanding the research. The discussion begins with warm dense matter, focusing on the fundamental parameters that characterise this unique state of matter and the various theoretical approaches used to model it. Following this, the physics of XFELs and their interaction with matter is examined, particularly emphasizing the mechanisms relevant to the experiments. The final part addresses the properties of non-thermal equilibrium states, which play a central role in the relaxation dynamics studied in this work.

1.2.1 Warm Dense Matter

Generally speaking, plasma is usually treated as a system with free electrons and ions interacting through Coulomb interactions. The properties of plasmas can be first characterised by two key dimensionless parameters: the coupling parameter β_{coup} and β_{deg}.

The coupling parameter β_{coup} describes the ratio of Coulomb potential energy to kinetic energy for the free electron system:

$$\beta_{\mathrm{coup}} = \left| \frac{\langle W_{\mathrm{pot}} \rangle}{\langle W_{\mathrm{kin}} \rangle} \right| . \tag{1.1}$$

For sufficiently high temperatures, the kinetic energy is primarily thermal, with $\langle W_{\mathrm{kin}} \rangle \sim \frac{3}{2} k_{\mathbf{B}} T$. Because electrons are lighter and move faster than ions, the properties of WDM are primarily determined by electron behaviour. Following this definition, the electron-electron coupling parameter is:

$$\beta_{\mathrm{coup,e\text{-}e}} = \frac{q_{\mathbf{e}}^2}{4\pi\varepsilon_{\mathbf{0}} r_{\mathrm{ws}}} \frac{1}{\frac{3}{2} k_{\mathbf{B}} T} , \tag{1.2}$$

where $r_{\mathrm{WS}} = (3/4\pi\rho_{N_\mathrm{e}})^{1/3}$ is the average inter-particle spacing (Wigner Seitz radius), ρ_{N_e} is the number density of free electrons, $q_\mathbf{e}$ is the electron charge, $k_\mathbf{B}$ is the Boltzmann constant, and T is the temperature of electrons. As the coupling parameter is only used as an order-of-magnitude estimate, the factor of 3/2 is often omitted, leading to

$$\beta_{\mathrm{coup,e\text{-}e}} \sim \frac{q_\mathbf{e}^2}{4\pi\varepsilon_\mathbf{0} r_{\mathrm{ws}} k_\mathbf{B} T} , \tag{1.3}$$

which is more frequently seen in the literature on plasma physics [31].

While the electron-ion coupling parameter can be defined similarly, the e-e coupling parameter is more commonly used in distinguishing between strongly coupled ($\beta_{\mathrm{coup}} > 1$) and weakly coupled ($\beta_{\mathrm{coup}} < 1$) systems. When weakly coupled, the electrons can be treated as ideal gas to the first order, with interaction seen as a perturbation, whereas for strongly coupled systems, the Coulomb interactions dominate the behaviour, leading to a richer variety of phenomena, including crystallisation [32–34], collisional effects [35, 36], electron rebinding [37] and collective excitations [24].

For systems with higher electron density, quantum effects become important due to the Pauli exclusion principle. The degeneracy parameter β_{deg} characterises the quantum mechanical nature of the system and is defined as:

$$\beta_{\mathrm{deg}} = \frac{T}{T_\mathrm{F}} , \tag{1.4}$$

where T_F is the Fermi temperature given by:

$$T_\mathrm{F} = \frac{\hbar^2}{2m_\mathbf{e}k_\mathbf{B}}(3\pi^2\rho_{N_\mathrm{e}})^{2/3} , \tag{1.5}$$

where $m_\mathbf{e}$ is the mass of electrons, ρ_{N_e} is the number density of the electrons and $\hbar$ is the reduced Planck constant.

When $\beta_{\mathrm{deg}} \gg 1$, the system can be treated classically with electrons seen as point-like particles, while $\beta_{\mathrm{deg}} \ll 1$, the electron system is strongly degenerate and must be treated quantum mechanically using methods such as density functional theory (DFT) [38, 39], linear response theory (LRT) [40] or quantum Monte Carlo (QMC) [41].

Importantly, for degenerate systems at the aero temperature limit, their kinetic energy is characterised by the Fermi energy instead of $k_\mathbf{B}T$:

$$\langle W_{\mathrm{kin}} \rangle = \frac{3}{5} k_\mathbf{B} T_\mathrm{F} . \tag{1.6}$$

Therefore, Eq. 1.2 should be modified as

$$\beta_{\mathrm{coup}} = \frac{q_\mathbf{e}^2}{4\pi\varepsilon_\mathbf{0} r_{\mathrm{ws}}} \frac{1}{\frac{3}{5}k_\mathbf{B}T_\mathrm{F}} . \tag{1.7}$$

For this reason, plasma with extremely high density but low temperature may also be weakly coupled due to its high Fermi energy. Examples of such systems include those at surfaces of

white dwarfs with temperatures of only a few eV but densities several orders of magnitude higher than that of a solid under ambient conditions [42].

These two parameters, β_{coup} and β_{deg}, divide the temperature-density phase diagram of plasma into distinct regions, as illustrated in Fig. 1.1. The blue dashed lines represent contours

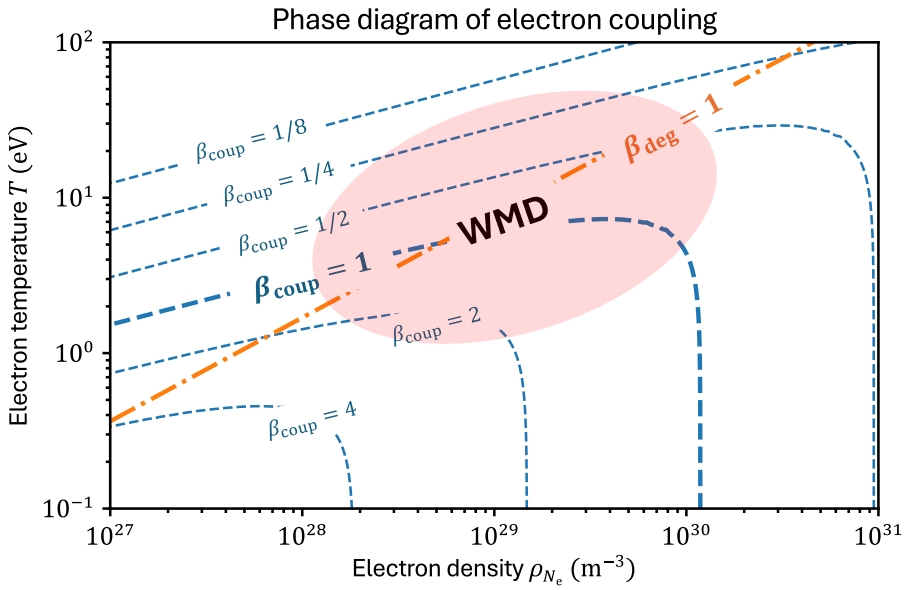


Figure 1.1: Phase diagram of a fully-ionised hydrogen plasma in the temperature-density plane. The blue dashed lines show contours of constant coupling parameter β_{coup}. The orange dash-dotted line represents $\beta_{\text{deg}} = 1$, separating classical ($\beta_{\text{deg}} > 1$) and quantum ($\beta_{\text{deg}} < 1$) regimes. The warm dense matter (WDM) regime, highlighted in pink, exists in the region where both coupling and degeneracy parameters are of order unity.

of constant coupling parameter, while the orange dash-dotted line represents $\beta_{\text{deg}} = 1$. The upper region represents ideal classical plasma, characterised by weak coupling ($\beta_{\text{coup}} \ll 1$) and negligible degeneracy ($\beta_{\text{deg}} \gg 1$). The left region contains strongly coupled ($\beta_{\text{coup}} \gg 1$) but classical plasmas. At high densities, the lower region represents strongly coupled and degenerate matter, while the right region describes weakly coupled but degenerate systems that behave similarly to an ideal Fermi gas.

The WDM regime (highlighted in pink) typically exists where both parameters are of order unity, with temperatures ranging from 1 eV to a few tens of eV, and densities typically of a solid metal. These systems are particularly difficult to model as approximations where one effect dominates another are no longer applicable. This complexity makes WDM a challenging but crucial area of research, particularly relevant to understanding planetary interiors, inertial confinement fusion, and laser-matter interactions. The study of WDM thus represents an active field in HED physics.

1.2.2 X-ray Free Electron Lasers (XFELs)

Because the formation of plasma is usually [1] accompanied by heating and volume expansion, experimental creation and study of WDM in laboratory conditions has historically been difficult. The simultaneous requirements of high temperature and high density were particularly challenging to achieve. However, in the past decade, X-ray Free Electron Lasers have demonstrated their unique capability of isochorically heating matter to create well-defined WDM states. Specifically, plasmas with temperatures of hundreds of eV while remaining at exactly solid density have been created at facilities such as the Linac Coherent Light Source (LCLS) and European XFEL (EuXFEL) through isochoric X-ray heating. This remarkable capability is enabled by the ultrashort (femtosecond) pulse duration of XFEL beams. During a typical ∼30 fs XFEL pulse, the sample has no time to volumetrically expand, thus remaining at its original solid density. This approach enables the study of transient warm dense plasmas under well-defined thermodynamic conditions densities, electron temperatures and ion temperatures[15, 43]. XFELs are also distinguished by several key characteristics beyond their ultrashort pulses, including fully tunable wavelength, narrow bandwidth, and ultrahigh brilliance. These properties make them ideal not only for generating matter under precise conditions but also for serving as powerful diagnostic probes. As a result, XFELs have become indispensable tools across multiple disciplines beyond WDM and HED science, extending to atomic, molecular and optical (AMO) physics, condensed matter physics, materials science, chemistry, and biology.

First proposed by John Madey in 1971 [44], and later experimentally demonstrated by Luis R. Elias [45], XFELs represent a revolutionary advancement in laser technology. FLASH (Free-Electron Laser in Hamburg) became the first operational XFEL facility for user experiments in 2005, demonstrating SASE lasing in the extreme ultraviolet and soft X-ray regime. Since then, several XFEL facilities have been established worldwide, including:

- **Germany:** FLASH and European XFEL at DESY (Deutsches Elektronen-Synchrotron) in Hamburg
- **United States:** LCLS at SLAC (Stanford Linear Accelerator Center) National Accelerator Laboratory in Stanford
- **Japan:** SACLA (SPring-8 Angstrom Compact Free Electron Laser) at SPring-8 (Super Photon ring-8 GeV) in Harima
- **South Korea:** PAL-XFEL at PAL (Pohang Accelerator Laboratory) in Pohang

[1] This refers to the plasmas generated during welding or semiconductor manufacturing, which typically starts from energising a gas.

- **Italy:** FERMI (Free Electron Laser Radiation for Multidisciplinary Investi-gations) at Elettra in Trieste
- **Switzerland:** SwissFEL (Swiss XFEL) at PSI (Paul Scherrer Institute) in Villigen
- **China:** SXFEL (Shanghai XFEL) at SARI (Shanghai Advanced Research Institute) in Shanghai

Several new facilities are currently under development or in the planning phase. Notable examples include the SHINE (Shanghai High Repetition Rate XFEL and Extreme Light Facility) project in China and the proposed UK-XFEL in the UK. Additionally, LCLS has been recently upgraded to LCLS-II, which allows operation at a higher repetition rate and will continue to be upgraded to LCLS-II-HE, which allows for operation at higher photon energy. These emerging facilities promise to expand the frontiers of X-ray science with enhanced capabilities and improved accessibility to the international scientific community.

The operation principle of XFELs can be briefly divided into three steps: electron acceleration, undulation, and self-amplified spontaneous emission (SASE). Electrons are first accelerated by a linear accelerator (Linac) to relativistic speeds, typically reaching energies of several GeV. These relativistic electrons then enter an undulator - a periodic array of

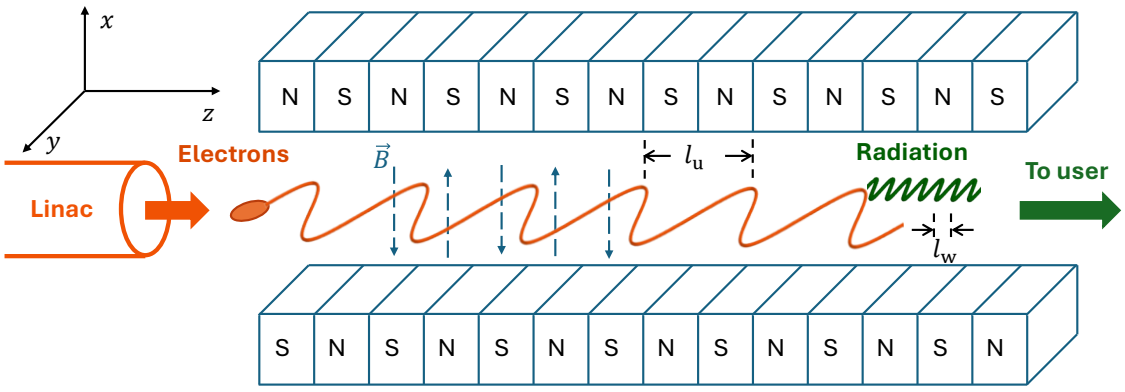


Figure 1.2: The operation principle of XFEL. Electrons accelerated by a linear accelerator enter an undulator consisting of alternating magnetic poles. The periodic magnetic field forces the electrons to oscillate transversely, causing them to emit synchrotron radiation.

magnets aligned along the electron beam path (z direction). As illustrated in Figure 1.2, the undulator magnets are positioned with alternating north (N) and south (S) poles, generating a magnetic field perpendicular to the electron travel direction (z direction). The magnetic field strength B_x varies sinusoidally along the beam axis according to:

$$B_x = B_0 \mathrm{Cos}\left[2\pi \frac{z}{l_u}\right] , \tag{1.8}$$

where l_{u} is the spatial period of the magnetic (known as the undulator period), and B_0 is the amplitude of the magnetic field strength.

Under the influence of this periodic magnetic field, electrons execute transverse oscillations while propagating forward, following a sinusoidal trajectory. This oscillatory motion causes the electrons to emit synchrotron radiation whose wavelength l_{w} is given by:

$$l_{\mathrm{w}} = \frac{l_{\mathrm{u}}}{2\beta_{\mathrm{L}}^2}\left(1 + \frac{1}{2}\left(\frac{q_{\mathbf{e}} B_0 l_{\mathrm{u}}}{2\pi m_{\mathbf{e}} v_{\mathbf{c}}}\right)^2\right) , \tag{1.9}$$

where β_{L} is the Lorentz factor of the electrons, and $v_{\mathbf{c}}$ the speed of light in vacuum. For such emission, individual electrons initially radiate randomly and out of phase, producing incoherent radiation. However, due to the radiation field itself, the electrons undergo spatial modulation along their propagation direction. Electrons with a positive phase relative to the radiation field lose energy to the field and slow down, while those with a negative phase gain energy from the field and speed up. This mechanism, known as micro-bunching, causes

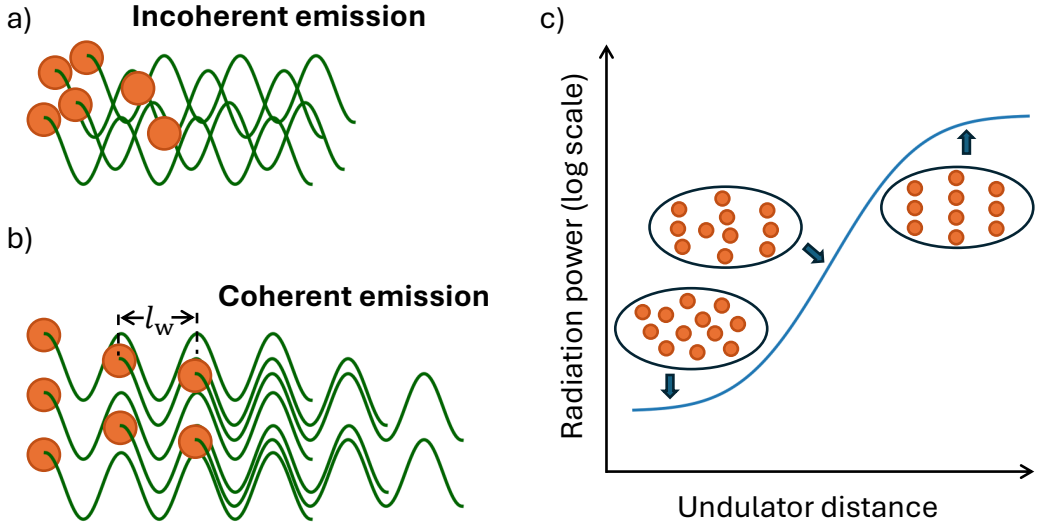


Figure 1.3: Illustration of the SASE process in XFEL. (a) Initially, electrons emit radiation incoherently, with random phases. (b) Through interaction with the radiation field, electrons become microbunched with spacing equal to the radiation wavelength l_{w}, leading to coherent emission. (c) Evolution of radiation power along the undulator length, showing exponential growth due to the SASE process. The insets show the progression of electron bunching from initial random distribution to well-defined microbunches that enable coherent emission.

slow electrons to catch up with fast electrons. Therefore, electrons will form discrete bunches separated by one radiation wavelength. As these micro-bunched electrons emit in phase with each other, their radiation fields add constructively, leading to coherent emission and exponential growth of the radiation intensity along the undulator, as shown in Fig. 1.3. The exponential growth of radiation power through this process cannot continue infinitely and will eventually reach saturation. This occurs when the electron beam has transferred a significant

portion of its kinetic energy to the radiation field. At this point, the energy spread of the electron beam becomes too large to maintain the resonant condition necessary for further amplification. Nevertheless, the saturation power can reach levels of 10-100 GW in modern XFELs. This self-organizing process of the electron beam is the essence of Self-Amplified Spontaneous Emission (SASE), which enables XFELs to achieve unprecedented brilliance compared to conventional synchrotron sources. Fig. 1.4 demonstrates the peak brightness of several selected XFEL and synchrotron facilities.

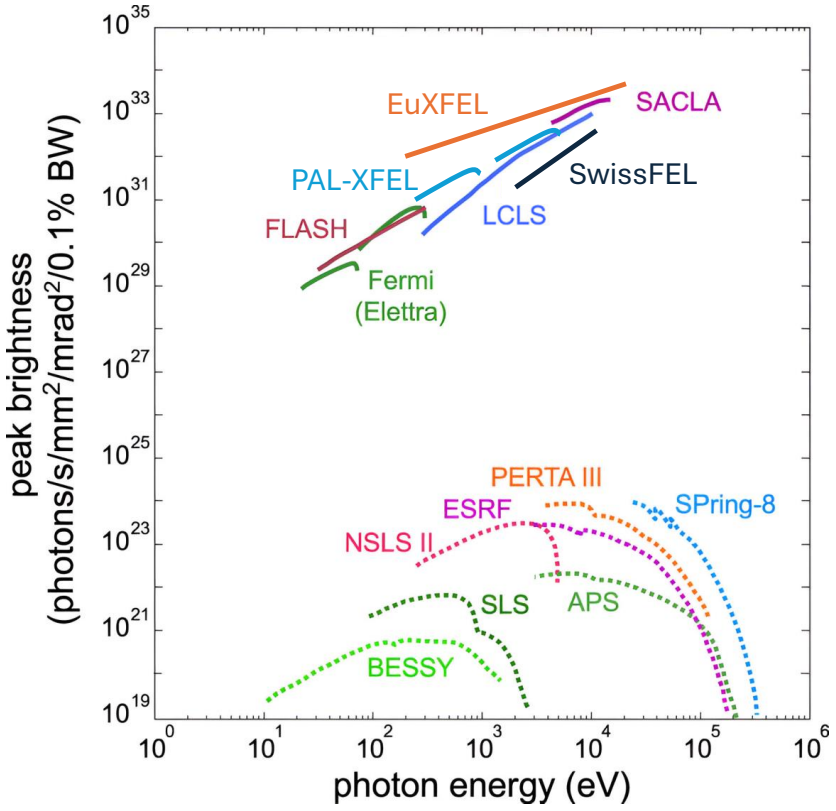


Figure 1.4: Peak Brightness of several selected XFEL and synchrotron facilities. Figure adapted from [46]

When a beam of XFEL photons hits a thin metal target, photo-ionisation (PI) of inner-shell electrons creates core-holes in the atomic structure. These core-holes can relax through two competing processes: radiative decay (emission of a photon) or Auger decay (AD). For low to mid-Z elements, Auger decay is the dominant relaxation mechanism [47]. Because the electrons produced by these mechanisms are highly energetic (typically hundreds or thousands of eV), they serve as the major heating mechanism for the target material. As the target has no time to expand, the free electron density exceeds that of an ambient solid metal. This enables the creation of well-defined warm, dense matter states. The electrons created through

photo-ionisation and subsequent Auger processes are initially not in thermal equilibrium with the lower energy valence electrons. The system gradually approaches thermal equilibrium through various collision processes, including collisional ionisation (CI), recombination (CR), excitation (CE), and de-excitation (CD). These collisional processes typically occur very rapidly, driving the electron population toward thermal equilibrium on femtosecond timescales ([48, 49]). For this reason, plasmas are usually modelled assuming Local Thermal Equilibrium (LTE), where the electron energy distribution can be described by a single temperature. However, for the purposes of this thesis, the electrons are modelled in a non-equilibrium state to explicitly resolve the electron collisional dynamics.

1.2.3 Electron Collision Dynamics

The study of electron collisional dynamics is fundamental to understanding plasma transport properties. For example, the electrical conductivity in metals is traditionally described through electron-ion collisions within the Drude model [50]:

$$\sigma_{q,\mathrm{dc}} = \frac{\rho_{N_\mathrm{e}} q_{\mathbf{e}}^2 t_{\text{e-i}}}{m_{\mathbf{e}}} \tag{1.10}$$

where $t_{\text{e-i}}$ is the electron-ion collision time. This can be understood through a simple model where electrons gain constant acceleration due to the external electric field but collide with static ions and have an average velocity of 0 after collision every $t_{\text{e-i}}$ [50]. Electron-electron collisions are typically neglected in this picture as they conserve the overall energy and momentum in the charge carrier system and, thus, do not directly contribute to electrical resistivity. More detailed theoretical treatments, such as the Bhatnagar-Gross-Krook (BGK) model [51, 52], have been developed to describe electron transport in metals while maintaining this basic picture. This model assumes a constant collision time for all electrons and is, therefore, also referred to as relaxation time approximation (RTA).

Instead of considering individual particles, RTA considers the evolution of the electron distribution function $\varrho[\vec{r}, \vec{v}, t]$ in phase space. The electron distribution function for an N-particle system indicates the number of electrons within the infinitesimal volume element $\mathrm{d}\Upsilon_{\vec{r}}\mathrm{d}\Upsilon_{\vec{v}} := \mathrm{d}x\mathrm{d}y\mathrm{d}z\mathrm{d}v_x\mathrm{d}v_y\mathrm{d}v_z$ in phase space. This statistical approach effectively reduces the degrees of freedom from $6N$ to 6, making the problem tractable. The temporal evolution of the electron distribution function is governed by the Boltzmann equation:

$$\frac{\partial \varrho}{\partial t} + \vec{v} \cdot \vec{\nabla}_{\vec{r}} \varrho + \frac{\vec{F}}{m_{\mathbf{e}}} \cdot \vec{\nabla}_{\vec{v}} \varrho = \hat{\mathcal{O}}_{\mathrm{coll}}[\varrho] \ , \tag{1.11}$$

where $\vec{F}$ represents external forces acting on the electrons. Under the RTA, the collision term is approximated as:

$$\hat{\mathcal{O}}_{\mathrm{coll}}[\varrho] = -\frac{\varrho - \varrho_0}{t_{\mathrm{rlx}}} \ , \tag{1.12}$$

where t_{rlx} is a constant known as the characteristic relaxation time and ϱ_0 is the equilibrium distribution function, typically taken as the Fermi-Dirac distribution at low temperature and Maxwell-Boltzmann distribution at high temperature. This approximation assumes that collisions drive the system toward equilibrium at a rate proportional to the deviation from equilibrium. It can be shown that using RTA, one can retrieve the Drude model [53]:

$$\sigma_{q,\mathrm{dc}} = \frac{\rho_{N_\mathrm{e}} q_\mathbf{e}^2 t_{\mathrm{rlx}}}{m_\mathbf{e}}. \tag{1.13}$$

However, this model fails in plasma systems where long-range, small-angle cumulative Coulomb collisions dominate the dynamics. Unlike the simple binary collision picture in metals, electrons in plasmas lose their energy through multiple consecutive small-angle deflections. This problem was first solved by Spitzer and Härm [30], who developed a model based on kinetic theory where both e-e and e-i collisions are considered. Contrary to Drude's picture, e-e collision is also considered in this model. While these collisions do not directly contribute to resistance, they play a crucial role in redistributing energy among electrons, affecting the overall transport properties. Importantly, this cumulative small-angle scattering process cannot be described within RTA, as a well-defined relaxation time cannot be consistently established [40, 54, 55].

The core of Spitzer and Härm's treatment lies in replacing the simple collision term with the Fokker-Planck collision operator, which accounts for the cumulative effect of many small-angle deflections. The transport coefficients in this framework are expressed in terms of the Coulomb Logarithm (CL)[2]:

$$\mathrm{Ln}\left[\Lambda\right] = \mathrm{Ln}\left[\frac{r_{\mathrm{max}}}{r_{\mathrm{min}}}\right] . \tag{1.14}$$

The CL emerges naturally when considering the cumulative impact of all plasma particles on a test electron with initial energy $\frac{1}{2} m_\mathbf{e} v^2$ through Coulomb interactions. When integrating over all possible impact parameters r_b, a term $\displaystyle\int \frac{\mathrm{d}r_\mathrm{b}}{r_\mathrm{b}}$ appears, which would diverge logarithmically due to the long-range nature of the Coulomb force. This divergence reflects the failure of the small-angle Coulomb scattering assumption at both extremes of small and large impact parameters, thus necessitating the introduction of cutoff parameters r_{max} and r_{min}. Typically, r_{min} represents the minimal impact parameter for two-body collisions, taken as the classical distance of closest approach

$$r_{\mathrm{min}} = \frac{q_\mathbf{e}^2}{4\pi\epsilon_0 k_\mathbf{B} T} . \tag{1.15}$$

The minimal impact parameter r_{min} effectively distinguishes between small-angle and large-angle collisions. For impact parameters below r_{min}, the picture of cumulative small-angle scattering breaks down, leading to significant deflection angles and large energy and

[2] See Sec. 2.2 for details.

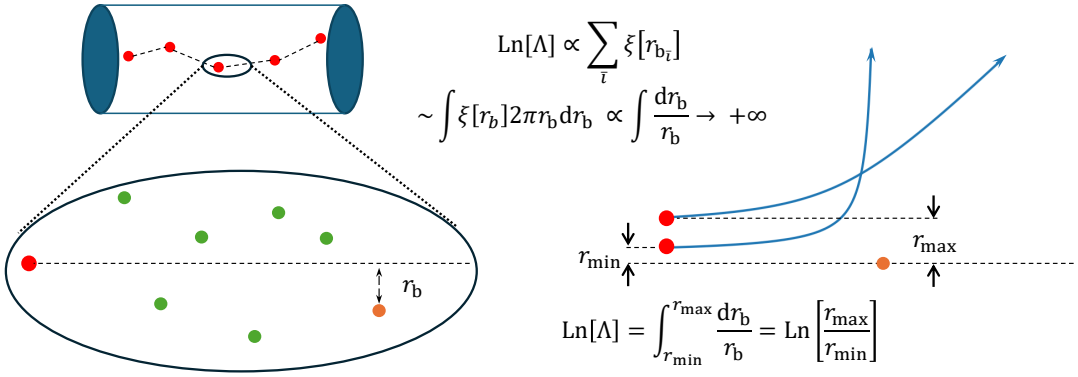


Figure 1.5: Illustration of the physical origin of the Coulomb logarithm. The top left shows an electron (red) traversing through a plasma, experiencing multiple small-angle deflections. The magnified view shows the impact parameter r_b between the test electron and background particles (green). The right panel demonstrates how the integral over impact parameters diverges logarithmically, necessitating the introduction of cutoff parameters r_{min} and r_{max}. Here ξ is some function indicating the impact due to one single electron.

momentum transfer. The maximum impact parameter r_{max} is determined by the plasma Debye length, beyond which the Coulomb interaction is effectively screened:

$$r_{\mathrm{max}} = \sqrt{\frac{\epsilon_0 k_\mathbf{B} T}{\rho_{Ne} q_\mathbf{e}^2}} \,. \tag{1.16}$$

While this framework works well for low-density plasmas where the Debye length is much larger than the average interparticle distance, it breaks down at solid density. In dense plasmas, where $\rho_{Ne} \gtrsim 10^{23}\,\mathrm{cm}^{-3}$, the Debye length becomes comparable to or smaller than the interparticle spacing, and CL approach 0 or even negative values. Thus, alternative theoretical frameworks become necessary when dealing with dense plasmas. Nevertheless, the classical CL model's simplicity and computational efficiency have contributed to its continued widespread use in simulation codes [57].

Numerous efforts have been made to extend the validity of the CL to higher density regimes while maintaining its tractable form. Within the semi-classical framework of Coulomb or Yukawa potential scattering, several approaches have emerged. Notable developments include the application of Born's approximation to the two-body scattering [58] and the implementation of partial wave analysis methods [59, 60]. These modifications attempt to better capture the physics of dense plasmas while preserving the computational advantages of the original CL formulation. Beyond these semi-classical extensions, fully quantum mechanical treatments have also been developed that lie within the framework of the linear response theory (LRT) [13, 61–63], which provides a systematic way to include quantum effects in

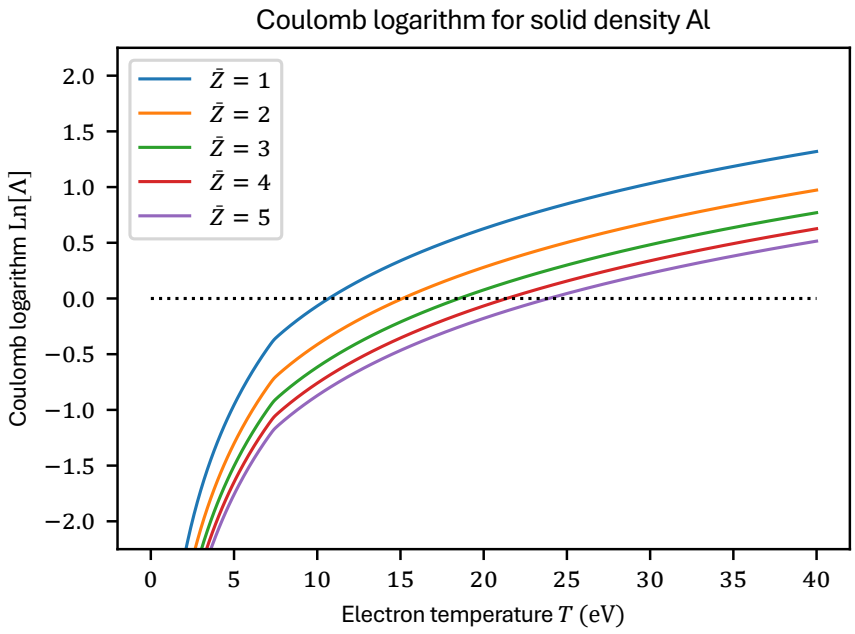


Figure 1.6: Breakdown of Coulomb Logarithm in solid density Al. The expression of CL is taken from [56], with some quantum mechanical corrections considered.

transport processes, or other advanced approaches [64–67]. Chapter 2 provides a thorough review of the theoretical developments in this field.

Despite significant advances on the theoretical side, experimental validation of these models remains limited. This limitation stems not only from the ultrafast timescales of the collision processes but also from the challenge of isolating and distinguishing these collisions from other concurrent e-i interactions in dense plasma environments.

This thesis presents a novel approach that utilises non-thermal electrons in WDM generated by a free-electron laser. Electrons generated directly through PI or Auger processes initially possess well-defined energies significantly above the thermal background. As these electrons thermalise via collisions with both the background electrons and ions, they provide a unique opportunity to investigate electron collision dynamics in dense plasma. The well-defined initial energy and the ability to track the thermalisation process through various experimental signatures offer a new window into testing theoretical predictions of electron transport in dense plasma systems.

1.3 Thesis Structure

This thesis is organised into six chapters that systematically develop the theoretical framework, experimental techniques, and results of studying electron relaxation dynamics in warm dense matter:

Chapter 1 provides the background and motivation for studying electron collision dynamics in warm dense matter, introducing key concepts including warm dense matter, X-ray Free Electron Lasers (XFELs), and electron collision dynamics.

Chapter 2 presents a comprehensive literature review of the theoretical framework developed in the past several decades on free electron relaxation dynamics. Beginning with classical treatments in ideal plasmas through the Boltzmann-Vlasov equation and Fokker-Planck collision operator, it progresses to quantum mechanical descriptions necessary for dense plasma systems. Special attention is given to the limitations of conventional approaches and recent theoretical developments.

Chapter 3 introduces a novel approach to studying electron thermalisation and collision times using XFEL-driven non-thermal electrons. It details the creation and observation of non-thermal electron populations, supported by collisional-radiative simulations that utilised the `CCFLY` atomic kinetics code. It demonstrates the feasibility of using these electrons to probe collision dynamics, especially the potential of utilizing a pulse duration scan of XFEL to measure the electron collision time.

With the feasibility demonstrated through the collisional-radiative simulation, Chapter 4 focuses on experimental techniques developed for non-thermal electron measurements, with particular emphasis on the Single-Photon Counting (SPC) technique. It covers detection methods, data processing algorithms, and specific applications to radiative recombination and inverse Compton scattering measurements.

Chapter 5 reports the experiment fielded at the LCLS XFEL facility, including experimental design, measurements of ultrafast electron collision times, and detailed analysis of the results. The chapter concludes with the electron relaxation rates measured in terms of e-e and e-i collision times.

Finally, Chapter 6 summarises the work of this thesis, discusses its implications for the understanding of electron dynamics in warm dense matter, and suggests directions for future research.

1.4 Author Contributions

It has to be stated that the research conducted in this thesis, similar to all other research, emerges from extensive collaborations among international teams across multiple institutions. The fundamental concept of investigating electron collisional dynamics through non-thermal electrons was originally proposed by Prof. Sam M. Vinko and Prof. Justin S. Wark, who supervised this work. Their intellectual contributions are deeply interwoven throughout this research and have significantly shaped its development.

The theoretical framework presented in Chapters 1 and 2 synthesises existing literature to provide a comprehensive foundation for understanding electron dynamics in warm dense matter. While containing no original theoretical developments, these chapters establish the essential context for the novel experimental approaches and results presented in subsequent chapters.

The innovative method of measuring electron collision times using XFEL pulse duration scans (Chapter 3) represents the author's primary theoretical contribution. This work builds upon the `CCFLY` code, developed by numerous contributors over many years [17, 27, 48, 68–70]. Particular acknowledgement is due to Dr. Quincy van den Berg and Dr. Shenyuan Ren for their development of the Fokker-Planck module in the non-thermal version of `CCFLY`.

The Single-Photon Counting (SPC) methodology detailed in Chapter 4 evolved from collaborative discussions with Dr. Oliver Humphries, who made substantial contributions to the deconvolution algorithm (Sec. 4.2.3). Mr. Karim Alaa-El-Din significantly enhanced the SPC codes, while the author independently developed their novel application, particularly the unprecedented use of inverse Compton scattering (ICS) to probe non-thermal electron distributions.

The LCLS experiment (Chapter 5) was conceived and led by the author as a co-principal-investigator. The experimental design, organisation, and implementation benefited from crucial contributions from Dr. Bob Nagler, Dr. Hae Ja Lee, Dr. Dimitri Khahgani, Dr. Thomas Preston, Dr. Oliver Humphries, Dr. Cèline Crèpisson, Dr. Thomas Gawne, Mr. Alessandro Forte, Mr. Thomas Campbell, Mr. Karim Alaa-El-Din, and Mr. Domenic Peake. The post-experimental analysis correlating experimental observables with simulation results was conducted with valuable assistance from Mr. Yizhen Wang. Additionally, the author acknowledges, in particular, Prof. Sam M. Vinko's encouragement to pursue independent research directions and explore research initiatives freely, which was instrumental in the success of this experiment.

For the sake of completeness, the author's list of publications is included.

- Shenyuan Ren et al. "Non-thermal evolution of dense plasmas driven by intense x-ray fields". In: *Communications Physics* 6.1 (2023), p. 99
- Josef Krása et al. "Ion emission from warm dense matter produced by irradiation with a soft x-ray free-electron laser". In: *Matter and Radiation at Extremes* 9.1 (Nov. 2023)
- Céline Crépisson et al. *Shock-driven amorphization and melt in Fe_2O_3*. 2024. arXiv: `2408.17204 [cond-mat.mtrl-sci]`
- A. Amouretti et al. *Phase transitions of Fe_2O_3 under laser shock compression*. 2024. arXiv: `2402.18432 [cond-mat.mtrl-sci]`

- Y.-F. Shi et al. “Exploring relaxation dynamics in warm dense plasmas by tailoring non-thermal electron distributions with a free electron laser”. In: *Physics of Plasmas* 31.8 (Aug. 2024)
- Alessandro Forte et al. “Resonant inelastic x-ray scattering in warm-dense Fe compounds beyond the SASE FEL resolution limit”. In: *Communications Physics* 7.1 (Aug. 2024)
- Alessandro Forte et al. *Methods for energy dispersive x-ray spectroscopy with photon-counting and deconvolution techniques*. 2024. arXiv: `2411.16581 [physics.app-ph]`

We hold these truths to be thermodynamically evident, that all states are created equal, that they are occupied by particles with certain unequivocal probability, and that among these are Energy, Entropy, and the pursuit of Equilibrium.

— Ludwig Boltzmann (Parody)

2

Free Electron Relaxation Dynamics

Contents

2.1 Introduction 17
2.2 Electron Relaxation in Ideal Plasmas 19
2.2.1 Boltzmann-Vlasov Equation 19
2.2.2 Landau-Fokker-Planck Collision Operator 23
2.2.3 Coulomb Logarithm and Collisional Times 28
2.3 Electron Relaxation in Quantum Plasmas 33
2.3.1 Quantum Mechanical Corrections for Coulomb Logarithms 33
2.3.2 Quantum-Landau-Fokker-Planck Collision Operator 41
2.4 Summary 43

2.1 Introduction

Electron relaxation dynamics play a fundamental role in warm, dense plasmas, which are characterised by their high electron density. The relaxation processes govern essential transport properties through electron-electron and electron-ion interactions, determining phenomena such as electrical and thermal conductivity [28, 30, 75], temperature equilibration [29, 67], and stopping power [76]. Understanding these dynamics is crucial for applications ranging from inertial confinement fusion to astrophysical phenomena.

Although the theory of individual two-body charged particle interactions (collisions) is well established, the collisional dynamics of such a many-body system presents significant theoretical challenges. The complexity of modelling warm dense matter roots fundamentally from the huge number of free electrons interacting simultaneously in the system. Even when modelled with classical physics, the complete description of such a many-body system requires consideration of the full phase space (-space), which is a $6N$-dimensional space - three position $\vec{r}_{\bar{i}}$ and three momentum coordinates $\vec{p}_{\bar{i}}$ for each particle. The -space represents all possible combinations of particle positions and momenta, and the state of the system at any instant is represented by a single point in the -space. The temporal evolution of this point follows Hamilton's equations of motion:

$$\dot{\vec{r}}_{\bar{i}} = \vec{\nabla}_{\vec{p}_{\bar{i}}}\mathcal{H}, \quad \dot{\vec{p}}_{\bar{i}} = -\vec{\nabla}_{\vec{r}_{\bar{i}}}\mathcal{H} \ , \tag{2.1}$$

where $\mathcal{H}$ is the system Hamiltonian. With typical solid-density plasmas containing $N \sim 10^{23}$ particles per cubic centimetre, direct computational approaches become practically impossible. Quantum mechanical effects, which become significant at high densities or low temperatures, add further complications through the many-body wave function and electron degeneracy effects.

This problem of dimensionality was first solved by Boltzmann in 1872, who established the transport equation that now bears his name. His fundamental insight was to introduce the single-particle distribution function $\varrho[\vec{r}, \vec{v}, t]$ in a reduced 6-dimensional phase space (-space), consisting of three-dimensional position and velocity coordinates. The distribution function represents the density of particles within an infinitesimal volume element $\mathrm{d}\Upsilon_{\vec{r}}\mathrm{d}\Upsilon_{\vec{v}} := \mathrm{d}x\mathrm{d}y\mathrm{d}z\mathrm{d}v_x\mathrm{d}v_y\mathrm{d}v_z$ in the -space, such that $\varrho(\mathbf{r}, \mathbf{v}, t)\mathrm{d}\Upsilon_{\vec{r}}\mathrm{d}\Upsilon_{\vec{v}}$ gives the probable number of particles in this phase space element at time t. The distribution function satisfies the normalisation condition:

$$\int \varrho[\vec{r}, \vec{v}, t]\mathrm{d}\Upsilon_{\vec{r}}\mathrm{d}\Upsilon_{\vec{v}} = N \ . \tag{2.2}$$

This statistical approach significantly reduces the complexity of the problem by decreasing the degrees of freedom from 6N to 6, while still capturing the essential physics of the many-body system. The price paid for this reduction is that the detailed correlations between particles are replaced by statistical averages, and the evolution equations become non-linear.

This chapter first introduces the treatment of electron relaxation dynamics in an ideal plasma using the Boltzmann transport equation. The foundational results are primarily from Landau's pioneering work on Coulomb collisions in 1936 [77][1], and Spitzer's seminal work on transport processes [30]. In this classical treatment, an artificial cut-off known as

[1] Due to language barriers, the author did not read the original work by Landau

the Coulomb logarithm is introduced to handle the divergent nature of Coulomb collisions. However, this approach becomes problematic in warm, dense matter where strong coupling effects become significant. The discussion then proceeds to modern treatments, focusing on various theoretical approaches to address these limitations: modifications to the Coulomb logarithm and quantum mechanical collision operators. The chapter concludes by introducing recent advances in electron relaxation dynamics, including developments in linear response theory and quantum kinetic theory, which provide more rigorous treatments for strongly coupled and degenerate systems.

2.2 Electron Relaxation in Ideal Plasmas

The discussion of electron relaxation dynamics begins with ideal plasmas, which are characterised by weak coupling and non-degeneracy. Although collisions do not dominate the dynamics in ideal plasmas as they do in neutral gases due to the relatively small collision frequency compared with the plasma frequency [78], Landau established the theory of electron relaxation by cumulative small-angle Coulomb collisions. Building upon this foundation, Spitzer derived the transport coefficients that now form the cornerstone of classical plasma transport theory [30].

For warm dense plasmas, where both coupling and degeneracy effects become non-negligible, collisional processes take on importance. However, the collision theory developed for ideal plasmas cannot be directly applied to dense plasma states, as the fundamental framework of the Coulomb logarithm breaks down (as discussed in detail in Sec. 1.2.3). This breakdown occurs when the plasma coupling parameter approaches or exceeds unity, indicating that the key assumptions of binary collisions and weak coupling are no longer valid. Nevertheless, understanding the collision theory in ideal plasmas remains crucial as it provides the theoretical framework from which more sophisticated treatments are developed.

2.2.1 Boltzmann-Vlasov Equation

When Boltzmann derived his transport equation for ideal gases, his famous molecular chaos assumption (Stosszahlansatz) led to a collision integral operator that accounts for the change in the distribution function due to binary particle collisions, which reads:

$$\begin{aligned}&\hat{\mathcal{O}}_{\mathrm{coll}}[\varrho][\vec{r},\vec{v},t]\\&\quad=\iint\left(\varrho[\vec{r},\vec{v}',t]\varrho[\vec{r},\vec{v}'_\star,t]-\varrho[\vec{r},\vec{v},t]\varrho[\vec{r},\vec{v}_\star,t]\right)|\vec{v}_\star-\vec{v}|\frac{\mathrm{d}S}{\mathrm{d}\Omega'}\mathrm{d}\Omega'\mathrm{d}\Upsilon_{\vec{v}_\star}\ ,\end{aligned}\tag{2.3}$$

where $\frac{\mathrm{d}S}{\mathrm{d}\Omega'}$ indicate the differential cross-section of the collision, $\vec{v}_\star$ indicates the velocity of the incident particle, and $\vec{v}'$ and $\vec{v}'_\star$ indicates the velocity of the particles after collision, with the

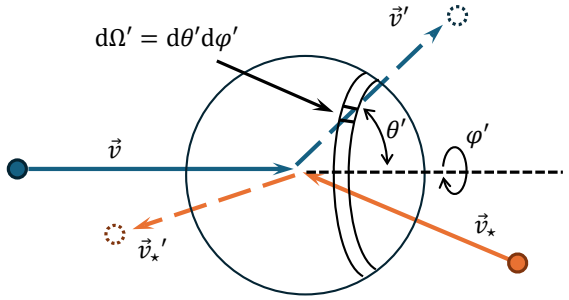


Figure 2.1: two-body collision in the Boltzmann equation. A test particle with velocity $\vec{v}$ collides with an incident particle with velocity $\vec{v}_\star$. The test particle is scattered into the solid angle $d\Omega'$ defined by the scattering angles θ' and φ'. Due to the conservation of energy and momentum, these two angles determine the velocities after collision $\vec{v}'$ and $\vec{v}'_\star$.

test particle having velocity $\vec{v}'$ after collision being scattered into solid angle $d\Omega' = d\theta' d\varphi'$ (Fig. 2.1). Due to the conservation of energy and momentum, $\vec{v}'$ and $\vec{v}'_\star$ are not completely independent but are functions of the scattering angles θ' and φ'. The general form of the Boltzmann transport equation is therefore:

$$\begin{aligned} &\frac{\partial \varrho}{\partial t}[\vec{r},\vec{v},t] + \vec{v}\cdot\vec{\nabla}_{\vec{r}}\varrho[\vec{r},\vec{v},t] + \frac{\vec{F}}{m}\cdot\vec{\nabla}_{\vec{v}}\varrho[\vec{r},\vec{v},t] \\ &\qquad = \iint \left(\varrho[\vec{r},\vec{v}',t]\varrho[\vec{r},\vec{v}'_\star,t] - \varrho[\vec{r},\vec{v},t]\varrho[\vec{r},\vec{v}_\star,t]\right) v_\mathrm{r}\frac{\mathrm{d}S}{\mathrm{d}\Omega'}\mathrm{d}\Omega'\mathrm{d}\Upsilon_{\vec{v}_\star} \ , \end{aligned} \tag{2.4}$$

where $v_\mathrm{r} := |\vec{v}_\star - \vec{v}|$ is the relative speed.

For neutral ideal gases, the force term $\vec{F}$ typically represents external forces such as gravity, which can often be neglected. However, in plasmas, the force term becomes crucial due to the collective behaviour of charged particles. Vlasov's key insight was to treat plasmas as ideal gases of charged particles under the influence of self-consistent electromagnetic fields. In the collisionless limit, where binary collisions are less important than collective effects, the collision term vanishes. This leads to the Vlasov equation:

$$\frac{\partial \varrho}{\partial t} + \vec{v}\cdot\vec{\nabla}_{\vec{r}}\varrho + \frac{q}{m}(\vec{E} + \vec{v}\times\vec{B})\cdot\vec{\nabla}_{\vec{v}}\varrho = 0 \ . \tag{2.5}$$

where $\vec{E}$ and $\vec{B}$ should be understood as ensemble-averaged fields, indicating the mean-field nature of this approximation. These fields are determined self-consistently through Maxwell's equations:

$$\begin{cases} \vec{\nabla}_{\vec{r}}\cdot\vec{E} = \dfrac{\rho_q}{\varepsilon_\mathbf{0}} = \dfrac{q}{\varepsilon_\mathbf{0}}\displaystyle\int \varrho \mathrm{d}\Upsilon_{\vec{v}} \\[2ex] \vec{\nabla}_{\vec{r}}\times\vec{B} = \mu_0\vec{j}_q + \mu_0\varepsilon_\mathbf{0}\dfrac{\partial\vec{E}}{\partial t} = \mu_0 q\displaystyle\int \vec{v}\varrho\mathrm{d}\Upsilon_{\vec{v}} + \mu_0\varepsilon_\mathbf{0}\dfrac{\partial\vec{E}}{\partial t} \end{cases} . \tag{2.6}$$

In a plasma where collisions play a significant role, the Boltzmann collision term and

Vlasov mean-field terms combine to form the Boltzmann-Vlasov equation:

$$\begin{aligned}\frac{\partial \varrho}{\partial t}[\vec{r},\vec{v},t] + \vec{v}\cdot\vec{\nabla}_{\vec{r}}\varrho[\vec{r},\vec{v},t] + \frac{q}{m}(\vec{E}[\vec{r},t]+\vec{v}\times\vec{B}[\vec{r},t])\cdot\vec{\nabla}_{\vec{v}}\varrho[\vec{r},\vec{v},t] \\ = \iint (\varrho[\vec{r},\vec{v}',t]\varrho[\vec{r},\vec{v}'_\star,t] - \varrho[\vec{r},\vec{v},t]\varrho[\vec{r},\vec{v}_\star,t])\, v_\mathrm{r}\frac{\mathrm{d}S}{\mathrm{d}\Omega'}\mathrm{d}\Omega'\mathrm{d}\Upsilon_{\vec{v}_\star}\ .\end{aligned} \tag{2.7}$$

This kinetic equation provides the fundamental link between microscopic particle dynamics and macroscopic transport properties, describing how the system evolves towards thermodynamic equilibrium. Importantly, the equilibrium state can only be achieved when the distribution function takes the form of a global Maxwellian:

$$\varrho_\mathrm{M}[\vec{v}] = \rho_N\left(\frac{m}{2\pi k_\mathbf{B}T}\right)^{3/2}\mathrm{e}^{-\frac{m(\vec{v}-\vec{v}_0)^2}{2k_\mathbf{B}T}}\ , \tag{2.8}$$

where n, T, and $\vec{v}_0$ are constants throughout the system. This can be rigorously proved using Boltzmann's H-theorem, which can be found in textbooks such as [79]. Of particular interest for transport theory is the case of local Maxwellian distributions, where density and temperature gradients exist:

$$\varrho_\mathrm{LM}[\vec{r},\vec{v},t] = \rho_N[\vec{r},t]\left(\frac{m}{2\pi k_\mathbf{B}T[\vec{r},t]}\right)^{3/2}\mathrm{e}^{-\frac{m(\vec{v}-\vec{v}_0[\vec{r},t])^2}{2k_BT[\vec{r},t]}}\ . \tag{2.9}$$

Here, the density $\rho_N[\vec{r},t]$ and temperature $T[\vec{r},t]$ are functions of position and time, evolving towards uniformity through transport processes. Since collisions occur locally, the collision integral for a local Maxwellian vanishes:

$$\begin{aligned}&\iint (\varrho_\mathrm{LM}[\vec{r},\vec{v}',t]\varrho_\mathrm{LM}[\vec{r},\vec{v}'_\star,t] - \varrho_\mathrm{LM}[\vec{r},\vec{v},t]\varrho_\mathrm{LM}[\vec{r},\vec{v}_\star,t])\, v_\mathrm{r}\frac{\mathrm{d}S}{\mathrm{d}\Omega'}\mathrm{d}\Omega'\mathrm{d}\Upsilon_{\vec{v}_\star} \\ &\quad= \rho_N[\vec{r},t]\left(\frac{m}{2\pi k_\mathbf{B}T[\vec{r},t]}\right)^{3/2} \\ &\quad\times\iint\left(\mathrm{e}^{-\frac{m(\vec{v}'-\vec{v}_0[\vec{r},t])^2}{2k_\mathbf{B}T[\vec{r},t]}}\mathrm{e}^{-\frac{m(\vec{v}'_\star-\vec{v}_0[\vec{r},t])^2}{2k_\mathbf{B}T[\vec{r},t]}} - \mathrm{e}^{-\frac{m(\vec{v}-\vec{v}_0[\vec{r},t])^2}{2k_\mathbf{B}T[\vec{r},t]}}\mathrm{e}^{-\frac{m(\vec{v}_\star-\vec{v}_0[\vec{r},t])^2}{2k_\mathbf{B}T[\vec{r},t]}}\right) v_\mathrm{r}\frac{\mathrm{d}S}{\mathrm{d}\Omega'}\mathrm{d}\Omega'\mathrm{d}\Upsilon_{\vec{v}_\star} \\ &\quad= \rho_N[\vec{r},t]\left(\frac{m}{2\pi k_\mathbf{B}T[\vec{r},t]}\right)^{3/2} \\ &\quad\times\iint\left(\mathrm{e}^{-\frac{\frac{1}{2}m(\vec{v}'-\vec{v}_0[\vec{r},t])^2+\frac{1}{2}m(\vec{v}'_\star-\vec{v}_0[\vec{r},t])^2}{k_\mathbf{B}T[\vec{r},t]}} - \mathrm{e}^{-\frac{\frac{1}{2}m(\vec{v}-\vec{v}_0[\vec{r},t])^2+\frac{1}{2}m(\vec{v}_\star-\vec{v}_0[\vec{r},t])^2}{k_\mathbf{B}T[\vec{r},t]}}\right) v_\mathrm{r}\frac{\mathrm{d}S}{\mathrm{d}\Omega'}\mathrm{d}\Omega'\mathrm{d}\Upsilon_{\vec{v}_\star} \\ &\quad= \rho_N[\vec{r},t]\left(\frac{m}{2\pi k_\mathbf{B}T[\vec{r},t]}\right)^{3/2}\times\iint 0\, v_\mathrm{r}\frac{\mathrm{d}S}{\mathrm{d}\Omega'}\mathrm{d}\Omega'\mathrm{d}\Upsilon_{\vec{v}'} \\ &\quad= 0\ ,\end{aligned} \tag{2.10}$$

where the conservation of energy

$$\frac{1}{2}m(\vec{v}'-\vec{v}_0[\vec{r},t])^2 + \frac{1}{2}m(\vec{v}'_\star-\vec{v}_0[\vec{r},t])^2 = \frac{1}{2}m(\vec{v}-\vec{v}_0[\vec{r},t])^2 + \frac{1}{2}m(\vec{v}_\star-\vec{v}_0[\vec{r},t])^2 \tag{2.11}$$

has been used.

The local Maxwellian distribution, while eliminating the collision integral, is not an exact solution to the full Boltzmann-Vlasov equation due to the spatial gradients. This can be seen by substituting Eq. 2.9 into the left-hand side of Eq. 2.7:

$$\begin{aligned}
&\frac{\partial \varrho_{\mathrm{LM}}}{\partial t} + \vec{v}\cdot\vec{\nabla}_{\vec{r}}\varrho_{\mathrm{LM}} + \frac{q}{m}(\vec{E}+\vec{v}\times\vec{B})\cdot\vec{\nabla}_{\vec{v}}\varrho_{\mathrm{LM}} \\
&\quad = \varrho_{\mathrm{LM}}\left(\frac{1}{\rho_N}\frac{\partial \rho_N}{\partial t} - \frac{3}{2T}\frac{\partial T}{\partial t} + \frac{m(\vec{v}-\vec{v}_0)^2}{2k_{\mathbf{B}}T^2}\frac{\partial T}{\partial t} - \frac{m(\vec{v}-\vec{v}_0)}{k_{\mathbf{B}}T}\cdot\frac{\partial \vec{v}_0}{\partial t}\right) \\
&\quad + \varrho_{\mathrm{LM}}\left(\frac{\vec{v}\cdot\vec{\nabla}_{\vec{r}}\rho_N}{\rho_N} - \frac{3}{2T}\vec{v}\cdot\vec{\nabla}_{\vec{r}}T + \frac{m(\vec{v}-\vec{v}_0)^2}{2k_{\mathbf{B}}T^2}\vec{v}\cdot\vec{\nabla}_{\vec{r}}T - \frac{m(\vec{v}-\vec{v}_0)}{k_{\mathbf{B}}T}\cdot(\vec{v}\cdot\vec{\nabla}_{\vec{r}})\vec{v}_0\right) \\
&\quad + \frac{q}{m}(\vec{E}+\vec{v}\times\vec{B})\cdot\varrho_{\mathrm{LM}}\left(-\frac{m(\vec{v}-\vec{v}_0)}{k_{\mathbf{B}}T}\right) \neq 0 \ .
\end{aligned} \tag{2.12}$$

This non-zero result indicates that the local Maxwellian distribution does not satisfy the Boltzmann equation. To account for this, a correction term must be introduced:

$$\varrho[\vec{r},\vec{v},t] = \varrho_{\mathrm{LM}}[\vec{r},\vec{v},t] + \Delta\varrho[\vec{r},\vec{v},t] \ . \tag{2.13}$$

when the system is near equilibrium, $\Delta\varrho[\vec{r},\vec{v},t]$ represents a small correction $\Delta\varrho \ll \varrho$ that captures the non-equilibrium effects. It is worth noticing that the heat flux is entirely determined by the correction term rather than the local Maxwellian:

$$\begin{aligned}
\vec{j}_Q[\vec{r},t] :&= \frac{1}{2}m\int(\vec{v}-\vec{v}_0)|\vec{v}-\vec{v}_0|^2\varrho[\vec{r},\vec{v},t]\mathrm{d}\Upsilon_{\vec{v}} \\
&= \frac{1}{2}m\int(\vec{v}-\vec{v}_0)|\vec{v}-\vec{v}_0|^2(\varrho_{\mathrm{LM}}+\Delta\varrho)[\vec{r},\vec{v},t]\mathrm{d}\Upsilon_{\vec{v}} \\
&= \frac{1}{2}m\int(\vec{v}-\vec{v}_0)|\vec{v}-\vec{v}_0|^2\Delta\varrho[\vec{r},\vec{v},t]\mathrm{d}\Upsilon_{\vec{v}} \ ,
\end{aligned} \tag{2.14}$$

where the corresponding integral for ϱ_{LM} vanishes due to its even symmetry in $(\vec{v}-\vec{v}_0)$. The heat flux can only be computed once the correction term $\Delta\varrho$ is known. One method to determine $\Delta\varrho$ is through the Chapman-Enskog perturbation expansion [80]:

$$\Delta\varrho = \beta\Delta\varrho_1 + \beta^2\Delta\varrho_2 + \beta^3\Delta\varrho_3 + \cdots = \sum_{\bar{i}}\beta^{\bar{i}}\Delta\varrho_{\bar{i}} \ , \tag{2.15}$$

where β is a small parameter characterising the deviation from equilibrium (typically the Knudsen number: the ratio of the mean free path to the characteristic gradient length). Substituting this expansion into the Boltzmann equation and collecting terms of the same order in β allows for a systematic determination of the correction terms $\Delta\varrho_n$, therefore determining the heat flux.

An alternative approach to determine $\Delta\varrho$ is through the relaxation time approximation (Sec. 1.2.3), where the collision operator is simplified to:

$$\hat{\mathcal{O}}_{\mathrm{coll}}[\varrho] \approx -\frac{\varrho-\varrho_{\mathrm{LM}}}{t_{\mathrm{rlx}}} = -\frac{\Delta\varrho}{t_{\mathrm{rlx}}} \ , \tag{2.16}$$

where t_{rlx} is the characteristic relaxation time. This approximation assumes that collisions tend to restore the distribution to the local Maxwellian at a rate proportional to the deviation from equilibrium. Under RTA, the correction can be written down straightforwardly:

$$\Delta\varrho \approx -t_{\mathrm{rlx}} \left(\left(\frac{\partial}{\partial t} + \vec{v} \cdot \vec{\nabla}_{\vec{r}} + \frac{\vec{F}}{m} \cdot \vec{\nabla}_{\vec{v}} \right) \varrho_{\mathrm{LM}} \right) \ . \tag{2.17}$$

It shall be noted that as the local equilibrium distribution ϱ_{LM} evolves with time, the evolution of the correction term $\Delta\varrho$ does not directly follow an exponential decay form of $\Delta\varrho[t = 0]\mathrm{e}^{-t/t_{\mathrm{rlx}}}$.

To study the effect of heat transport alone, one can assume $\vec{F} = 0$. It can thus be shown that [53]:

$$\begin{aligned}
&\vec{j}_Q \\
&= -\frac{t_{\mathrm{rlx}} m^2}{2} \int \frac{1}{T} \left((\vec{v} - \vec{v}_0) \cdot \vec{\nabla}_{\vec{r}} \right) T \left(\frac{m(\vec{v} - \vec{v}_0)^2}{2k_{\mathbf{B}}T} - \frac{5}{2} \right) (\vec{v} - \vec{v}_0)^2 (\vec{v} - \vec{v}_0) f_{\mathrm{LM}}[\vec{r}, \vec{v}, t] \mathrm{d}\Upsilon_{\vec{v}} \\
&= -\frac{t_{\mathrm{rlx}} m^2}{2} \int \frac{1}{T} \left(\vec{v}'' \cdot \vec{\nabla}_{\vec{r}} \right) T \left(\frac{m v''^2}{2k_{\mathbf{B}}T} - \frac{5}{2} \right) v''^2 \vec{v}'' f_{\mathrm{LM}}[\vec{r}, \vec{v}'' + \vec{v}, t] \mathrm{d}\Upsilon_{\vec{v}''} \\
&= -\sum_{\bar{i}} \frac{t_{\mathrm{rlx}} m^2}{2} \int \frac{1}{T} \sum_{\bar{j}} \vec{v}''_{\bar{j}} \frac{\partial T}{\partial x_{\bar{j}}} \left(\frac{m v''^2}{2k_{\mathbf{B}}T} - \frac{5}{2} \right) v''^2 v''_{\bar{i}} f_{\mathrm{LM}}[\vec{r}, \vec{v}'' + \vec{v}, t] \mathrm{d}\Upsilon_{\vec{v}''} \vec{e}_{\bar{i}} \ .
\end{aligned} \tag{2.18}$$

Because $\forall \bar{i} \neq \bar{j}, \int v''_{\bar{i}} v''_{\bar{j}} \mathrm{e}^{-\frac{m v''^2}{k_{\mathbf{B}}T}} \mathrm{d}\Upsilon_{\vec{v}''} = 0,$

$$\begin{aligned}
\vec{j}_Q &= -\sum_{\bar{i}} \frac{t_{\mathrm{rlx}} m^2}{2} \int \frac{1}{T} \vec{v}''_{\bar{i}} \frac{\partial T}{\partial x_{\bar{i}}} \left(\frac{m v''^2}{2k_{\mathbf{B}}T} - \frac{5}{2} \right) v''^2 v''_{\bar{i}} f_{\mathrm{LM}}[\vec{r}, \vec{v}'' + \vec{v}, t] \mathrm{d}\Upsilon_{\vec{v}} \vec{e}_{\bar{i}} \\
&\propto \vec{\nabla}_{\vec{r}} T \, ,
\end{aligned} \tag{2.19}$$

hence the Fourier's law of heat transport $\vec{j}_Q = -\sigma_Q \vec{\nabla}_{\vec{r}} T$ is retrieved.

Other transport phenomena, such as electrical conductivity, viscosity, and particle diffusion, can be discussed similarly. Therefore, the Boltzmann equation establishes a fundamental framework for understanding transport processes in plasmas. The core challenge in transport theory boils down to the proper treatment of the collisional operator.

2.2.2 Landau-Fokker-Planck Collision Operator

Plasma consists of multiple species of particles. Eq. 2.3 must take into account all possible collision pairs:

$$\frac{\partial \varrho_{\bar{i}}}{\partial t} + \vec{v} \cdot \vec{\nabla}_{\vec{r}} \varrho_{\bar{i}} + \frac{q}{m} (\vec{E} + \vec{v} \times \vec{B}) \cdot \vec{\nabla}_{\vec{v}} \varrho_{\bar{i}} = \sum_{\bar{j}} \hat{\mathcal{O}}_{\mathrm{coll}}[\varrho_{\bar{i}}, \varrho_{\bar{j}}] \ , \tag{2.20}$$

where the collisional operator for species $\bar{i}$ due to species $\bar{j}$ is

$$\begin{aligned}
&\hat{\mathcal{O}}_{\mathrm{coll}}[\varrho_{\bar{i}}, \varrho_{\bar{j}}][\vec{r}, \vec{v}_{\bar{i}}, t] \\
&\quad = \iint \left(\varrho_{\bar{i}}[\vec{r}, \vec{v}'_{\bar{i}}, t] \varrho_{\bar{j}}[\vec{r}, \vec{v}'_{\bar{j}}, t] - \varrho_{\bar{i}}[\vec{r}, \vec{v}_{\bar{i}}, t] \varrho_{\bar{j}}[\vec{r}, \vec{v}_{\bar{j}}, t] \right) v_{\mathrm{r}} \frac{\mathrm{d}S}{\mathrm{d}\Omega'} \mathrm{d}\Omega' \mathrm{d}\Upsilon_{\vec{v}_{\bar{j}}} \ ,
\end{aligned} \tag{2.21}$$

where $\varrho_{\bar{i}}, \varrho_{\bar{j}}$ is the distribution function for species $\bar{i}, \bar{j}$ respectively, and $\vec{v}_{\bar{i}}$, $\vec{v}_{\bar{j}}, \vec{v}'_{\bar{i}}$, $\vec{v}'_{\bar{j}}$ are the velocities of the colliding particles before and after collisions.

For two-body Coulomb interactions, the discussion is simplified in the centre-of-mass (COM) frame with velocity $\vec{v}_{\mathrm{c}} = \frac{m_{\bar{i}}\vec{v}_{\bar{i}} + m_{\bar{j}}\vec{v}_{\bar{j}}}{m_{\bar{i}} + m_{\bar{j}}}$. The velocities of two incident particles can be expressed by $\vec{v}_{\mathrm{c}}$ and the relative velocity $\vec{v}_{\mathrm{r}} := \vec{v}_{\bar{i}} - \vec{v}_{\bar{j}}$ as:

$$\vec{v}_{\bar{i}} = \vec{v}_{\mathrm{c}} + \frac{m_{\bar{j}}}{m_{\bar{i}} + m_{\bar{j}}}\vec{v}_{\mathrm{r}} \ , \qquad \vec{v}_{\bar{j}} = \vec{v}_{\mathrm{c}} - \frac{m_{\bar{i}}}{m_{\bar{i}} + m_{\bar{j}}}\vec{v}_{\mathrm{r}} \ , \tag{2.22}$$

where $m_{\mathrm{r}} := \frac{m_{\bar{i}} m_{\bar{j}}}{m_{\bar{i}} + m_{\bar{j}}}$ is the reduced mass. Similarly, the velocities after collision can be expressed by $\vec{v}'_{\mathrm{r}} := \vec{v}'_{\bar{i}} - \vec{v}'_{\bar{j}}$ and $\vec{v}'_{\mathrm{c}}$.

$$\vec{v}'_{\bar{i}} = \vec{v}'_{\mathrm{c}} + \frac{m_{\bar{j}}}{m_{\bar{i}} + m_{\bar{j}}}\vec{v}'_{\mathrm{r}} \ , \qquad \vec{v}'_{\bar{j}} = \vec{v}'_{\mathrm{c}} - \frac{m_{\bar{i}}}{m_{\bar{i}} + m_{\bar{j}}}\vec{v}'_{\mathrm{r}} \ , \tag{2.23}$$

As the collision is elastic, $\vec{v}'_{\mathrm{c}} = \vec{v}_{\mathrm{c}}$ and $|\vec{v}'_{\mathrm{r}}| = |\vec{v}_{\mathrm{r}}|$. It follows that:

$$\vec{v}'_{\bar{i}} - \vec{v}_{\bar{i}} = \frac{m_{\mathrm{r}}}{m_{\bar{i}}}\Delta\vec{v}_{\mathrm{r}} \ , \qquad \vec{v}'_{\bar{j}} - \vec{v}_{\bar{j}} = -\frac{m_{\mathrm{r}}}{m_{\bar{j}}}\Delta\vec{v}_{\mathrm{r}} \ , \tag{2.24}$$

where $\Delta\vec{v}_{\mathrm{r}} := \vec{v}'_{\mathrm{r}} - \vec{v}_{\mathrm{r}}$. The Rutherford scattering cross-section is given by:

$$\frac{\mathrm{d}S}{\mathrm{d}\Omega'_{\mathrm{r}}} = \frac{1}{4}\left(\frac{q_{\bar{i}} q_{\bar{j}}}{4\pi\epsilon_0 m_{\mathrm{r}} v_{\mathrm{r}}^2}\right)^2 \frac{1}{(\mathrm{Sin}\,[\theta'_{\mathrm{r}}/2])^4} \ , \tag{2.25}$$

where θ'_{r} and Ω'_{r} are the scattering (solid) angles measured in the COM frame, and $q_{\bar{i}}$, $q_{\bar{j}}$ the charges of the respective species.

For small-angle collisions, expanding ϱ to second order in $\Delta\vec{v}_{\bar{i}}$ gives

$$\begin{aligned}
\varrho_{\bar{i}}[\vec{r}, \vec{v}'_{\bar{i}}, t] &\approx \varrho_{\bar{i}}[\vec{r}, \vec{v}_{\bar{i}}, t] + \frac{m_{\mathrm{r}}}{m_{\bar{i}}}\Delta\vec{v}_{\mathrm{r}} \cdot \vec{\nabla}_{\vec{v}_{\bar{i}}}\varrho_{\bar{j}} + \frac{1}{2}\left(\frac{m_{\mathrm{r}}}{m_{\bar{i}}}\right)^2 \Delta\vec{v}_{\mathrm{r}}\Delta\vec{v}_{\mathrm{r}} : \vec{\nabla}_{\vec{v}_{\bar{i}}}\vec{\nabla}_{\vec{v}_{\bar{i}}}\varrho_{\bar{i}} \\
\varrho_{\bar{j}}[\vec{r}, \vec{v}'_{\bar{j}}, t] &\approx \varrho_{\bar{j}}[\vec{r}, \vec{v}_{\bar{j}}, t] - \frac{m_{\mathrm{r}}}{m_{\bar{j}}}\Delta\vec{v}_{\mathrm{r}} \cdot \vec{\nabla}_{\vec{v}_{\bar{j}}}\varrho_{\bar{j}} + \frac{1}{2}\left(\frac{m_{\mathrm{r}}}{m_{\bar{j}}}\right)^2 \Delta\vec{v}_{\mathrm{r}}\Delta\vec{v}_{\mathrm{r}} : \vec{\nabla}_{\vec{v}_{\bar{j}}}\vec{\nabla}_{\vec{v}_{\bar{j}}}\varrho_{\bar{j}} \ ,
\end{aligned} \tag{2.26}$$

Where : is the double dot product. The product $\varrho_{\bar{i}}[\vec{r}, \vec{v}'_{\bar{i}}, t]\varrho_{\bar{j}}[\vec{r}, \vec{v}'_{\bar{j}}, t] - \varrho_{\bar{i}}[\vec{r}, \vec{v}_{\bar{i}}, t]\varrho_{\bar{j}}[\vec{r}, \vec{v}_{\bar{j}}, t]$ in the collision operator can thus be approximated as:

$$\begin{aligned}
&\varrho_{\bar{i}}[\vec{r}, \vec{v}'_{\bar{i}}, t]\varrho_{\bar{j}}[\vec{r}, \vec{v}'_{\bar{j}}, t] - \varrho_{\bar{i}}[\vec{r}, \vec{v}_{\bar{i}}, t]\varrho_{\bar{j}}[\vec{r}, \vec{v}_{\bar{j}}, t] \\
&\quad \approx m_{\mathrm{r}}\Delta\vec{v}_{\mathrm{r}} \cdot \left(\frac{\varrho_{\bar{j}}}{m_{\bar{i}}}\vec{\nabla}_{\vec{v}_{\bar{i}}}\varrho_{\bar{i}} - \frac{\varrho_{\bar{i}}}{m_{\bar{j}}}\vec{\nabla}_{\vec{v}_{\bar{j}}}\varrho_{\bar{j}}\right) \\
&\qquad + \frac{1}{2}m_{\mathrm{r}}^2\Delta\vec{v}_{\mathrm{r}}\Delta\vec{v}_{\mathrm{r}} : \left(\frac{\varrho_{\bar{j}}}{m_{\bar{i}}^2}\vec{\nabla}_{\vec{v}_{\bar{i}}}\vec{\nabla}_{\vec{v}_{\bar{i}}}\varrho_{\bar{i}} + \frac{\varrho_{\bar{i}}}{m_{\bar{j}}^2}\vec{\nabla}_{\vec{v}_{\bar{j}}}\vec{\nabla}_{\vec{v}_{\bar{j}}}\varrho_{\bar{j}} - \frac{2}{m_{\bar{i}}m_{\bar{j}}}\vec{\nabla}_{\vec{v}_{\bar{i}}}\varrho_{\bar{i}}\vec{\nabla}_{\vec{v}_{\bar{j}}}\varrho_{\bar{j}}\right) \ ,
\end{aligned} \tag{2.27}$$

It follows that

$$\begin{aligned}
\hat{\mathcal{O}}_{\mathrm{coll}}[\varrho_{\bar{i}}, \varrho_{\bar{j}}] \approx \frac{1}{4}&\left(\frac{q_{\bar{i}} q_{\bar{j}}}{4\pi\epsilon_0 m_{\mathrm{r}}}\right)^2 \\
&\iint \left(m_{\mathrm{r}}\Delta\vec{v}_{\mathrm{r}} \cdot \vec{\xi}_1 + \frac{1}{2}m_{\mathrm{r}}^2\Delta\vec{v}_{\mathrm{r}}\Delta\vec{v}_{\mathrm{r}} : \left(\frac{1}{m_{\bar{i}}}\vec{\nabla}_{\vec{v}_{\bar{i}}} - \frac{1}{m_{\bar{j}}}\vec{\nabla}_{\vec{v}_{\bar{j}}}\right)\vec{\xi}_1\right) \frac{\mathrm{d}\Upsilon_{\vec{v}_{\bar{j}}}\mathrm{d}\Omega'_{\mathrm{r}}}{v_{\mathrm{r}}^3(\mathrm{Sin}\,[\theta'_{\mathrm{r}}/2])^4} \ ,
\end{aligned} \tag{2.28}$$

where

$$\vec{\xi}_1 := \frac{\varrho_{\bar{j}}}{m_{\bar{i}}}\vec{\nabla}_{\vec{v}_{\bar{i}}}\varrho_{\bar{i}} - \frac{\varrho_{\bar{i}}}{m_{\bar{j}}}\vec{\nabla}_{\vec{v}_{\bar{j}}}\varrho_{\bar{j}} \ . \tag{2.29}$$

For integration over $\Omega'_{\rm r}$, it is easier to set up coordinates where the relative velocity lies along $\vec{e}_{x_{\rm r}}$ before the collision. Suppose that $\vec{v}_{\rm r} = v_{\rm r}\vec{e}_{x_{\rm r}}$ and $\vec{v}'_{\rm r} = v'_{\rm r}{\rm Cos}\,[\theta'_{\rm r}]\,\vec{e}_{x_{\rm r}} + v'_{\rm r}{\rm Sin}\,[\theta'_{\rm r}]\,{\rm Cos}\,[\varphi'_{\rm r}]\,\vec{e}_{y_{\rm r}} + v'_{\rm r}\vec{e}_{x_{\rm r}}{\rm Sin}\,[\theta'_{\rm r}]\,{\rm Sin}\,[\varphi'_{\rm r}]\,\vec{e}_{z_{\rm r}}$.

$$\Delta\vec{v}_{\rm r} = v_{\rm r}[({\rm Cos}\,[\theta'_{\rm r}]-1)\vec{e}_{x_{\rm r}} + {\rm Sin}\,[\theta'_{\rm r}]\,{\rm Cos}\,[\varphi'_{\rm r}]\,\vec{e}_{y_{\rm r}} + {\rm Sin}\,[\theta'_{\rm r}]\,{\rm Sin}\,[\varphi'_{\rm r}]\,\vec{e}_{z_{\rm r}}] \ . \tag{2.30}$$

As the integration over $\Omega'_{\rm r}$ is independent of $v_{\bar{i}}$ and $v_{\bar{j}}$, the $\Delta\vec{v}_{\rm r}$ term can be integrated first. It follows from $\int_0^{2\pi}{\rm Cos}\,[\varphi'_{\rm r}]\,{\rm d}\varphi'_{\rm r} = \int_0^{2\pi}{\rm Sin}\,[\varphi'_{\rm r}]\,{\rm d}\varphi'_{\rm r} = 0$ that:

$$\begin{aligned}
&\int\frac{\Delta\vec{v}_{\rm r}}{({\rm Sin}\,[\theta'_{\rm r}/2])^4}{\rm d}\Omega'_{\rm r}\\
&= \int_0^{2\pi}\int v_{\rm r}\frac{({\rm Cos}\,[\theta'_{\rm r}]-1)\vec{e}_{x_{\rm r}} + {\rm Sin}\,[\theta'_{\rm r}]\,{\rm Cos}\,[\varphi'_{\rm r}]\,\vec{e}_{y_{\rm r}} + {\rm Sin}\,[\theta'_{\rm r}]\,{\rm Sin}\,[\varphi'_{\rm r}]\,\vec{e}_{z_{\rm r}}}{({\rm Sin}\,[\theta'_{\rm r}/2])^4}{\rm Sin}\,[\theta'_{\rm r}]\,{\rm d}\theta'_{\rm r}{\rm d}\varphi'_{\rm r}\\
&= 2\pi v_{\rm r}\vec{e}_{x_{\rm r}}\int\frac{(1-2({\rm Sin}\,[\theta'_{\rm r}/2])^2-1)\times 2{\rm Sin}\,[\theta'_{\rm r}/2]\,{\rm Cos}\,[\theta'_{\rm r}/2]}{({\rm Sin}\,[\theta'_{\rm r}/2])^4}{\rm d}\theta'_{\rm r}\\
&= -8\pi v_{\rm r}\vec{e}_{x_{\rm r}}\int\frac{{\rm Cos}\,[\theta'_{\rm r}/2]\,{\rm d}\theta'_{\rm r}}{{\rm Sin}\,[\theta'_{\rm r}/2]}\vec{v}_{\rm r}\\
&= -16\pi\vec{v}_{\rm r}\int\frac{{\rm d}\eta}{\eta} \ .
\end{aligned} \tag{2.31}$$

Where $\eta := {\rm Sin}\,[\theta'_{\rm r}/2]$ is the dummy variable for integration. Similarly, the off-diagonal terms for the rank-2 tensor $\int\frac{\Delta\vec{v}_{\rm r}\Delta\vec{v}_{\rm r}}{({\rm Sin}\,[\theta'_{\rm r}/2])^4}{\rm d}\Omega'_{\rm r}$ vanish for due to the $\varphi'_{\rm r}$ integration of ${\rm Sin}\,[\varphi'_{\rm r}]$, ${\rm Cos}\,[\varphi'_{\rm r}]$, and ${\rm Sin}\,[\varphi'_{\rm r}]\,{\rm Cos}\,[\varphi'_{\rm r}]$ over $0\rightarrow 2\pi$. For the diagonal terms, the $\vec{e}_{x_{\rm r}}\vec{e}_{x_{\rm r}}$ term csn be directly evaluated as

$$2\pi v_{\rm r}^2\int\frac{({\rm Cos}\,[\theta'_{\rm r}]-1)^2{\rm Sin}\,[\theta'_{\rm r}]}{({\rm Sin}\,[\theta'_{\rm r}/2])^4}{\rm d}\theta'_{\rm r} = 16\pi v_{\rm r}^2 \ . \tag{2.32}$$

As $\int_0^{2\pi}({\rm Cos}\,[\varphi'_{\rm r}])^2{\rm d}\varphi'_{\rm r} = \int_0^{2\pi}({\rm Sin}\,[\varphi'_{\rm r}])^2{\rm d}\varphi'_{\rm r} = \pi$. Similarly, both the $\vec{e}_{y_{\rm r}}\vec{e}_{y_{\rm r}}$ and $\vec{e}_{z_{\rm r}}\vec{e}_{z_{\rm r}}$ terms are:

$$\begin{aligned}
\pi v_{\rm r}^2\int\frac{({\rm Sin}\,[\theta'_{\rm r}])^2{\rm Sin}\,[\theta'_{\rm r}]}{({\rm Sin}\,[\theta'_{\rm r}/2])^4}{\rm d}\theta'_{\rm r} &= \pi v_{\rm r}^2\int\frac{8({\rm Sin}\,[\theta'_{\rm r}/2])^3({\rm Cos}\,[\theta'_{\rm r}/2])^3}{({\rm Sin}\,[\theta'_{\rm r}/2])^4}{\rm d}\theta'_{\rm r}\\
&= 16\pi v_{\rm r}^2\int\frac{1-({\rm Sin}\,[\theta'_{\rm r}/2])^2}{{\rm Sin}\,[\theta'_{\rm r}/2]}{\rm d}({\rm Sin}\,[\theta'/2])\\
&= 16\pi v_r^2(\int\frac{{\rm d}\eta}{\eta} - \int\eta{\rm d}\eta) \ .
\end{aligned} \tag{2.33}$$

Therefore

$$\begin{aligned}
&\int\frac{\Delta\vec{v}_{\rm r}\Delta\vec{v}_{\rm r}}{({\rm Sin}\,[\theta'_{\rm r}/2])^4}{\rm d}\Omega'_{\rm r}\\
&\quad= 16\pi v_{\rm r}^2\left(\vec{e}_{x_{\rm r}}\vec{e}_{x_{\rm r}} + \left(\int\frac{{\rm d}\eta}{\eta} - \int\eta{\rm d}\eta\right)\vec{e}_{y_{\rm r}}\vec{e}_{y_{\rm r}} + \left(\int\frac{{\rm d}\eta}{\eta} - \int\eta{\rm d}\eta\right)\vec{e}_{z_{\rm r}}\vec{e}_{z_{\rm r}}\right) \ .
\end{aligned} \tag{2.34}$$

As $\theta'_{\mathrm{r}} : 0 \to \pi$, $\eta : 0 \to 1$, the integration $\int \frac{\mathrm{d}\eta}{\eta}$ diverges and must be cut-off at some $\eta^\star$. This cut-off can be elaborated by considering the geometry of Coulomb collisions. As the scattering angle θ'_{r} satisfies

$$\tan\left[\theta'_{\mathrm{r}}/2\right] = \frac{q_{\bar{i}} q_{\bar{j}}}{4\pi\varepsilon_{\mathbf{0}} m_{\mathrm{r}} v_r^2 r_{\mathrm{b}}} = \frac{r_{\mathrm{b}_0}}{r_{\mathrm{b}}} \ , \tag{2.35}$$

where r_{b} is the impact parameter, and $r_{\mathrm{b}_0} := \frac{q_{\bar{i}} q_{\bar{j}}}{4\pi\varepsilon_{\mathbf{0}} m_{\mathrm{r}} v_r^2}$ is the classical distance of closest approach [2], where $r_{\mathrm{b}} \to \infty$ for $\theta'_{\mathrm{r}} \to 0$. However, this violates the Coulomb interaction assumption as the potential is effectively screened and becomes a Yukawa potential. The typical cut-off is chosen to be the Debye length r_{D}. Thus, it is useful to define

$$\begin{aligned} \Lambda := (\eta^\star)^{-1} &= \left(\mathrm{Sin}\left[\theta'^\star_{\mathrm{r}}/2\right]\right)^{-1} = \sqrt{1 + \left(\tan\left[\theta'^\star_{\mathrm{r}}/2\right]\right)^{-2}} = \sqrt{1 + \left(r_{\mathrm{D}}/r_{\mathrm{b}_0}\right)^2} \\ \mathrm{Ln}\left[\Lambda\right] &= \int_{\eta^\star}^{1} \frac{\mathrm{d}\eta}{\eta} = -\mathrm{Ln}\left[\eta^\star\right] = \frac{1}{2}\mathrm{Ln}\left[1 + \left(r_{\mathrm{D}}/r_{\mathrm{b}_0}\right)^2\right] \end{aligned} \ . \tag{2.36}$$

The quantity $\mathrm{Ln}\left[\Lambda\right]$, although defined slightly differently from 1.14, is also called Coulomb Logarithm[3]. Using CL, the integrals can be obtained:

$$\int \frac{\Delta\vec{v}_{\mathrm{r}}}{\left(\mathrm{Sin}\left[\theta'/2\right]\right)^4} \mathrm{d}\Omega'_{\mathrm{r}} = -16\pi\vec{v}_{\mathrm{r}} \int_{\Lambda^{-1}}^{1} \frac{\mathrm{d}\eta}{\eta} = -16\pi\vec{v}_{\mathrm{r}}\mathrm{Ln}\left[\Lambda\right] \ . \tag{2.37}$$

$$\begin{aligned} &\int \frac{\Delta\vec{v}_{\mathrm{r}}\Delta\vec{v}_{\mathrm{r}}}{\left(\mathrm{Sin}\left[\theta'_{\mathrm{r}}/2\right]\right)^4} \mathrm{d}\Omega'_{\mathrm{r}} \\ &\quad = 16\pi v_{\mathrm{r}}^2 \left(\vec{e}_{x_{\mathrm{r}}}\vec{e}_{x_{\mathrm{r}}} + \left(\int_{\Lambda^{-1}}^{1} \frac{\mathrm{d}\eta}{\eta} - \int_{\Lambda^{-1}}^{1} \eta \mathrm{d}\eta\right)\left(\vec{e}_{y_{\mathrm{r}}}\vec{e}_{y_{\mathrm{r}}} + \vec{e}_{z_{\mathrm{r}}}\vec{e}_{z_{\mathrm{r}}}\right)\right) \\ &\quad = 16\pi v_{\mathrm{r}}^2 \left(\vec{e}_{x_{\mathrm{r}}}\vec{e}_{x_{\mathrm{r}}} + \left(\mathrm{Ln}\left[\Lambda\right] - \frac{1}{2}(1 - \Lambda^{-2})\right)\left(\vec{e}_{y_{\mathrm{r}}}\vec{e}_{y_{\mathrm{r}}} + \vec{e}_{z_{\mathrm{r}}}\vec{e}_{z_{\mathrm{r}}}\right)\right) \ . \end{aligned} \tag{2.38}$$

Though $\mathrm{Ln}\left[\Lambda\right]$ is dependent on v_{r} through r_{b_0}, it is often treated as a constant that only depends on the plasma condition, representing its effect averaged over all collision events. Therefore, the collision operator can be written in the form

$$\begin{aligned} &\hat{\mathcal{O}}_{\mathrm{coll}}[\varrho_{\bar{i}}, \varrho_{\bar{j}}] = 4\pi \left(\frac{q_{\bar{i}} q_{\bar{j}}}{4\pi\epsilon_0 m_{\mathrm{r}}}\right)^2 \mathrm{Ln}\left[\Lambda\right] \\ &\int \left(-\frac{m_{\mathrm{r}}}{v_{\mathrm{r}}^2}\vec{\xi}_1 \cdot \vec{e}_{x_{\mathrm{r}}} + \frac{m_{\mathrm{r}}^2}{2} \overrightarrow{\overrightarrow{\xi}}_2 : \left(\frac{1}{m_{\bar{i}}}\vec{\nabla}_{\vec{v}_{\bar{i}}} - \frac{1}{m_{\bar{j}}}\vec{\nabla}_{\vec{v}_{\bar{j}}}\right)\vec{\xi}_1\right) \mathrm{d}\Upsilon_{\vec{v}_{\bar{j}}} \ , \end{aligned} \tag{2.39}$$

where

$$\overrightarrow{\overrightarrow{\xi}}_2 := \frac{1}{v_{\mathrm{r}}}\left(\frac{1}{\mathrm{Ln}\left[\Lambda\right]}\vec{e}_{x_{\mathrm{r}}}\vec{e}_{x_{\mathrm{r}}} + \left(1 - \frac{1 - \Lambda^{-2}}{2\mathrm{Ln}\left[\Lambda\right]}\right)\left(\vec{e}_{y_{\mathrm{r}}}\vec{e}_{y_{\mathrm{r}}} + \vec{e}_{z_{\mathrm{r}}}\vec{e}_{z_{\mathrm{r}}}\right)\right) \ . \tag{2.40}$$

[2] This is also the boundary for small-angle scattering $\theta'_{\mathrm{r}} < \pi/2 \Leftrightarrow r_{\mathrm{b}} > r_{\mathrm{b}_0}$ and large angle scattering $\theta'_{\mathrm{r}} > \pi/2 \Leftrightarrow r_{\mathrm{b}} < r_{\mathrm{b}_0}$

[3] The difference arises from different approximations used. See Sec. 2.2.3 for details.

As for weakly coupled plasmas, the Debye length is substantially larger than the classical distance of closest approach [79], $\mathrm{Ln}\left[\Lambda\right] \gg 1$. Thus $\overset{\rightarrow\!\!\!\!\rightarrow}{\xi}_2$ can be decomposed as

$$\begin{aligned}
\overset{\rightarrow\!\!\!\!\rightarrow}{\xi}_2 &= \overset{\rightarrow\!\!\!\!\rightarrow}{\xi}'_2 + \overset{\rightarrow\!\!\!\!\rightarrow}{\xi}''_2 \\
\overset{\rightarrow\!\!\!\!\rightarrow}{\xi}'_2 &= \frac{\overset{\rightarrow\!\!\!\!\rightarrow}{\mathbb{1}} - \vec{e}_{x_\mathrm{r}}\vec{e}_{x_\mathrm{r}}}{v_\mathrm{r}} \\
\overset{\rightarrow\!\!\!\!\rightarrow}{\xi}''_2 &= \frac{1}{v_\mathrm{r}}\left(\frac{1}{\mathrm{Ln}\left[\Lambda\right]}\vec{e}_{x_\mathrm{r}}\vec{e}_{x_\mathrm{r}} - \left(\frac{1-\Lambda^{-2}}{2\mathrm{Ln}\left[\Lambda\right]}\right)\left(\vec{e}_{y_\mathrm{r}}\vec{e}_{y_\mathrm{r}} + \vec{e}_{z_\mathrm{r}}\vec{e}_{z_\mathrm{r}}\right)\right)
\end{aligned} \quad , \tag{2.41}$$

where $\overset{\rightarrow\!\!\!\!\rightarrow}{\xi}''_2 \ll \overset{\rightarrow\!\!\!\!\rightarrow}{\xi}'_2$ and can be neglected. As the tensor is diagonal (hence symmetric), its divergence can be defined without ambiguity:

$$\begin{aligned}
\vec{\nabla}_{\vec{v}_\mathrm{r}} \cdot \overset{\rightarrow\!\!\!\!\rightarrow}{\xi}'_2 &:= \partial_{\underline{m}}\xi'_{2\overline{m,n}}\vec{e}_{\underline{n}} = \partial_{\underline{n}}\xi'_{2\overline{m,n}}\vec{e}_{\underline{m}} \\
&= \frac{\partial}{\partial v_{\mathrm{r}_{\bar{m}}}}\left(\frac{\delta_{\overline{m,n}}}{v_\mathrm{r}} - \frac{v_{\mathrm{r}_{\bar{m}}}v_{\mathrm{r}_{\bar{n}}}}{v_\mathrm{r}^3}\right)\vec{e}_{\underline{n}} \\
&= \frac{\partial}{\partial v_{\mathrm{r}_{\bar{m}}}}\left(\delta_{\overline{m,n}}(v_\mathrm{r}^2)^{-1/2} - v_{\mathrm{r}_{\bar{m}}}v_{\mathrm{r}_{\bar{n}}}(v_\mathrm{r}^2)^{-3/2}\right)\vec{e}_{\underline{n}} \\
&= \left(-\delta_{\overline{m,n}}\frac{1}{2}v_\mathrm{r}^{-3}2v_{\mathrm{r}_{\underline{m}}} - 3v_{\mathrm{r}_{\bar{n}}}v_\mathrm{r}^{-3} - v_{\mathrm{r}_{\bar{m}}}\delta_{\underline{m},\overline{n}}v_\mathrm{r}^{-3} - v_{\mathrm{r}_{\bar{m}}}v_{\mathrm{r}_{\bar{n}}}\left(\frac{-3}{2}v_\mathrm{r}^{-5}\right)2v_{\mathrm{r}_{\underline{m}}}\right)\vec{e}_{\underline{n}} \\
&= \left(-v_\mathrm{r}^{-3}v_{\bar{\mathrm{n}}} - 3v_{\mathrm{r}_{\bar{n}}}v_\mathrm{r}^{-3} - v_{\mathrm{r}_{\bar{n}}}v_\mathrm{r}^{-3} + 3v_{\mathrm{r}_{\bar{m}}}v_{\mathrm{r}_{\bar{n}}}v_\mathrm{r}^{-5}v_{\mathrm{r}_{\underline{m}}}\right)\vec{e}_{\underline{n}} \\
&= -2\frac{\vec{v}_\mathrm{r}}{v_\mathrm{r}^3} = -2\frac{\vec{e}_{x_\mathrm{r}}}{v_\mathrm{r}^2} \ ,
\end{aligned} \tag{2.42}$$

where the identity $\frac{\partial v_\mathrm{r}^2}{\partial v_{\mathrm{r}_{\bar{m}}}} = \frac{\partial v_{\mathrm{r}_{\bar{l}}}v_{\mathrm{r}_{\bar{l}}}}{\partial v_{\mathrm{r}_{\bar{m}}}} = v_{\mathrm{r}_{\bar{l}}}\delta_{\underline{l,m}} + \delta_{\bar{l},\underline{m}}v_{\mathrm{r}_{\underline{l}}} = 2v_{\mathrm{r}_{\underline{m}}}$ have been used. This leads to the simplification of Eq. 2.39 when the $\overset{\rightarrow\!\!\!\!\rightarrow}{\xi}''_2$ term is neglected:

$$\begin{aligned}
&\hat{\mathcal{O}}_{\mathrm{coll}}[\varrho_{\bar{i}}, \varrho_{\bar{j}}] \approx 4\pi\left(\frac{q_{\bar{i}}q_{\bar{j}}}{4\pi\epsilon_0 m_\mathrm{r}}\right)^2 \mathrm{Ln}\left[\Lambda\right] \\
&\int\left(\frac{m_\mathrm{r}}{2}\vec{\xi}_1\cdot\left(\vec{\nabla}_{\vec{v}_\mathrm{r}}\cdot\overset{\rightarrow\!\!\!\!\rightarrow}{\xi}'_2\right) + \frac{m_\mathrm{r}^2}{2}\overset{\rightarrow\!\!\!\!\rightarrow}{\xi}'_2 : \left(\frac{1}{m_{\bar{i}}}\vec{\nabla}_{\vec{v}_{\bar{i}}} - \frac{1}{m_{\bar{j}}}\vec{\nabla}_{\vec{v}_{\bar{j}}}\right)\vec{\xi}_1\right)\mathrm{d}\Upsilon_{\vec{v}_{\bar{j}}} \\
&= 4\pi\left(\frac{q_{\bar{i}}q_{\bar{j}}}{4\pi\epsilon_0 m_\mathrm{r}}\right)^2 \mathrm{Ln}\left[\Lambda\right] \\
&\int\left(\frac{m_\mathrm{r}}{2}\vec{\xi}_1\cdot\left(\vec{\nabla}_{\vec{v}_\mathrm{r}}\cdot\overset{\rightarrow\!\!\!\!\rightarrow}{\xi}'_2\right) + \frac{m_\mathrm{r}^2}{2m_{\bar{i}}}\overset{\rightarrow\!\!\!\!\rightarrow}{\xi}'_2 : \vec{\nabla}_{\vec{v}_{\bar{i}}}\vec{\xi}_1 - \frac{m_\mathrm{r}^2}{2m_{\bar{j}}}\overset{\rightarrow\!\!\!\!\rightarrow}{\xi}'_2 : \vec{\nabla}_{\vec{v}_{\bar{j}}}\vec{\xi}_1\right)\mathrm{d}\Upsilon_{\vec{v}_{\bar{j}}} \ .
\end{aligned} \tag{2.43}$$

As $\vec{\nabla}_{\vec{v}_{\bar{j}}}\cdot\left(\overset{\rightarrow\!\!\!\!\rightarrow}{\xi}'_2\cdot\vec{\xi}_1\right) = \left(\vec{\nabla}_{\vec{v}_{\bar{j}}}\cdot\overset{\rightarrow\!\!\!\!\rightarrow}{\xi}'_2\right)\cdot\vec{\xi}_1 + \overset{\rightarrow\!\!\!\!\rightarrow}{\xi}'_2 : \left(\vec{\nabla}_{\vec{v}_{\bar{j}}}\vec{\xi}_1\right)$, integration by parts yield

$$\begin{aligned}
\int\overset{\rightarrow\!\!\!\!\rightarrow}{\xi}'_2 : \left(\vec{\nabla}_{\vec{v}_{\bar{j}}}\vec{\xi}_1\right)\mathrm{d}\Upsilon_{\vec{v}_{\bar{j}}} &= \int\vec{\nabla}_{\vec{v}_{\bar{j}}}\cdot\left(\overset{\rightarrow\!\!\!\!\rightarrow}{\xi}'_2\cdot\vec{\xi}_1\right)\mathrm{d}\Upsilon_{\vec{v}_{\bar{j}}} - \int\left(\vec{\nabla}_{\vec{v}_{\bar{j}}}\cdot\overset{\rightarrow\!\!\!\!\rightarrow}{\xi}'_2\right)\cdot\vec{\xi}_1\mathrm{d}\Upsilon_{\vec{v}_{\bar{j}}} \\
&= -\int\left(\vec{\nabla}_{\vec{v}_{\bar{j}}}\cdot\overset{\rightarrow\!\!\!\!\rightarrow}{\xi}'_2\right)\cdot\vec{\xi}_1\mathrm{d}\Upsilon_{\vec{v}_{\bar{j}}} \ .
\end{aligned} \tag{2.44}$$

It thus follows that

$$\begin{aligned}
&\hat{\mathcal{O}}_{\text{coll}}[\varrho_{\bar{i}}, \varrho_{\bar{j}}] \approx 4\pi \left(\frac{q_{\bar{i}} q_{\bar{j}}}{4\pi\epsilon_0 m_{\text{r}}}\right)^2 \text{Ln}\,[\Lambda] \\
&\int \left(\frac{m_{\text{r}}}{2}\vec{\xi}_1 \cdot \left(\vec{\nabla}_{\vec{v}_{\text{r}}} \cdot \overrightarrow{\overrightarrow{\xi}}'_2\right) + \frac{m_{\text{r}}^2}{2m_{\bar{i}}} \overrightarrow{\overrightarrow{\xi}}'_2 : \vec{\nabla}_{\vec{v}_{\bar{i}}} \vec{\xi}_1 + \frac{m_{\text{r}}^2}{2m_{\bar{j}}} \left(\vec{\nabla}_{\vec{v}_{\bar{j}}} \cdot \overrightarrow{\overrightarrow{\xi}}'_2\right) \cdot \vec{\xi}_1\right) \mathrm{d}\Upsilon_{\vec{v}_{\bar{j}}} \\
&= 4\pi \left(\frac{q_{\bar{i}} q_{\bar{j}}}{4\pi\epsilon_0 m_{\text{r}}}\right)^2 \text{Ln}\,[\Lambda] \\
&\int \left(\frac{m_{\text{r}}}{2}\vec{\xi}_1 \cdot \left(\vec{\nabla}_{\vec{v}_{\bar{i}}} \cdot \overrightarrow{\overrightarrow{\xi}}'_2\right) + \frac{m_{\text{r}}^2}{2m_{\bar{i}}} \overrightarrow{\overrightarrow{\xi}}'_2 : \vec{\nabla}_{\vec{v}_{\bar{i}}} \vec{\xi}_1 - \frac{m_{\text{r}}^2}{2m_{\bar{j}}} \left(\vec{\nabla}_{\vec{v}_{\bar{i}}} \cdot \overrightarrow{\overrightarrow{\xi}}'_2\right) \cdot \vec{\xi}_1\right) \mathrm{d}\Upsilon_{\vec{v}_{\bar{j}}} \\
&= 4\pi \left(\frac{q_{\bar{i}} q_{\bar{j}}}{4\pi\epsilon_0 m_{\text{r}}}\right)^2 \text{Ln}\,[\Lambda] \int \left(\frac{m_{\text{r}}}{2}\left(1 - \frac{m_{\text{r}}}{m_{\bar{j}}}\right)\vec{\xi}_1 \cdot \left(\vec{\nabla}_{\vec{v}_{\bar{i}}} \cdot \overrightarrow{\overrightarrow{\xi}}'_2\right) + \frac{m_{\text{r}}^2}{2m_{\bar{i}}} \overrightarrow{\overrightarrow{\xi}}'_2 : \vec{\nabla}_{\vec{v}_{\bar{i}}} \vec{\xi}_1\right) \mathrm{d}\Upsilon_{\vec{v}_{\bar{j}}} \\
&= 2\pi \left(\frac{q_{\bar{i}} q_{\bar{j}}}{4\pi\epsilon_0}\right)^2 \frac{\text{Ln}\,[\Lambda]}{m_{\bar{i}}} \vec{\nabla}_{\vec{v}_{\bar{i}}} \cdot \int \left(\vec{\xi}_1 \cdot \overrightarrow{\overrightarrow{\xi}}'_2\right) \mathrm{d}\Upsilon_{\vec{v}_{\bar{j}}} \,.
\end{aligned} \tag{2.45}$$

This collision operator, first derived by Landau in 1936, was usually referred to as the Landau-Fokker-Planck (LFP) operator because the distribution function is expanded to second order in velocity space, equivalent to describing their evolution by drift and diffusion terms. It has to be noted that the screening effect, handled here through an artificial cut-off via CL, can be more rigorously discussed using the Balescu-Lenard collision operator [81, 82] derived from BBGKY (Bogoliubov-Born-Green-Kirkwood-Yvon) hierarchy where screening emerges naturally through dielectric response. Because its derivation relies fundamentally on the expansion of the coupling parameter, it becomes extremely hard to generalise to the strongly coupled WDM regime, with only a few attempts being made decades ago [83–85] and being severely obstructed by the complicated mathematics involved. An alternative to this is to expand the distribution function into higher orders in the velocity space, known as the Kramers-Moyal Expansion [86, 87], but also has complexity of its own. Therefore, the discussion in this thesis will focus on extensions of the Landau collision operator that can be generalised to coupled systems.

2.2.3 Coulomb Logarithm and Collisional Times

Although Landau derived his collision operator in 1936, he did not provide an explicit evaluation of the important Coulomb Logarithm term that emerged in the collisional integral, but rather left the integral without the cut-off at the Debye length. Cut-off similar to the discussion in Eq. 2.36 was first introduced by Spitzer in his pioneering work in 1950 and 1953 ([28, 30]), where the Coulomb logarithm is defined through integration over the impact parameter r_{b} rather than the deflection angle θ'_{r}. This derivation emerges when

making the small-angle approximation in Eq. 2.31

$$\int \frac{\mathrm{Cos}\left[\theta_\mathrm{r}'/2\right]\mathrm{d}\theta_\mathrm{r}'}{\mathrm{Sin}\left[\theta_\mathrm{r}'/2\right]} \approx 2\int \frac{\mathrm{d}(\theta_\mathrm{r}'/2)}{\theta_\mathrm{r}'/2} \tag{2.46}$$

using $\mathrm{Cos}\left[\theta_\mathrm{r}'/2\right] \approx 1, \mathrm{Sin}\left[\theta_\mathrm{r}'/2\right] \approx \theta_\mathrm{r}'/2$. From Eq. 2.35, the small-angle approximation gives $\theta_\mathrm{r}'/2 \approx \tan\left[\theta_\mathrm{r}'/2\right] = \frac{r_{\mathrm{b}_0}}{r\mathrm{b}}$, allowing to transform to impact parameter:

$$\int \frac{\mathrm{Cos}\left[\theta_\mathrm{r}'/2\right]\mathrm{d}\theta_\mathrm{r}'}{\mathrm{Sin}\left[\theta_\mathrm{r}'/2\right]} \approx 2\int \frac{\mathrm{d}(r_\mathrm{b}^{-1})}{r_\mathrm{b}^{-1}} = -2\int_{-} \frac{r_\mathrm{b}^{-2}\mathrm{d}(r_\mathrm{b})}{r_\mathrm{b}^{-1}} = 2\int_{+} \frac{\mathrm{d}(r_\mathrm{b})}{r_\mathrm{b}} \ . \tag{2.47}$$

Here, $\int_{-}$ denotes integration from smaller to larger values. This integral diverges at both limits, necessitating two cut-offs. The upper limit is naturally set by the Debye length r_D as discussed in section Sec. 2.2.2, while the lower cut-off is the classical distance of closest approach r_{b_0} because the small-angle approximation fails for $r_\mathrm{b} < r_{\mathrm{b}_0}$ where $\theta_\mathrm{r}' > \pi/2$. Therefore, the Coulomb logarithm in this formulation becomes:

$$\mathrm{Ln}\left[\Lambda_\mathrm{C}\right] \coloneqq \mathrm{Ln}\left[\frac{r_\mathrm{D}}{r_{\mathrm{b}_0}}\right] \ . \tag{2.48}$$

This definition given by Spitzer [28, 30] will be referred to as the original classical CL in this thesis, whereas that defined in Eq. 2.36 will be referred to as the modified classical CL $\mathrm{Ln}\left[\Lambda_{\mathrm{C}'}\right]$.

To estimate the average effect of CL on the collision operator, one usually assumes that for e-e collision:

$$\begin{aligned}
\mathrm{Ln}\left[\Lambda_{\mathrm{C}'}\right] &\simeq \mathrm{Ln}\left[\frac{r_\mathrm{D}}{\langle r_{\mathrm{b}_0}\rangle}\right] \simeq \mathrm{Ln}\left[r_\mathrm{D}\frac{4\pi\varepsilon_\mathbf{0} m_\mathrm{r}\langle v_\mathrm{r}^2\rangle}{q_\mathbf{e}^2}\right] = \mathrm{Ln}\left[r_\mathrm{D}\frac{8\pi\varepsilon_\mathbf{0}\langle\frac{1}{2}m_\mathrm{r}v_\mathrm{r}^2\rangle}{q_\mathbf{e}^2}\right] \\
&= \mathrm{Ln}\left[\sqrt{\frac{\varepsilon_\mathbf{0}k_\mathbf{B}T}{\rho_N q_\mathbf{e}^2}}\frac{8\pi\varepsilon_\mathbf{0}\times\frac{3}{2}k_\mathbf{B}T}{q_\mathbf{e}^2}\right] = \mathrm{Ln}\left[\frac{12\pi\varepsilon_\mathbf{0}^{3/2}}{q_\mathbf{e}^3}\frac{\left(k_\mathbf{B}T\right)^{3/2}}{\rho_N^{1/2}}\right] \\
&\approx 23.1 - \frac{1}{2}\mathrm{Ln}\left[\frac{\rho_N}{(1\ \mathrm{cm}^{-3})}\right] + \frac{3}{2}\mathrm{Ln}\left[\frac{k_\mathbf{B}T}{(1\ \mathrm{eV})}\right] \ ,
\end{aligned} \tag{2.49}$$

where $\langle\frac{1}{2}m_\mathrm{r}v_\mathrm{r}^2\rangle = \frac{3}{2}k_\mathbf{B}T$ because

$$\langle v_\mathrm{r}^2\rangle = \langle(\vec{v}_1 - \vec{v}_2)^2\rangle = \langle v_1^2\rangle + \langle v_2^2\rangle = \frac{6k_\mathbf{B}T}{m_\mathbf{e}} \ , \tag{2.50}$$

and $m_\mathrm{r} = \frac{1}{2}m_\mathbf{e}$. For the modified result:

$$\mathrm{Ln}\left[\Lambda_{\mathrm{C}'}\right] \simeq \frac{1}{2}\mathrm{Ln}\left[1 + \Lambda_\mathrm{C}^2\right] \ , \tag{2.51}$$

It can be seen that for weakly coupled systems, the two definitions are consistent to first order:

$$\begin{aligned}
\mathrm{Ln}\left[\Lambda_{\mathrm{C}'}\right] &= \frac{1}{2}\mathrm{Ln}\left[1 + (r_\mathrm{D}/r_{\mathrm{b}_0})^2\right] \approx \frac{1}{2}\mathrm{Ln}\left[(r_\mathrm{D}/r_{\mathrm{b}_0})^2\right] \\
&= \mathrm{Ln}\left[r_\mathrm{D}/r_{\mathrm{b}_0}\right] \ .
\end{aligned} \tag{2.52}$$

However, for strongly coupled systems where $r_\mathrm{D} \sim r_{\mathrm{b}_0}$, the original classical CL gives negative results when $r_\mathrm{D} < r_{\mathrm{b}_0}$, as demonstrated in Fig. 2.2, while the modified classical CL does not

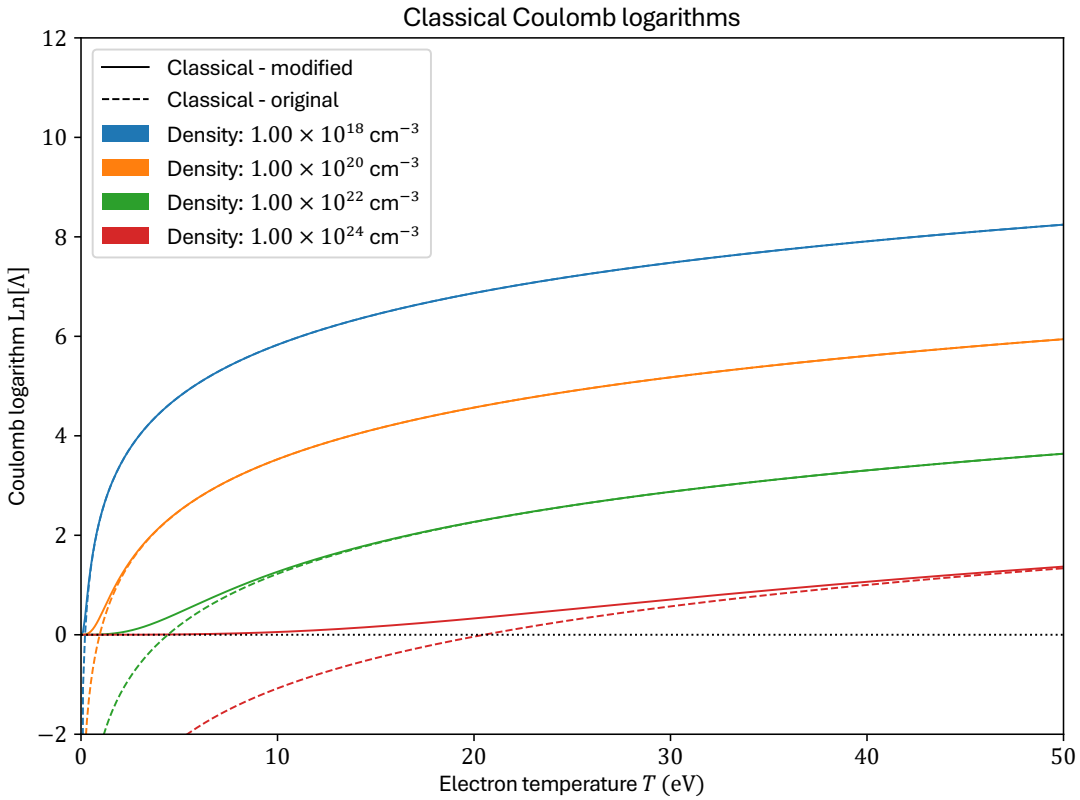


Figure 2.2: The comparison between the modified and original classical Coulomb logarithm reveals significant differences, particularly at low temperatures and high densities. The modified version (solid lines) maintains physically meaningful positive values across all temperature ranges, while the original formulation (dashed lines) can yield negative values at low temperatures, especially for higher densities.

suffer this problem as it remains positive for all parameter regimes. Moreover, the nature of the integral over deflection angle in Sec. 2.2.2 does not diverge at large deflection angles, making the cut-off at small impact parameters less physically reasonable [77]. For this reason, the modified classical CL will usually be preferred in this thesis.

It should be noted that while the velocity-independent CL approximation is conventional in plasma kinetics, it is not well justified across a broad range of parameters. In particular, for high-velocity electrons where $v \gg v_{\mathrm{th}} := \sqrt{\frac{2k_{\mathrm{B}}T}{m_{\mathrm{e}}}}$, the effective CL needs to be modified to accurately describe electron relaxation [58, 88]. This becomes evident when examining the Landau collision operator (Eq. 2.45) with an explicit velocity-dependent CL:

$$\begin{aligned}\hat{\mathcal{O}}_{\mathrm{coll}}[\varrho,\varrho] &= \frac{2\pi}{m_{\mathrm{e}}}\left(\frac{q_{\mathrm{e}}^2}{4\pi\epsilon_0}\right)^2 \int \mathrm{Ln}\left[\Lambda[v_{\mathrm{r}}]\right] \vec{\nabla}_{\vec{v}} \cdot \left(\vec{\xi}_1 \cdot \overrightarrow{\vec{\xi}}'_2\right) \mathrm{d}\Upsilon_{\vec{v}_\star} \\ &\propto \int \mathrm{Ln}\left[\Lambda\left[|\vec{v}-\vec{v}_\star|\right]\right] \vec{\nabla}_{\vec{v}} \cdot \left(\left(\varrho[\vec{v}_\star]\vec{\nabla}_{\vec{v}}\varrho[\vec{v}] - \varrho[\vec{v}]\vec{\nabla}_{\vec{v}_\star}\varrho[\vec{v}_\star]\right) \cdot \frac{\overrightarrow{\mathbb{1}} - \vec{e}_{x_{\mathrm{r}}}\vec{e}_{x_{\mathrm{r}}}}{|\vec{v}-\vec{v}_\star|} \right) \mathrm{d}\Upsilon_{\vec{v}_\star} \,.\end{aligned} \tag{2.53}$$

For near-Maxwellian electron distributions, the integral over $\vec{v}_\star$ is dominated by thermal velocities $v_\star \sim v_{\mathrm{th}}$. When $v \gg v_{\mathrm{th}}$, it follows that $\mathrm{Ln}\left[\Lambda\left[|\vec{v}-\vec{v}_\star|\right]\right] \approx \mathrm{Ln}\left[\Lambda[v]\right] > \mathrm{Ln}\left[\Lambda[v_{\mathrm{th}}]\right]$.

While this difference is often negligible when $\mathrm{Ln}\,[\Lambda[v_{\mathrm{th}}]] \gg 1$ due to the logarithmic dependence, it becomes significant in high-density, low-temperature plasmas where $\mathrm{Ln}\,[\Lambda[v_{\mathrm{th}}]]$ is small. Despite these limitations, the velocity-independent CL approximation remains widely used due to its mathematical simplicity, and this thesis will primarily employ this averaged approach.

Once a velocity-independent CL is assumed, the e-e collision rate can be characterised by a key quantity known as collision time. While its definition varies under different scenarios, this thesis adopts the definition given by [79]:

$$t_{\text{e-e}} = 12\pi^{3/2}\frac{m_{\mathbf{e}}^{1/2}\epsilon_0^2(k_{\mathbf{B}}T_{\mathrm{e}})^{3/2}}{\rho_N q_{\mathbf{e}}^4 \mathrm{Ln}\,[\Lambda_{\text{e-e}}]}\ . \tag{2.54}$$

Strictly speaking, this quantity is defined by considering a plasma of two particle species at the same temperature but with a small relative COM velocity. Due to Coulomb collisions, the relative COM velocity decreases exponentially until both species have the same COM velocity. The collision time defined in Eq. 2.54 characterises the rate of this damping process. Importantly, although derived for a two-species scenario, this timescale also proves useful for describing transport processes of a single species, and is thus widely used by the plasma physics community.

Another commonly used timescale is the 90-degree-deflection time, which represents the average time required for the direction of motion of an electron to be deflected by $\pi/2$ through multiple small-angle collisions [89]. As a test electron interacts with the background plasma, while its average deflection angle remains zero, its mean square angular deviation grows steadily with time. As it turns out, this 90-degree-deflection time has a similar expression to Eq. 2.54, differing only by numerical constants. This thesis will prefer to use Eq. 2.54 for the discussion of collision time.

A similar discussion can apply to e-i collisions to obtain the e-i collision time and the relevant CL. For brevity, its discussion is not included here but can be found in literature such as [57].

It should be stressed that the collision time defined in this thesis has a different origin from the "relaxation time" defined in RTA. In general, RTA does not hold in a plasma environment unless some additional assumption is made. This can be done using the linearised collisional operator without writing it explicitly in the LFP form, and expanding the distribution into spherical harmonics [57, 90]:

$$\varrho[\vec{r},\vec{v},t] = \varrho'_{\underline{l,m}}[\vec{r},|\vec{v}|,t]\mathrm{Y}_{\underline{l,m}}[\theta,\varphi], \tag{2.55}$$

where $[|\vec{v}|,\theta,\varphi]$ is the spherical coordinate in the velocity space. However, the different components will have different relaxation times and thus can not be captured by a single

timescale, bringing difficulties to further analysis. This stands in contrast with the collision time defined here. Therefore, this thesis will stick to using the terminology "collision time" instead of "relaxation time".

Nevertheless, the LFP collision operators can also be linearised to obtain a simple expression for the transport coefficients, which is also done by Spitzer [28, 30]. For instance, the electrical conductivity can be written in the form of [91]:

$$\sigma_{q,\mathrm{dc}} \approx 1.95 \frac{\rho_{N_\mathrm{e}} q_{\mathbf{e}}^2 t_{\text{e-i}}}{m_{\mathbf{e}}}, \tag{2.56}$$

where $t_{\text{e-i}}$ is the e-i collision time. This can be directly compared to the Drude model result (Eq. 1.13) derived from RTA, which only deviates by a factor of around 2. This similarity suggests that RTA, although not strictly held in a plasma environment, can also be used as a reasonable simplification in understanding transport phenomena in WDM. It is worth noticing that the linearisation procedure involves expanding the distribution function to spherical harmonics to the first order ($\mathrm{Y}_{1,0} = \mathrm{Cos}\,[\theta]$), indicating the relaxation time used in RTA does characterise the first order change due to the external electric field. This can be seen by considering a homogeneous steady state solution [4] of the Boltzmann equation under the presence of an external electric field $\vec{E} = E\vec{e}_z$ [5]. Using RTA (Eq. 2.17), one obtain

$$\begin{aligned}
\Delta\varrho &\approx -t_{\mathrm{rlx}} \left(\left(\frac{\partial}{\partial t} + \vec{v} \cdot \vec{\nabla}_{\vec{r}} + \frac{\vec{F}}{m_{\mathbf{e}}} \cdot \vec{\nabla}_{\vec{v}} \right) \varrho_{\mathrm{LM}} \right) \\
&\approx -t_{\mathrm{rlx}} \left(\frac{-q_{\mathbf{e}}\vec{E}}{m_{\mathbf{e}}} \cdot \vec{\nabla}_{\vec{v}} \varrho_{\mathrm{LM}} \right) \\
&= \frac{t_{\mathrm{rlx}} q_{\mathbf{e}}}{m_{\mathbf{e}}} \varrho_{\mathrm{LM}} \left(-\frac{m_{\mathbf{e}}\vec{v}}{k_{\mathbf{B}}T} \right) \cdot \vec{E} \\
&= \frac{t_{\mathrm{rlx}} q_{\mathbf{e}} E}{k_{\mathbf{B}}T} \varrho_{\mathrm{LM}} v \mathrm{Cos}\,[\theta] \ ,
\end{aligned} \tag{2.57}$$

where $\vec{v}_0 = \vec{0}$ has been assumed in Eq. 2.9, and the approximation $\varrho \approx \varrho_{\mathrm{LM}}$ has been used. Eq. 2.57 suggests that the first order change of the electron distribution has the form of $\varrho'_{1,0}[v]\mathrm{Y}_{1,0}[\theta,\varphi] = \varrho'_{1,0}[v]\mathrm{Cos}\,[\theta]$, which is consistent with the spherical harmonics expansion scheme. On the other hand, this relaxation time does not reflect the relaxation process of other components of the distribution, for example, an isotropic non-thermal distribution that is thermalising due to e-e collisions.

[4] Therefore $\frac{\partial \varrho}{\partial t} = 0$ and $\nabla_{\vec{r}}\varrho = 0$.

[5] The angle θ is defined as that between $\vec{v}$ and $\vec{e}_z$.

2.3 Electron Relaxation in Quantum Plasmas

The discussion in the previous section, although complete within its scope, is fundamentally based on classical physics. However, in many scenarios of interest, electrons interact through quantum mechanical processes. This quantum nature manifests in two distinct ways: First, as the relative velocity $v_{\mathrm{r}} \to 0$, the classical distance of closest approach $r_{\mathrm{b}_0} \propto v_{\mathrm{r}}^{-2}$, while the (reduced) de-Broglie wavelength of each particle $l_{\mathrm{dB}} = \frac{\hbar}{p}$ scales roughly as v_{r}^{-1}. Therefore, when $l_{\mathrm{dB}} > r_{\mathrm{b}_0}$, the scattering process must be treated quantum-mechanically. Second, in warm, dense plasmas, degeneracy effects become significant, and electrons relax to a Fermi-Dirac distribution instead of a Maxwellian, despite the classical Boltzmann equation predicting Maxwellian equilibrium.

This section discusses these quantum effects through two main approaches: by introducing quantum-mechanical corrections to the CL, and by examining the quantum Landau-Fokker-Planck collision operator based on the Boltzmann-Uehling-Uhlenbeck (BUU) equation.

2.3.1 Quantum Mechanical Corrections for Coulomb Logarithms

The first quantum mechanical correction to the Coulomb logarithm was proposed by Spitzer in 1953 [30]. Because the classical treatment becomes invalid at small impact parameters r_{b} (corresponding to $\theta_{\mathrm{r}}' \to \pi$ or equivalently $\eta = \mathrm{Sin}\,[\theta_{\mathrm{r}}'/2] \to 1$), he suggested cutting off the upper limit of the integration in Eq. 2.36 at $r_{\mathrm{b}}^{\star\star} = l_{\mathrm{dB}} = \frac{\hbar}{m_{\mathrm{e}} v_{\mathrm{r}}}$, where l_{dB} is the reduced de Broglie wavelength (the de Broglie wavelength divided by 2π). When expressed in terms of η, this is equivalent to:

$$\eta^{\star\star} = \mathrm{Sin}\,[\theta_{\mathrm{r}}'^{\star\star}/2] = \frac{1}{\sqrt{1 + (\tan\,[\theta_{\mathrm{r}}'^{\star\star}/2])^{-2}}} = \frac{1}{\sqrt{1 + (l_{\mathrm{dB}}/r_{\mathrm{b}_0})^2}}\ . \tag{2.58}$$

Therefore, the quantum-corrected Coulomb logarithm becomes:

$$\begin{aligned} \mathrm{Ln}\left[\Lambda_{\mathrm{Q}'}\right] &= \int_{\eta^\star}^{\eta^{\star\star}} \frac{\mathrm{d}\eta}{\eta} = \mathrm{Ln}\left[\frac{\eta^{\star\star}}{\eta^\star}\right] \\ &= \mathrm{Ln}\left[\frac{\sqrt{1 + (r_{\mathrm{D}}/r_{\mathrm{b}_0})^2}}{\sqrt{1 + (l_{\mathrm{dB}}/r_{\mathrm{b}_0})^2}}\right] \\ &= \frac{1}{2}\mathrm{Ln}\left[\frac{r_{\mathrm{D}}^2 + r_{\mathrm{b}_0}^2}{l_{\mathrm{dB}}^2 + r_{\mathrm{b}_0}^2}\right]\ . \end{aligned} \tag{2.59}$$

As this cut-off reduces the integration range, CL is decreased, consistent with Spitzer's original statement. For weakly-coupled, non-degenerate plasmas, the Debye length r_{D} is larger than both the de Broglie's wavelength l_{dB} and the classical distance of closest approach r_{b_0}. Therefore, Eq. 2.59 can be approximated in two ways:

a) When electrons are at sufficiently low temperatures, the vast majority of collisions will take place at low relative velocities. Thus $l_{\mathrm{dB}} \ll r_{\mathrm{b}_0}$, and the quantum correction can be neglected:

$$\mathrm{Ln}\left[\Lambda_{\mathrm{Q}'}\right] \approx \frac{1}{2}\mathrm{Ln}\left[1+\left(r_{\mathrm{D}}/r_{\mathrm{b}_0}\right)^2\right] = \mathrm{Ln}\left[\Lambda_{\mathrm{C}'}\right] \ . \tag{2.60}$$

b) When electrons are at sufficiently high temperatures, $l_{\mathrm{dB}} \gg r_{\mathrm{b}_0}$, Eq. 2.59 simplifies to $\mathrm{Ln}\left[\frac{r_{\mathrm{D}}}{l_{\mathrm{dB}}}\right]$. Similar to the classical situation, this is the form proposed originally by Spitzer in 1953 and is more widely accepted by the plasma kinetics community, which will be referred to as the original quantum CL, whereas the formulation given by Eq. 2.59 will be referred to as the modified quantum CL. By averaging over all collision events and assuming

$$\langle l_{\mathrm{dB}}\rangle \simeq \frac{\hbar}{m_{\mathbf{e}}\langle v_{\mathrm{r}}\rangle} \simeq \frac{\hbar}{m_{\mathbf{e}}\sqrt{\langle v_{\mathrm{r}}^2\rangle}} = \frac{\hbar}{\sqrt{6k_{\mathbf{B}}Tm_{\mathbf{e}}}} \ , \tag{2.61}$$

one obtains:

$$\mathrm{Ln}\left[\Lambda_{\mathrm{Q}}\right] \simeq 24.3 - \frac{1}{2}\mathrm{Ln}\left[\frac{\rho_N}{(1\ \mathrm{cm}^{-3})}\right] + \mathrm{Ln}\left[\frac{k_{\mathbf{B}}T}{(1\ \mathrm{eV})}\right] \ . \tag{2.62}$$

The critical temperature separating the classical and quantum regimes can be determined by equating the characteristic lengths:

$$\begin{aligned} &\langle l_{\mathrm{dB}}\rangle \simeq \langle r_{\mathrm{b}_0}\rangle \\ \Leftrightarrow &\frac{\hbar}{\sqrt{6k_{\mathbf{B}}Tm_{\mathbf{e}}}} \simeq \frac{q_{\mathbf{e}}^2}{8\pi\varepsilon_0 \times \frac{3}{2}k_{\mathbf{B}}T} \\ \Leftrightarrow &k_{\mathbf{B}}T \simeq \frac{q_{\mathbf{e}}^4 m_{\mathbf{e}}}{24\pi^2\varepsilon_0^2\hbar^2} \approx 18\ \mathrm{eV} \ . \end{aligned} \tag{2.63}$$

Therefore, CL after quantum correction takes the form:

$$\mathrm{Ln}\left[\Lambda\right] = \begin{cases} 23.1 - \frac{1}{2}\mathrm{Ln}\left[\frac{\rho_N}{(1\ \mathrm{cm}^{-3})}\right] + \frac{3}{2}\mathrm{Ln}\left[\frac{k_{\mathbf{B}}T}{(1\ \mathrm{eV})}\right] & (k_{\mathbf{B}}T < 18\ \mathrm{eV}) \\ 24.3 - \frac{1}{2}\mathrm{Ln}\left[\frac{\rho_N}{(1\ \mathrm{cm}^{-3})}\right] + \mathrm{Ln}\left[\frac{k_{\mathbf{B}}T}{(1\ \mathrm{eV})}\right] & (k_{\mathbf{B}}T > 18\ \mathrm{eV}) \end{cases} . \tag{2.64}$$

Contrary to common intuition, the quantum-mechanical correction applies at high temperatures instead of low temperatures. As the critical temperature is only an estimation from averaging over the electron distribution, this could vary substantially in different literature. For example, Spitzer [30] used 36.2 eV, while Fitzpatrick [79] used 10 eV.

Since the two regimes in Eq. 2.64 are separated by comparing l_{dB} with r_{b_0}, it is more often described in the compact form $\mathrm{Ln}\left[\Lambda\right] = \mathrm{Ln}\left[\frac{r_{\mathrm{D}}}{r_{\mathrm{min}}}\right]$ with $r_{\mathrm{min}} = \mathrm{Max}[r_{\mathrm{b}_0}, l_{\mathrm{dB}}]$. The two temperature regimes can also be linked by using interpolation methods, such as that given by Huba in [56], which will be called Huba's formula:

$$\begin{aligned} &\mathrm{Ln}\left[\Lambda\right] = \\ &23.5 - \frac{1}{2}\mathrm{Ln}\left[\frac{\rho_N}{(1\ \mathrm{cm}^{-3})}\right] + \frac{5}{4}\mathrm{Ln}\left[\frac{k_{\mathbf{B}}T}{(1\ \mathrm{eV})}\right] - \left(10^{-5} + \left(\mathrm{Ln}\left[\frac{k_{\mathbf{B}}T}{(1\ \mathrm{eV})}\right] - 2\right)^2\right)^{-1/2} \ . \end{aligned} \tag{2.65}$$

It should be noted that Eqs. 2.60, 2.62, 2.64, and 2.65 are all approximations of the more fundamental expression in Eq. 2.59. Their prevalence in literature is largely due to historical reasons. In contrast, Eq. 2.59 provides a more rigorous and unified description of the Coulomb logarithm across different parameter regimes. It naturally incorporates both classical and quantum effects without artificial transitions. Therefore, it is preferable to use Eq. 2.59 directly. The comparison between these CLs is depicted in Fig. 2.3.

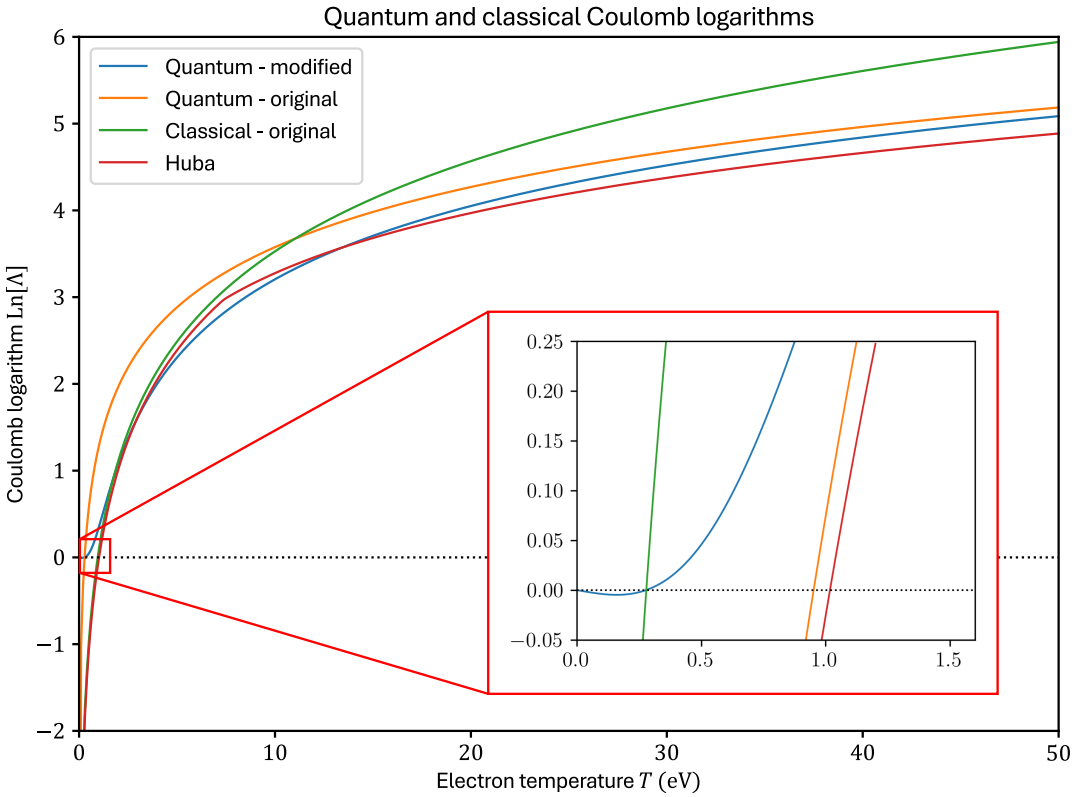


Figure 2.3: Different formulations of Coulomb Logarithms at $\rho_N = 1.0 \times 10^{20}\text{cm}^{-3}$. At the higher temperature end, the modified quantum CL (blue) given by Eq. 2.59 is reduced from the classical value (orange) and can be approximated by Eq. 2.62 (green), whereas at the lower temperature end the modified quantum CL is approximated by the classical version given by Eq. 2.49 (orange). Huba's formula in [56] (red) represents an interpolation between the quantum version and the classical version. All formulations predict unphysical negative results at the lowest temperature.

For plasmas with electron density lower than that of a typical solid metal ($\rho_N \sim 10^{22}$ cm^{-3}), the modified quantum CL given by Eq. 2.59 will not predict a negative result unless the temperature is extremely low such that a plasma state can barely be formed (For example $k_\mathbf{B}T \sim 0.3$ eV for $\rho_N = 1.0 \times 10^{20}$ cm^{-3}, as illustrated in Fig. 2.3.). However, when the electron density starts to approach or exceed that of a solid metal, the Debye length r_D that decreases with the electron density will approach and become smaller than the de

Broglie wavelength l_{dB} for many of the electrons, leading to unphysical negative values of $\mathrm{Ln}\,[\Lambda]$, as illustrated in Fig. 2.4 Therefore, the modified quantum CL is not satisfactory in

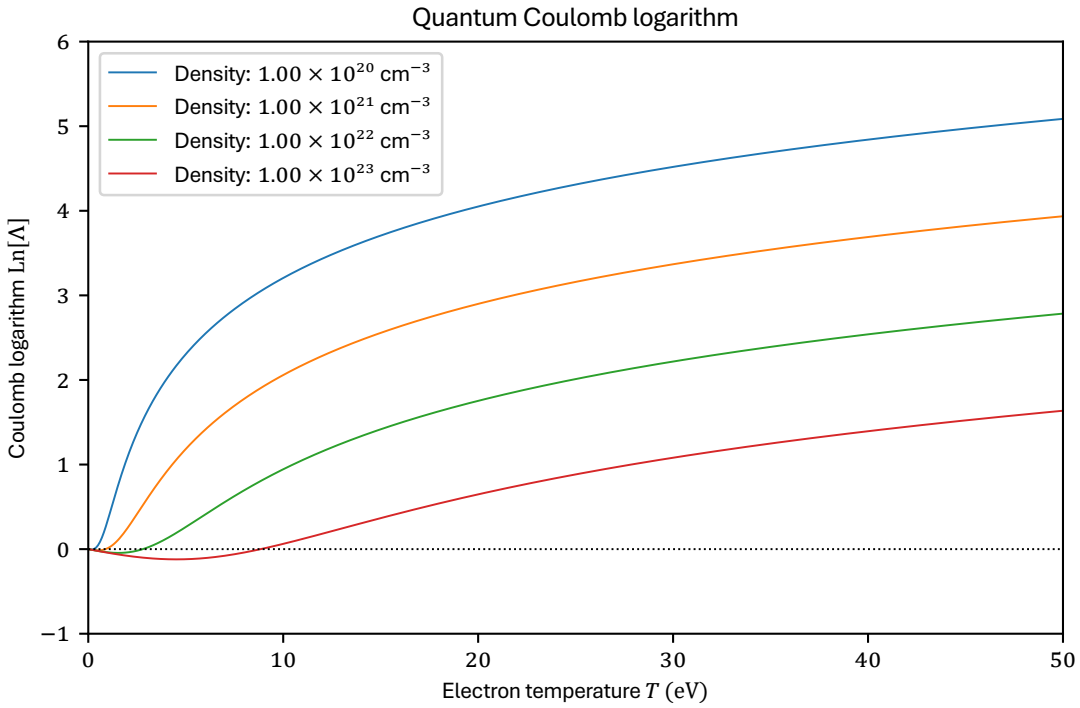


Figure 2.4: The modified quantum CL predicts negative values at high densities and low temperatures.

this regime. This originates from a fundamental problem that the contribution from small impact parameters r_{b} is neglected instead of being treated properly using quantum mechanics. A full quantum mechanical treatment of close-range electron-electron interactions would be necessary to accurately describe the Coulomb logarithm in these high-density regimes.

An immediate correction to this treatment can be made by replacing classical electron-electron collisions with quantum scattering, as first proposed by Mulser *et. al.* [58]. This approach considers scattering in a Yukawa potential instead of a Coulomb potential. The advantages are significant: the Yukawa potential has a finite range, avoiding the need for an artificial cut-off. Furthermore, the plasma screening effect makes the Yukawa potential a better representation of the actual interaction.

When scattered by a Yukawa potential, using the First Born approximation, the differential cross-section is given by:

$$\frac{\mathrm{d}S}{\mathrm{d}\Omega'_{\mathrm{r}}} = \frac{r_{\mathrm{b}_0}^2}{\left(4(\mathrm{Sin}\,[\theta'_{\mathrm{r}}/2])^2 + (l_{\mathrm{dB}}/r_{\mathrm{D}})^2\right)^2}\ , \tag{2.66}$$

Where l_{dB} is the de Broglie wavelength, r_{b_0} is the classical distance of closest approach, and r_{D} is the Debye length, maintaining the same physical interpretation as in previous formulations.

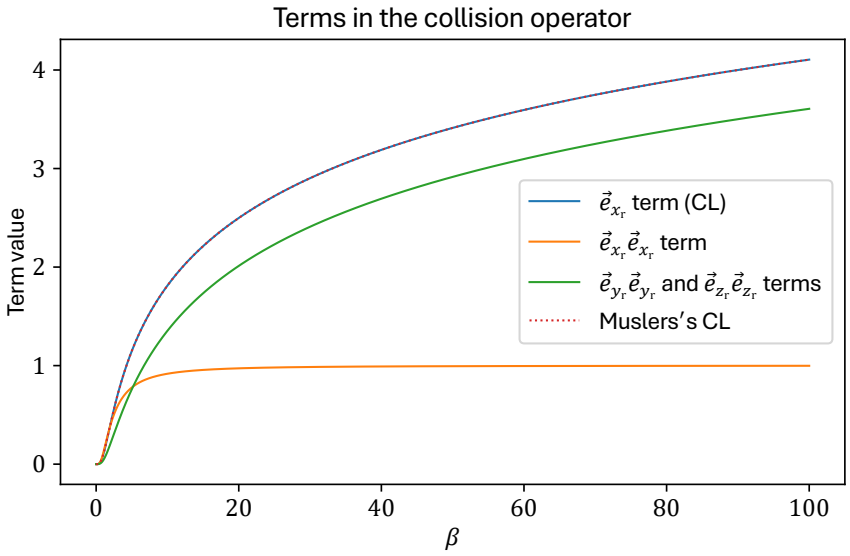


Figure 2.5: Comparison between Mulser CL and the coefficients of terms in the collision operator.

When substituted into the LFP collision operator, Eq. 2.31 becomes

$$\begin{aligned}\int \frac{\Delta\vec{v}_{\mathrm{r}}}{\left((\mathrm{Sin}\left[\theta'_{\mathrm{r}}/2\right])^2+\beta^{-2}\right)^2}\mathrm{d}\Omega'_{\mathrm{r}} &= 2\pi v_{\mathrm{r}}\int_0^{\pi}\frac{\mathrm{Cos}\left[\theta'_{\mathrm{r}}\right]-1}{\left((\mathrm{Sin}\left[\theta'_{\mathrm{r}}/2\right])^2+\beta^{-2}\right)^2}\mathrm{Sin}\left[\theta'_{\mathrm{r}}\right]\mathrm{d}\theta'_{\mathrm{r}}\ \vec{e}_{x_{\mathrm{r}}}\\ &= 2\pi\left(\frac{4\beta^2}{1+\beta^2}-4\mathrm{Ln}\left[1+\beta^2\right]\right)\vec{v}_{\mathrm{r}} = -16\pi\vec{v}_{\mathrm{r}}\times\frac{1}{2}\left(\mathrm{Ln}\left[1+\beta^2\right]-\frac{\beta^2}{1+\beta^2}\right)\ ,\end{aligned} \tag{2.67}$$

where $\beta := \frac{2r_{\mathrm{D}}}{l_{\mathrm{dB}}}$. By comparing to the classical result:

$$\int\frac{\Delta\vec{v}_{\mathrm{r}}}{(\mathrm{Sin}\left[\theta'_{\mathrm{r}}/2\right])^4}\mathrm{d}\Omega'_{\mathrm{r}} = -16\pi\vec{v}_{\mathrm{r}}\mathrm{Ln}\left[\Lambda_{\mathrm{C}'}\right]\ , \tag{2.68}$$

Mulser's CL can be defined as:

$$\mathrm{Ln}\left[\Lambda_{\mathrm{Mulser}}\right] = \frac{1}{2}\left(\mathrm{Ln}\left[1+\beta^2\right]-\frac{\beta^2}{1+\beta^2}\right)\ . \tag{2.69}$$

Mulser's CL has some direct advantages compared to the modified quantum CL. First, the three terms r_{D}, l_{dB}, and r_{b_0} emerge naturally in the Yukawa potential cross-section, with no artificial cut-off included. The integration is regular and performed from $\theta'_{\mathrm{r}} : 0 \to \pi$. The $r_{\mathrm{b}} \to 0$ domain is by no means special, and $r_{\mathrm{b}_0} > r_{\mathrm{D}}$ is also included due to the consideration of the Yukawa potential itself, making it physically more reasonable. It should also be noted that the integration is performed over θ'_{r} instead of over r_{b} as the impact parameter r_{b} has no direct physical significance in quantum scattering theory and the electrons do not follow a classical trajectory. Second, the result is also regular on the whole domain of β, with no unphysical result of negative values even for $\beta \to 0$ (Fig. 2.5). Because the conventional argument of choosing $r_{\mathrm{min}} = \mathrm{Max}[r_{\mathrm{b}_0}, l_{\mathrm{dB}}]$ plays no role, the result is smooth, with no critical

temperature involved or interpolation needed, providing a unified expression across regimes. Finally, for $r_{\mathrm{D}} \gg l_{\mathrm{dB}}$, $\beta \gg 1$, Mulser's CL can be approximated with

$$\begin{aligned} \mathrm{Ln}\left[\Lambda_{\mathrm{Mulser}}\right] &\approx \frac{1}{2}\left(\mathrm{Ln}\left[\beta^2\right]-1\right) \approx \mathrm{Ln}\left[\beta\right]-\frac{1}{2} = \mathrm{Ln}\left[\frac{2r_{\mathrm{D}}}{l_{\mathrm{dB}}}\right]-\frac{1}{2} \\ &= \mathrm{Ln}\left[\frac{r_{\mathrm{D}}}{l_{\mathrm{dB}}}\right]+\left(\mathrm{Ln}\left[2\right]-\frac{1}{2}\right) \approx \mathrm{Ln}\left[\Lambda_{\mathrm{Q}}\right]+0.2\ , \end{aligned} \tag{2.70}$$

thus recovering the quantum result with a small correction.

Using similar methods the coefficients $\vec{e}_{x_{\mathrm{r}}}$ and $\vec{e}_{y_{\mathrm{r}}}\vec{e}_{y_{\mathrm{r}}}$, $\vec{e}_{z_{\mathrm{r}}}\vec{e}_{z_{\mathrm{r}}}$ terms of the rank-2 tensor in Eq. 2.34 can be obtained

$$\begin{array}{ll} \vec{e}_{x_{\mathrm{r}}}\vec{e}_{x_{\mathrm{r}}}: & \dfrac{2+\beta^2}{1+\beta^2}-\dfrac{2}{\beta^2}\mathrm{Ln}\left[1+\beta^2\right] \\ \vec{e}_{y_{\mathrm{r}}}\vec{e}_{y_{\mathrm{r}}} \text{ and } \vec{e}_{z_{\mathrm{r}}}\vec{e}_{z_{\mathrm{r}}}: & \left(\dfrac{1}{2}+\dfrac{1}{\beta^2}\right)\mathrm{Ln}\left[1+\beta^2\right]-1 \end{array} . \tag{2.71}$$

For a wide range of β it still holds that the $\vec{e}_{y_{\mathrm{r}}}\vec{e}_{y_{\mathrm{r}}}$, $\vec{e}_{z_{\mathrm{r}}}\vec{e}_{z_{\mathrm{r}}}$ term coefficient $\approx$ CL, and that the $\vec{e}_{x_{\mathrm{r}}}\vec{e}_{x_{\mathrm{r}}}$ coefficient is much smaller than both (Fig. 2.5), making the treatment of decomposing $\vec{\xi}_2$ into $\vec{\xi}'_2$ and $\vec{\xi}''_2$ (Eq. 2.41) valid. Thus, $\vec{\xi}''_2$ can be neglected to construct the Landau collision operator. Using a similar technique of substituting l_{dB} of individual particles by its characteristic value averaged over the distribution and expressed in terms of temperature, one can conveniently use Mulser's CL for the electron relaxation process. The only exception is when $\beta \to 0$, where the $\vec{e}_{x_{\mathrm{r}}}\vec{e}_{x_{\mathrm{r}}}$ becomes larger. This can only happen when the temperature of the system is very low such that $r_{\mathrm{D}} = \sqrt{\frac{\varepsilon_0 k_{\mathbf{B}} T}{\rho_N q_{\mathbf{e}}^2}} \to 0$, where the Debye screening should be replaced by the Thomas-Fermi screening [92].

Under the Thomas-Fermi model, the screening length of electrons remains finite even as $T \to 0$ due to Fermi-Dirac statistics. Using the local density approximation and local chemical potential $\mathcal{U}$, the screening length is given by:

$$r_{\mathrm{TF}} = \left(\frac{q_{\mathbf{e}}^2}{\varepsilon_0}\left.\frac{\partial \rho_{N_{\mathrm{L}}}[\mathcal{U},T]}{\partial \mathcal{U}}\right|_{\mathcal{U}=\mathcal{U}_0}\right)^{-1/2} , \tag{2.72}$$

where $\mathcal{U}_0$ is the global chemical potential, and $\rho_{N_{\mathrm{L}}}[\mathcal{U},T]$ is the local density written as a function of $\mathcal{U}$ and T. For a Fermi-Dirac distribution, this becomes

$$\rho_{N_{\mathrm{L}}}[\mathcal{U},T] = \int \boldsymbol{n}[W_{\mathrm{K}}]\frac{\mathrm{d}W_{\mathrm{K}}}{\mathrm{e}^{\frac{W_{\mathrm{K}}-\mathcal{U}}{k_{\mathbf{B}}T}}+1} , \tag{2.73}$$

where W_{K} is the kinetic energy of electrons, and $\boldsymbol{n}[W_{\mathrm{K}}]$ is the density of state as a function of kinetic energy. For $T \to 0$ this gives

$$\rho_{N_{\mathrm{L}}}[\mathcal{U},T] = \frac{1}{2\pi^2}\left(\frac{2m_{\mathbf{e}}}{\hbar^2}\right)^{3/2}\int_0^{\mathcal{U}}\sqrt{W_{\mathrm{K}}}\mathrm{d}W_{\mathrm{K}} = \frac{1}{3\pi^2}\left(\frac{2m_{\mathbf{e}}}{\hbar^2}\right)^{3/2}\mathcal{U}^{3/2} . \tag{2.74}$$

As the chemical potential $\mathcal{U}_0$ equates the Fermi energy

$$W_{\mathrm{F}} = \frac{\hbar^2}{2m_{\mathbf{e}}}(3\pi^2\rho_N)^{2/3} \tag{2.75}$$

at $T = 0$, Eq. 2.72 gives a finite screening length at zero temperature:

$$r_{\mathrm{TF}} = \frac{\pi^{2/3}}{3^{1/6}}\frac{\varepsilon_0^{1/2}\hbar}{m_{\mathbf{e}}^{1/2}q_{\mathbf{e}}}\rho_N^{-1/6} = \sqrt{\frac{\varepsilon_0 \times \frac{2}{3}k_{\mathbf{B}}T_{\mathrm{F}}}{\rho_N q_{\mathbf{e}}^2}} \ . \tag{2.76}$$

With increasing temperature, the screening length increases and the Fermi-Dirac distribution approaches the Boltzmann distribution, where

$$\rho_{N_{\mathrm{L}}}[\mathcal{U}, T] \sim \mathrm{e}^{\frac{\mathcal{U}}{k_{\mathbf{B}}T}} \ , \tag{2.77}$$

and

$$\frac{\partial\rho_{N_{\mathrm{L}}}[\mathcal{U}, T]}{\partial\mathcal{U}} = \frac{\rho_{N_{\mathrm{L}}}}{k_{\mathbf{B}}T} \approx \frac{\rho_N}{k_{\mathbf{B}}T} \ . \tag{2.78}$$

Therefore, the Debye length $r_{\mathrm{D}} = \sqrt{\frac{\varepsilon_0 k_{\mathbf{B}}T}{\rho_N q_{\mathbf{e}}^2}}$ is recovered.

For intermediate temperatures, the screening length can be obtained through the integration of the Fermi-Dirac distribution. This does not have an analytical closed form and can only be computed numerically. A simpler approach is to link the two extremes using the approximation:

$$r'_{\mathrm{D}} \approx \left(1 + \left(\frac{3}{2}\frac{T}{T_{\mathrm{F}}}\right)^2\right)^{1/4} r_{\mathrm{TF}} \ . \tag{2.79}$$

Similarly, for the characteristic de Broglie wavelength, one can continue to assume that at zero temperature, $\sqrt{\langle v_{\mathrm{r}}^2\rangle} = \sqrt{2\langle v^2\rangle} = \sqrt{2 \times \frac{6W_{\mathrm{F}}}{5m_{\mathbf{e}}}}$ [6]. Thus

$$\langle l_{\mathrm{dB}}\rangle_0 \simeq \frac{\hbar}{m_{\mathbf{e}}\langle v_{\mathrm{r}}\rangle} \simeq \frac{\hbar}{m_{\mathbf{e}}\sqrt{\langle v_{\mathrm{r}}^2\rangle}} = \frac{\hbar}{\sqrt{\frac{12}{5}k_{\mathbf{B}}T_{\mathrm{F}}m_{\mathbf{e}}}} \ . \tag{2.80}$$

And for connecting the lower temperature end with the higher:

$$\langle l_{\mathrm{dB}}\rangle \simeq \frac{1}{\left(1 + \left(\frac{5}{2}\frac{T}{T_{\mathrm{F}}}\right)^2\right)^{1/4}}\langle l_{\mathrm{dB}}\rangle_0 \ . \tag{2.81}$$

For arbitrary degeneracy, $\beta = \frac{2r'_{\mathrm{D}}}{\langle l_{\mathrm{dB}}\rangle}$, which can be used for Mulser's CL. Notably, β reaches its minimal value at $T \to 0$:

$$\begin{aligned}\beta_{\mathrm{min}} &= \frac{2r_{\mathrm{s}}}{\langle l_{\mathrm{dB}}\rangle_0} = 2\sqrt{\frac{\varepsilon_0 \times \frac{2}{3}k_{\mathbf{B}}T_{\mathrm{F}}}{\rho_N q_{\mathbf{e}}^2}}\frac{\sqrt{\frac{12}{5}k_{\mathbf{B}}T_{\mathrm{F}}m_{\mathbf{e}}}}{\hbar} \\ &= 2\left(\frac{8}{5}\right)^{1/2}(3\pi^2)^{2/3}\left(\frac{\varepsilon_0}{m_{\mathbf{e}}}\right)^{1/2}\frac{\hbar}{q_{\mathbf{e}}}\rho_N^{1/6} \ .\end{aligned} \tag{2.82}$$

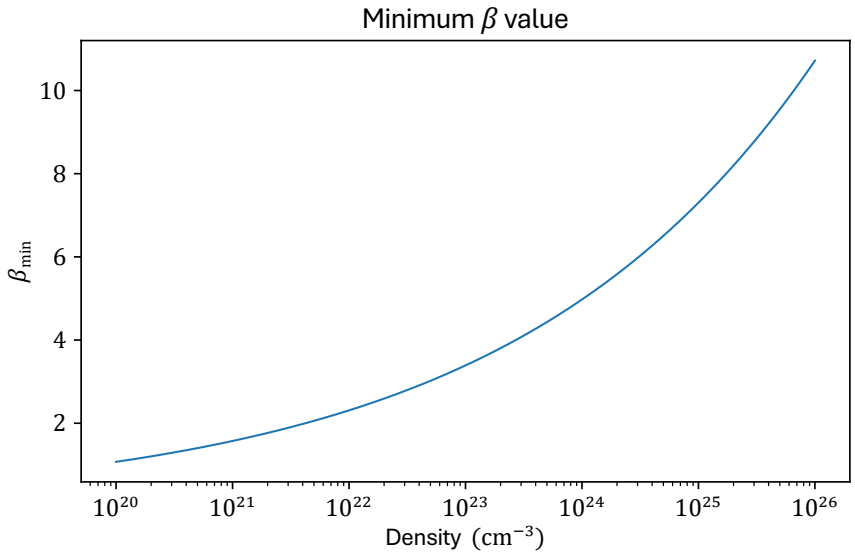


Figure 2.6: Minimal β value at the low temperature limit $T = 0$

The minimal value of β is depicted in Fig. 2.6. For WDM of interest, this minimal value remains $\gtrsim 2$, validating the argument that $\vec{\xi}''_2$ is negligible in the Landau collision operator with Mulser's CL. Using the $\beta = \frac{2r'_{\mathrm{D}}}{\langle l_{\mathrm{dB}} \rangle}$, Mulser's CL is strictly positive and regular for density and temperature and can be used to model electron relaxation in WDM.

Mulser's Coulomb logarithm represents a significant improvement over the modified quantum Coulomb logarithm. However, its theoretical basis raises some concerns: The First Born approximation becomes questionable for scattering with low-energy electrons, which is particularly problematic for low-temperature plasmas. Mora ([60]) argues that when $r_{\mathrm{b}_0} \simeq l_{\mathrm{dB}}$, Mulser's approach becomes invalid. His more rigorous approach involves using partial wave decomposition to treat components from large and small angular momentum quantum numbers separately, then reconnecting these terms for summation over arbitrary angular momentum quantum numbers. For the sake of brevity, only the results are quoted:

$$\mathrm{Ln}\left[\Lambda_{\mathrm{Mora}}\right] = \mathrm{Ln}\left[\frac{0.6811 r_{\mathrm{D}}}{\left(r_{\mathrm{b}_0}^2 + \left(0.5615 l_{\mathrm{dB}}\right)^2\right)^{1/2}}\right] . \tag{2.83}$$

Because Mora's formula takes the form of $\mathrm{Ln}\left[\frac{r_{\max}}{r_{\min}}\right]$, when $r_{\mathrm{b}_0} \gg l_{\mathrm{dB}}$, it reduces to Spitzer's classical result and therefore faces the same divergence problem at high density. This limitation arises because Mora's separate treatment of decomposition with large and small angular momentum quantum numbers fundamentally assumes that the screening length is much greater than both the de Broglie wavelength and the classical distance of closest approach. While other approaches for correcting the Coulomb logarithm exist (for example

[6] This is because $\frac{1}{2} m_{\mathrm{e}} \langle v^2 \rangle = \frac{3}{5} W_{\mathrm{F}}$ for Fermi-Dirac distribution at $T = 0$.

[67, 93]), they each encounter their own theoretical limitations, and the proper treatment of electron relaxation under the CL remains an open question.

2.3.2 Quantum-Landau-Fokker-Planck Collision Operator

The previous discussion of the Coulomb logarithm at low temperatures necessitates consideration of the Fermi-Dirac distribution. However, any discussion of CL assuming a Fermi-Dirac distribution would be incomplete without addressing the equations governing relaxation to this distribution. This becomes particularly relevant for warm dense plasmas exhibiting quantum degeneracy. For instance, metallic plasmas at solid density with temperatures of a few eV, created through isochoric heating by XFELs (as described in Sec. 1.2.2), have been experimentally achieved. The relaxation in such systems requires careful consideration and cannot be treated directly through the Boltzmann equation, even with the cross-section inferred from quantum scattering, as its steady-state solution is the Maxwell-Boltzmann distribution, even when using quantum scattering cross-sections.

Interestingly, for weakly interacting quantum systems where many-body effects are negligible [7], when the de Broglie wavelength is sufficiently small such that the particles propagate as classical point objects between localized binary scattering events [8], the semi-classical description of the system using a distribution function can still be adopted[9], whose evolution can be characterized using the Boltzmann-Uehling-Uhlenbeck (BUU) equation:

$$\begin{aligned}&\frac{\partial\tilde{\varrho}}{\partial t}+\frac{\vec{p}}{m}\cdot\vec{\nabla}_{\vec{r}}\tilde{\varrho}+\vec{F}\cdot\vec{\nabla}_{\vec{p}}\tilde{\varrho}\\&\quad=\iint\left(\tilde{\varrho}'\tilde{\varrho}'_{\star}(1-\tilde{\varrho})(1-\tilde{\varrho}_{\star})-\tilde{\varrho}\tilde{\varrho}_{\star}(1-\tilde{\varrho}')(1-\tilde{\varrho}'_{\star})\right)\frac{|\vec{p}_{\star}-\vec{p}|}{m}\frac{\mathrm{d}S}{\mathrm{d}\Omega'}\mathrm{d}\Omega'\frac{\mathrm{d}\Upsilon_{\vec{p}_{\star}}}{(2\pi\hbar)^3}\ ,\end{aligned}\tag{2.84}$$

where $\tilde{\varrho}$ is defined as the probability of occupation per phase space elementary cell:

$$\tilde{\varrho}[\vec{r},\vec{p},t]=(2\pi\hbar)^3\,\frac{\varrho[\vec{r},\vec{v},t]}{2m^3}\ ,\tag{2.85}$$

and $\tilde{\varrho}_{\star}$, $\tilde{\varrho}'$, $\tilde{\varrho}'_{\star}$ are shorthands for $\tilde{\varrho}[\vec{r},\vec{p}_{\star},t]$, $\tilde{\varrho}[\vec{r},\vec{p}\,',t]$ and $\tilde{\varrho}[\vec{r},\vec{p}\,'_{\star},t]$ respectively.

The definition of $\tilde{\varrho}$ (Eq. 2.85) can be understood as the distribution function in the position-momentum phase space $\varrho_{\vec{p}}[\vec{r},\vec{p},t]=\frac{\varrho[\vec{r},\vec{v},t]}{m^3}$ [10] modified by the volume of phase space elementary cell $(2\pi\hbar)^3$ and the spin degeneracy of electron which is 2. For this reason, $\tilde{\varrho}$ represents the probability that a quantum state is occupied. Due to the Pauli exclusion

[7] This happens when the system is sufficiently decoherent such that single-particle states form an adequate basis to describe the system, and the number density is low enough for simultaneous three-body (or higher) collisions to be improbable.

[8] This happens when the de Broglie wavelength is smaller than (or at most comparable to) the characteristic gradient length of the system as well as the mean-free-path of the particles.

[9] This is done by using the Wigner distribution function and integrating over all other particles to get the marginal single-particle distribution function.

[10] This is because $\varrho_{\vec{p}}\mathrm{d}\Upsilon_{\vec{p}}=\varrho\mathrm{d}\Upsilon_{\vec{v}}$ and $\vec{p}=m\vec{v}$.

principle, a scattering event $(\vec{p}, \vec{p}_\star) \rightarrow (\vec{p}', \vec{p}'_\star)$ can only occur when the final states are unoccupied, which is reflected by the $(1-\tilde{\varrho}')(1-\tilde{\varrho}'_\star)$ terms in the BUU equation, and vice versa for the inverse collision. This quantum statistical effect represents the key physical distinction between the BUU and classical Boltzmann equations. The other differences in terms arise from the transformation from velocity space to momentum space.

It can be shown that the steady-state solution of the BUU equation is the Fermi-Dirac distribution [90]. This can be demonstrated through an argument similar to the H-theorem proof by setting the terms in the brackets of the collision integral to zero:

$$\begin{aligned} \tilde{\varrho}'\tilde{\varrho}'_\star(1-\tilde{\varrho})(1-\tilde{\varrho}_\star) &= \tilde{\varrho}\tilde{\varrho}_\star(1-\tilde{\varrho}')(1-\tilde{\varrho}'_\star) \\ \Leftrightarrow \frac{\tilde{\varrho}}{1-\tilde{\varrho}}\frac{\tilde{\varrho}_\star}{1-\tilde{\varrho}_\star} &= \frac{\tilde{\varrho}'}{1-\tilde{\varrho}'}\frac{\tilde{\varrho}'_\star}{1-\tilde{\varrho}'_\star} \\ \Leftrightarrow \tilde{\varrho} &= \frac{1}{\mathrm{e}^{\frac{W-\mathcal{U}}{k_\mathrm{B}T}}+1} \, . \end{aligned} \tag{2.86}$$

Though initially developed for heavy ion collisions in nuclear physics experiments, the BUU equation is gradually gaining attention in plasma physics. By expanding to second order in momentum transfer $\Delta\vec{p} := \vec{p}' - \vec{p} = \vec{p}_\star - \vec{p}'_\star$, one can derive the quantum Landau-Fokker-Planck (qLFP) operator. While the detailed calculation is somewhat cumbersome, the procedure follows the same approach as in Eqs. 2.26 to 2.45 with no fundamental difference. The qLFP collision operator can thus be obtained

$$\begin{aligned} \hat{\mathcal{O}}_{\mathrm{coll}}[\tilde{\varrho},\tilde{\varrho}] \approx &\left(\frac{q_\mathsf{e}^2}{4\pi\epsilon_0}\right)^2 \\ &\iint \left(\Delta\vec{p}\cdot\vec{\xi}_1 + \frac{1}{2}\Delta\vec{p}\Delta\vec{p} : \left(\vec{\nabla}_{\vec{p}} - \vec{\nabla}_{\vec{p}_\star}\right)\vec{\xi}_1\right) \frac{m\mathrm{d}\Upsilon_{\vec{p}_\star}\mathrm{d}\Omega'_\mathrm{r}}{p_\mathrm{r}^3(\mathrm{Sin}\,[\theta'_\mathrm{r}/2])^4(2\pi\hbar)^3} \, , \end{aligned} \tag{2.87}$$

where

$$\vec{\xi}_1 := \tilde{\varrho}_\star\,(1-\tilde{\varrho}_\star)\,\vec{\nabla}_{\vec{p}}\tilde{\varrho} - \tilde{\varrho}\,(1-\tilde{\varrho})\,\vec{\nabla}_{\vec{p}_\star}\tilde{\varrho}_\star \, . \tag{2.88}$$

Using the change of relative momentum $\Delta\vec{p}_\mathrm{r} = \Delta\vec{p}/2$ one can evaluate the angular integrals $\int \frac{\Delta\vec{p}_\mathrm{r}}{(\mathrm{Sin}\,[\theta'_\mathrm{r}/2])^4}\mathrm{d}\Omega'_\mathrm{r}$ and $\int \frac{\Delta\vec{p}_\mathrm{r}\Delta\vec{p}_\mathrm{r}}{(\mathrm{Sin}\,[\theta'_\mathrm{r}/2])^4}\mathrm{d}\Omega'_\mathrm{r}$. This leads to the emergence of the Coulomb logarithm term, which can be evaluated using the methods discussed above, including the substitution of $(\mathrm{Sin}\,[\theta'_\mathrm{r}/2])^4$ with $((\mathrm{Sin}\,[\theta'_\mathrm{r}/2])^2 + \beta^{-2})^2$ in Mora's formalism of Yukawa potential scattering. The resulting form of the Coulomb logarithm matches the previous discussion, and the final collision operator takes the same structural form as shown in Eq. 2.45.

As it self-consistently incorporates Pauli blocking and quantum scattering, and removes the need for an artificial Coulomb-logarithm cut-off, the qLFP collision operator offers significant advantages over the classical LFP operator. Nevertheless, it has yet to receive adequate attention in the plasma physics community. Still, some recent works [92, 94, 95] have demonstrated its potential for modelling collisional processes in warm dense matter

and other degenerate plasma systems. For a detailed derivation of the qLFP operator and its applications in various aspects, references [92, 94] are recommended.

The qLFP formalism provides a physically reliable framework for treating quantum statistical effects while maintaining the computational advantages of the Fokker-Planck approach, opening new opportunities for accurate modelling of e-e collisions in regimes where both quantum degeneracy and Coulomb coupling effects are significant. This approach is particularly relevant for emerging applications in warm dense matter physics and ultrafast laser-matter interactions.

2.4 Summary

The analysis of the Boltzmann equation in this chapter, while physically comprehensive, unveils its inherent mathematical complexity. The challenges in working with this equation arise from several fundamental aspects. From a mathematical perspective, the existence and uniqueness of solutions remain unproven in the general case [96], with only a limited number of analytical solutions known [97–100]. The BUU equation presents particular mathematical difficulties, and its non-linear integral-differential structure makes analytical treatment extremely challenging. The computational challenges are equally significant. The non-linear nature demands substantial computational resources, especially when dealing with spatially inhomogeneous, velocity anisotropic distributions. The multi-dimensional nature of the collision integral poses numerical difficulties, and real-time evolution calculations become prohibitively expensive for complex systems.

Despite these challenges, significant progress has been made in practical applications. Numerical codes based on the Boltzmann equation have been successfully developed [14, 57, 69, 72, 101–104], with isotropic distribution approximations in velocity space proving particularly effective. These developments form the foundation for detailed modelling of electron-electron interactions, finding extensive applications in plasma physics transport phenomena.

Recent years have witnessed flourishing developments in understanding plasma transport phenomena extending beyond the traditional Boltzmann equation framework. Linear Response Theory has emerged as a powerful tool for calculating transport coefficients [40, 55] and studying systems slightly perturbed from equilibrium. This approach offers mathematical tractability for many practical applications, though it falls short in capturing strongly non-equilibrium phenomena. Quantum Kinetic Theory, based on non-equilibrium Green's functions, provides a more fundamental quantum mechanical description [105, 106]. This framework naturally incorporates quantum coherence effects and many-body interactions and has also seen application in plasma physics [107, 108]. However, it presents even greater mathematical challenges than the classical Boltzmann approach. This is because the

underlying quantum transport equation is described using a two-time correlation function, which retains the full history of quantum evolution, rather than a much simpler single-time distribution function. These mathematical challenges, both from the analytical and numerical side, often make practical calculations intractable for complex systems. For these reasons, both frameworks lie beyond the scope of this thesis.

The theoretical frameworks developed in this chapter provide the essential foundation for the detailed analysis of electron-electron interactions in subsequent chapters. While alternative approaches offer powerful tools for specific scenarios, the Boltzmann equation remains central to this thesis, balancing physical insight with mathematical tractability despite its inherent challenges.

This line should have been left blank due to the inability to find a suitable quotation.

3

Electron Thermalisation and Collision Time

Contents

3.1 Introduction 46
3.2 Non-thermal Electrons in XFEL-driven Plasmas 47
3.2.1 Creating Non-thermal Electrons 48
3.2.2 Observing Non-thermal Electrons 49
3.2.3 Effect of the Pulse Duration 50
3.3 Collisional-radiative Simulation 50
3.3.1 Atomic Kinetics 51
3.3.2 Electron Relaxation 53
3.3.3 Emission Spectra 56
3.4 Feasibility Demonstration 57
3.4.1 Tailoring Non-thermal Electrons 57
3.4.2 Varying Pulse Durations 60
3.4.3 Electron-electron and Electron-ion Collisions 61
3.4.4 Effect of Collision Times 62
3.5 Summary 64

3.1 Introduction

The previous chapter has demonstrated the complexity in modelling the relaxation process of free electrons in plasmas of solid density. Although a rich collection of theoretical developments exists, the progress on the experimental side is severely hampered. This calls for a reliable measurement of the electron relaxation (or collision) time in warm, dense plasmas to assist in the validation of these theoretical models. Unfortunately, very few attempts have been made to measure this properly in the warm, dense plasma regime. This is primarily because the relaxation process in solid-density systems happens on the ultra-short timescale, usually sub-fs, ruling out the possibility of time-resolved observation under the current technologies. Instead, the collision time is often measured using transport properties, given their close relation. Another challenge is the strong Coulomb coupling nature of such systems, which also implies the difficulty in disentangling electron-electron processes from electron-ion processes.

Among the most notable results, Sun *et al.* reported a measured value of $t_{\text{e-e}} \approx 1.7$ fs in fused silica [109] through the assessment of plasma opacity in an optical laser pump-probe experiment. This methodological approach was subsequently refined by Pan *et al.* [110] to investigate the relationship between collision time and electron density. It is noteworthy that the highest density they have achieved is still more than two orders of magnitude lower than that in a solid metal. Therefore, experimental data for systems at or exceeding typical solid densities remain scarce. Furthermore, it is crucial to emphasise that the determination of plasma opacities itself presents significant challenges within the warm dense matter regime [111, 112]. Consequently, the extrapolation of collisional rates from such opacity data is often heavily dependent on the theoretical models employed [113, 114], necessitating careful interpretation and analysis.

This chapter will propose a novel method to measure the collision time more directly. Instead of observing transport quantities like opacity, this approach focuses on tracking the evolution of non-thermal electrons within a broader electron distribution in dense plasma on ultrafast time scales. This is achievable through the use of an XFEL, which can photo-ionise core electrons from atoms in a plasma, resulting in sustained and well-defined non-thermal electron distributions.

Simulations were conducted using the `CCFLY` collisional-radiative atomic kinetics code [17, 68–70, 72]. Results indicate that adjusting the XFEL pulse duration from sub-femtoseconds to a few femtoseconds enables measurement of the collision time scale of non-thermal electrons in the plasma. This approach allows insights into electron interaction processes on ultra-fast time scales and assessment of the Coulomb logarithm framework's validity in describing dense plasma systems more generally.

3.2 Non-thermal Electrons in XFEL-driven Plasmas

At thermal equilibrium, electrons in a non-degenerate plasma form a Maxwell-Boltzmann distribution. For electrons that are yet to reach thermal equilibrium, the distribution is non-thermal. As the thermalisation happens, the distribution function evolves towards the Maxwellian distribution. Distribution functions deviate from a Maxwellian distribution in various ways, but one case of particular interest is that the vast majority of those electrons still form a Maxwellian distribution, with only a small portion outside the thermal bulk with substantially higher energies, as illustrated in Fig. 3.1. Those non-thermal electrons thermalise via collisions, whose timescale can be associated with the electron collision time. The observation of the electron thermalisation process provides an excellent opportunity to measure the electron collision time.

Notably, non-thermal electrons are prevalent in XFEL-driven plasmas. Electrons ionised from ion core-holes are inherently non-thermal. As these electrons subsequently collide and their distribution thermalises, they also recombine into core-holes, emitting photons that encode their distribution. Observation of the emission spectrum from these non-thermal electrons can thus reveal information regarding the electron distribution function and the collision time.

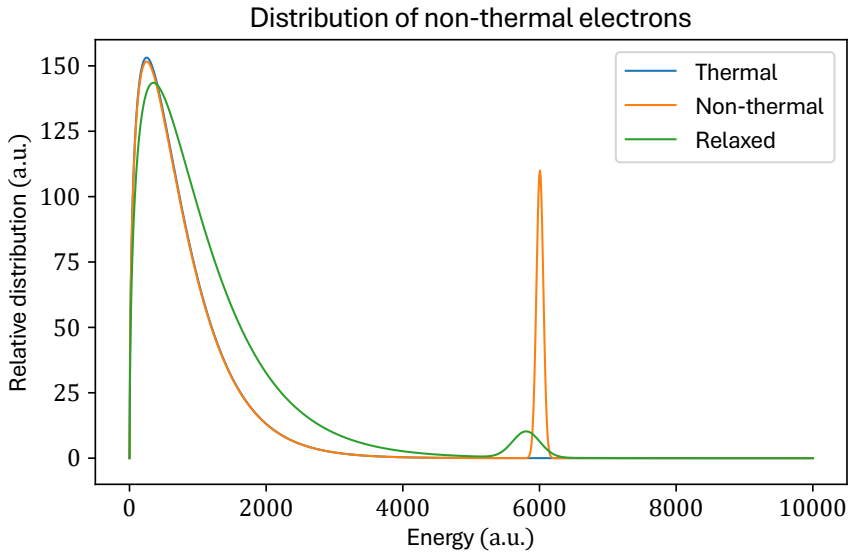


Figure 3.1: Distribution of thermal and non-thermal electrons at a certain temperature. Because of the existence of non-thermal electrons, the thermalised distribution will have a higher temperature.

3.2.1 Creating Non-thermal Electrons

When a sample is exposed to an XFEL beam with photon energy exceeding the 1s ionisation energy (above the K-edge), the main absorption mechanism is K-shell photo-ionisation (PI). In a low-Z element, the dominant relaxation of a 1s core-hole takes place via Auger decay, which further excites an electron from a bound state into the continuum. These processes produce free electrons with well-defined energies, leading to non-thermal peaks in the electron energy distribution, as shown in Fig. 3.2.

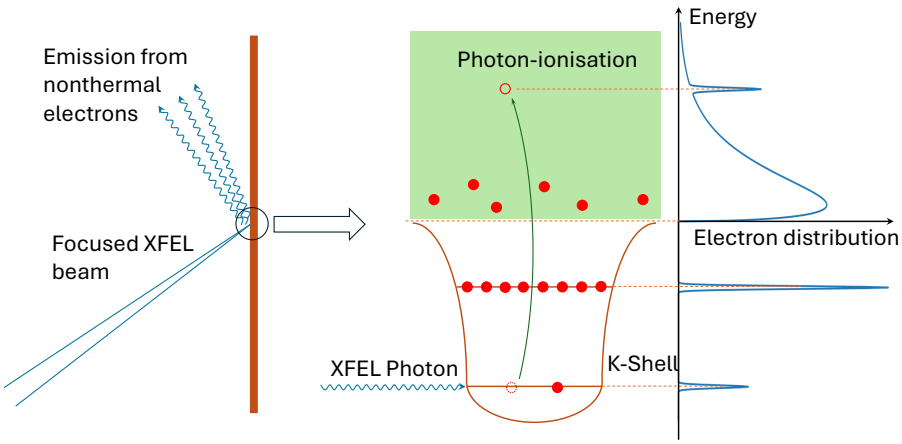


Figure 3.2: When a sample is driven by an intense x-ray pulse, K-shell photo-ionisation and Auger decay create copious populations of non-thermal electrons at well-defined energies. These electrons thermalise collisionally with ions and other electrons in the system on electron thermalisation timescales.

Because the cross-section for multi-photon absorption is relatively small, the vast majority of electrons created in an XFEL-driven plasma will be centralised only at these energies and have little energy spread upon creation. For typical hard XFELs, the energy of those electrons will be of the order of keV, and the energy spread, which is mainly determined by the bandwidth of the XFEL, is of 10 eV order. This is in sharp contrast with non-thermal electrons created by optical lasers, which are continuously accelerated by the radiation field and can reach MeV energy scales [1] and have considerable energy spread, making the investigation of electron thermalisation difficult.

As the wavelength of the XFEL is tunable, non-thermal electrons' energies can be tailored as needed. The number of these non-thermal electrons can also be altered by tuning the intensity of the XFEL. This has made XFELs ideal for investigating the relaxation process using non-thermal electrons.

[1] This can also be seen by noticing the difference in the ponderomotive energy that scales as ω^{-2}, where ω is the radiation frequency.

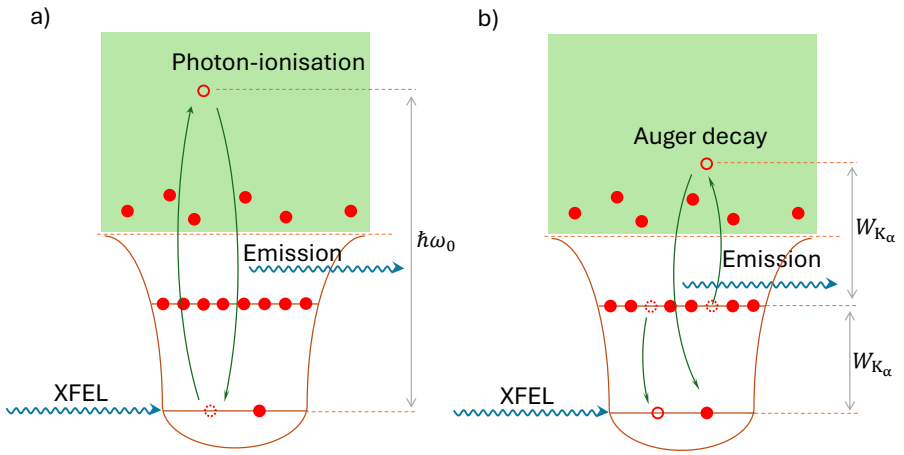


Figure 3.3: Emission from non-thermal electrons features prominently at photon energies corresponding to the process that created the non-thermal electrons. (a) Quasi-elastic: an electron photo-ionised from the K-shell recombines back into the K-shell, emitting a photon with energy approximately equal to the incident XFEL photon energy. (b) Auger: the non-thermal electrons created by Auger processes recombine, emitting a photon with twice the energy of a K_β photon.

3.2.2 Observing Non-thermal Electrons

The non-thermal electrons created by the XFEL thermalise rapidly, yet they are continuously replenished within the pulse duration of the driving XFEL beam. Therefore, there is a non-negligible probability for the non-thermal electrons to radiatively recombine into a core-hole before the electron distribution fully thermalises. Therefore, the radiative recombination (RR) emission from those non-thermal electrons at energies significantly above the thermal bulk becomes a clear experimental observable.

Because the major channel of recombination will be to the K-shell core-holes, the emitted photons will have energies corresponding to the electron energy plus the K-shell absorption edge. This essentially serves as a map between electron distribution and emission spectra. For the interest of this chapter, two major cases can be distinguished: recombination from PI electrons, with emitting photon energies similar to that of the driving x-ray, and recombination of Auger-excited electrons, emitted at energies twice the K_β energy approximately, as illustrated in Fig. 3.3. Other processes, such as L-shell photo-ionisation followed by K-shell recombination, or vice versa, are also possible but have a much lower cross-section. In a case where electrons do not have time to exchange energy with other particles before recombination, the emission peak will have a narrow bandwidth. However, as the thermalisation takes place, the emission peak starts to deform, leaving an abundance of information for understanding the rate at which electrons relax.

3.2.3 Effect of the Pulse Duration

Over the course of XFEL-plasma interaction, radiative recombination to the K-shell can only take place in the presence of a K-shell core-hole. These core-holes are predominately produced through PI, with only a small fraction produced by collisional ionisation due to the relatively low temperature compared with the K-shell ionisation energy. Since these holes are majorly created by the XFEL beam, the X-ray pulse duration will determine the window within which emission can be observed. For a pulse length significantly shorter than the typical thermalisation time, the majority of these RR events will occur before thermalisation can happen, leading to a strong non-thermal signature in the emission spectrum.

In contrast, if the XFEL beam delivers the same number of photons but in a significantly longer pulse duration, then the same number of non-thermal electrons (and core-holes) will be created in a much longer period. As these non-thermal electrons will recombine eventually, the total number of recombinations remains roughly the same. However, the emission spectra will look very different. In the long pulse case, the density of both non-thermal electrons and core-holes will be lower at any time snapshot, thus suppressing the portion of the non-thermal electrons to recombine. As more electrons tend to thermalise before recombining, a larger proportion of emission will occur from where electrons have undergone substantial thermalisation, leading to a weaker non-thermal signature in the emission spectrum. For a pulse significantly longer than the thermalisation timescale, most RR from the free electrons will come from the thermalised distribution, and non-thermal features in the emission spectra will be vanishingly small.

Varying the pulse duration between these two cases produces spectra spanning these extremes, which can be directly observed in a dedicated experiment. This mechanism can be exploited to measure the electron collision timescale. The short thermalisation timescale in dense plasmas necessitates the use of femtosecond pulse lasers, rendering XFELs among the few facilities capable of investigating electron relaxation dynamics. Importantly, the thermalisation timescale often exceeds the sub-femtosecond collision time, as non-thermal electrons require multiple collisions to lose energy. Consequently, this technique remains effective with pulses longer than one femtosecond, enhancing experimental feasibility given the ongoing challenges in generating sub-femtosecond pulses at XFELs.

3.3 Collisional-radiative Simulation

The feasibility of the proposed method can be tested by modelling XFEL-plasma interactions with varying pulse durations using the `CCFLY` code. `CCFLY` is a non-LTE, collisional-radiative atomic-kinetics code derived from the widely-used `SCFLY` simulation

suite, frequently employed in modelling isochoric heating experiments at XFEL facilities [68, 70]. `CCFLY` extends `SCFLY`'s capabilities by incorporating Fokker-Planck modelling, enabling time-resolved analysis of non-thermal electron distribution functions within the same non-LTE atomic-kinetics framework.

`CCFLY` generates plasma emission spectra based on initial target conditions (material, density, initial charge state, and temperature) and XFEL beam characteristics (intensity and pulse duration). The simulation employs atomic rate equations to self-consistently calculate ionic charge state distributions in the presence of an external radiation field. This model utilises transition rates to describe various physical processes, including electron capture, collisional ionisation and recombination, collisional transitions, stimulated transitions [2], photo-ionisation, inverse bremsstrahlung, and radiative recombination [68]. These transition rates are coupled with the electron distribution, described by the Fokker-Planck equation, incorporating collisional operators and source terms. The kinetics simulation yields the evolution of atomic-level population $\rho_{N_i}[t]$ and electron distribution function $f[W, t]$.

`CCFLY` assumes a spatially homogeneous electron and ion distribution; hence, the kinetics simulation is zero-dimensional. It is followed by a one-dimensional emissivity and opacity calculation based on the resulting atomic-level population and electron distribution. This process ultimately produces time-integrated emission spectra, representing the experimental observable.

3.3.1 Atomic Kinetics

In `CCFLY`, the atomic state of an ion is represented by electron occupation numbers $N_{\bar{n}}$ for each electron energy level (shell), which is determined by principal quantum number $\bar{n}$. For an atom with atomic number N_0, the atomic state of an ion is denoted as:

$$|\psi\rangle = |\bar{n} = 1\rangle^{N_1} |\bar{n} = 2\rangle^{N_2} \cdots |\bar{n} = \bar{n}^*\rangle^{N_{\bar{n}^*}} \ , \tag{3.1}$$

where $\bar{n}^*$, the maximum principal quantum number, is determined by a chosen continuum lowering model, in this case, the modified Ecker-Kröll model [17, 115]. For clarity, electron energy levels are denoted as K, L, M, $\cdots$ in this thesis. The sum of occupation numbers for each shell indicates the total number of electrons in the ion. Consequently, the ionisation stage of the ion is:

$$\bar{Z} = N_0 - \sum_{\bar{n}} N_{\bar{n}} \ . \tag{3.2}$$

To manage data efficiently, atomic states are grouped by ionisation stage, with each state assigned a serial number from lowest to highest energy within its group. This atomic

[2] This is more commonly referred to as photon excitations and stimulated emissions.

dataset, referred to as a super configuration, differs from those accounting for subshells (angular momenta). While significantly smaller and computationally more efficient, it still captures the primary spectral signatures in XFEL-plasma interactions.

Now let $\rho_{N_{\bar{i}}}$ be the density of ion species in an atomic state $\bar{i}$. The evolution of the population is determined by the rate equation:

$$\frac{\mathrm{d}\rho_{N_{\bar{i}}}}{\mathrm{d}t} = \sum_{\bar{j}} K_{\bar{i},\bar{j}} \rho_{N_{\bar{j}}}, \tag{3.3}$$

where the matrix elements are determined by the transition rates $_{\bar{i}\to\bar{j}}$ through:

$$K_{\bar{i},\bar{j}} = \begin{cases} K_{\bar{j}\to\bar{i}} & (\bar{j} \neq \bar{i}) \\ -\sum_{\bar{m}} K_{\bar{i}\to\bar{m}} & (\bar{j} = \bar{i}) \end{cases} . \tag{3.4}$$

The transition rates are calculated for each of the different processes. Generally speaking, these can be categorised into two types: bound-bound (b-b) transitions and bound-free (b-f) transitions.

Bound-bound transitions are such that electrons are moved from one shell to another. Therefore, b-b transitions are always within the same ionisation stage. These b-b transitions can be further categorised into three groups: the spontaneous process which is spontaneous decay (SpD), photon-induced processes, including stimulated decay (StD) and photon excitation (PE); and collision-related processes, including collisional excitation (CE) and collisional de-excitation (CD).

Unlike b-b transitions, b-f transitions remove electrons from the atomic shell and release them to the continuum, or vice versa. Therefore, b-f transitions always happen between different ionisation stages. This can be categorised into three groups: spontaneous processes, including Auger decay (AD) and dielectric recombination (DR); Photon-induced processes, including photo-ionisation (PI) and radiative recombination (RR); and collision-induced processes, including collisional ionisation (CI) and collisional recombination (CR, also known as three-body recombination).

Some of these rates are coupled with the distribution function of the free electrons. As an example, these two states:

$$|\mathrm{u}\rangle = |\mathrm{K}\rangle^2|\ \mathrm{L}\rangle^1, |\mathrm{l}\rangle = |\mathrm{K}\rangle^1|\ \mathrm{L}\rangle^2\ . \tag{3.5}$$

are related by an excitation/de-excitation process. The rate of a collisional excitation is obtained using a cross-section model:

$$K_{\mathrm{CE,l\to u}} = \int_{\vec{v}} v\varrho[\vec{v}] S_{\mathrm{CE,l\to u}}[W]\ \mathrm{d}\Upsilon_{\vec{v}}\ , \tag{3.6}$$

where $S_{\mathrm{CE,l\to u}}[W]$ is the collisional excitation cross-section for an electron with energy $W = \frac{1}{2} m_{\mathbf{e}} v^2$. It is also possible to radiatively or spontaneously excite/de-excite between

the two states, in which case the electron distribution function will be altered. This shows that the distribution of non-thermal electrons is coupled with the rate equations. The distribution function $f[W,t]$ will affect all processes involving free electrons, and Appendix A summarises how `CCFLY` computes the transition rates. Details of how those rates are derived can be found in [68, 116].

3.3.2 Electron Relaxation

`CCFLY` describes the evolution of the free electron system using the Boltzmann transport equation, incorporating additional inelastic collision operators and source operators that reflect the aforementioned interactions between electrons and ions:

$$\frac{\partial \varrho[\vec{r},\vec{v},t]}{\partial t} + \vec{v}\cdot\vec{\nabla}\varrho[\vec{r},\vec{v},t] + \frac{q_{\mathbf{e}}}{m_e}(\vec{E}+\vec{v}\times\vec{B})\cdot\vec{\nabla}_{\vec{v}}\varrho[\vec{r},\vec{v},t] = \hat{\mathcal{O}}_{\mathrm{e}}[\varrho] + \hat{\mathcal{O}}_{\mathrm{i}}[\varrho] + \hat{\mathcal{O}}_{\mathrm{S}}[\varrho]\ , \tag{3.7}$$

Here, $\hat{\mathcal{O}}_{\mathrm{e}}[\varrho]$ is the elastic collision operator describing energy-conserving electron-electron and electron-ion collisions. $\hat{\mathcal{O}}_{\mathrm{i}}[\varrho]$ captures non-energy-conserving processes that involve the excitation of the internal-energy-level of the ion (collisional excitation and de-excitation). $\hat{\mathcal{O}}_{\mathrm{s}}[\varrho]$ represents ionisation and recombination processes that do not conserve total free electron number.

Assuming homogeneity, the second term on the left-hand side is neglected. The third term is also ignored, as collisions dominate over acceleration due to the macroscopic fields in dense plasmas [3].

Elastic collisional operators are treated as classical accumulative small-angle Coulomb interactions, employing the Landau-Fokker-Planck collisional operator given by [57]. With an assumed isotropic distribution in velocity space, $\varrho[\vec{v}]$ can be replaced by $\varrho[v]$. Utilising the Rosenbluth potentials [117], the collision operator due to e-e collision for an isotropic distribution of electrons in the velocity space can be reorganised as :

$$\hat{\mathcal{O}}_{\mathrm{e,\ e\text{-}e}}[\varrho] = \frac{q_{\mathbf{e}}^4 \mathrm{Ln}\left[\Lambda_{\mathrm{e\text{-}e}}\right]}{3\epsilon_0^2 m_{\mathbf{e}}^2}\frac{1}{v^2}\frac{\partial}{\partial v}\left[\frac{1}{v}\frac{\partial \hat{\mathcal{O}}'[\varrho]}{\partial v}\right]\ , \tag{3.8}$$

where

$$\hat{\mathcal{O}}'[\varrho] = \varrho[v]\int_0^v \varrho\left[v'\right] v'^4\ \mathrm{d}v' + v^3\varrho[v]\int_v^\infty \varrho\left[v'\right] v'\mathrm{d}v' - 3\int_v^\infty \varrho\left[v'\right] v'\mathrm{d}v' \int_0^v \varrho\left[v'\right] v'^2\ \mathrm{d}v'\ , \tag{3.9}$$

Because ions have much smaller velocities, elastic e-i collisions that do not involve the excitation of the internal-energy-level of the ion will not modify the speed of the electrons but

[3] This can be understood as electron dense plasmas typically have very small collision time, and electron can only gain a negligible velocity change due to the macroscopic fields

only change their velocity vector. Therefore, its effect on the isotropic part of the distribution in the velocity space can be ignored, and only the anisotropic part is affected. Since `CCFLY` assumes an isotropic distribution, elastic e-i collision plays no role, thus:

$$\hat{\mathcal{O}}_{\mathrm{e}}[\varrho] = \hat{\mathcal{O}}_{\mathrm{e,\ e\text{-}e}}[\varrho] \tag{3.10}$$

The inelastic collision operator $\hat{\mathcal{O}}_{\mathrm{i}}[\varrho]$ reflects interactions that do not conserve the total energy. This can be caused by either CE/CD or Bremsstrahlung / inverse Bremsstrahlung. For simplicity reasons, the current version of `CCFLY` neglects Bremsstrahlung / inverse Bremsstrahlung, which could be implemented in the future, but CE/CD is included. A collisional excitation event that excites an ion from a lower atomic level $|\mathrm{l}\rangle$ to an upper atomic level $|\mathrm{u}\rangle$ absorbs energy $W_{\mathrm{l,u}}$ from the free electron. This moves electrons with energy W to $W - W_{\mathrm{l,u}}$, but also moves electrons with energy $W + W_{\mathrm{l,u}}$ to W. For this reason, it is far more convenient to evaluate the collision operator in the energy space, with the transformation

$$f[W]\mathrm{d}W = 4\pi v^2 \varrho[\vec{v}]\mathrm{d}\Upsilon_{\vec{v}} \ . \tag{3.11}$$

The collisional operator for electron distribution $f[W,t]$ is [101]:

$$\hat{\mathcal{O}}_{\mathrm{CE,l\to u}}[f] = \rho_{N_{\mathrm{l}}} \left(K'_{\mathrm{CE,l\to u}} \left[W + W_{\mathrm{l,u}} \right] f \left[W + W_{\mathrm{l,u}} \right] - K'_{\mathrm{CE,l\to u}}[W] f[W] \right) \ . \tag{3.12}$$

Here, the transition rate K' differs slightly from that defined in 3.6, as that one is the total rate accounting for integrated overall electron energies, whereas the rate here is only for electrons with energy W. Using the same cross-section model, it can be easily obtained that

$$K'_{\mathrm{CE,l\to u}}[W] = S_{\mathrm{CE}}[W] \sqrt{\frac{2W}{m_{\mathbf{e}}}} \ , \tag{3.13}$$

and

$$\begin{aligned} \int f[W] K'_{\mathrm{CE,l\to u}}[W] \mathrm{d}W &= \int f[W] S_{\mathrm{(l\to u),CE}}[W] \sqrt{\frac{2W}{m_{\mathbf{e}}}} \mathrm{d}W \\ &= \int 4\pi v^2 \varrho[\vec{v}] S_{\mathrm{(l\to u),CE}} v \mathrm{d}v \\ &= \int_{\vec{v}} v \varrho[\vec{v}] S_{\mathrm{(l\to u),CE}} \left[W \right] \ \mathrm{d}v_x \mathrm{d}v_y \mathrm{d}v_Z \\ &= K_{\mathrm{CE,l\to u}} \ . \end{aligned} \tag{3.14}$$

CD can be evaluated in a similar manner, and the overall inelastic operator takes the form

$$\hat{\mathcal{O}}_{\mathrm{i},f}[f] = \sum_{\text{all } (\mathrm{l\to u})\in \mathrm{CE}} \hat{\mathcal{O}}_{\mathrm{CE,(l\to u)}}[f] + \sum_{\text{all } (\mathrm{u\to l})\in \mathrm{CD}} \hat{\mathcal{O}}_{\mathrm{CD,(l\to u)}}[f] \ . \tag{3.15}$$

Processes that do not conserve the total number of electrons, which are represented by the source term $\hat{O}_{\mathrm{S}}[\varrho]$, involve collisional ionisation and recombination, photo-ionisation

and radiative recombination, as well as Auger decay and dielectric recombination. For the same reason, these are evaluated in the energy space

$$\hat{\mathcal{O}}_{\mathrm{S},f} = \left(\hat{\mathcal{O}}_{\mathrm{CI}} + \hat{\mathcal{O}}_{\mathrm{CR}}\right) + \left(\hat{\mathcal{O}}_{\mathrm{PI}} + \hat{\mathcal{O}}_{\mathrm{RR}}\right) + \left(\hat{\mathcal{O}}_{\mathrm{AD}} + \hat{\mathcal{O}}_{\mathrm{DR}}\right) \ , \tag{3.16}$$

where $\mathcal{O}_{\mathrm{X}}$ is the operator corresponding to process X. These terms are somewhat cumbersome; detailed expressions can be found in Appendix A [116]. Similar to the inelastic operator, the source operators are evaluated for each transition, and then summed over all transitions.

As the inelastic operator $\hat{O}_{\mathrm{i},f}$ and the source term $\hat{\mathcal{O}}_{\mathrm{S},f}$ is exerted on the energy space distribution function $f[W]$, but the elastic operator $\hat{\mathcal{O}}_{\mathrm{e},\varrho}$ on the distribution function of speed $\varrho[v]$, `CCFLY` needs to transform between the two constantly. For practical purposes, the master equation was chosen to be evaluated in the energy space, with only the elastic e-e part being in the velocity space.

$$\begin{cases} \dfrac{\partial f}{\partial t} = \hat{\mathcal{O}}_{\mathrm{e},f}[f] + \hat{\mathcal{O}}_{\mathrm{i},f}[f] + \hat{\mathcal{O}}_{\mathrm{s},f}[f] \\ \hat{\mathcal{O}}_{\mathrm{e},f}[f]\ \mathrm{d}W = \hat{\mathcal{O}}_{\mathrm{e},\varrho}[\varrho] 4\pi v^2 \mathrm{d}v \\ f[W]\ \mathrm{d}W = 4\pi v^2 \varrho[v] \mathrm{d}v \end{cases} \tag{3.17}$$

For the interest of this chapter, `CCFLY` employs specific cross-section models for various processes: the cross-section model by Lotz [118] for collisional ionisation and recombination, that of Van Regenmorter [119] for collisional excitation and de-excitation, and that of Veigele *et al.* [120] for photon-ionisation and recombination. Auger decay / dielectric recombination rates are treated as constants depending only on configurations, as they remain relatively stable across various plasma conditions [116].

When considering relaxation as redistributing the electrons, e-e and e-i collisions play crucial roles, while other processes (PI/RR, AD/CR) only affect the distribution function point-wise. Interestingly, e-e and e-i collisions thermalise the non-thermal electrons in two different ways. Typically, e-e collisions only change the energy of the electrons by a small amount per collision, but e-i collisions can remove a large amount of energy at a time. Intuitively, e-e collisions will thus tend to cause non-thermal peaks in the electron distribution to broaden while largely conserving the total number of electrons within it. In contrast, e-i collisions act to depopulate the non-thermal electron peaks but cause little broadening. It should be noticed that due to the consideration of isotropic distribution, all e-e collisions here are considered elastic, and all e-i collisions are inelastic [4]

[4] This is because, under the assumption of an isotropic distribution, elastic e-i collisions only change the direction of an electron's velocity, not its speed, and thus do not affect the energy distribution.

3.3.3 Emission Spectra

The CCFLY ODE solver self-consistently solves the Fokker-Planck equation and the rate equation until the population and the distribution function at each user-set time step are computed. Then CCFLY computes both the bound-bound and bound-free emissivity and opacity of each radiative transition $\mathrm{u} \to \mathrm{l}$ as a function of emission photon energy $\hbar\omega$ and computes the corresponding spectral intensity:

$$\dot{\Psi}_{\mathrm{u}\to\mathrm{l}}[\omega, t] = \frac{\mathcal{E}_{\mathrm{u}\to\mathrm{l}}[\omega]}{\kappa_{\mathrm{u}\to\mathrm{l}}[\omega]} \left(1 - \mathrm{e}^{-\kappa_{\mathrm{u}\to\mathrm{l}}[\omega]\Delta x}\right) \ , \tag{3.18}$$

where the emissivity $\mathcal{E}_{\mathrm{u}\to\mathrm{l}}[\omega]$ and the opacity $\kappa_{\mathrm{u}\to\mathrm{l}}[\omega]$ of the transition are determined by the relevant ion population and transition rate, the electron distribution function $f[W]$, the Gaunt factor of the transition, and the thickness of the target Δx [68]. The emissions are assumed to be uniformly distributed across the thickness of the target, yielding the $1 - \mathrm{e}^{-\kappa\Delta x}$ form of 3.18 as integrating over different depths from the surface of the target. Various broadening effects have also been accounted for in this calculation [68].

The individual emissions are then summed up and integrated over time to obtain the final output spectra:

$$\Psi[\omega] = \int \sum_{\text{all } \mathrm{u}\to\mathrm{l}} \dot{\Psi}_{\mathrm{u}\to\mathrm{l}}[\omega, t] \mathrm{d}t \ . \tag{3.19}$$

As the emission from non-thermal electrons is coming from the b-f transitions, the summation can run over only b-f transitions instead to reduce complexity.

Because the spectrum is determined by the electron distribution and the ion state populations, Eq. (3.8) establishes a connection between spectral emission and the collisional model determining the collision time. For the classical collision model, the e-e collision time adopts the same definition as in Sec. 2.2.3 and Eq. 2.54 [79]:

$$t_{\text{e-e}} = 12\pi^{3/2} \frac{m_{\mathbf{e}}^{1/2} \epsilon_0^2 (k_{\mathbf{B}} T_{\mathrm{e}})^{3/2}}{\rho_{N_{\mathrm{e}}} q_{\mathbf{e}}^4 \mathrm{Ln}\left[\Lambda_{\mathrm{ee}}\right]} \ . \tag{3.20}$$

The simulated emission spectrum is determined by the relaxation speed given by Eq. (3.8), dependent on the CL, which links to the collision time via Eq. (3.20). Here, Huba's expression is used for the CL. However, the Fokker-Planck treatment is compatible with other approaches and can be used to evaluate a broad range of different collision models.

Importantly, this collision time can only be used to quantify the collision frequency in the thermal bulk, as discussed in Sec. 2.2.3 and the timescale for non-thermal electrons reaching a thermalised distribution (the "relaxation time" in RTA), as well as the timescales at which the highly-energetic electrons diffuse or slow down, can be different. In general, electrons will higher energy will thermalise more slowly. However, the operator nature of $\hat{\mathcal{O}}'[\varrho]$ on the right-hand side of Eq. 3.8 indicates no simple way to define such a quantity

consistently as one does in RTA, even if an explicit dependence on electron energy is included [5], echoing the discussion in Sec. 2.2.3. Nevertheless, assuming that the non-thermal fraction remains small, the timescale given by Eq. 3.20 still indicates the overall collision rate, which is the key quantity of interest that captures the dependence on collision models and can be evaluated by this method. Therefore, this thesis will focus on the discussion of the collision time instead of the more widely used relaxation time.

3.4 Feasibility Demonstration

This section evaluates the feasibility of exploring electron relaxation dynamics using the XFEL pulse duration effect by performing `CCFLY` simulation at different conditions and shows the spectra response to pulse durations under various assumptions. The target material is chosen to be Al, with a reasonably small atomic database, yet a high electron density.

3.4.1 Tailoring Non-thermal Electrons

The first simulation shows the interaction of a 10 μm thick Al foil at ambient conditions with an x-ray pulse with photon energy $\hbar\omega_0 = 2000$ eV, pulse duration of 0.5 fs, and a peak intensity of 10^{19} W·cm^{-2} on target. In this simulation, a Gaussian-shaped beam profile both in the time and frequency domains is assumed. The bandwidth is chosen to be 0.8% $\times$ incident photon energy, in this case, 16 eV, which is achievable at XFEL facilities under the XLEAP operation mode [121] for sub-fs pulse duration. In general, the intrinsic Fourier limit of the X-ray pulse becomes larger for shorter pulse operations. However, this only becomes comparable to the 16 eV simulation set-up when the pulse duration is reduced to less than $4\mathrm{Ln}\,[2]\,\frac{\hbar}{10\ \mathrm{eV}} \approx 0.1$ fs, validating the assumption of XFEL bandwidth. The Al K-edge is located at $W_{1\mathrm{s}} = 1560$ eV, so the photons carry sufficient energy to ionise the 1s electrons. The chosen focus spot sizes of 1 μm^2 allow for the heating of solid density plasmas to electron temperatures of $\sim$70 eV. This equates to having 50 μJ energy, or $\sim 10^{11}$ photons in the beam. Both the pulse energy and the focusing are readily achievable at various endstations in conventional XFEL facilities, like MEC at LCLS and HED at EuXFEL. Better focusing may be achieved by the nanofocusing technique [122], whilst defocusing is more interesting as this would help to emphasise low-temperature relaxation dynamics where the classical picture breaks down. The combined condition of focusing and short pulse is readily available as of 2024.

The evolution of the electron distribution is plotted in Fig. 3.4. Clear non-thermal features are visible, corresponding to electrons ejected into the continuum via K- and L-shell

[5] This is because the rate evaluated at a certain energy W is not only affected by the point-wise value $f[W]$, but rather the whole distribution.

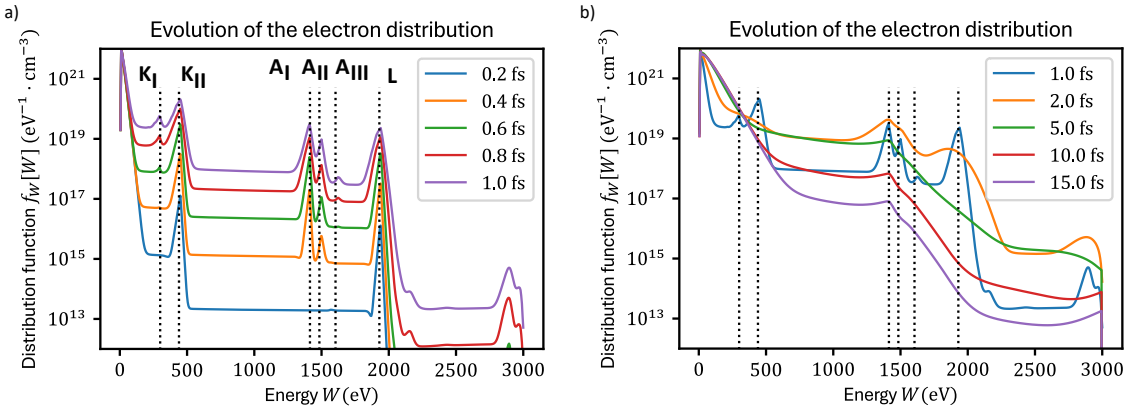


Figure 3.4: Evolution of the non-thermal electron distribution. (a) Non-thermal electrons are created via photo-ionisation and Auger decay in the first fs of the pulse. (b) The electron distribution function thermalised to equilibrium after the x-ray pulse peaked at 1 fs. Note that the electron density is not a constant, as electrons are removed by recombination and collisional processes.

photo-ionisation and from Auger decay processes on ultrafast timescales. The simulated XFEL pulse reaches its peak at 1.0 fs, and the simulation window is 40 fs, chosen to allow sufficient time for electron thermalisation to occur.

From Fig.3.4, it is evident that as the intensity of the XFEL beam gradually increases and reaches its peak at 1.0 fs, two PI channels and one Auger channel continuously produce non-thermal electrons. Electrons ionised from the K-shell sit at $W = \hbar\omega_0 - W_{1s} \approx 440$eV, and those from the L-shell sit at ≈ 1900 eV. As the intensity of the X-ray pulse rises, an increasing number of K-shell core-holes are created in the Al sample. The presence of a core-hole increases the K-edge energy by some 170 eV. Thus, the appearance of a small satellite peak at around 270 eV in Fig. 3.4 and at times after 0.6 fs is observed. The electrons created by KLL Auger decay around 1400 eV also exhibit multiple peaks in the electron distribution, corresponding to photoelectrons emitted from different charge states.

Furthermore, at $t = 1$ fs, a small peak occurs above 2 keV, which is not created by direct PI but rather by collisional K→L de-excitations that transfer energy to the free electrons. This mechanism is also responsible for producing the highest energy feature near 3 keV. It is worth noting that these features are weak – – some four orders of magnitude weaker than those due to PI. It is unlikely that such features could easily be observed experimentally.

The various processes generating non-thermal electrons are listed in Table 3.1, where electrons are labelled as K, L or A according to the producing mechanism (K-shell PI, L-shell PI, Auger decay), and Roman numerals denote peaks arising from different ion configurations.

The ability to tailor the electron distribution function is essential for measuring electron collision time. It is evident that the non-thermal electron distribution can be easily altered by tuning the XFEL photon energy: the energies of the PI electrons are shifted by the same amount as the XFEL photon energy shift, whilst the Auger decay peaks remain

Electron Label	Energy (eV)	Producing Process
K_I	270	PI: $K^2L^{\bar{y}} \rightarrow K^1L^{\bar{y}}$
K_{II}	440	PI: $K^1L^{\bar{y}} \rightarrow K^0L^{\bar{y}}$
A_I	1410	AD: $K^1L^8 \rightarrow K^2L^6$
A_{II}	1500	AD: $K^1L^7 \rightarrow K^2L^5$
A_{III}	1625	AD: $K^0L^8 \rightarrow K^1L^7$
L	1900	PI: $K^{\bar{x}}L^{\bar{y}} \rightarrow K^{\bar{x}}L^{\bar{y}-1}$

Table 3.1: Energy of non-thermal electrons shown in Fig. 3.4. $K^{\bar{m}}L^{\bar{n}}$ denotes the configuration of $\bar{m}$ electrons in the K-shell and $\bar{n}$ in the L-shell. $\bar{x}$ and $\bar{y}$ are arbitrary integers.

unchanged. This represents a useful experimental technique, as it allows for the distinction of various emission signals in the emission spectrum and the identification of features exclusively due to non-thermal electrons.

This capability is illustrated with a set of simulations. The XFEL photon energy was set to 2000 eV in the first simulation and then gradually increased in 100 eV steps to 2300 eV. In each case, the XFEL reaches its peak intensity at $t = 0.5$ fs. The pulse duration of this set of simulations is 0.2 fs, and they are run for 1 fs, ensuring that the electrons do not undergo significant thermalisation and the emission spectra exhibit strong non-thermal features which are easily tracked in energy. Fig. 3.5 demonstrates that as the XFEL photon energies increase, the energies of the PI electrons are shifted by the same amount, while that of the Auger electrons remains constant, as their energy depends solely on the binding

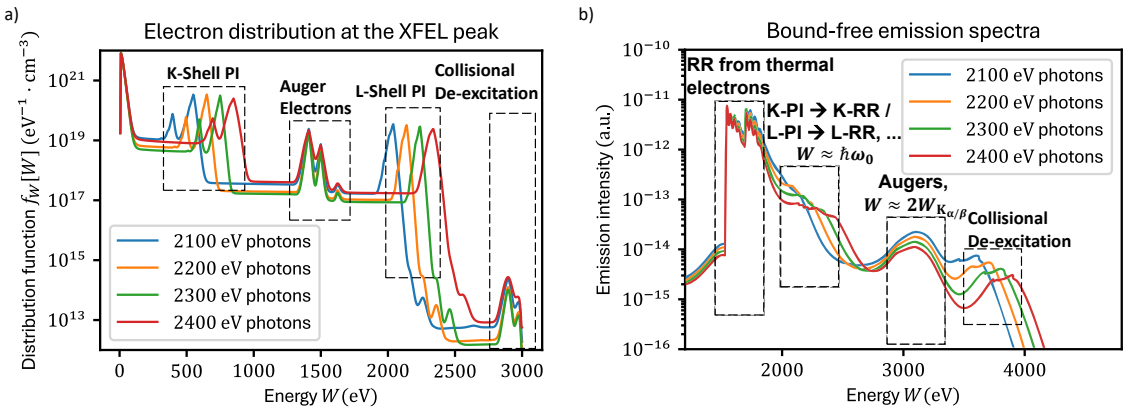


Figure 3.5: Tailoring non-thermal electron distributions by tuning the XFEL photon energy. (a) The distribution of electrons when XFEL pulses reach peak intensities. The energies of the PI electrons are shifted by the same amount as the XFEL photon energy, while the Auger electrons stay unaffected. (b) The time-integrated bound-free emissions from PI electrons shift with the photon energy, while those from Auger electrons remain unchanged. Please note that the b-b emissions are not shown in the spectra as those peaks would be substantially higher.

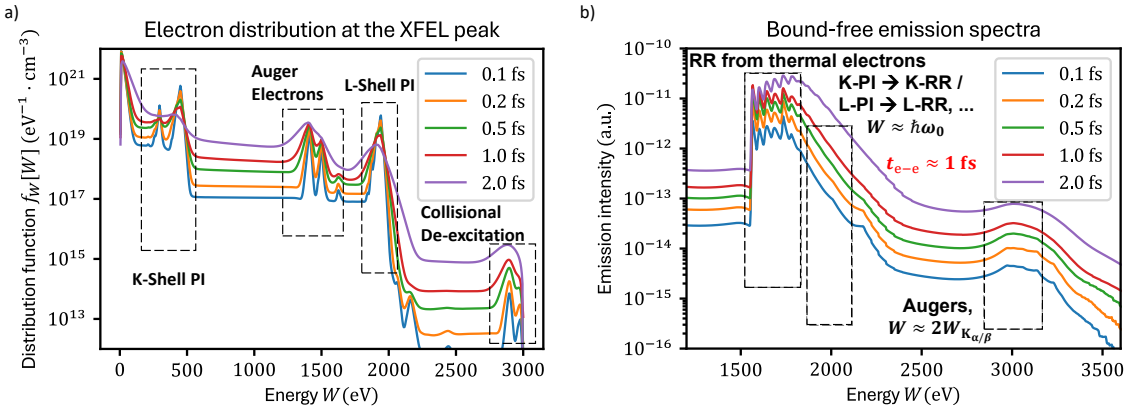


Figure 3.6: The effect of the XFEL pulse duration on the emission spectrum at constant pulse energy. a) The electron distribution when the XFEL intensity reaches its peak is drawn to show that for longer pulse durations, the electron distribution has been significantly thermalised. (b). Corresponding bound-free emission spectra show that the non-thermal feature vanishes when the pulse duration is long. Emission spectra from pulses with different durations have been offset on the y-axis to provide a clearer comparison. The actual overall intensities are similar across various pulse durations. Please note that the labels indicate the pulse durations of the XFEL.

energies of relevant shells. The peaks are less pronounced at higher photon energies because the cross-sections for absorption and emission are lower.

3.4.2 Varying Pulse Durations

The investigation now proceeds to examine the emission spectrum as a function of pulse duration. As pulse durations increase, the non-thermal features will be damped due to thermalisation, which can be quantified through the simulation.

X-ray pulses are simulated with a fixed pulse energy of 20 μJ and a photon energy of 2000 eV. The pulse durations are varied between 0.1 fs and 2 fs, leading to a range of different thermalisation timescales and x-ray intensities on target, with the highest corresponding to $2 \times 10^{19}\mathrm{W}\cdot\mathrm{cm}^{-2}$. The simulation window is switched back to 40 fs to ensure that electrons are fully relaxed and the emission spectra can represent the experimental observable. The emission spectra are shown in Fig. 3.6. It is evident that longer pulses sample more extended periods of electron thermalisation, exhibiting smoother electron distributions and emission spectra compared with the sharper features visible for the shortest pulses.

For the shortest 0.2 fs pulse, the emission peaks from PI and Auger electrons, including the satellite peaks, are clearly seen. For pulses around 1 fs, the peaks are still visible, but due to extensive electron thermalisation, they begin to wash out for pulse durations above 2 fs. This serves as clear evidence that the relaxation process can be revealed by altering the pulse duration.

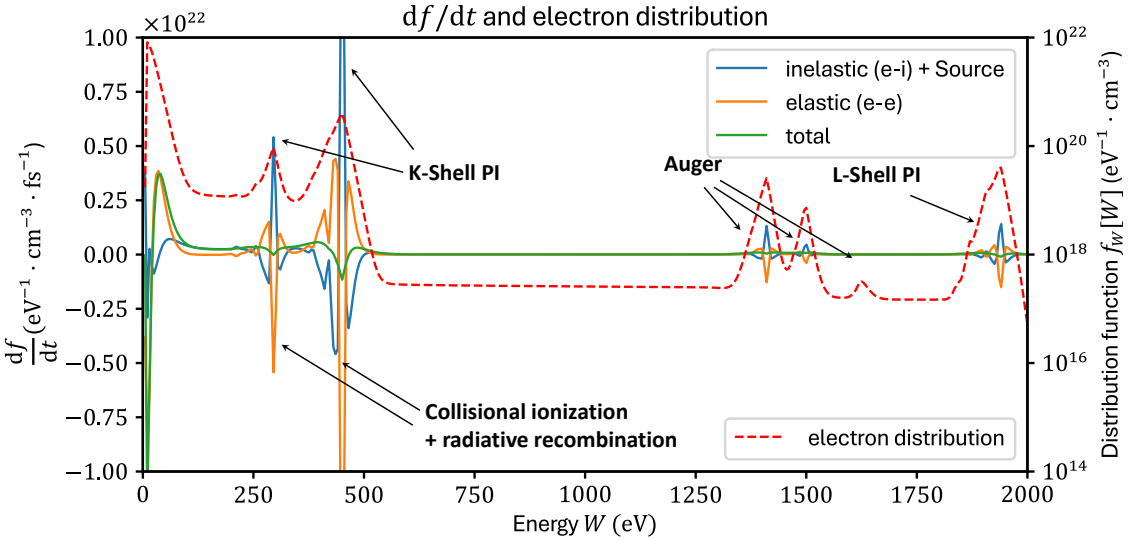


Figure 3.7: Contribution of e-e collisions to $\frac{\partial f}{\partial t}$ compared to that of e-i collisions and source term. The two components thermalise the electron distribution differently, but the overall magnitude is similar.

As the energy of this set of simulations is kept constant, the electrons gain approximately the same energy across the various pulse durations and reach overall temperatures of around 70 eV. The collision time given by Eq. (3.20) is about 1 fs.

3.4.3 Electron-electron and Electron-ion Collisions

In the preceding section, the relaxation of the electron distribution function was tracked by varying the pulse duration of the XFEL. This process, however, includes the contributions of both inelastic e-i and elastic e-e collisions, both of which thermalise the distribution, albeit in different ways. To better understand their relative roles, an examination of how the electron distribution function changes in time due to these two types of collisions is now presented.

The simulation corresponds to a 10 μm thin Al foil irradiated by an x-ray pulse with a photon energy of 2000 eV, pulse duration of 0.5 fs, and a peak intensity of 10^{19} W $\cdot$ cm^{-2}. Fig. 3.7 shows the derivative of the electron distribution $\frac{\partial f}{\partial t}$ at the XFEL's peak intensity. This is split into two contributions: the e-e contribution and everything else. It can be observed that the e-e contribution to $\frac{\partial f}{\partial t}$ is negative at the centres of the non-thermal peaks but positive in the outer wings. These collisions tend to transfer relatively small amounts of energy, and their effect is thus to gradually broaden the non-thermal peaks. In contrast, the combined effect of inelastic collisions and the source term, which includes both e-i collisions and photo-ionisation and radiative recombination, manifests differently. Here, the contribution is positive at the centre of the peak due to non-thermal electron generation via PI or Auger processes. In the surrounding areas, the contribution turns negative as collisional ionisation redistributes the non-thermal electrons.

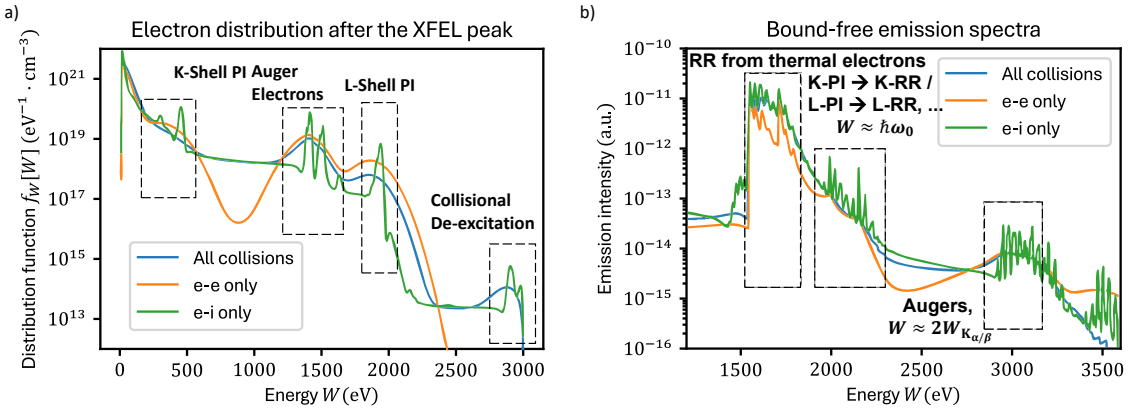


Figure 3.8: Contribution of e-i and e-e collisions to thermalisation. The electron distribution function is shown in (a), and the emission spectrum in (b). e-e collisions drive the relaxation of the electron spikes, while e-i collisions primarily determine the overall equilibration across a larger energy range.

The effect of collisional processes on the electron distribution and the observed spectrum can be further explored by selectively deactivating them in the atomic kinetics simulations and computing the emission spectrum. These results are shown in Fig. 3.8. When only e-e collisions are active, the shape of the non-thermal peaks in the distribution function remains similar to those with the full simulation. In turn, the region around 800 eV, far from the K-shell photo-ionisation and Auger features, differs significantly. This indicates that e-i collisions are critical to redistributing energy away from the non-thermal peaks across a wide energy range, where e-e collisions play a negligible role. Similarly, e-i collisions only have a minor effect in determining the shape of the non-thermal peaks, which are, instead, predominantly broadened by e-e collisions.

A similar observation can be made for the emission spectrum, shown in Fig. 3.8b. It is evident that the e-i collisions predominantly redistribute the non-thermal electrons across a wide energy range, filling in the gaps between various non-thermal peaks, whereas the e-e collisions broaden them, producing a smooth emission spectrum.

3.4.4 Effect of Collision Times

The exploration now turns to how different electron collision times, particularly for e-e collisions, affect the spectral emission. These timescales are important in determining relaxation and transport in warm-dense plasmas, and such a comparison sheds light on how these processes are impacted by the accuracy of collisional models, often described in terms of a CL. It has been demonstrated that the pulse duration of an XFEL largely determines the shape of the emission spectrum. This suggests an experimental approach where multiple pulse durations are used to drive a system to the plasma state, with the emission spectrum

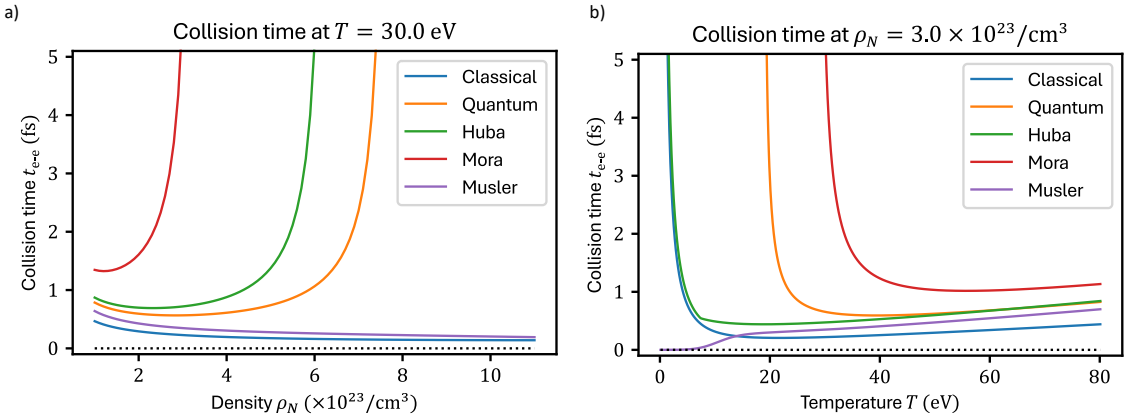


Figure 3.9: Different CL models can lead to unphysically diverging collision times at high densities (a) and low temperatures (b).

recorded for each. The electron collision time could then be determined by scanning across collisional models in the simulations until agreement with the experiment is achieved.

The previous simulations assumed a collision time determined by Huba's CL. This could be expanded by adding additional models, as shown in Fig. 3.9. However, it quickly becomes apparent that at the solid densities of interest, many models suffer from unphysical divergences. In practice, simulations deploying CL models, such as `CCFLY`, tend to check for such divergences and replace the CL with a constant (often $\mathrm{Ln}\,[\Lambda] = 1$) once it starts approaching 0. Therefore, rather than using different CL models to demonstrate the impact on collision time, the collision time of ∼1 fs given by Huba's CL will be scaled instead.

Two sets of simulations were performed where the elastic e-e collision operator in Eq. (3.17) is manually rescaled by a factor of 0.1 or 10. Simulations were run over a range of pulse durations, and the results for the emission spectra are shown in Fig. 3.10. For

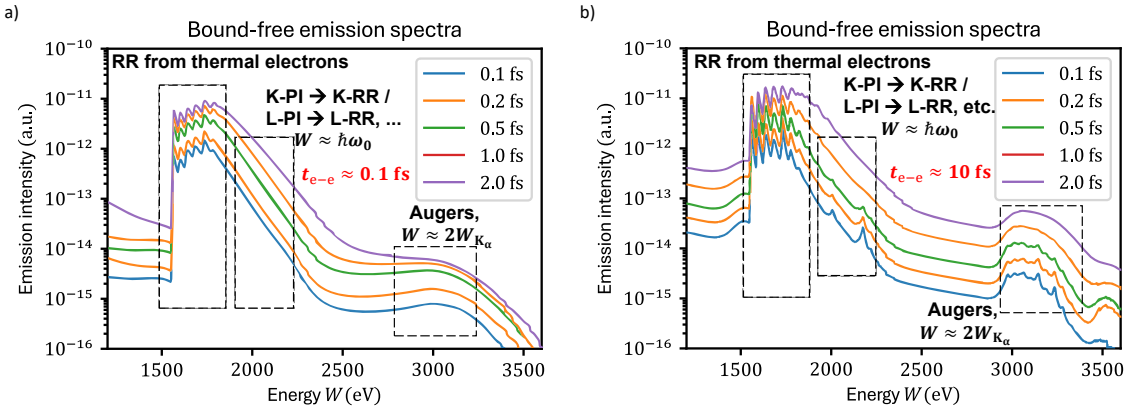


Figure 3.10: Non-thermal features under different assumptions of e-e collision times. a). The relaxation is assumed to be 10 times as fast. Non-thermal features are weak even for the shortest pulse duration. b). The relaxation is 0.1 times as fast, and non-thermal features are prominent. Even the L-shell RR become observable under this assumption. Note that, similar to Fig. 3.6, offsets are applied to emission spectra.

all simulations, the normal cross-section for all e-i collisions was maintained; these are not affected by any scaling factor. The primary interest is how the spectra change as a function of the e-e collisional rate only.

When the collision rate is 10 times as fast as that predicted by the Huba model, even the shortest simulated XFEL pulse of 0.1 fs cannot detect any noticeable non-thermal features in the emission spectrum apart from the Auger knee just above 3 keV. It is noteworthy that at present, x-ray pulse durations shorter than this are not readily accessible at XFEL facilities [121].

The contrasting case where the collision time is made 10 times as long (10 fs) is shown in Fig. 3.10b. In this scenario, the non-thermal emission features are clearly visible. For the shortest 0.1 fs x-ray pulses, a multitude of satellite peaks are observed, including those from L-shell recombination. As non-thermal electrons persist for longer, many of them can recombine at a later time when various configurations of ions with a K-shell core-hole have appeared, resulting in richer emission features.

The distinction between panels a and b in Fig. 3.10 demonstrates how the different relaxation rates influence the spectral response to pulse durations scan and serves as a key indicator for measuring the collision time in warm dense matter. Moreover, if the collision time is close to that in 3.10a (much smaller than that predicted by the CL model with Huba's formula), the difference between spectra is subtle, indicating the primary limitation of the proposed method.

3.5 Summary

This study has described a method for inferring the collision time of free electrons in the warm dense matter regime from emission spectra created by tailored non-thermal electron distributions. By varying the pulse duration of an ultra-short-pulse XFEL beam, the thermalisation process of non-thermal electrons can be observed and studied without the need for time-resolved measurements. For the non-thermal features to be prominent in the emission spectrum, it is necessary for the x-ray pulse duration to be comparable in length to the typical e-e thermalisation timescale.

The collision time has been estimated as 1 fs in warm dense Al using the standard CL model. Because electrons with higher energies typically take longer to thermalise, the thermalisation time in a mid- or high-Z material is expected to be longer than that in Al, though the collision time may be similar.

The capability of modern XFELs to generate narrow-bandwidth, energetic attosecond pulses makes them ideally suited for such measurements. This work outlines an approach that

may soon be viable to directly explore the validity of e-e collisional models, including those based on the CL framework, in describing equilibration and transport in warm dense plasmas.

The proposed method offers several advantages. Firstly, it provides a means to probe electron relaxation processes without requiring complex time-resolved experimental set-ups. This simplification could potentially allow for more widespread and routine investigations of electron thermalisation in warm dense matter. Secondly, by utilising the variable pulse duration capabilities of XFELs, the method allows for a systematic exploration of the thermalisation process across different timescales. This approach opens up new possibilities for testing and refining theoretical models of electron-electron interactions in extreme conditions. This could lead to improvements in the understanding of electron dynamics in warm dense plasmas. This, in turn, could have far-reaching implications for fields such as inertial confinement fusion, astrophysics, and materials science under extreme conditions.

However, it is important to note the limitations and challenges associated with this method. The subtle differences in spectra for certain collision time regimes, as highlighted in the previous discussion, underscore the need for high-precision measurements and careful analysis. Additionally, the interpretation of results may be complicated by the interplay between various physical processes occurring simultaneously in the warm dense plasma.

Despite these challenges, the described approach represents a significant step forward in the ability to probe electron relaxation processes in warm dense matter. As XFEL technology continues to advance, enabling even shorter pulse durations and higher intensities, the potential for more detailed and precise measurements of electron thermalisation will likely increase. This could lead to further refinements of the method and potentially new insights into the fundamental physics of warm dense plasmas.

From targets to CCDs, photons will be free.

— Unknown Author

4

Experimental Techniques for Non-thermal Experiments

Contents

4.1 Introduction 66
4.2 Single-photon Counting Technique 69
4.2.1 Photon Detection via Pixel Detector 70
4.2.2 Clustering Algorithm 74
4.2.3 Deconvolution Algorithm 76
4.2.4 Error Estimation 82
4.2.5 Benchmarking SPC Capability by Synthetic Data 83
4.3 Application of SPC in Non-thermal Experiments 88
4.3.1 Radiative Recombination Emissions 88
4.3.2 Inverse Compton Scattering 91
4.3.3 Optimal SPC Detection Configuration 99
4.4 Summary 99

4.1 Introduction

With Chapter 3 proposing a novel method to investigate the electron collision dynamics from the emission spectra of non-thermal electrons, it is essential to develop the relevant

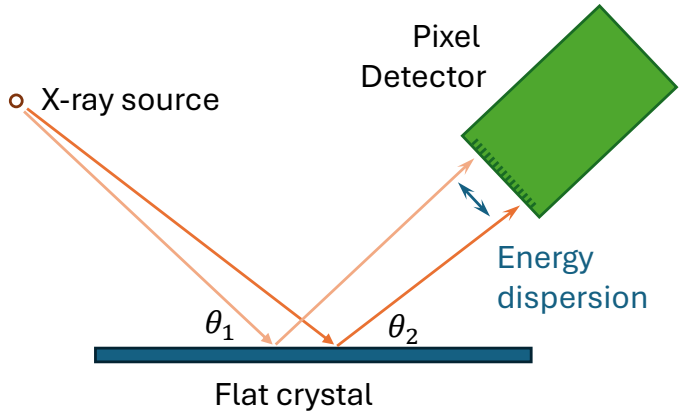


Figure 4.1: Illustration of a flat crystal spectrometer. X-rays incident on the flat crystal at a glancing angle θ form constructive interference only when Bragg's Law is satisfied. As the incident X-rays contain different wavelength components, various pixels on the detector will select different wavelengths according to the angle associated with them, enabling spectral analysis of the polychromatic source.

experimental techniques that enable detecting those signals.

Usually, spectroscopic diagnostics in XFEL experiments utilise energy-dispersive spectrometers. This can be made with a diffraction grating (usually for soft X-rays) or a crystal (usually for hard X-rays). These spectrometers have been widely used in X-ray Thomson scattering (XRTS) [123–127], X-ray emission Spectroscopy (XES) [15, 48, 49, 111], X-ray Raman scattering (XRS) [128–130], Resonant inelastic X-ray scattering (RIXS) [73, 131], and helped to diagnose the plasma density and temperature [26, 43, 132–134], electronic structure [135, 136] and much else ([137, 138]). The principle behind this is X-ray diffraction, thoroughly described in textbooks and literature [50, 139–141]. The key concept is that when a monochromatic X-ray with wavelength l_w is diffracted by a flat crystal by an angle 2θ, constructive interference can only occur if they meet the Bragg's law condition

$$2l_\mathrm{d}\mathrm{Sin}\left[\theta\right] = \bar{m}l_\mathrm{w} \ , \tag{4.1}$$

where l_d is the interplanar spacing in the crystal that can be determined by the Miller index and lattice constant, and $\bar{m} \in \mathbb{Z}$ is some arbitrary integer. For a polychromatic X-ray source in X-ray experiments, the constraint given by Bragg's law leads to an important consequence: X-rays of different energies will be diffracted at different angles and be captured by different pixels on the detector, as illustrated in Fig. 4.1. In practice, this detector is usually a camera with $O[10^6]$ pixels, such that the spectrum can be constructed from the number of photons hit on the pixel and the diffraction angle associated with that pixel according to the geometry of the camera and the crystal. When a diffraction grating is applied instead of a crystal, the main analysis follows a similar principle, though the grating equation should substitute Bragg's law. Grating spectrometers have also been widely used in X-ray experiments, especially in soft X-ray experiments, for example, in [142].

The use of energy-dispersive spectrometers, while highly effective for numerous applications, has some limitations when detecting emissions from non-thermal electrons in plasma. This constraint primarily arises from the fact that, even under intense X-ray drive conditions, the population of non-thermal electrons remains relatively small compared to that of thermal electrons. As non-thermal electrons at high energies have a much smaller cross-section for radiative recombination, the emission intensities are substantially lower than those of thermal electron emissions. These emissions are also markedly weaker than bound-bound (line) transitions for similar reasons[1]. Because an energy-dispersive spectrometer only selects X-rays' specific energies according to the glancing angle, X-rays with energies not corresponding to that angle will have a very low probability of reaching the detector. Consequently, a significant portion of the weak emission from non-thermal electrons may go undetected. An additional complication arises from the nature of non-thermal electrons themselves. As these electrons exchange energy with others, they develop a very broad distribution, necessitating a spectrometer with extensive spectral coverage. This brings complexity in designing the crystal geometry parameters as the crystal needs to be positioned close enough to the target to ensure large θ coverage. The pursuit of broad spectral coverage also introduces the challenge of higher-order diffraction from shorter-wavelength X-rays. As evident from Eq. 4.1, first-order ($\bar{m} = 1$) diffraction of X-rays with wavelength l_{w} will exhibit the same diffraction angle as second-order ($\bar{m} = 2$) diffraction from X-rays with half the wavelength $\frac{l_{\mathrm{w}}}{2}$ (and consequently, twice the energy). This phenomenon can potentially lead to ambiguities in spectral interpretation and requires careful consideration in experimental design and data analysis.

To effectively capture the emission from non-thermal electrons, researchers have developed the single-photon counting (SPC) technique [142, 143]. This method differs from crystal spectrometry as it directly records the energy of emitted photons using a pixel detector (camera). The underlying principle of SPC is relatively straightforward: when a photon hits an individual pixel on the camera, it generates a specific amount of charge within that pixel. This charge is directly proportional to the energy of the incident photon, allowing for a determination of the photon's energy through a well-defined charge-to-energy conversion process.

The SPC technique offers a unique advantage in its ability to construct a comprehensive energy spectrum generated by creating a histogram of the photon energies detected across all pixels of the camera. Each pixel functions as an independent detector, contributing to the overall spectral profile. This approach enables simultaneous capture of a wide photon energy range without the energy selectivity losses inherent in diffraction. The absence of crystals eliminates the difficulties associated with energy-dispersive spectrometers. It

[1] In this context, the cross-section should be replaced by the transition rates.

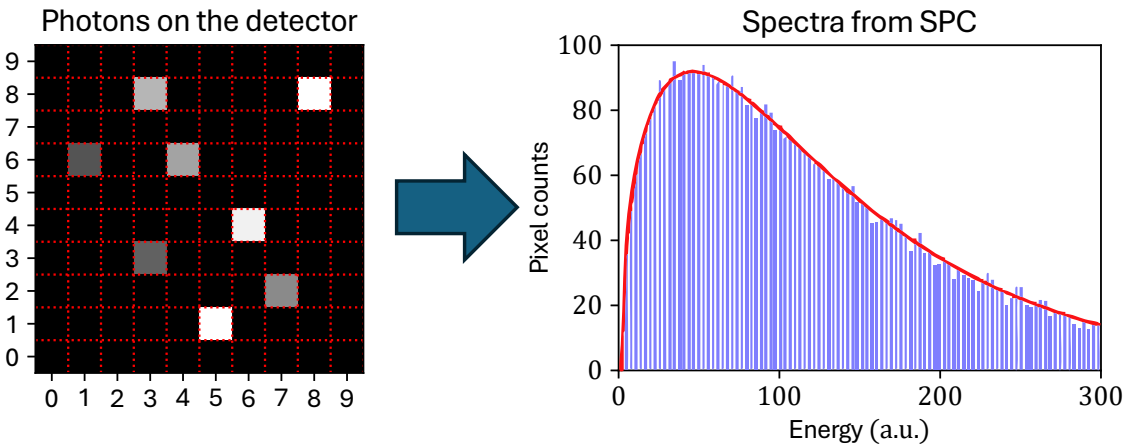


Figure 4.2: Illustration of the single-photon counting technique. Photons are detected by a CCD camera, and the energy can be read out through the charge it generates on the pixel. The histogram of energy of these photons thus forms the spectra.

provides a more direct and efficient means of measuring the entire spectrum of emitted photons, making it particularly well-suited for studying the broad energy distributions characteristic of non-thermal electron emissions.

This chapter presents a comprehensive guide to constructing spectra using the SPC technique, with a focus on problems related to non-thermal electrons. The discussion examines two distinct types of radiation: RR emission (as described in Chapter 3) and inverse Compton scattering (ICS) as detailed in Sec. 4.3.2. Given the isotropic nature of RR emission and the anisotropic character of electron scattering, proper detector positioning can be determined to help distinguish between these two types of radiation signals. The methodologies outlined in this chapter are directly applicable to specialised non-thermal experiments, such as the one detailed in Chapter 5. Notably, the SPC technique has been integrated with the conventional energy-dispersive spectroscopy technique to provide a better signal-to-noise ratio (SNR) for a wide range of applications [74].

4.2 Single-photon Counting Technique

This section outlines the procedure for constructing the spectrum from the camera image recorded in an experiment. Generally speaking, this can be divided into three steps:

1. **Characterisation of the photon energy**: This step involves determining the precise relationship between pixel readout values and the energy of incident photons. During charge generation, various sources of noise may introduce errors in energy conversion. Accurate characterisation of the photon signal and noise ensures reliable energy measurements across the detector's dynamic range.

2. **Clustering algorithm**: The mechanism of charge generation in pixel detectors often results in charge spreading to adjacent pixels. If treated independently, this spreading can lead to erroneous energy readouts. A clustering algorithm is employed to identify these multi-pixel events and correctly allocate them to the appropriate energy bins, thereby improving spectral accuracy.

3. **Deconvolution algorithm**: In scenarios where multiple photons may strike the same pixel, the recorded signal can be a superposition of individual photon energies. A deconvolution algorithm is applied to disentangle these events and reconstruct the true spectral distribution, accounting for the probability of multi-photon hits.

These steps collectively ensure the accurate transformation from raw camera data into a reliable spectral representation, addressing key challenges in SPC techniques.

4.2.1 Photon Detection via Pixel Detector

Pixel detectors are integrated devices capable of detecting photons and measuring their energies on individual pixels. These detectors aim to convert photon energy into electronic signals, often represented as Analog-to-digital units (ADUs), allowing for the inference of photon energy through a defined conversion process. Commonly, such detectors employ Charge-coupled devices (CCDs) [144], where photons generate electron-hole pairs as they travel through the depletion layer of the semiconductor substrate. The electrons generated through this process are collected in a series of potential wells and are subsequently transferred across the device for readout. An alternative design of pixel detectors involves hybrid detectors [145], which combine a separate semiconductor layer for photon detection with a readout integrated circuit (ROIC) for signal processing. This configuration offers enhanced speed and sensitivity, which is particularly beneficial for X-ray experiments. Despite their architectural differences, both CCD and hybrid detectors operate on a similar principle: the photon detection process can be conceptually divided into two primary steps - charge generation and signal readout.

When a photon hits the depletion layer in semiconductor substrates, it ionises atoms and generates electron-hole pairs. The number of these pairs is directly proportional to the energy of the incident photon. In silicon, which is commonly used in these detectors, an average energy of 3.65 eV is required to create one electron-hole pair. This relationship can be expressed as:

$$N_{\mathrm{eh}} = \frac{\hbar\omega}{3.65\mathrm{eV}} \ , \tag{4.2}$$

where N_{eh} is the number of electron-hole pairs generated by the incident photon, and $\hbar\omega$ is the energy of that photon. These generated electrons are temporarily stored in

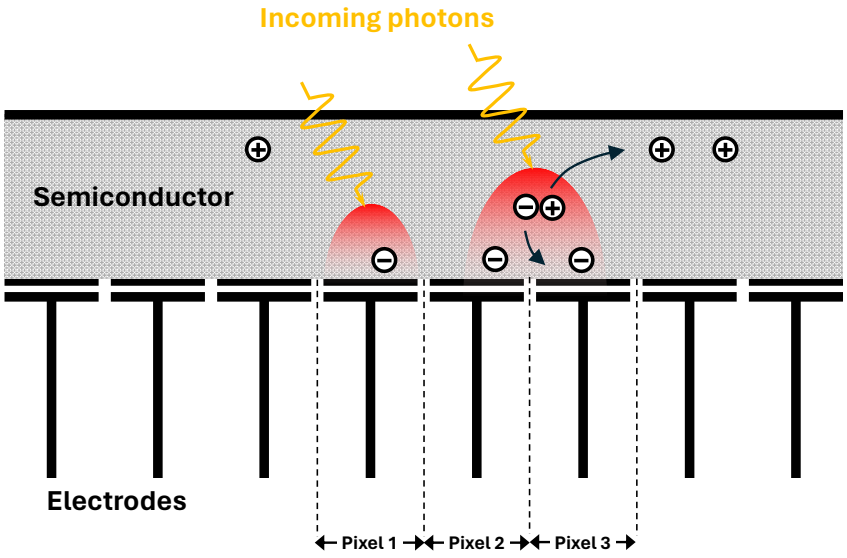


Figure 4.3: Illustration of charge generation in CCD. Charge cloud diffusion is more probable when the photons have higher energies. This is more of a problem when the pixel size is small compared with that of the charge cloud.

potential wells created by an array of electrodes on the detector surface before entering the readout process. As each pixel in the detector corresponds to a specific potential well, the energy of a photon striking that pixel can be inferred from the charge accumulated in that well, as illustrated in 4.3.

Several factors can affect the accuracy of this process. First, random fluctuations in the charge generation process lead to statistical variations. This is usually characterised by the Fano factor β_{f}, namely

$$\Delta_{\sigma} N_{\mathrm{eh}} = \sqrt{\beta_{\mathrm{f}} N_{\mathrm{eh}}}\,, \tag{4.3}$$

where $\Delta_{\sigma} N_{\mathrm{eh}}$ the standard deviation of the number of electron-hole pairs. For silicon, this factor is ~ 0.12 [146]. Additionally, quantum efficiency, representing the probability of a photon being absorbed, plays a crucial role in detector performance. It varies with photon energy and detector thickness, typically decreasing at higher energies due to increased photon penetration depth [147, 148]. For instance, a 300 μm thick silicon detector has nearly 100 % efficiency below 10 keV but drops to less than 50 % at 20 keV [149]. Furthermore, when the generated charge is high, there is a probability of diffusion to neighbouring pixels. This charge spreading can be described by a point spread function (PSF) [150, 151], often approximated as a two-dimensional Gaussian function with a characteristic radius [152]. The clustering algorithm is developed to account for this phenomenon and correctly determine the energy of the photon.

Once the exposure to the X-ray is finished, the charge generated will be transferred to the readout unit. In hybrid detectors, this is accomplished through direct connections between each pixel and its corresponding readout circuit, allowing for parallel and rapid charge collection [145]. For CCDs, however, the process is slightly more complicated. The charge is moved towards a readout register on the edge of the detector by applying a transverse voltage in a precisely timed sequence [144], as illustrated in Fig. 4.4. Because the spatial

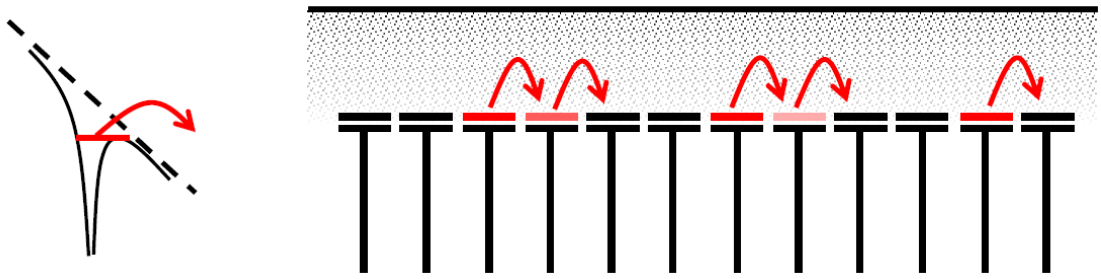


Figure 4.4: Charge transfer using a transverse voltage in a CCD detector. The charge is sequentially recorded on the edge of the detector, so the process must be performed carefully to preserve the spatial distribution. Courtesy of Dr. Oliver Humphries.

information is transformed into temporal during the charge transfer process, this operation must be carefully controlled to ensure charges of adjacent pixels are not mixed together[2]. The charge is then amplified by a charge amplifier that converts the accumulated charge to a voltage signal. Finally, this voltage is processed by an analogue-to-digital converter (ADC) that quantises the analogue signal into discrete digital values, typically expressed in ADUs. The conversion gain, usually expressed in e/ADU, relates the number of electrons generated by the photon to a digital output. This parameter is crucial for translating the digital readout into energy values (usually in eV).

The readout process introduces additional noise sources, primarily thermal fluctuation noise from the amplifier and quantisation noise from the ADC. Thermal fluctuations in the amplification process contribute to the overall noise as dark current and its associated shot noise. The dark current, which is temperature-dependent, adds spurious electrons to the signal even in the absence of incident photons [153]. Modern CCDs mitigate this effect through cooling systems. The shot noise associated with dark current follows a Poisson distribution, with its standard deviation equal to the square root of the number of thermal electrons generated [144]. Regarding the quantisation noise, ADCs in scientific-grade cameras often have a 16-bit resolution, providing a dynamic range of 65,536 levels, which allows for precise digitisation of the signal.

[2]This fundamentally limits the detection speed and is therefore usually replaced by modern hybrid detectors in high-repetition-rate XFEL experiments.

With the various noises discussed, for the application in XFEL experiments, their effect can all be categorised into two types. One is the error in ADU-eV conversion, and the other is the inaccuracy in photon detection. From a spectrum perspective, these correspond to errors on the x and y axes, respectively.

Error in the ADU-eV conversion arises from the various noises affecting the measurement of the photon energy. Notably, pixels will still have non-zero ADU readouts under no X-ray exposure due to dark current. This dark-level readout could be thought of as an offset to the true zero energy, which varies among pixels and must be subtracted using "dark runs", where the detector operates multiple times with the source blocked to determine the average dark-level on each pixel (Fig. 4.5) . Practically, dark runs are taken regularly in an experiment

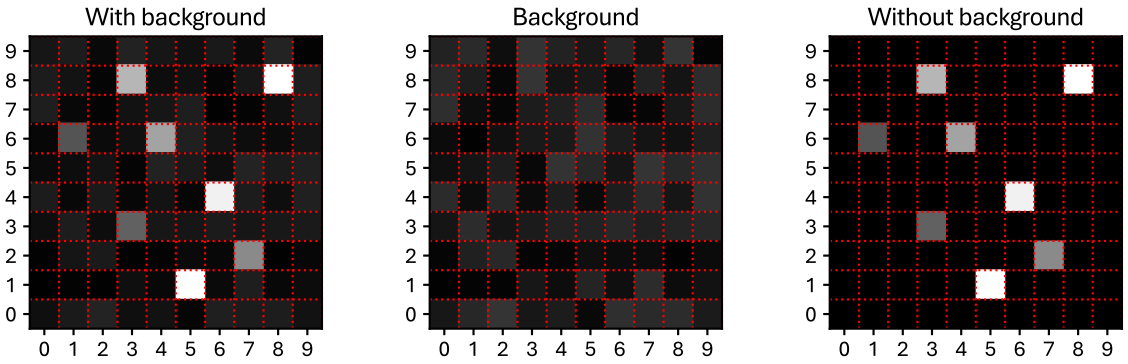


Figure 4.5: Pixels can have non-zero dark-level noise (left). The average dark-level noise is subtracted through dark runs (middle), but other sources of noise will still exist. Hence, the black pixels in the right figure will still have some residual subtle fluctuations.

to ensure that the energy measurement of the photons is unbiased. The dark-level-subtracted ADU readout is still affected by other sources of noise and will exhibit residual random fluctuations from shot to shot on each pixel. The ADU to eV conversion may also vary slightly for each pixel, as may the uncertainty level of this conversion. Calibration runs are essential to determine the exact conversion factors and uncertainties in photon energy measurements. Recent advancements have led to pre-calibrated detectors that automatically perform dark run subtraction and convert ADU readouts to eV with uncertainties as low as 1% for photons with ∼10 keV scale energy [154]. Due to the residual fluctuations on the pixels being approximately constant, the fractional uncertainty becomes larger for lower-energy photons. Additionally, users usually perform their own calibration using the characteristic X-ray emission lines during the beamtime, though not likely to be on a pixel basis.

The inaccuracy in photon detection predominantly arises from the quantum efficiency effect. This can be measured prior to the user experiment and must be accounted for if the quantum efficiency varies significantly over the detection energy range. Because this

requires knowledge of photon energies, it is always performed after the clustering algorithm and the deconvolution algorithm.

4.2.2 Clustering Algorithm

Once properly calibrated, the detector outputs a 2-D array where each element represents the energy (in eV) received by a corresponding pixel. Due to charge spread, the true energy of an incident photon typically corresponds to the total energy readout from a cluster of pixels (Fig. 4.6). An exception occurs when a cluster is formed by multiple photon hits,

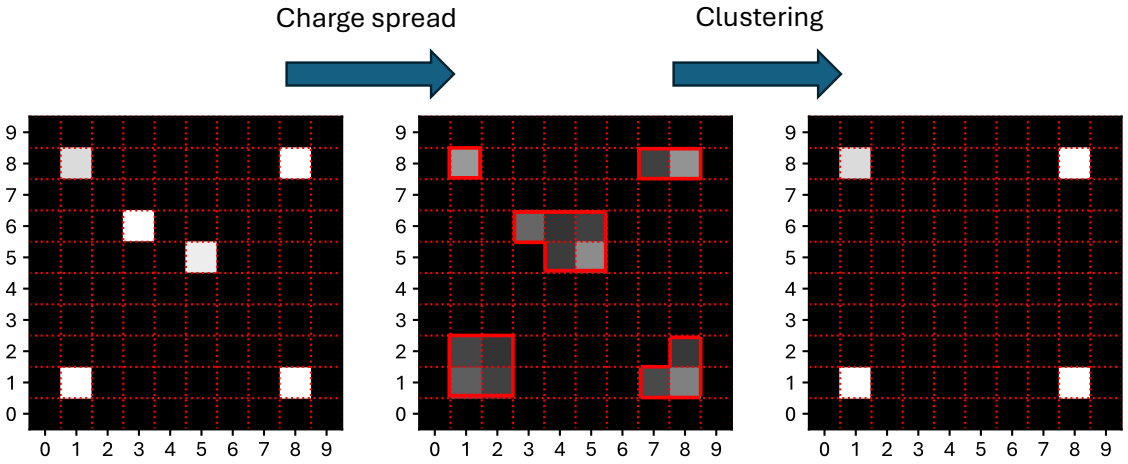


Figure 4.6: As charge spread causes the formation of clusters, the clustering algorithm retrieves the energy of the photons by summing up the energy readout in the cluster. When multiple photons land too close together, they may form large, indistinguishable charge clouds, making it difficult to retrieve individual photon energies. Such events are typically removed from analysis to maintain data quality.

a scenario discussed in detail in Sec. 4.2.3.

The aim of the clustering algorithm is to accurately determine photon energies by identifying clusters and summing the energy readouts within each cluster. This process involves three key steps: primary thresholding, cluster recognition, and secondary thresholding.

Primary thresholding looks for all pixels with a readout above the noise level. For pixel detectors properly calibrated by the dark runs, the remaining noise (called background noise in this scenario) on the pixel unaffected by a photon hit will form a Gaussian distribution centred at 0. The standard deviation of this background noise can be used as a threshold to determine whether a pixel is affected by a photon hit. For practical purposes, this threshold (called the primary threshold) is chosen to be 3σ of the background noise. This can be, in principle, chosen as other values, such as 1.5σ, and will not significantly affect the outcome of the spectra analysis. It is crucial to evaluate the background noise level after dark-run subtraction, as each pixel may have a different baseline dark-level. Pixels with readouts

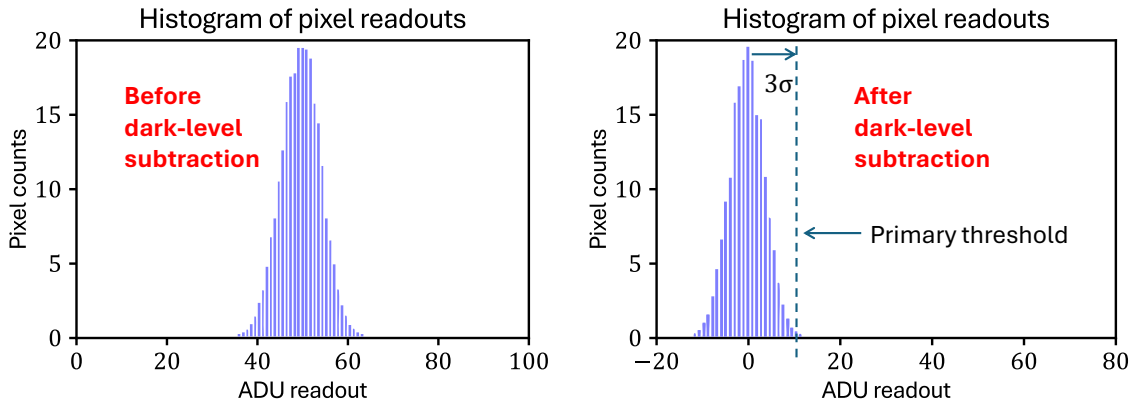


Figure 4.7: Statistics of dark pixels. Before subtraction, these pixels have a significant non-zero readout due to dark current. After subtraction, the statistics can be used to determine a primary threshold for photon detection. Because each pixel will have a different dark-level, the distribution before subtraction will be broader than that after subtraction.

below the primary threshold are assigned a value of 0, indicating "no photon", while other pixels retain their original values (Fig. 4.7).

Cluster recognition is the process of identifying and validating individual clusters by comparing them to "standard" layouts, as illustrated in Fig. 4.8. Typically, pixel

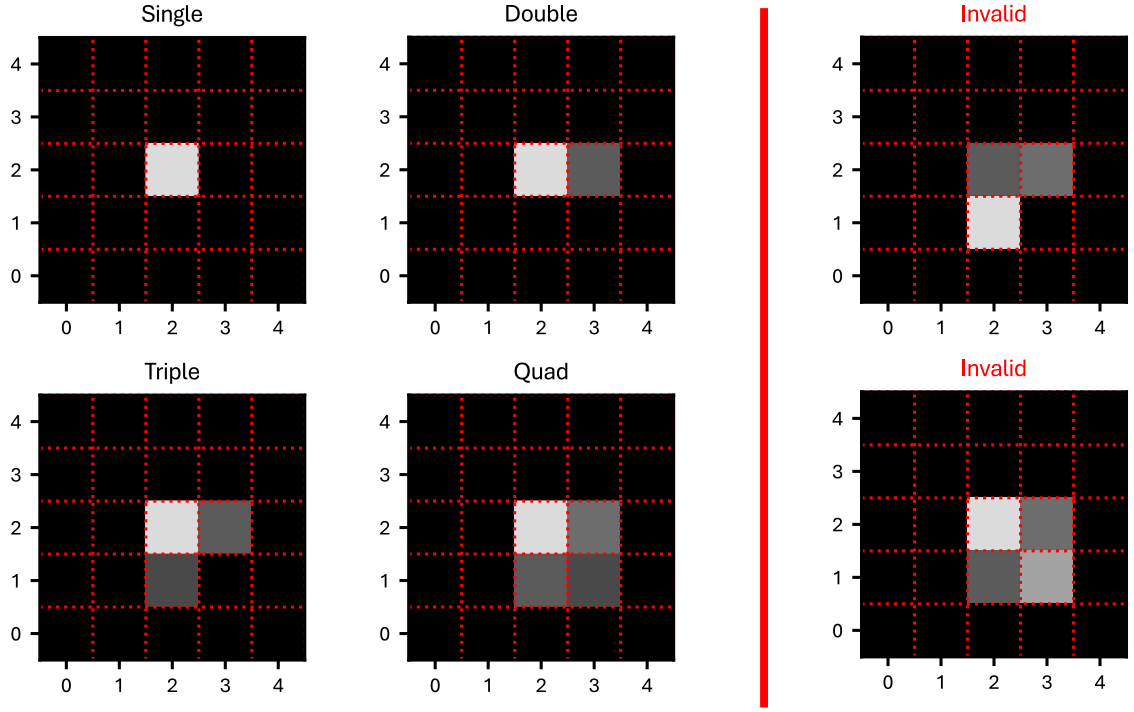


Figure 4.8: Based on the assumption that charge does not spread beyond two-pixel widths, only four primary layouts (shown on the left) are considered valid for single-photon hits. Each multi-pixel layout can be rotated by 90°, 180°, and 270°, resulting in a total of 13 valid configurations. The validity of a layout is further verified by examining the relative brightness of pixels within the cluster. Layouts depicted on the right of the figure are considered invalid.

detectors are designed so that charge spread is limited to approximately two-pixel widths. Consequently, only 13 specific cluster layouts are considered valid [155]. Cluster configurations that deviate from these 13 types, such as three pixels in a straight line, are more likely to represent multi-photon hit events.

Due to the charge spread mechanism, the validity of a cluster is also constrained by the relative brightness of each pixel within the cluster. For a three-pixel layout, the brightest pixel must be sitting in the turning corner, while for a quad-pixel layout, the brightest and darkest pixels must be sitting diagonally. These criteria help ensure that the cluster represents a single-photon hit rather than multiple-photon events. In this procedure, clusters that do not satisfy these criteria will also be assigned a value of 0.

Secondary thresholding is a process implemented to further ensure that detected signals originate from genuine photon hits rather than noise or artefacts. This threshold is typically set based on the specific requirements of the experiment. For instance, if the experimental objective is to detect Kα emissions, the secondary threshold might be set at 3σ lower than the K_α line.

The purpose of this higher threshold is to discriminate against low-energy events that may have passed the primary threshold but are unlikely to represent the photons of interest. Only clusters with a total energy exceeding the secondary threshold are included in the final analysis of constructing the energy histogram. This histogram serves as a representation of the X-ray source's energy spectrum.

4.2.3 Deconvolution Algorithm

When considering multi-pixel events, there is a non-negligible probability that two adjacent pixels illuminated by separate photons are misinterpreted as a single-photon event. Moreover, even a single pixel can potentially detect multiple photons. To mitigate these multi-photon detection errors, a key parameter called the fill fraction β_{px} is controlled. The fill fraction is defined as the ratio of pixels with signals above the primary threshold ($N_{>\mathrm{thres1}}$) to the total number of detector pixels (N_{det}):

$$\beta_{\mathrm{px}} = \frac{N_{>\mathrm{thres1}}}{N_{\mathrm{det}}} \ . \tag{4.4}$$

The fill fraction is closely related to another key parameter known as photon density β_{ph}, which is defined as the ratio between the number of photons received by the detector area[3] (N_{ph}) and

[3]This is essentially the number of photons hitting the detector times the quantum efficiency.

the number of pixels. In the limit of very small photon density, the ratio of the two indicates the size of the charge cluster, as the probability of cluster overlapping is negligibly small.

$$\lim_{\beta_{\mathrm{ph}}\to 0}\frac{\beta_{\mathrm{px}}}{\beta_{\mathrm{ph}}} = [\text{average size of cluster}] \ . \tag{4.5}$$

If one further assumes that the charge spread can be neglected, then the two quantities are identical. For the purpose of counting single photons. The maximal fill fraction should be controlled such that the error due to overlapping is not significant. If the charge spread is negligible, the upper limit of the fill fraction is 25%, equivalent to having one photon in every 2-pixel × 2-pixel square. Typically, SPC operates at a fill fraction far below this limit to ensure that the vast majority of photons can be counted instead of being neglected in the clustering algorithm.

The significance of these two parameters also lies in the fact that they control the probability of multi-photon detections relative to single-photon detections. As the photon flux incident on the detector decreases, both the photon density and the fill fraction decrease. However, the probability of receiving n photons on adjacent pixels scales as ${\beta_{\mathrm{ph}}}^{n}$. This relationship indicates that a lower fill fraction significantly reduces the likelihood of multiple photons hitting adjacent pixels. Therefore, one simple way of minimising multi-photon detection errors is to operate at the extremely low photon density regime ($\beta_{\mathrm{px}} \ll 1\%$) by applying substantial filtering on the detector. This, however, necessitates more repeated exposures to compensate for the reduced photon count per shot to improve the statistics. Another method is to make use of the deconvolution algorithm, which allows operating at $\beta_{\mathrm{px}} \sim 5\%$. This subsection provides a detailed mathematical derivation of the deconvolution process under the assumption that $\beta_{\mathrm{px}} \leq 5\%$

Deconvolution is based on the statistics of multi-photon hits. A simplified statistical model considering single-pixel events (no charge spread or clustering) is first presented. Let $f[W]$ denote the probability density function of the detector receiving a photon with energy W, normalised such that $\int f[W]\mathrm{d}W = 1$. The probability density of a pixel receiving one photon with energy W is simply $f[W]$. For two photons with total energy W, it becomes:

$$\begin{aligned}\int f[W_1]f[W_2]\mathrm{d}W_1 \mid_{W_1+W_2=W} &= \int f[W']f[W-W']\mathrm{d}W' \\ &= f \otimes f[W] \\ &= f^{\otimes 2}[W] \ ,\end{aligned} \tag{4.6}$$

Where $\otimes$ is the convolution product. Generally, for $\bar{i}$ photons with total energy W, the probability is

$$\boldsymbol{p}[W|\bar{i}] = f^{\otimes\bar{i}}[W] = f^{\otimes\bar{i}-1}[W] \otimes f[W] \ . \tag{4.7}$$

However, the probability of one pixel receiving $\bar{i}$ photons follows a Poisson distribution with parameter β_{P}. Let the random variable $\bar{n}$ be the number of photons hitting that pixel; this can be expressed as:

$$\mathbf{P}[\bar{n}=\bar{i}]=\frac{{\beta_{\mathrm{P}}}^{\bar{i}}\mathrm{e}^{-\beta_{\mathrm{P}}}}{\bar{i}!}\ , \tag{4.8}$$

As the Poisson parameter indicates the average number of photons received by that pixel, $\beta_{\mathrm{P}}=\beta_{\mathrm{ph}}$. Because charge spread is temporarily neglected in this derivation, and the photon density $\beta_{\mathrm{ph}}\sim 5\%$ indicates that pixels with multi-photon detection only contribute to a small fraction of the illuminated pixels, the fill fraction can still be approximated as the photon density. Therefore,

$$\beta_{\mathrm{P}}=\beta_{\mathrm{ph}}\approx\beta_{\mathrm{px}}\ . \tag{4.9}$$

The probability of one pixel to produce an energy readout W is essentially the observed spectrum:

$$f'[W]=\sum_{\bar{i}=1}^{\infty}\frac{{\beta_{\mathrm{P}}}^{\bar{i}}\mathrm{e}^{-\beta_{\mathrm{P}}}}{\bar{i}!}f^{\otimes\bar{i}}[W]\ . \tag{4.10}$$

The inverse transformation of Eq. 4.10 is:

$$f[W]=\sum_{\bar{m}=1}^{\infty}\frac{(-1)^{\bar{m}-1}}{\bar{m}}\frac{1}{\beta_{\mathrm{P}}}\mathrm{e}^{\bar{m}\beta_{\mathrm{P}}}f'^{\otimes\bar{m}}[W]\ . \tag{4.11}$$

This can be proved easily by applying a Laplacian transform to both sides of Eq. 4.10:

$$\hat{\mathrm{L}}f'[\xi]=\sum_{\bar{i}=1}^{\infty}\frac{{\beta_{\mathrm{P}}}^{\bar{i}}\mathrm{e}^{-\beta_{\mathrm{P}}}}{\bar{i}!}\left(\hat{\mathrm{L}}f[\xi]\right)^{\bar{i}}\ , \tag{4.12}$$

where $\hat{\mathrm{L}}$ is the Laplacian transformation operator that satisfies

$$\hat{\mathrm{L}}f[\xi]=\int_0^{\infty}f[W]\mathrm{e}^{-\xi W}\mathrm{d}W\ , \tag{4.13}$$

and

$$\left(\hat{\mathrm{L}}f^{\otimes\bar{i}}\right)[\xi]=\left(\hat{\mathrm{L}}f[\xi]\right)^{\bar{i}}\ . \tag{4.14}$$

By reorganizing the terms in 4.12 one obtains:

$$\begin{aligned}\hat{\mathrm{L}}f'[\xi]&=\mathrm{e}^{-\beta_{\mathrm{P}}}\sum_{\bar{i}=1}^{\infty}\frac{{\beta_{\mathrm{P}}}^{\bar{i}}\left(\hat{\mathrm{L}}f[\xi]\right)^{\bar{i}}}{\bar{i}!}\\&=\mathrm{e}^{-\beta_{\mathrm{P}}}\sum_{\bar{i}=1}^{\infty}\frac{\left(\beta_{\mathrm{P}}\hat{\mathrm{L}}f[\xi]\right)^{\bar{i}}}{\bar{i}!}\\&=\mathrm{e}^{-\beta_{\mathrm{P}}}\left(\mathrm{e}^{\beta_{\mathrm{P}}\hat{\mathrm{L}}f[\xi]}-1\right)\ .\end{aligned} \tag{4.15}$$

This could be inverted to get $\hat{\mathrm{L}}f[\xi]$ in terms of $\hat{\mathrm{L}}f'[\xi]$:

$$\begin{aligned}\hat{\mathrm{L}}f[\xi] &= \frac{1}{\beta_{\mathrm{P}}}\mathrm{Ln}\left[1+\mathrm{e}^{\beta_{\mathrm{P}}}\hat{\mathrm{L}}f'[\xi]\right] \\ &= \frac{1}{\beta_{\mathrm{P}}}\sum_{\bar{m}=1}^{\infty}\frac{(-1)^{\bar{m}-1}}{\bar{m}}\left(\mathrm{e}^{\beta_{\mathrm{P}}}\hat{\mathrm{L}}f'[\xi]\right)^{\bar{m}} \\ &= \frac{1}{\beta_{\mathrm{P}}}\sum_{\bar{m}=1}^{\infty}\frac{(-1)^{\bar{m}-1}}{\bar{m}}\mathrm{e}^{\bar{m}\beta_{\mathrm{P}}}\hat{\mathrm{L}}f'^{\otimes\bar{m}}[\xi]\ .\end{aligned} \tag{4.16}$$

Applying inverse Laplacian transformation to Eq. 4.16 yields Eq. 4.11, which can be used to reconstruct the true spectrum from the observed SPC spectrum.

Although the observed spectrum f' can be measured by the SPC histogram, its value in the unit of eV^{-1} must be determined by normalising correctly. This is essential as Eq. 4.11 is non-linear with respect to the scaling of f'. The correct normalisation can be obtained by considering the fact that $f[W]$ is normalised to 1. Two methods for normalisation are considered:

a) From Eq. 4.10, since $\frac{{\beta_{\mathrm{P}}}^{\bar{i}}}{\bar{i}!}$ and $f^{\otimes\bar{i}}[W]$ both decay quickly with $\bar{i}$:

$$\begin{aligned}\int f'[W]\mathrm{d}W &= \sum_{\bar{i}=1}^{\infty}\frac{{\beta_{\mathrm{P}}}^{i}\mathrm{e}^{-\beta_{\mathrm{P}}}}{\bar{i}!}\int f^{\otimes\bar{i}}[W]\mathrm{d}W \\ &\approx \beta_{\mathrm{P}}\mathrm{e}^{-\beta_{\mathrm{P}}}\int f[W]\mathrm{d}W \\ &= \beta_{\mathrm{P}}\mathrm{e}^{-\beta_{\mathrm{P}}}\end{aligned}\ . \tag{4.17}$$

b) Experimentally, $f'[W]$ represents the probability of one pixel with energy readout W. Multiplying $f'[W]$ by the total number of pixels N_{det} yields the raw histogram of the photon distribution from the experimental data.

The equivalence of these two methods is shown as follows. As the Poisson parameter, β_{P} characterises the probability of multi-photon hits, the probability of no photon hit is $\mathbf{P}[\bar{n}=0] = \mathrm{e}^{-\beta_{\mathrm{P}}}$. Therefore, the probability of at least one photon hit is

$$\mathbf{P}[\bar{n}\geq 1] = 1-\mathrm{e}^{-\beta_{\mathrm{P}}}\ , \tag{4.18}$$

and the total number of illuminated pixels is

$$N_{\mathrm{det}}\mathbf{P}[\bar{n}\geq 1] = N_{\mathrm{det}}\left(1-\mathrm{e}^{-\beta_{\mathrm{P}}}\right)\ . \tag{4.19}$$

On the other hand, method (b) indicates that $N_{\mathrm{det}}f'[W]$ is the raw histogram from the SPC experiment. Therefore $\int N_{\mathrm{det}}f'[W]\mathrm{d}W$ is also the total number of illuminated pixels, thus according to method (a):

$$\int N_{\mathrm{det}}f'[W]\mathrm{d}W = N_{\mathrm{det}}\beta_{\mathrm{P}}\mathrm{e}^{-\beta_{\mathrm{P}}}. \tag{4.20}$$

As Eq. 4.19 and Eq. 4.20 are identical to second order in β_{P}, it demonstrates the equivalence of the two methods. Noticeably, this normalisation indicates that $\int f'[W]\mathrm{d}W < 1$. This is exactly because the summation in Eq. 4.10 starts from $\bar{i} = 1$ instead of 0, as it is impossible to have a non-zero readout with zero photon hits. Therefore, Eq. 4.17 should be interpreted as:

$$\int_{W>0} f'[W]\mathrm{d}W \approx \beta_{\mathrm{P}} \approx \mathbf{P}[\bar{n} \geq 1] \ . \tag{4.21}$$

corresponding to the total number of illuminated pixels in Eq. 4.19, with the remaining probability $\mathbf{P}[\bar{n} \geq 1] \approx 1 - \beta_{\mathrm{P}}$ being zero photon detection corresponding to $W = 0$.

The deconvolution transformation, originally derived for single-pixel events, can be generalised to accommodate clustering statistics. When charge spread is considered, the condition for multi-photon detection is modified: instead of considering the probability of one pixel being illuminated by multiple photons (as in Eq. 4.8), deconvolution now considers the probability of multiple photons hit within a cluster, as illustrated in Fig. 4.8. This modification implies that the effective β_{P} is larger than that calculated from the simple photon density.

Precise determination of the actual β_{P} is challenging due to the complex nature of charge spreading and cluster formation. To account for these factors, the deconvolution process can be iteratively applied with different β_{P} values, and the results can be compared to calibration data. For example, exposing the detector to a well-controlled K_{α} X-ray source allows for optimisation of β_{P}. As double photon hits produce a peak at twice the K_{α} energy (which is not present in the original X-ray emission), the optimal deconvolution parameter β_{P} can be determined by iterating until this spurious peak vanishes.

Practically, this deconvolution procedure should be performed discretely, as the energy histogram is binned by index rather than running on continuous values. The discrete transformation is given by:

$$f_{\bar{i}} = \sum_{\bar{m}=1}^{\infty} \mathrm{e}^{\bar{m}\beta_{\mathrm{P}}} \left(f'^{\otimes \bar{m}}\right)_{\bar{i}} \ , \tag{4.22}$$

where $\bar{i}$ denotes the energy bins and the discrete convolution given by

$$\begin{aligned} (f_1 \otimes f_2)_{\bar{i}} &= \sum_{\bar{j}} f_{1\bar{j}} f_{2\bar{i}-\bar{j}} \\ (f^{\otimes \bar{m}})_{\bar{i}} &= (f \otimes f^{\otimes \bar{m}-1})_{\bar{i}} \end{aligned} \ . \tag{4.23}$$

The $f'_{\bar{i}}$ values can be directly calculated from the normalised raw spectrum (histogram) of detection:

$$f'_{\bar{i}} = \frac{N_{\bar{i}}}{N_{\mathrm{det}}} \ , \tag{4.24}$$

where $N_{\bar{i}}$ is the number of clusters in the $\bar{i}^{\mathrm{th}}$ energy bin, and N_{det} is the total number of pixels on the detector. This normalisation ensures the correct scaling of the observed spectrum.

In practical applications, only the first few orders of Eq. 4.22 are typically considered, as higher-order terms rapidly diminish in significance. The number of orders included in the deconvolution transformation depends on the desired accuracy and computational constraints.

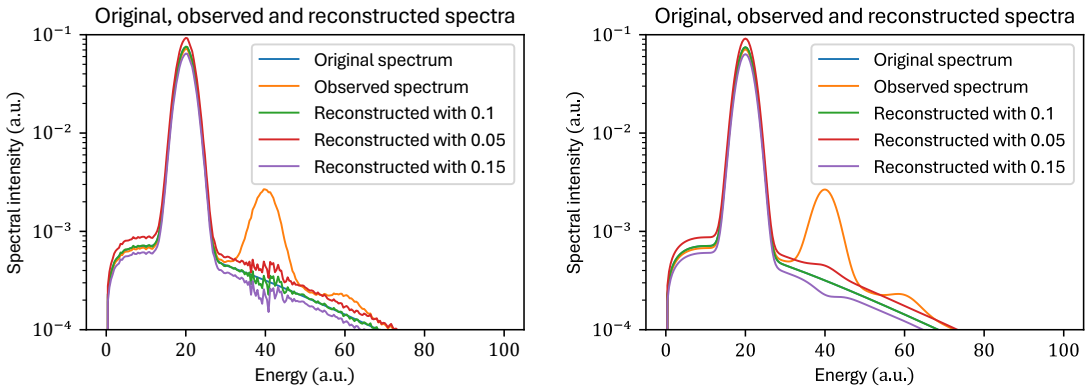


Figure 4.9: Demonstration of the deconvolution algorithm for SPC. (a) Comparison of synthetic spectrum (blue), observed spectrum with $\beta_{\mathrm{P}} = 0.1$ (orange), and reconstructed spectra using different β_{P} values (0.05, 0.10, 0.15). For $\beta_{\mathrm{P}} = 0.1$, the reconstructed curve (green) perfectly overlaps the original (blue) curve, validating the algorithm's effectiveness. (b) Reconstruction results with 2% noise added to $f'_{\bar{i}}(f'[W])$. The reconstruction using the correct β_{P} shows only minor deviations from the original curve, demonstrating the algorithm's robustness to experimental noise. For clarity purposes, both spectra are re-normalised to 1.

Figure 4.9 demonstrates the effectiveness of the deconvolution algorithm. Panel (a) shows a synthetic spectrum $f_{\bar{i}}(f[W])$ with a peak at $W = 20$, and the corresponding observed spectrum $f'_{\bar{i}}(f'[W])$. The auto-convolution effect creates additional peaks at $W = 40, 60, \cdots$, representing multiple photon detections. Applying the deconvolution transformation with the correct $\beta_{\mathrm{P}} = 0.1$ successfully recovers the original spectrum (blue line). To illustrate the algorithm's robustness to parameter uncertainty, reconstructions using $\beta_{\mathrm{P}} = 0.05$ and $\beta_{\mathrm{P}} = 0.15$ are also shown. The lower value ($\beta_{\mathrm{P}} = 0.05$) leaves some residual signal in the second peak, while the higher value ($\beta_{\mathrm{P}} = 0.15$) slightly over-suppresses it. However, these deviations from the correct reconstruction are subtle, demonstrating the algorithm's effectiveness even without precise knowledge of β_{P}. This is crucial to the applicability of the deconvolution algorithm, as the optimal β_{P} is usually unknown in a real-world experiment.

Panel (b) further illustrates the algorithm's robustness by successfully reconstructing the spectrum in the presence of 2% noise in $f'_{\bar{i}}(f'[W])$. This showcases the robustness of the algorithm under various noises and demonstrates the deconvolution method's practical applicability in real-world data.

4.2.4 Error Estimation

The error of SPC comes primarily from the detector effects and Poisson statistics. The detector effect, as discussed in Sec. 4.2.1, includes the uncertainty in the energy readout and the quantum efficiency of photon detection. Because of the energy readout uncertainty, the energy bin must be set bigger than that uncertainty. Even for detectors calibrated at the pixel level, achieving energy readout uncertainty of less than 1% is challenging for photons with ∼10 keV energy (Sec. 4.2.1). As the incident photons typically have energies of ∼10 keV, the various emission signals from non-thermal electrons are typically of the same order. Therefore, the energy uncertainty is unlikely to be better than 100 eV, which represents the main limitation of SPC. On the other hand, the quantum efficiency effect must be considered for higher-energy photon detections. This correction should be applied to the reconstructed spectra after deconvolution and clustering. For pixel detectors used in XFEL facilities, the quantum efficiency can be obtained from the detector scientists.

This subsection mainly focuses on the discussion of errors coming from the Poisson statistics. As different pixels correspond to different solid angles relative to the X-ray source, they can be treated as independent random variables; thus, the variance of the number of photons in any energy bin equates to the number of photons in the bin

$$\mathbf{Var}[N] = \sum_{\bar{i},\bar{j}} \mathbf{Var}[N_{\bar{i},\bar{j}}] = \sum_{\bar{i},\bar{j}} \mathbf{E}[N_{\bar{i},\bar{j}}] = \mathbf{E}[N] \ , \tag{4.25}$$

where N denotes the number of photons in that energy bin, $N_{\bar{i},\bar{j}}$ denotes that on pixel $[\bar{i},\bar{j}]$, and the summation over $\bar{i},\bar{j}$ runs over all the pixels on the detector. Therefore, the uncertainty of the number of photons in bin $\bar{k}$ can be simply estimated as :

$$u_{N_{\bar{k}}} = \sqrt{N_{\bar{k}}} \ . \tag{4.26}$$

This uncertainty can be directly used in Eq. 4.24 to obtain the uncertainty of the observed spectrum:

$$u_{f'_{\bar{k}}} = \frac{\sqrt{N_{\bar{k}}}}{N_{\mathrm{det}}} \ , \tag{4.27}$$

and propagated through Eq. 4.22 to obtain the uncertainty of the original spectra through

$$u_{f_{\bar{i}}} = \sqrt{\sum_{\bar{j}} \left(\frac{\partial f_{\bar{i}}}{\partial f'_{\bar{j}}} u_{f'_{\bar{j}}} \right)^2} \ . \tag{4.28}$$

The derivatives in Eq. 4.28 are usually computed numerically instead of analytically due to complications arising from the auto-convolution transformation in Eq. 4.23. As indicated in 4.26, increasing the signal level will increase the SNR, as is often the case. In real experiments, the SPC histogram is integrated over thousands of shots of the same condition. For the

purpose of proper deconvolution, the normalisation factor in Eq. 4.24 and 4.27 should be corrected by the number of shots integrated.

More sophisticated methods for estimating uncertainties have been proposed, such as those discussed by Swift [156]. Notably, Garwood [157] suggested estimating the confidence interval of the Poisson parameter based on the observed mean using Gamma distribution integrals.

$$\begin{aligned} \int_0^{\beta'_{\mathrm{P}}} \frac{\xi^{\beta^*_{\mathrm{P}}} \mathrm{e}^{\xi}}{\Gamma[\beta^*_{\mathrm{P}}]} \mathrm{d}\xi &= \frac{\eta}{2} \\ \int_0^{\beta''_{\mathrm{P}}} \frac{\xi^{\beta^*_{\mathrm{P}}+1} \mathrm{e}^{\xi}}{\Gamma[\beta^*_{\mathrm{P}}+1]} \mathrm{d}\xi &= 1 - \frac{\eta}{2} \end{aligned} , \tag{4.29}$$

where β'_{P} and β''_{P} denote the lower and upper limit of the confidence interval of β_{P} parameter with a confidence level of $1-\eta$, under observed $\beta_{\mathrm{P}} = \beta^*_{\mathrm{P}}$. Γ denotes the Gamma function:

$$\Gamma[\beta] = \int_0^{\infty} \mathrm{e}^{-\xi} \xi^{\beta-1} \mathrm{d}\xi \ . \tag{4.30}$$

Other approaches can also be considered in general. However, these methods often involve numerical integration and parameter optimisation, significantly complicating the data analysis procedure. Consequently, they are not routinely employed in practice.

Another source of error in SPC arises from the uncertainty in estimating β_{P}. As demonstrated in Fig. 4.9, this error can often be considered negligible, given that the reconstructed spectrum is not significantly affected even when β_{P} deviates by as much as 50% from its true value. However, in rare circumstances where this uncertainty becomes crucial, this can be done by exposing the detector multiple times to an X-ray source with a fixed photon density, where the uncertainty of β_{P} can be estimated from the distribution of the optimal β_{P} required for deconvolution across these exposures. As more shots are integrated, the uncertainty in β_{P} decreases, which should be taken into account.

4.2.5 Benchmarking SPC Capability by Synthetic Data

The capability of SPC can be benchmarked by generating synthetic data that closely represents experimental observations. This subsection employs Monte Carlo (MC) simulations to generate the SPC data, which is subsequently processed using the previously discussed SPC algorithms.

The simulation process begins by sampling photons from a given energy distribution. These photons are then randomly distributed across a 2-D array of pixels, mimicking the detector's spatial response to photons. The total number of photons is controlled by the photon density parameter β_{ph}. Fig. 4.10 illustrates an example of a generated image where the photons are sampled from a distribution with a narrow peak and a broad background

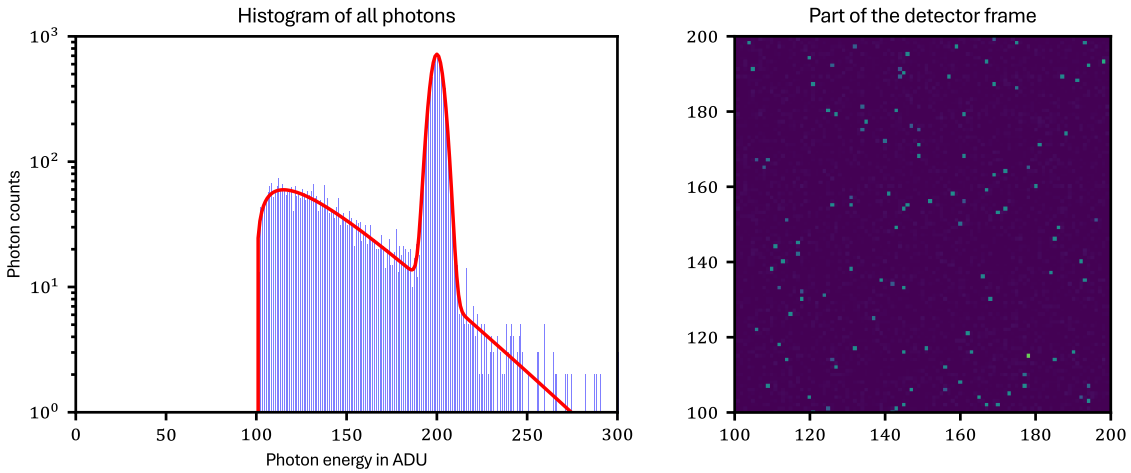


Figure 4.10: Generation of synthetic data by MC simulation based on a predefined photon energy distribution. This image represents the detector response after dark-level subtraction. Residual fluctuations from shot to shot on the pixels remain present. The effect of charge spread is not included in this image.

radiation. The photon density of this example image is set to $\beta_{\mathrm{ph}} = 1\%$. To simulate real-world conditions, background noise is added to individual pixels with a standard deviation of 5 ADUs. This stands for the detector image after dark-level subtraction, with the 5 ADUs noise representing the residual fluctuation from shot to shot, which is assumed to be constant across various pixels.

An important aspect of the simulation is the modelling of the charge spread effect. Ideally, this should be modelled using a PSF specific to the detector and dependent on photon energy. However, obtaining accurate PSFs requires dedicated experiments, as demonstrated in studies like [158], which is a complicated task itself and lies beyond the scope of this thesis. To capture the essential characteristics of charge spread without introducing undue complexity, this simulation employs a simplified model, where the charge cloud is represented by a circle with a constant radius r_{s}, independent of photon energy, as illustrated in Fig. 4.11. The energy of each photon is distributed among the affected pixels proportionally

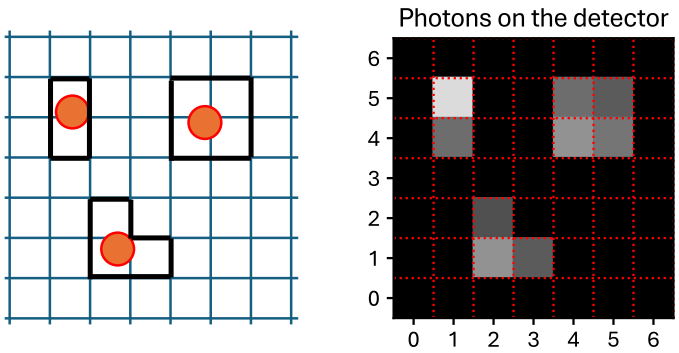


Figure 4.11: Charge spread effect is simulated using circles with a fixed radius r_{s}. The photon energy is distributed among affected pixels proportionally to the area of overlap.

to the area of overlap between the circle and each pixel.

Though assumed to be unaffected by photon energy, the radius of charge spread remains an unknown parameter that can be adjusted in MC data generation. Because the radius

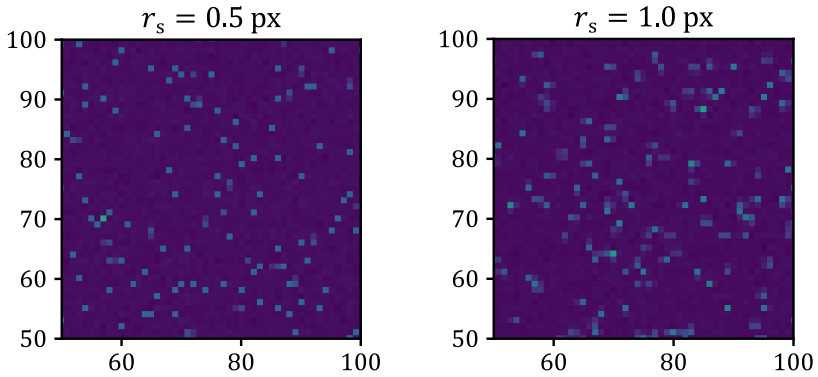


Figure 4.12: The effect of charge spread radius on size of clusters. Clusters under assumption of $r_s = 1.0$ px are sustainably larger than that under $r_s = 0.5$ px.

affects the size of pixel clusters, the value of r_s can be inferred by comparing it to experimental results. Fig. 4.12 demonstrates the effect of the charge spread radius on the cluster sizes using two examples: $r_s = 0.5$ px and $r_s = 1.0$ px.

The capability of SPC is assessed by a synthetic dataset with a fixed charge spread radius $r_s = 0.4$ px that matches the results obtained from ePix 100a, a CCD detector widely used in various endstations at XFEL facilities, including HED at EuXFEL, or MEC at LCLS. As shown in Fig. 4.13, the energy of photons is sampled from a distribution that

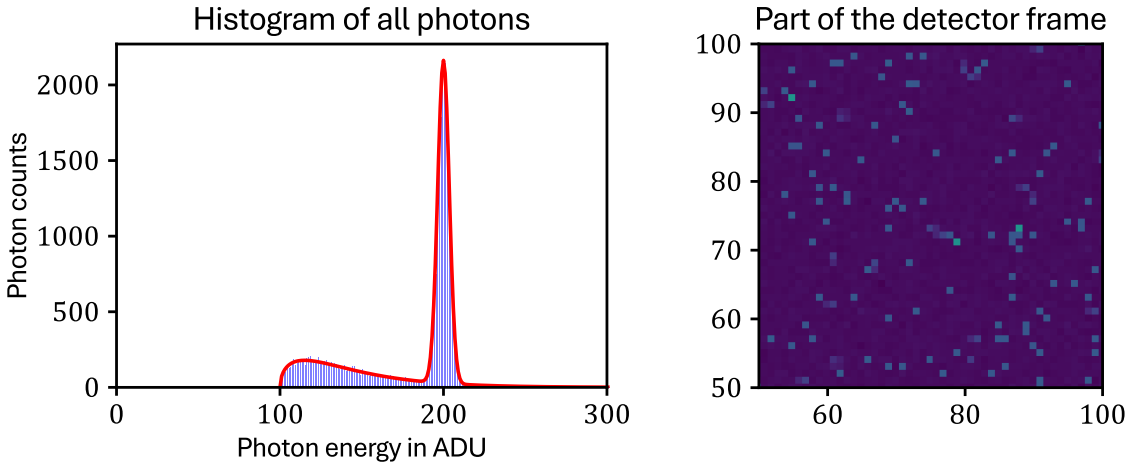


Figure 4.13: Monte Carlo simulation of SPC data. Left: Photon ADU distribution used for the simulation. The blue histogram shows the actual photon distribution, while the orange line represents the probability distribution from which photons are sampled. Right: A 100×100 pixel section of the simulated detector image. The colour scale represents ADU values, with darker colours indicating lower intensities (background) and brighter colours showing detected photons.

simulates realistic experimental conditions, including a narrow bandwidth peak around 200 ADU and the presence of background radiation represented by a broader distribution centred around 120 ADU. Gaussian noise is added to each pixel with a standard deviation of 5 ADUs to simulate electronic noise. The simulation uses a frame size of 1000×1000 pixels and is repeated 100 times to ensure statistical significance. The photon density is set to be 5% to demonstrate the SPC's capability under the reasonably dense photon regime. The right panel displays a 100×100 pixel section of a simulated frame after processing. The colour scale represents the ADU values, with most pixels showing a low-intensity background (dark purple), while scattered pixels display higher intensities (lighter colours) corresponding to detected photons. Some pixels show very high intensities (yellow/green), representing instances where multiple photons were detected in close proximity.

The generated data is then collected and processed by the SPC algorithm, with the clustering algorithm working on individual frames and the spectral reconstruction working on the integrated histogram. Fig. 4.14 shows the histogram of pixel readouts on the left panel and the reconstructed spectra after clustering on the right panel.

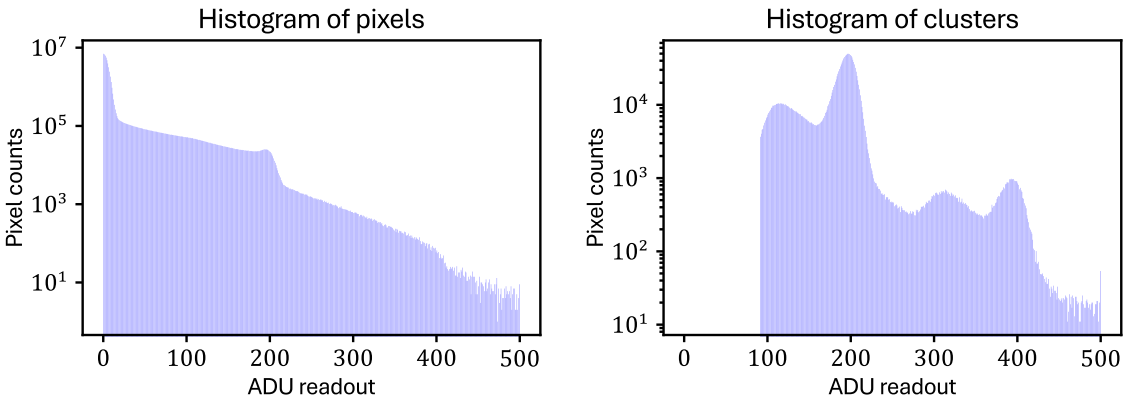


Figure 4.14: Comparison of pixel and cluster histograms. Left: Histogram of individual pixel readouts, showing a continuous distribution due to charge spread and multiple-photon events. Right: Histogram of clusters after applying the SPC clustering algorithm. The main photon energy peak at 200 ADU is clearly reconstructed, along with the background radiation peak around 120 ADU. Additional peaks at higher ADU values represent multiple-photon events.

In the left panel, a prominent peak can be seen at 200 ADU, representing the original photon energy peak as shown in the previous figure. Although photons are generated with a minimum energy of 100 ADU and most of them have an energy of 200 ADU, the histogram of pixel readouts has a distribution between 0-100 ADU, indicating the effect of charge spread. Similarly, the continuous distribution between 100-200 ADU and beyond 200 ADU is caused by a combination of charge spread and multiple-photon hit events.

The histogram of the clustered data after applying the clustering algorithm is shown in the right panel. Here, the energy of photons is more accurately retrieved, and the

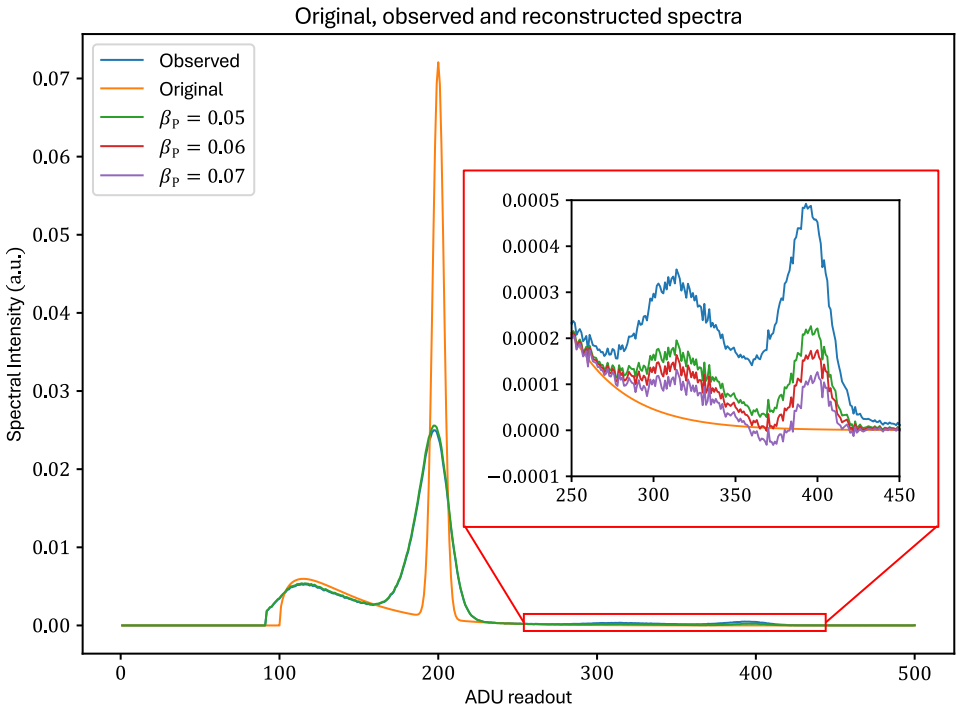


Figure 4.15: Comparison of observed, true, and reconstructed spectra in SPC. Main panel: Full spectrum showing observed data (blue), true input spectrum (orange), and reconstructed spectrum with $\beta_P = 0.05$ (green). Inset: Magnified view of the high-energy tail (250-450 ADU), displaying reconstructions with various β_P values. The reconstruction effectively eliminates artificial peaks from multi-hit events and approximates the true spectrum, demonstrating the SPC algorithm's capability to recover the underlying photon energy distribution.

continuous distribution is largely removed as the energy on the pixels is attributed to the corresponding clusters. The clustering process has successfully reconstructed the main peak at 200 ADU and the secondary peak around 120 ADU. Additionally, smaller peaks at higher ADU values (around 300 and 400 ADU) are visible, representing multiple-photon events that the clustering algorithm has identified. These multi-photon detections can be eliminated by applying the deconvolution algorithm.

The effectiveness of the deconvolution process in reconstructing the true photon energy distribution is illustrated in Fig. 4.15. The main panel shows the full spectrum, comparing the observed data, true input spectrum, and reconstructed spectrum using $\beta_P = 0.05$. The inset provides a magnified view of the high-energy tail, which is crucial for assessing the algorithm's performance with multi-hit effects.

Given that the optimal β_P is not known a priori, a range of values has been employed for reconstruction. As shown in the inset, $\beta_P = 0.07$ nearly eliminates peaks caused by multiple hits but introduces unphysical negative values between 300 ADU and 400 ADU. This phenomenon underscores how the clustering process alters the underlying Poisson

statistics, making the deconvolution transformation slightly imprecise. Nevertheless, the deconvolution successfully suppresses multi-hit artefacts, particularly the multi-photon peaks at 300 and 400 ADU, closely approximating the smooth decline of the true spectrum in this region. The reconstructed spectrum exhibits slight broadening and lower peak intensities compared to the original, primarily due to ADU noise and the rejection of some photons by the SPC algorithm in high-density regions.

Overall, the SPC algorithm effectively recovers the underlying photon energy distribution, even in the presence of detector effects and multi-hit events. The reconstruction quality could potentially be improved by decreasing the photon density in the experiment.

4.3 Application of SPC in Non-thermal Experiments

Building upon the SPC procedure and its limitations discussed in the previous section, this section now focuses on its application in non-thermal experiments, addressing key adaptations of SPC due to various signals from non-thermal electrons.

In non-thermal experiments, two distinct types of X-ray signals from non-thermal electrons can be detected:

1. **Radiation Recombination (RR) emission signal**: This phenomenon, previously discussed in Chapter 3, results from the interaction between high-energy electrons and intense electromagnetic fields.

2. **Inelastic scattering signal**: This is primarily induced by the inverse Compton effect, where high-energy electrons scatter incident photons to higher or lower energies.

A key distinction between these signals lies in their spatial distribution. The RR emission signal exhibits an isotropic distribution, whereas the inelastic scattering signal, resulting from interactions with linearly polarised XFEL radiation, displays an anisotropic spatial (angular) distribution. This informs the optimal detector set-up for capturing X-ray signals from non-thermal electrons and helps to distinguish one from the other.

4.3.1 Radiative Recombination Emissions

Chapter 3 has already discussed two main types of RR: those involving recombination from KLL Auger electrons to the K-shell and the semi-elastic process where K-shell PI electrons undergo RR to the K-shell or L-shell electrons to the L-shell. This subsection extends the discussion to other processes. The process of X-shell PI followed by Y-shell RR will be denoted concisely as X-PI $\rightarrow$ Y-RR, and that of ABC Auger followed by Y-shell RR will be denoted as ABC-Auger $\rightarrow$ Y-RR.

Apart from the KLL Auger process, mid-Z metals can also undergo KLM and KMM processes. The RR emissions from these electrons have distinct energies:

1. KLM Auger: The RR emission from KLM Auger electrons will have an energy of approximately $W_{K_\alpha} + W_{K_\beta}$.

2. KMM Auger: The RR emission from KMM Auger electrons will have an energy of approximately $2W_{K_\beta}$.

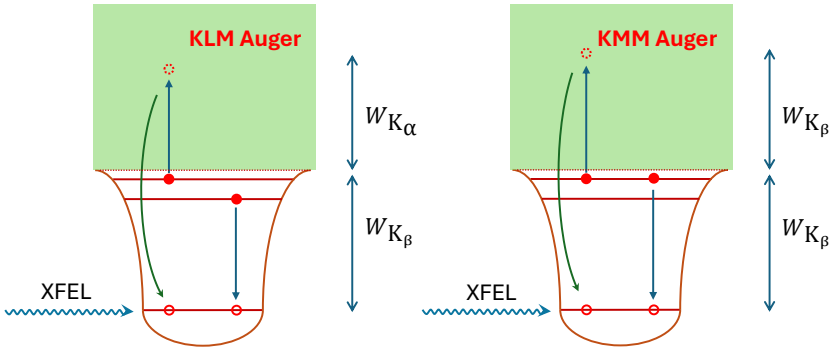


Figure 4.16: Energy-level diagrams illustrating the RR emissions from KLM and KMM Auger processes. Left: KLM Auger process, where the RR emission has an energy of approximately $W_{K_\alpha} + W_{K_\beta}$. Right: KMM Auger process, resulting in an RR emission with an energy of approximately $2W_{K_\beta}$.

These processes are illustrated in Fig. 4.16, which shows the energy-level diagrams for both KLM and KMM Auger processes and their subsequent RR emissions. However, it is important to note that due to the limited energy resolution of SPC techniques, distinguishing these different RR emission lines in a real experiment can be challenging. A similar energy analysis can also be done for Auger electrons recombining to the L-shell, resulting in a richer emission feature.

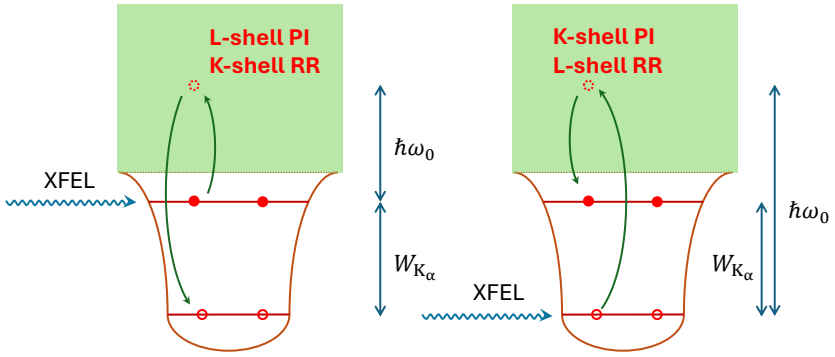


Figure 4.17: Energy-level diagrams illustrating different PI and RR processes. Left: L-PI → K-RR. The energy of the RR photon will be approximately the incident photon energy plus the K_α energy. Right: K-PI → L-RR. The energy of the RR photon will be approximately the incident photon energy minus the K_α energy.

Similar discussions apply to the PI electrons. ne will observe L-PI → K-RR, K-PI → L-RR, and processes involving the M-shell as well. Figure 4.17 demonstrates L-PI

→ K-RR and K-PI → L-RR processes. While these processes are possible, they occur with relatively lower probability.

As the PI cross-section is relatively small for L-shell electrons when the XFEL energy is sufficient to photo-ionise the K-shell, the probability of L-PI → K-RR is low. Similarly, electrons photo-ionised from the K-shell will have too much energy to efficiently undergo radiative recombination to L-shell core-holes if the XFEL photon energy is substantially higher than the K-shell edge. Although the RR efficiency can be improved by reducing the XFEL photon energy, this approach has a drawback: the energies of the non-thermal electrons are also lowered, and the detection of those photons will be strongly affected by the background noise on the dark pixels.

It is also important to note that most of the energies discussed approximate the combination of two photons. This similarity to double-hit events interferes with the actual detection of non-thermal electrons. For instance, double K_α photon hits can be mistaken for a photon from KLL-Auger → L-RR (with energy of $2W_{K_\alpha}$). Similarly, double photon hits from one W_{K_α} photon and one elastic scattering photon can be mistaken for a photon from L-PI → K-RR (with energy of $W_{K_\alpha} + \hbar\omega$).

To solve this issue, one approach involves reducing photon density at the detector to ensure that double-hit events do not exceed non-thermal electron RR emissions. The contribution from elastic scattering can be minimised by positioning the detector along the polarisation direction of the incident beam, where elastic scattering is suppressed. This not only reduces the probability of having a double photon event with one K_α photon and one elastic scattering photon and preserves the ability to detect L-PI → K-RR process, but also rescues processes such as K-PI → K-RR or L-PI → L-RR that directly have energies approximately equal to the incident XFEL. As for the emission from bound-bound transitions, for example, K_α photons, this can be done through appropriate filtering. As the energy of RR photons from non-thermal electrons is typically much higher than that from bound-bound transitions, increasing the filter thickness can significantly reduce the probability of detecting two photons while not affecting the detection of RR photons from non-thermal electrons. However, this solution compromises overall signal intensity, so the experiment will require substantial repetition, which may be limited by the detector's operating frequency, as well as the operating frequency of XFEL.

An alternative strategy focuses on the K-PI → L-RR process, which yields an energy signature that is the difference between two photon energies instead of the sum of them. For instance, when exposing Fe plasma to 10 keV X-rays, this channel will generate photons with energies around 3.6 keV. While this energy is distinguishable from background noise, it still challenges the limited energy resolution of SPC techniques. Additionally, the smaller cross-section of the L-shell RR process necessitates increased photon density for detection, which

also introduces more K_α photons with a far higher emission intensity and will overlap with the emission from non-thermal electrons due to the increased photon density and inevitably interfere with the detection. Therefore, this approach requires sophisticated filtering to mitigate interference from K_α emissions at higher energies.

These considerations demonstrate the complex interplay between XFEL energy, electron shell energies, and detection capabilities in non-thermal experiments. The challenge lies in balancing the excitation energy to promote desired processes while maintaining sufficient energy separation for accurate detection and analysis. This underscores the need for careful experimental design.

4.3.2 Inverse Compton Scattering

Inverse Compton scattering (ICS) is a non-elastic process in which photons gain energy from highly energetic electrons. The energy transfer from electron to photon is dependent on the electron's energy, making ICS a potential tool for probing electron energy distributions. The non-relativistic limit of ICS, known as X-ray Thomson Scattering (XRTS), has been widely employed in plasma temperature measurements, with the principles and various applications detailed in [24], and has been applied in various experiments. However, the potential of utilizing ICS in characterising complete distributions of non-thermal electrons remains largely unexplored.

Significant efforts have been made to analyse the effects of ICS under various assumptions. For instance, Lefa *et al.* [159] derived the ICS spectrum from Maxwellian-distributed electrons. Moderski *et al.* [160] extended this work to non-thermal electrons, focusing on highly relativistic regimes. However, neither of these studies incorporated the effects of photon polarisation. This effect is later incorporated by Krawczynski[161], who employed large-scale Monte Carlo simulations to investigate ICS from a uniformly and isotropically distributed mono-energetic electron population. Despite the advancements, these works primarily focus on astrophysical or high-energy physics contexts. There is a notable gap in the application of ICS to high-energy-density science scenarios. Furthermore, experimental validation of ICS as a diagnostic tool for measuring non-thermal electron distributions in laboratory plasmas is lacking.

To retrieve the electron distribution from ICS spectra, one must first determine the ICS spectra from a uniform electron gas with an isotropic velocity distribution before diving into the inverse problem. This can potentially be solved by implementing the full differential cross-section given by Curatolo *et al.* [162], which considers both the angle between the electron and the photon and the polarisation direction of the photon. As electrons from various

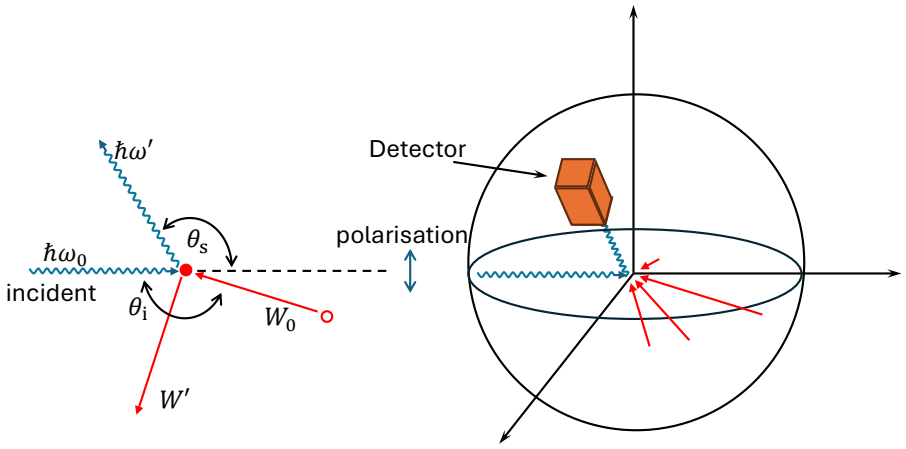


Figure 4.18: Schematic representation of Inverse Compton Scattering. The incident photon ($\hbar\omega_0$) scatters off an electron, resulting in a scattered photon ($\hbar\omega'$) with altered energy and direction. The detector placement and polarisation effects are shown.

directions will all contribute to the scattering process, the differential cross-section must be integrated to obtain the spectra for an arbitrary given direction of detection (Fig. 4.18).

This comprehensive approach to ICS involves a quantum electrodynamics (QED) treatment of the scattering process. The inverse problem of retrieving the non-thermal electron distribution from the ICS spectra is, therefore, complicated and sits beyond the scope of this thesis. However, a simplified analysis based on Compton scattering and Lorentz transformation can already provide valuable insights.

The analysis starts from the Klein-Nishina formula ([163]) that gives the cross-section of Compton scattering where the electron is initially at rest:

$$\frac{\mathrm{d}S}{\mathrm{d}\Omega} = \frac{1}{2} r_{\mathrm{e}}^2 \left(\frac{\omega'}{\omega_0}\right)^2 \left(\frac{\omega'}{\omega_0} + \frac{\omega}{\omega'} - 2\left(\mathrm{Sin}\left[\theta_{\mathrm{s}}\right]\mathrm{Cos}\left[\theta_{\mathrm{p}}\right]\right)^2\right) \ , \tag{4.31}$$

where θ_{s} the scattering angle, θ_{p} the azimuthal scattering angle (as shown in Figure 4.19),

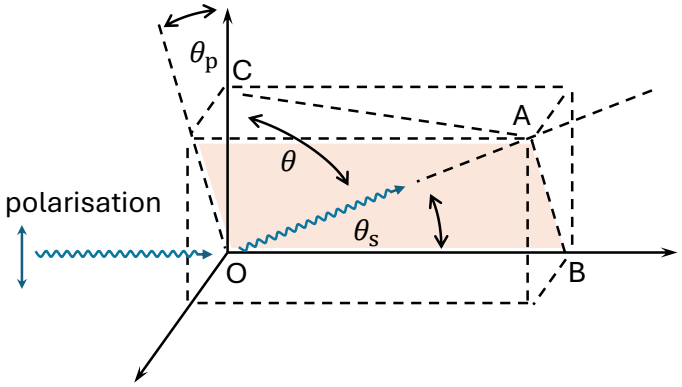


Figure 4.19: Schematic representation of Compton Scattering. The incident photon scatters off a stationary electron, resulting in a scattered photon with altered energy and direction. The scattering angles θ_s and θ_p, and the polarisation angle θ are shown. The scattering plane is shown in light orange.

$r_{\mathbf{e}} = \frac{1}{4\pi\varepsilon_{\mathbf{0}}} \frac{q_{\mathbf{e}}^2}{m_{\mathbf{e}} v_{\mathbf{c}}^2} \approx 2.82$ fm is the classical electron radius, and $\frac{\omega'}{\omega_0}$ the ratio of the photon energy before and after scattering determined by the Compton shift formula

$$\hbar\omega' = \frac{\hbar\omega_0}{1 + (\hbar\omega_0 / m_{\mathbf{e}} v_{\mathbf{c}}^2)\,(1 - \mathrm{Cos}\,[\theta_{\mathrm{s}}])}\ , \tag{4.32}$$

where $v_{\mathbf{c}}$ is the speed of light in vacuum.

In the limit of $\hbar\omega_0 \to 0$, the scattering is elastic; thus, the Thomson cross-section is retrieved by defining the polarisation angle θ between the propagation direction of the scattered photon and the polarisation direction of the photon before scattering:

$$\frac{\mathrm{d}S}{\mathrm{d}\Omega} = r_{\mathbf{e}}^2\,(\mathrm{Sin}\,[\theta])^2\,. \tag{4.33}$$

The energy shift in Compton scattering depends solely on the scattering angle θ_{s}, allowing the determination of maximal and minimal cross-sections of Compton scattering by considering the azimuthal angle θ_{p}. Specifically, the minimal cross-section occurs when $\theta_{\mathrm{p}} = 0$, corresponding to a polarisation angle $\theta = 0$ as well. The maximal cross-section occurs when $\theta_{\mathrm{p}} = \pi/2$, corresponding to a polarisation angle $\theta = \pi/2$. These results are in accordance with the angular distribution observed in Thomson scattering, though the Compton scattering cross-section remains non-zero for $\theta = 0$. This indicates that if one wants to maximise the scattering signal, the detector should be placed in the equatorial plane relative to the polarisation direction of the incident XFEL beam.

For ICS, the situation becomes more complex. To accurately determine the energy shift and the cross-section, it is necessary to perform a Lorentz transformation into the electron rest frame, apply equations 4.31 and 4.32, and then transform back to the laboratory frame. These transformations affect the angular distribution of scattered photons. However, in the specific context of non-thermal electrons generated by XFELs, some simplifying assumptions can be made. Typically, these electrons have energies up to approximately 10 keV, which is about 1/50 of the electron rest mass energy (0.511 MeV). This energy range indicates that while the electrons are somewhat relativistic, their velocities introduce only minor effects on the angular distribution of scattered photons. The relatively low electron energies in this scenario result in angular deviations of only a fraction of a radian from the non-relativistic case. Consequently, for the practical purpose of maximising detection efficiency, the assumption can be made that the optimal detector placement remains in the equatorial plane relative to the XFEL polarisation, similar to the case of Compton scattering and XRTS with stationary electrons or the elastic scattering process.

A critical consideration in ICS experiments is maximising the energy gain from electron-photon interactions. This optimisation is particularly important due to the limited resolution of SPC detectors, which makes it challenging to distinguish inelastically scattered photons from elastically scattered ones unless there is sufficient energy separation. For ICS events

involving electrons of a fixed energy colliding with photons at various angles, the maximum energy transfer occurs in "head-on" collisions, where the angle between the incident electron and photon is π, and the electron scattering angle is also π. The energy gain from such head-on collisions can be determined through the conservation of energy and momentum:

$$\begin{cases} \hbar\omega_0 + \dfrac{m_e v_c^2}{\sqrt{1 - v_0^2/v_c^2}} = \hbar\omega' + \dfrac{m_e v_c^2}{\sqrt{1 - v'^2/v_c^2}} \\ \dfrac{\hbar\omega_0}{v_c} - \dfrac{m_e v_0}{\sqrt{1 - v_0^2/v_c^2}} = -\dfrac{\hbar\omega'}{v_c} - \dfrac{m_e v'}{\sqrt{1 - v'^2/v_c^2}} \end{cases}, \tag{4.34}$$

where v_0, v' represent the speed of the electron before and after scattering, respectively, and $\hbar\omega_0$, $\hbar\omega'$ the energy of the photon before and after scattering, respectively.

As shown in Figure 4.20, the energy gain from ICS exhibits a strong dependence on both electron and incident photon energies. For XFEL photons in the range of 4-10 keV interacting with electrons of 3-10 keV, the energy shifts are on the order of several keV. The relation between energy gain $\Delta\hbar\omega$ and the electron energy (W_e) is approximately quadratic ($(\Delta\hbar\omega + \Delta_0)^2 \sim W_e$), with an offset Δ_0. This is in accordance with the lower energy limit known as the Doppler shift of XRTS given by Eq. 11 in [24]. These shifts are sufficiently large to be resolved by SPC detectors, making the measurement of the electron distribution function feasible.

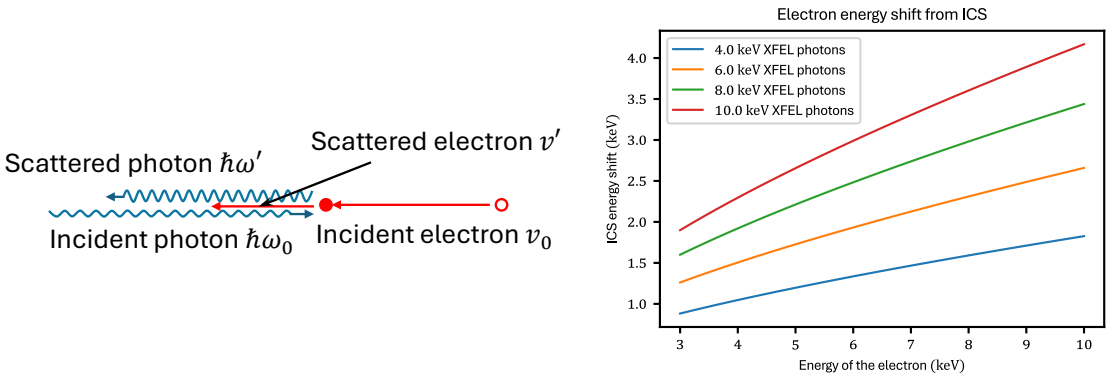


Figure 4.20: Energy shift in head-on Inverse Compton Scattering as a function of electron energy for different XFEL photon energies (4.0-10.0 keV). The energy shift is calculated for optimal collision geometry where both the incident angle and scattering angle are π.

For electrons with an isotropic velocity distribution, head-on collisions represent only a small fraction of all interaction events, with most collisions occurring at various angles. The conservation equations must, therefore, be modified to account for momentum conservation in both parallel and transverse directions relative to the photon propagation direction (denoted as

the x direction, as illustrated in Fig. 4.21 (a)). This leads to the following system of equations:

$$\begin{cases} \hbar\omega_0 + \dfrac{m_e v_c^2}{\sqrt{1 - v_0^2/v_c^2}} = \hbar\omega' + \dfrac{m_e v_c^2}{\sqrt{1 - v'^2/v_c^2}} \\ \dfrac{\hbar\omega_0}{v_c} - \dfrac{m_e v_0}{\sqrt{1 - v_0^2/v_c^2}}\mathrm{Cos}\left[\varphi_0\right] = -\dfrac{\hbar\omega'}{v_c} - \dfrac{m_e v'}{\sqrt{1 - v'^2/v_c^2}}\mathrm{Cos}\left[\varphi'\right] \\ \dfrac{m_e v_0}{\sqrt{1 - v_0^2/v_c^2}}\mathrm{Sin}\left[\varphi_0\right] = \dfrac{m_e v'}{\sqrt{1 - v'^2/v_c^2}}\mathrm{Sin}\left[\varphi'\right] \end{cases} , \tag{4.35}$$

where φ_0 and φ' represent the angles shown in the figure. The increased degree of freedom

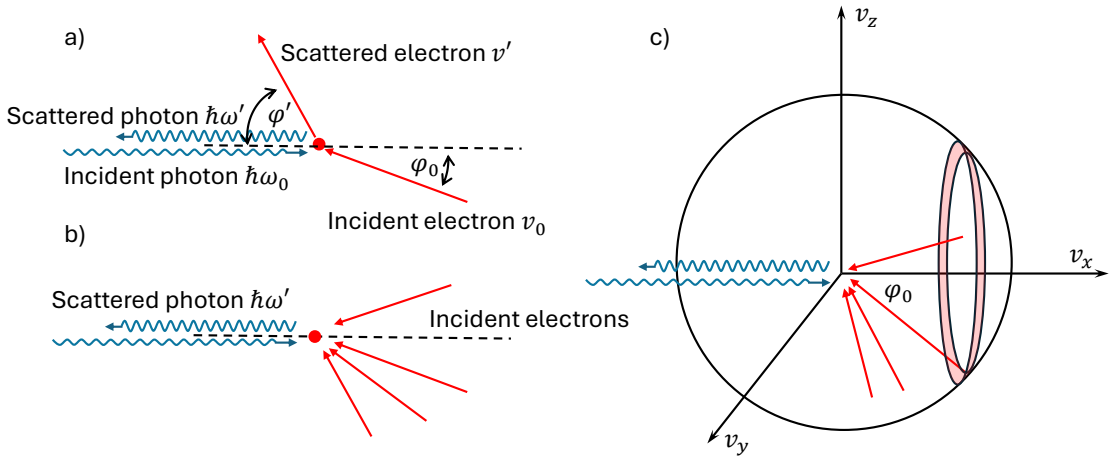


Figure 4.21: Angular geometry of ICS. (a) Single scattering event showing the incident photon ($\hbar\omega_0$), incident electron (v_0), scattered photon ($\hbar\omega'$), and scattered electron (v'). The angles φ_0 and φ' are measured relative to the incident photon direction. (b) Multiple electron trajectories can produce scattered photons of the same energy, illustrating the many-to-one nature of the interaction. (c) Velocity space representation showing the geometric constraints on electron velocities.

means that multiple combinations of electron speed v and angle θ can produce scattered photons of the same energy $\hbar\omega'$. By inverting these equations, one can determine the relationship between electron velocity and incident angle required to produce a scattered photon of a specific energy:

$$v = v[\hbar\omega', \varphi_0] \ , \tag{4.36}$$

This relationship enables the calculation of the scattered photon spectrum through integration over the electron distribution function:

$$f_{\mathrm{ICS}}[\hbar\omega']\mathrm{d}\hbar\omega' \propto \int 2\pi v^2 \varrho[v]\mathrm{Sin}\left[\varphi_0\right]\mathrm{d}v\mathrm{d}\varphi_0 \ , \tag{4.37}$$

where $\varrho[v]$ represents the electron velocity distribution function, and the factor $2\pi v^2\mathrm{Sin}\left[\varphi_0\right]$ accounts for the volume element in spherical coordinates. The complete ICS spectrum

can be determined by incorporating the scattering cross-section and experimental geometry parameters:

$$f_{\mathrm{ICS}}[\hbar\omega'] = \frac{\mathrm{d}S}{\mathrm{d}\Omega} \times \Delta\Omega \times \int 2\pi v^2 \varrho[v] \mathrm{Sin}\left[\varphi_0\right] \frac{\partial v}{\partial \hbar\omega'} \mathrm{d}\varphi_0 \times \#[\text{incident photons}] \ , \tag{4.38}$$

where $\Delta\Omega$ is the solid angle occupied by the detector. Because the energy of the electrons is still only a fraction of the electron's rest mass, as a first-order approximation, the cross-section can adopt the Klein-Nishina formula.

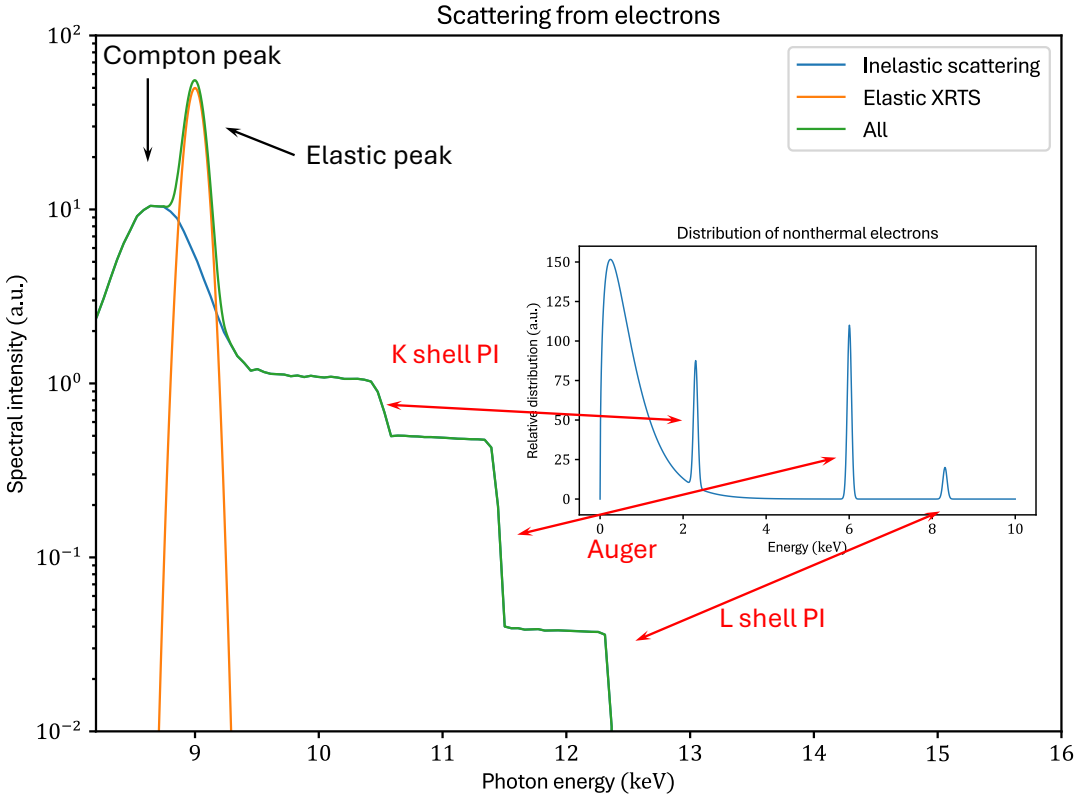


Figure 4.22: Calculated X-ray scattering spectrum showing combined ICS and XRTS features. The total spectrum (green) includes inelastic scattering (blue) and elastic XRTS (orange, schematic, not to scale). The spectrum shows the ICS plateaus corresponding to the non-thermal electrons shown in the inset.

Figure 4.22 demonstrates the ICS spectra computed from a non-thermal electron distribution featuring distinct peaks at 2.3, 5, and 8 keV, corresponding to K-shell photo-ionisation, Auger electrons, and L-shell photo-ionisation, respectively. The incident photon energy is assumed to be 9 keV. The spectrum exhibits several characteristic features: a Compton scattering peak at approximately 8800 eV from thermal electrons, an elastic XRTS peak from bound electrons at the incident photon energy of 9000 eV, and a series of plateaus

at higher energies resulting from ICS interactions with the non-thermal electron population. These plateaus directly correspond to the electron energy distribution shown in the inset, with each step in the spectrum mapping to a peak in the electron distribution.

The spectral features of ICS can be understood by considering that the photon recoil is predominantly determined by the longitudinal velocity $v_x = v\mathrm{Cos}\,[\varphi_0]$, with the transverse velocity playing a minor role. The number of photons scattered at a specific energy is therefore directly proportional to the number of electrons with the same longitudinal velocity v_x that satisfy the "head-on" collision conditions in Eq. 4.34. Under this approximation, Eq. 4.37 can be simplified to:

$$f_{\mathrm{ICS}}[\hbar\omega']\mathrm{d}\hbar\omega' \propto f_{v_x}[v_x]\mathrm{d}v_x \ , \tag{4.39}$$

where $f_{v_x}[v_x]$ is the distribution function with respect to v_x, equivalent to projecting the distribution function in the velocity space to the v_x axis (Fig. 4.23):

$$\begin{aligned} f_{v_x}[v_x] &= \int_{v_x}^{\infty} \varrho[v] 2\pi\sqrt{v^2 - v_x^2}\frac{\mathrm{d}v}{\mathrm{Sin}[\varphi_0]} \\ &= \int_0^{\frac{\pi}{2}} \varrho\left[\frac{v_x}{\mathrm{Cos}[\varphi_0]}\right] 2\pi \left(\frac{v_x}{\mathrm{Cos}[\varphi_0]}\right)^2 \mathrm{Tan}[\varphi_0]\mathrm{d}\varphi_0 \ . \end{aligned} \tag{4.40}$$

The equivalence can be seen by

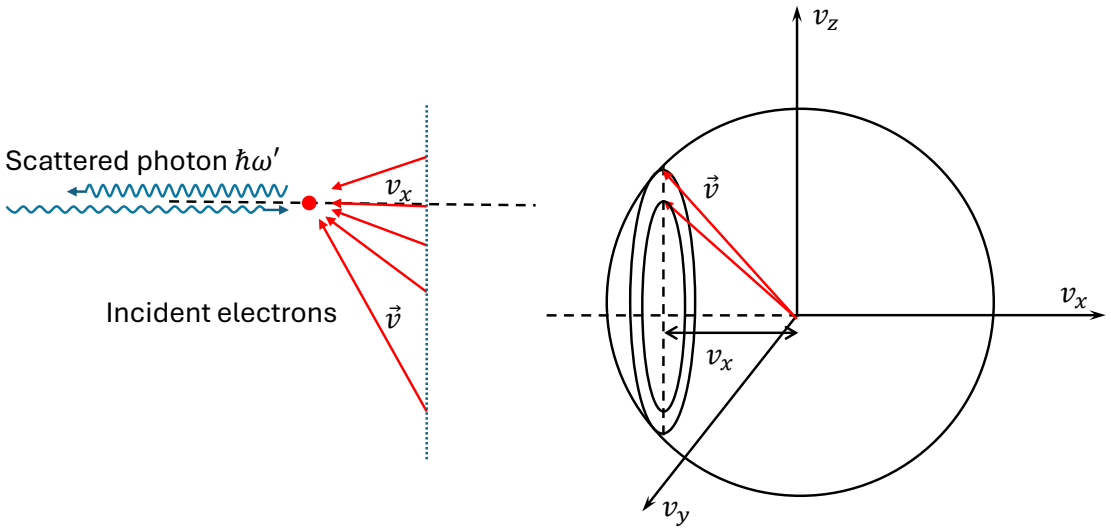


Figure 4.23: Transforming velocity space distribution to distribution with respect to v_x

$$\begin{aligned} f_{\mathrm{ICS}}[\hbar\omega']\mathrm{d}\hbar\omega' \propto f_{v_x}[v_x]\mathrm{d}v_x &= \int_0^{\frac{\pi}{2}} \varrho\left[\frac{v_x}{\mathrm{Cos}[\varphi_0]}\right] 2\pi \left(\frac{v_x}{\mathrm{Cos}[\varphi_0]}\right)^2 \mathrm{Tan}[\varphi_0]\mathrm{d}\varphi_0\mathrm{d}v_x \\ &= \int_0^{\frac{\pi}{2}} \varrho\,[v]\, 2\pi v^2 \mathrm{Sin}\,[\varphi_0]\,\frac{\mathrm{d}v_x}{\mathrm{Cos}\,[\varphi_0]}\mathrm{d}\varphi_0 \\ &= \int_0^{\frac{\pi}{2}} \varrho\,[v]\, 2\pi v^2 \mathrm{Sin}\,[\varphi_0]\,\mathrm{d}v\mathrm{d}\varphi_0 \ . \end{aligned} \tag{4.41}$$

For isotropic non-thermal electrons with a single energy $W_\mathrm{e} = \frac{1}{2} m_\mathbf{e} v_0^2$, the distribution function can be represented as a delta function $\varrho[v] \sim \frac{1}{4\pi v^2}\delta[v - v_0]$, corresponding to a spherical-shell in velocity space. Its projection onto the v_x axis yields a uniform distribution for $v_x < v_0$:

$$\begin{aligned} f_{v_x}[v_x] &= \int_0^{\frac{\pi}{2}} \varrho\left[\frac{v_x}{\mathrm{Cos}[\varphi_0]}\right] 2\pi \left(\frac{v_x}{\mathrm{Cos}[\varphi_0]}\right)^2 \mathrm{Tan}[\varphi_0]\mathrm{d}\varphi_0 \\ &= \int_0^{\frac{\pi}{2}} \frac{1}{4\pi v^2}\delta\left[\frac{v_x}{\mathrm{Cos}[\varphi_0]} - v_0\right] 2\pi v^2 \frac{\mathrm{Sin}\,[\varphi_0]}{\mathrm{Cos}\,[\varphi_0]}\mathrm{d}\varphi_0 \\ &= \frac{1}{2}\int_0^{\frac{\pi}{2}} \delta\left[v_x - v_0\,\mathrm{Cos}[\varphi_0]\right]\mathrm{dCos}\,[\varphi_0] = \frac{1}{2v_0}\ , \end{aligned} \tag{4.42}$$

with $f_{v_x} = 0$ for $v_x > v_0$.

Due to the quadratic relation between the electron energy and the photon energy gain as shown in Fig. 4.20, $\Delta\hbar\omega$ is also approximately proportional to v_x. Consequently, $\frac{\partial v_x}{\partial \hbar\omega'}$ can be treated as approximately constant with respect to $\hbar\omega'$. The resulting ICS spectrum for monoenergetic electrons with an isotropic velocity distribution takes the form:

$$f_\mathrm{ICS}[\hbar\omega'] \propto f_{v_x}[v_x]\frac{\mathrm{d}v_x}{\mathrm{d}\hbar\omega'} \propto \begin{cases} \text{constant} & \forall v < v_0 \\ 0 & \forall v > v_0 \end{cases}\ . \tag{4.43}$$

This explains the characteristic plateau structure observed in the ICS spectrum of non-thermal electron populations.

With the relative heights of these plateaus reflecting both the electron population at each energy and the ICS cross-section, ICS can be a potentially powerful diagnostic tool for measuring non-thermal electron distributions in plasmas. The intensity of each plateau provides direct information about the electron density at specific energies, while the sharp transitions between plateaus mark the maximum electron energies within each non-thermal peak.

While the discussion of ICS has primarily assumed the use of SPC detectors, the technique could, in principle, be implemented using crystal spectrometers if sufficient signal levels can be achieved.

The results presented here represent the first step toward developing ICS as a practical diagnostic technique. Future work should focus on experimental validation, refinement of the theoretical framework, and development of robust analysis methods for extracting electron distribution information from measured spectra. Additionally, the potential for time-resolved measurements of electron thermalisation processes could be explored, offering new insights into plasma dynamics.

4.3.3 Optimal SPC Detection Configuration

To effectively distinguish between RR and ICS signals from non-thermal electrons, a dual-detector configuration provides optimal detection capability. As illustrated in Fig. 4.24, this configuration employs two SPC detectors in dedicated positions:

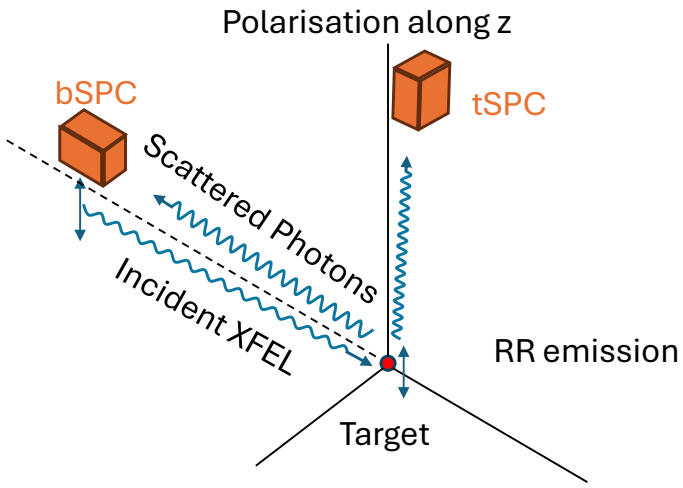


Figure 4.24: Optimal dual-detector configuration for distinguishing RR and ICS signals. The top SPC (tSPC) detector is aligned with the XFEL polarisation direction (z-axis) to minimise scattered photon detection, while the back SPC (bSPC) detector is positioned at π radian scattering angle to maximise both RR and ICS signal collection.

1. **A top SPC (tSPC) detector** aligned with the XFEL polarisation direction primarily detects RR emission while minimising elastic scattering and ICS contributions. This alignment exploits the dipole radiation pattern of Thomson scattering, where scattered intensity approaches zero along the polarisation axis.

2. **A back SPC (bSPC) detector** positioned at a π radian scattering angle in the equatorial plane captures both RR and ICS signals. This position maximises both the energy gain of scattered photons and the overall signal level for ICS events.

Since RR emission is isotropic, while ICS has a distinct angular distribution, comparing signals between the two detectors enables isolation of the pure ICS contribution. For optimal comparison, both detectors should ideally be positioned at equal distances from the target and utilise identical filtering arrangements. The setup helps to detect the emission of non-thermal electrons, as well as measure their distribution.

4.4 Summary

This chapter has presented a comprehensive analysis of detection and analysis techniques for studying non-thermal electron distribution in XFEL-driven plasmas. The work

explores several complementary approaches that together provide a framework for non-thermal experiments.

Single-photon counting (SPC) detection serves as the foundation of the measurement, offering a chance to detect extremely weak signals that are usually difficult for energy-dispersive spectrometers. The challenge of multi-photon detections in SPC data has been addressed through the development of the clustering algorithm and the deconvolution algorithm, allowing photon counting both in the high and low photon density regimes. The SPC algorithms have been benchmarked and tested through synthetic data generated by Monte Carlo simulation and have proven their effectiveness, though the relatively low resolution has restricted their application to detecting lower energy signals.

Two distinct physical processes - radiative recombination (RR) and inverse Compton scattering (ICS) - have been identified as key diagnostic tools for non-thermal electron characterisation. RR spectra serve as the main signal that can potentially reveal the collision time of electrons, while ICS produces distinctive plateau structures that reflect the electron energy distribution. The combination of these complementary processes, measured using an optimised dual-detector configuration, offers new insight into non-thermal electron dynamics.

The framework established in this chapter provides a foundation for future investigations of electron thermalisation processes and energy transport in warm dense matter. Further refinement of these techniques, particularly through experimental validation and improved cross-section calculations of ICS, will enhance the ability to study these fundamental plasma processes.

All models are wrong, but some are useful.

— George Box

5

Measuring the collision time at the LCLS XFEL Facility

Contents

5.1 Introduction 102
5.2 Design of the Experiment 103
5.2.1 Ultra-short Pulsed X-rays 105
5.2.2 SPC Detectors 110
5.3 Experimental Results 112
5.3.1 SPC Signal Processing 112
5.3.2 Non-thermal Electron Emissions 113
5.3.3 Pulse-Duration-Grouped Spectra 115
5.4 Inferred Collision Time 120
5.4.1 Simulation Set-up 121
5.4.2 Simulation Results 125
5.4.3 Collision Times 129
5.4.4 Discussions 134
5.5 Summary 136

5.1 Introduction

The study of electron relaxation dynamics in warm dense matter was extensively discussed in Chapter 3, where simulations based on Al plasmas pumped by soft X-rays revealed insights into the thermalisation of electrons. The simulated results demonstrated the potential to infer collision times by observing the thermalisation process through emission spectra. Following the simulation work, Chapter 4 introduced the experimental techniques required to measure non-thermal electron distributions in XFEL-driven plasmas by using the SPC technique assisted by the clustering and deconvolution algorithms. These form the foundation of a dedicated experiment to measure the electron collision time in WMD systems.

Building on these analyses, this chapter presents the first direct experimental measurement of electron collision times in WDM. This experiment, conducted at LCLS, targeted manganese (Mn) plasmas pumped by hard X-rays to generate and diagnose non-thermal electron distributions. The choice of Mn as the target material, driven by hard X-rays (at 9.5 keV), as opposed to Al driven by soft X-rays at around 2 keV discussed in chapter 3, was motivated by the need to create more energetic non-thermal electrons with longer thermalisation timescales, allowing the use of conventional XFEL pulses with durations ranging from a few femtoseconds to tens of femtoseconds. This stands in contrast to the sub-femtosecond pulses required for Al, which pose significant experimental challenges. Additionally, Mn's distinct K_α emission at 5.9 keV facilitates precise spectroscopic analysis of non-thermal electron features, making it an ideal target for this investigation.

This chapter details the design of the experiment, its results, and the inferred collision times. By combining the measured results obtained from this experiment with Fokker-Planck simulations similar to those discussed in Chapter 3, the work presented here bridges the gap between electron relaxation theories and experimental validation. Importantly, this measurement provides direct insight into both e-e and e-i collision times simultaneously, providing a comprehensive picture of electron collisionality in strongly coupled systems. The results are compared with previous measurements, including those reported in [109, 110, 164, 165]. Notably, the direct outcome of this experiment itself can be expressed in time constants with clear physical interpretations. This contrasts with previous experiments, which often rely on transport coefficients (for example, conductivity or opacity) and thus depend more heavily on theoretical models. This experimental framework can be easily extended to a broader range of electron density and temperature conditions, offering an unprecedented opportunity to advance the understanding of electron relaxation dynamics in WDM significantly.

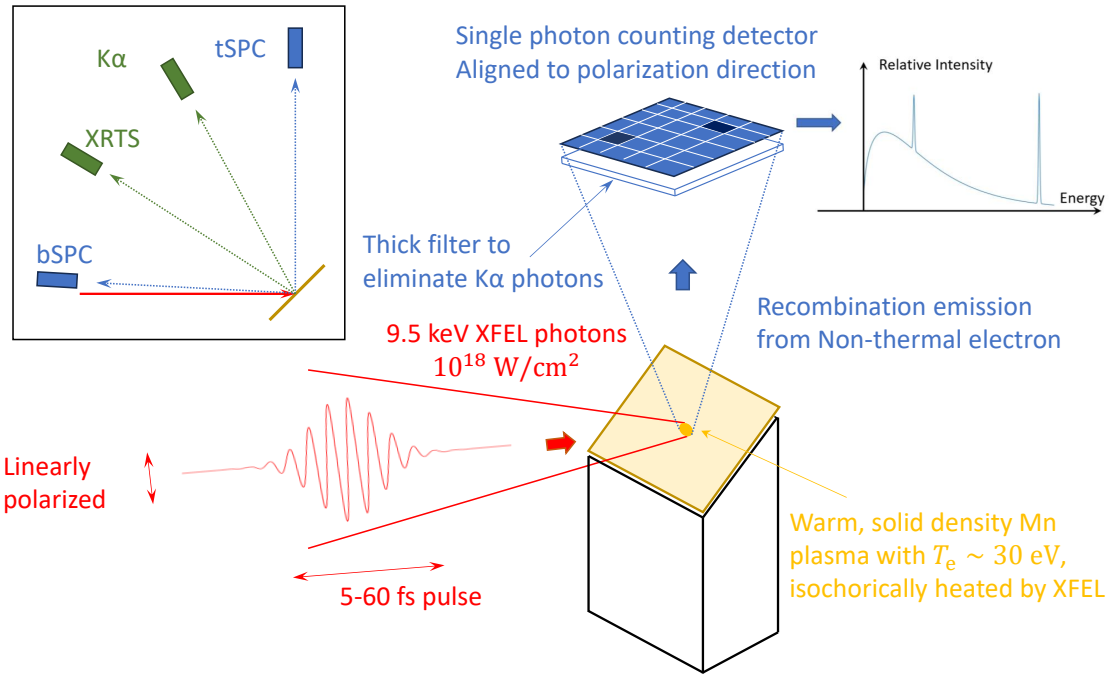


Figure 5.1: Schematic of the experimental set-up. The plasma is created by irradiating a solid-density Mn target with XFEL pulses at 9.5 keV. Four detectors are used: the SPC detectors (tSPC and bSPC) capture non-thermal recombination radiation, while the auxiliary K_α and XRTS detectors monitor thermal emission and plasma conditions. Filters are applied to the SPC detectors to suppress thermal RR and K_α photons. Detector positioning and filtering are optimised for isolating non-thermal features, as discussed in Sec. 4.3.3.

5.2 Design of the Experiment

The overall design of the experiment is depicted in Figure 5.1. The set-up consists of four detectors, with the two detectors shown in green (the K_α detector and the XRTS detector) serving as auxiliary diagnostics, while the two blue detectors (tSPC and bSPC) are the primary SPC detectors used to capture the weak emission signals from non-thermal electrons. The detectors are positioned as discussed in Sec. 4.3.3, with the tSPC detector aligned along the polarisation direction of the incident XFEL to suppress elastic scattering contributions and the back SPC detector (bSPC) positioned at a backscattering angle to collect complementary signals, primarily from ICS.

In this set-up, the plasma is created by irradiating a solid-density Mn target with linearly polarised XFEL pulses at 9.5 keV, with pulse durations ranging from 5 to 60 fs. The XFEL pulses ionise Mn atoms, producing a population of non-thermal electrons alongside the creation of a warm dense plasma. The recombination emission from these non-thermal electrons is captured by the SPC detectors, with the tSPC designed to capture RR from non-thermal electrons, while the bSPC is positioned at a backscattering angle and can capture both RR and ICS signals. Both detectors are equipped with a filter to suppress the intense

thermal RR and K_α emission signal at lower energy, which could interfere with the weaker non-thermal emissions. Because the ICS signal requires subtraction from the RR signal for accurate analysis, both detectors are positioned at the same distance from the plasma and use identical filtering, as discussed in Sec. 4.3.3.

The auxiliary detectors play supporting roles in characterising the plasma. The K_α detector monitors the characteristic Mn K_α emission at 5.9 keV. The XRTS detector was set up to measure the electron density and temperature of the plasma, providing additional contextual information about the plasma conditions, though it was later seen to be not very useful due to its limited energy resolution and the relative low temperature of the system. Together, the combination of primary and auxiliary detectors enables a comprehensive analysis of the plasma and non-thermal electron dynamics.

The choice of Mn as the target material is motivated by its ability to optimise the detection of non-thermal emission features. This arises fundamentally from the need to separate emission peaks sufficiently, given the relatively poor spectral resolution of SPC detectors (O[100 eV]), as well as the additional broadening of peaks due to thermalisation effects. For mid-Z metals irradiated by hard X-rays with photon energy $\hbar\omega_0 \sim 10$ keV, the two primary sources of non-thermal electrons arise from KLL Auger and L-shell PI. When recombining to the K-shell, these processes result in photons with energies of approximately $2 \times W_{K_\alpha}$ and $\hbar\omega_0 + W_{K_\alpha}$, respectively (see Sec. 4.3.1). Using the notation introduced in Sec. 4.3.1, these will be denoted as KLL-Auger $\rightarrow$ K-RR and L-PI $\rightarrow$ K-RR in this chapter, respectively. Ideally, higher K_α energy would further separate these peaks from the elastic scattering signal at $\hbar\omega_0$. However, the SPC spectroscopy would also register a peak at $2 \times \hbar\omega_0$ due to the possibility of double photon detection events of the elastically scattered photons, as discussed in Sec. 4.2.3. For this reason, it is essential that the two non-thermal peaks fall within the range of $1 - 2\ \hbar\omega_0$ to avoid overlap with other signals and ensure their distinguishability.

The energy levels of Mn, whose K_α energy is approximately 5.9 keV, are particularly advantageous for use with the LCLS XFEL, which performs optimally at photon energies around 9.5 keV. The elastic scattering signal ($\sim$9.5 keV), the KLL-Auger $\rightarrow$ K-RR ($2 \times W_{K_\alpha} \approx$ 11.8 keV), the L-PI $\rightarrow$ K-RR emission ($W_{K_\alpha} + \hbar\omega_0 \approx 15.4$ keV), and the double-photon detection peak ($\sim$19 keV) are all approximately evenly spaced in the spectrum (Fig. 5.2). This spacing facilitates the clear distinction of these signals, reducing the complication of spectral analysis of non-thermal processes.

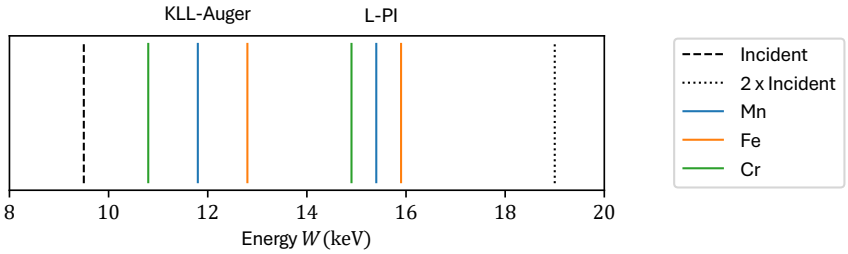


Figure 5.2: Energy levels of key signals for Mn (blue), Fe (orange), and Cr (green) targets. The dashed line marks the XFEL incident energy (9.5 keV), and the dotted line marks twice the incident energy (19 keV). Mn provides evenly spaced signals, aiding in distinguishing non-thermal radiation from elastic scattering and SPC artefacts. Note that the detector resolution decreases at higher energies, requiring greater spacing between signals. Therefore, Fe is less suitable than Mn.

5.2.1 Ultra-short Pulsed X-rays

The success of this experiment relies on the generation of ultra-short X-ray pulses, which have been inherently challenging due to the slippage between the electron beam and the emitted radiation. This slippage occurs because the electrons travel slightly slower than the X-ray radiation as they pass through the undulator. As a result, uncorrelated parts of the electron beam contribute to the lasing process individually, leading to multiple spikes in the emitted radiation that are separated by several femtoseconds. This makes it difficult to achieve a single, coherent, ultra-short pulse.

The XFEL community has seen significant advancements in the generation of ultra-short pulses over the past decade. Till now, three main techniques have been developed and commissioned on operating XFEL facilities, namely selective spoiling, low-charge operation (or normal charge compression), and Enhanced SASE (ESASE).

Selective Spoiling [166, 167] involves degrading the quality of most of the electron beam while preserving a small, high-quality slice (Fig. 5.3). This is typically achieved by passing the beam through a dispersive region and inserting a slotted foil that increases transverse emittance for most of the beam [168]. Only the unspoiled slice contributes to lasing, resulting in short X-ray pulses limited to one or a few spikes, effectively reducing the pulse duration to a few femtoseconds or sub-femtoseconds. Alternatively, selective spoiling can also be achieved using a temporally shaped laser or other advanced approaches that strategically manipulate the beam's phase space. While the slotted foil approach is limited in repetition rate due to mechanical constraints, laser-based spoiling methods are compatible with high repetition rate operation. The primary advantage of this technique lies in its relatively straightforward implementation at existing facilities. However, its main limitation is reduced efficiency, as the majority of electrons are effectively "wasted" in the spoiling process, leading to lower

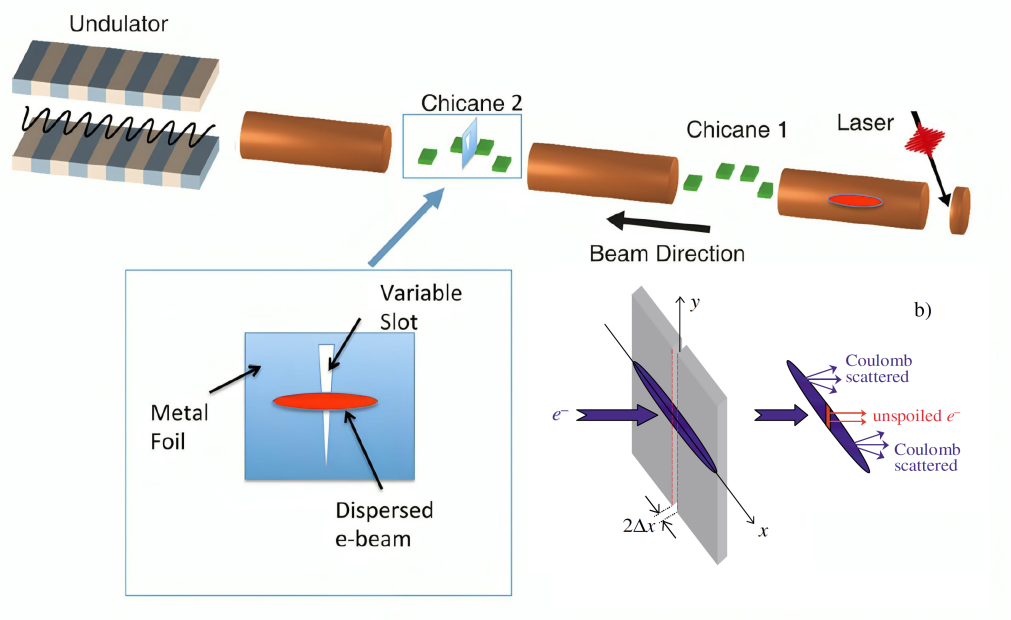


Figure 5.3: Sketch of the selective spoiling method for generating ultrashort X-ray pulses through a slotted foil. The electron beam passes through a chicane with a metal foil containing a narrow slot placed in a dispersive section. Due to the energy-dependent path length in the chicane, different temporal portions of the beam pass through different horizontal positions at the foil. Electrons passing through the slot remain unscattered and maintain their emittance (unspoiled), while those hitting the metal foil undergo Coulomb scattering, leading to emittance growth (spoiled). Only the unspoiled electrons will effectively contribute to the FEL process in the downstream undulator, resulting in an ultrashort X-ray pulse. Figures adapted from [168] and [167].

pulse energies. Despite this drawback, the method has been widely adopted at many XFEL facilities due to its reliability and relatively simple set-up.

The low-charge operation uses a photoinjector to generate electron bunches with very low charge [169], followed by strong magnetic compression. This reduces the bunch duration to a few femtoseconds or less. Alternatively, bunch compression can also be achieved with higher charge beams by applying advanced magnetic or RF compression techniques to shorten the bunch length [170]. In both cases, the shorter bunch length naturally reduces the lasing window in the undulator, producing shorter X-ray pulses with fewer lasing regions. The key advantage of this approach is its exceptional stability in operation, making it particularly suitable for experiments requiring high reproducibility. The primary drawback, however, is the inherently lower pulse energy due to the reduced number of electrons participating in the FEL process, though this trade-off is often acceptable for specific experimental requirements.

Enhanced SASE (ESASE) [171] works by using an external laser to modulate the electron beam at optical wavelengths before compression [172, 173]. This creates regions of extremely high peak current within the beam. These high-current spikes lase more efficiently in the FEL, leading to the generation of short X-ray pulses. The process is controlled by tuning

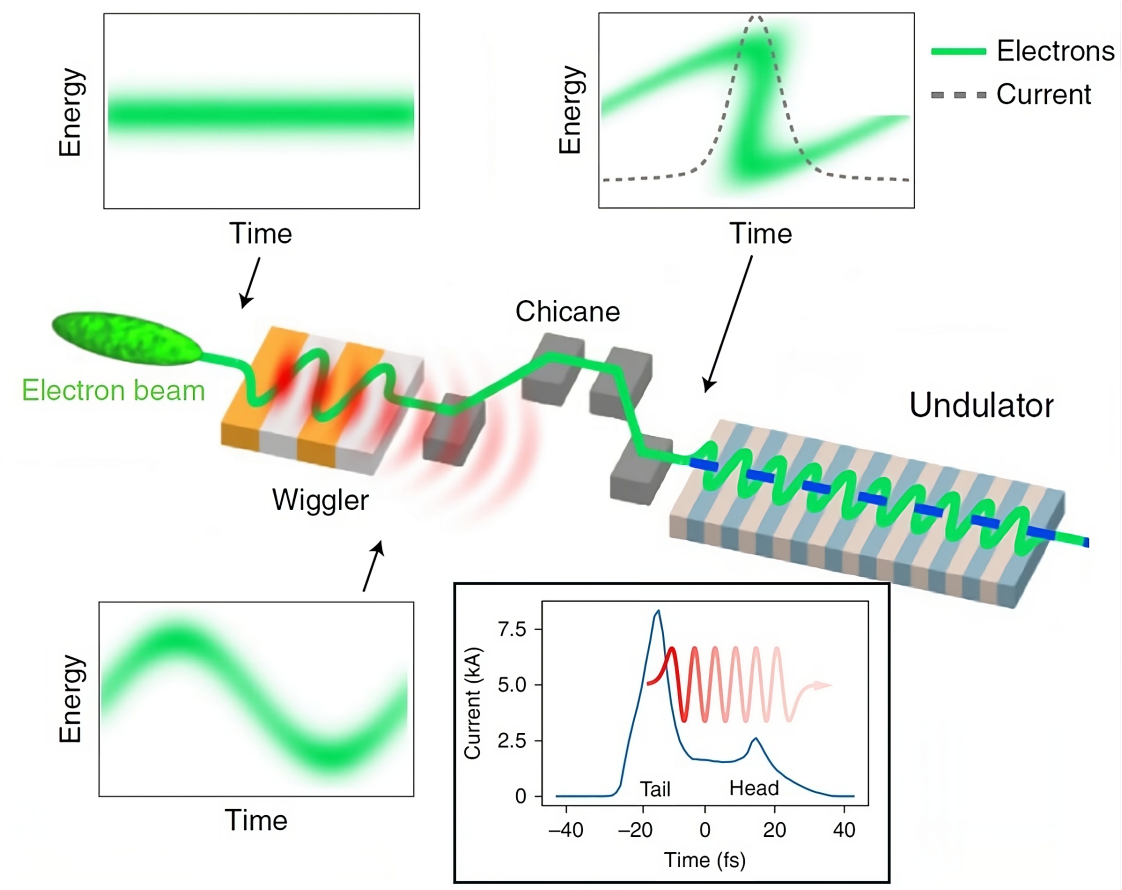


Figure 5.4: Illustration of the XLEAP technique for generating ultrashort X-ray pulses. The initially flat electron beam (top left) interacts with a laser-modulator wiggler, creating an energy modulation (bottom left). This energy modulation is converted into density modulation through a chicane, resulting in regions of high peak current (top right). The high-current spike enables faster FEL gain in the undulator, reducing the effective slippage length. The bottom right plot shows the resulting temporal profile with a sharp current spike that produces an ultrashort X-ray pulse. The blue curve shows the electron beam current profile, while the red oscillations represent the generated X-ray power. Figure adapted from [175].

the laser wavelength and compression strength and has been developed further into XLEAP (X-ray laser-enhanced attosecond pulse generation) [174, 175] as a standard operation mode available at LCLS [121] (Fig. 5.4). This method offers the significant advantage of providing clean, controllable pulse generation with maintained pulse energy. The main challenge lies in the requirement for precise laser timing and synchronisation, though recent developments have largely addressed these issues.

Several additional methods show promise for ultrashort pulse generation, though they have not yet been fully commissioned at operational XFELs. Echo-Enabled Harmonic Generation (EEHG) [176–178] employs sophisticated electron beam manipulation using two laser modulators and multiple dispersive sections to create precise density modulations at high harmonics of the laser frequency. While primarily developed for seeding applications,

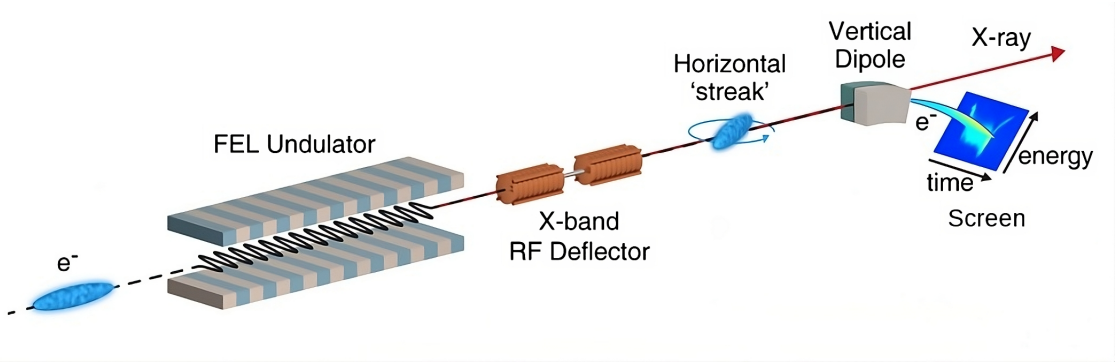


Figure 5.5: Schematic layout of the XTCAV diagnostic system at an XFEL. An electron bunch enters the FEL undulator, where X-ray radiation is generated. Downstream, the X-band RF deflector provides horizontal streaking of the electron bunch, followed by a vertical dipole magnet for energy dispersion. The combined horizontal (time) and vertical (energy) information is captured on a screen, enabling single-shot measurement of the longitudinal phase space of the electron beam and reconstruction of the X-ray pulse temporal profile. Figure taken from [182].

theoretical studies suggest its potential for generating ultrashort pulses through careful optimisation of the beam phase space. Chirped Pulse Amplification (CPA) [179, 180], borrowing concepts from optical laser technology, works directly with the X-ray field rather than the electron beam. The approach involves stretching, amplifying, and then recompressing the X-ray pulse using specialised X-ray optics. While both techniques show theoretical promise for generating ultrashort pulses with high stability and controllability, they face significant technical challenges in implementation, particularly in the development of suitable X-ray optics for CPA and the precise control requirements for EEHG.

Alongside the generation of ultra-short X-ray pulses, the success of this experiment is also critically dependent on the accurate measurement of the X-ray pulse duration. Without reliable, real-time, shot-to-shot pulse duration diagnostics, the proposed pulse duration scan to reveal the critical ultra-fast electron relaxation process would not be as meaningful. Unlike the generation of ultrashort pulses, where multiple techniques are available, the direct measurement of X-ray pulse duration has very limited options for implementation, especially in a user-accessible environment.

The X-band Transverse Deflecting Cavity (XTCAV) is currently the most established and widely used method for measuring X-ray pulse duration [181, 182]. It operates by applying a time-dependent transverse kick to the electron beam using an X-band (11.424 GHz) RF deflecting structure. This kick maps the temporal profile of the electron beam onto its spatial distribution, which can then be recorded downstream (Fig. 5.5). When combined with an energy spectrometer, XTCAV can provide a full longitudinal phase space measurement of the electron beam.

XTCAV reconstructs the X-ray temporal profile by comparing the electron beam longitudinal phase space in two conditions: "lasing-off," where the FEL process is suppressed to provide baseline measurements of the electron beam's natural energy spread and distribution, and "lasing-on," where normal FEL operation reveals FEL-induced effects such as energy loss and increased energy spread. By performing a time-slice analysis, the energy loss and energy spread changes for each time slice are calculated, and the X-ray power profile is reconstructed using either the energy loss method or the energy spread method. XTCAV offers a temporal resolution of 1 fs for soft X-rays and 4 fs for hard X-rays, with single-shot capability, non-invasive operation, and a wide dynamic range.

Two other advanced methods for temporal characterisation have been recently proposed. The spectral-temporal combined method [183] integrates temporal measurements such as XTCAV with high-resolution spectral measurements through an iterative reconstruction algorithm. While it offers enhanced resolution and can resolve individual SASE spikes, it is highly dependent on the spectrometer's resolution and the complexity of the pulse. AI-enhanced angular streaking [184] leverages convolutional neural networks to analyse angular streaking data obtained from an angular-resolved electron spectrometer and a circularly polarised infrared streaking laser. It can reconstruct the complete temporal structure of the X-ray pulse, including individual SASE spikes, with real-time processing capabilities. However, these methods remain in the experimental stage and have not been made available for routine user operations.

As XTCAV is the only fully commissioned and user-accessible tool for X-ray pulse duration measurement, the choice of pulse duration generation for this experiment must accommodate its resolution. Since the resolution of XTCAV is limited to 4 fs RMS for hard X-rays, generating pulses shorter than this duration would not provide meaningful additional benefits, as their temporal characteristics could not be reliably measured or confirmed. In this experiment, the combination of the slotted foil method and low-charge operation has been selected due to its maturity and relative ease of implementation compared to more pioneering techniques at the few-fs-pulse regime. This approach also provides a well-balanced compromise between pulse energy and pulse duration, making it highly suitable for the experimental requirements as it is capable of producing X-ray pulses with an energy of approximately 300 μJ within a 5 fs duration, along with a single spike occurrence rate of 65%. By comparison, non-linear bunch compression can achieve pulse durations as short as 200 as, but at the cost of significantly lower pulse energy (around 10 μJ) and a reduced single spike rate (45%) [121]. The single spike rate is particularly important as the analysis of the electron relaxation dynamics can be greatly simplified if the X-ray pulse itself exhibits a simple temporal profile. Therefore, the slotted foil and low-charge operation approach offers a practical and reliable solution for achieving the desired experimental conditions. Importantly,

to make the data comparable, x-ray shots with longer durations are attenuated such that the energy transfers to the target remains the same across various pulse durations.

It is worth noting that this experiment was performed in 2022, with access limited to the technological developments available at that time. More recent advancements in ultrashort pulse generation may enable further optimisation of pulse energy, duration, and single spike rates in the future. Recently, a self-chirping technique [185] has demonstrated attosecond pulses with unprecedented pulse energies by manipulating the electron beam's longitudinal phase space, representing a breakthrough in ultra-fast X-ray generation. As these technologies become more widely available and operationally mature, they could open new possibilities for enhancing the performance of similar experiments.

5.2.2 SPC Detectors

A wide variety of well-developed pixel detectors are available for X-ray detection, each offering specific features tailored to particular experimental requirements [186]. For the purpose of this experiment, it is essential to consider the suitability of the detector for SPC diagnostics. Due to the charge spread effect (Sec. 4.2.2) inherent in such detectors, the use of larger pixel sizes is preferred to ensure accurate signal reconstruction.

In this experiment, the ePix100a detector was employed, with a pixel size of 50 μm and spatial resolution of $704 \times 768 \approx 0.5 \times 10^6$ pixels. For comparison, detectors from the Princeton Instruments PIXIS family, which feature a smaller pixel size of 20 μm [155], exhibit considerable charge spread, making it challenging for clustering algorithms to function effectively. The ePix100a was selected for its proven reliability in past experiments and its ability to meet the specific requirements of SPC. While the ePix100a was chosen for this study, alternative detectors such as the Jungfrau or ePix10k [186] could also be considered for similar experiments, depending on the experimental conditions and desired resolution.

Applying a suitable filter in front of the detector is crucial for isolating the desired photon signal from other sources of photons. This is particularly important in this experiment because, as discussed in Sec. 4.3.1, the energy of RR photons from non-thermal electrons closely matches the combined energy of two photons originating from other processes, leading to potential signal misinterpretation.

In this experiment, the two primary detection channels are KLL-Auger $\rightarrow$ K-RR and L-PI $\rightarrow$ K-RR electrons. For KLL-Auger $\rightarrow$ K-RR electrons, signal contamination arises due to the detection of double K_α photons, which have the same total energy. Similarly, for L-PI $\rightarrow$ K-RR electrons, the signal overlaps with the combined energy of K_α photons and elastically scattered X-rays. These challenges were addressed by applying significant

filtering in front of the detector, which effectively blocked unwanted photon contributions while preserving the desired signal.

The effectiveness of the filtering approach can be analysed using a simple model of X-ray transmission. Let $l_{\mathrm{attn}}[W]$ represent the attenuation length of X-rays with photon energy W. For a filter of thickness l, the transmission $\beta_{\mathrm{trans}}[W]$ of X-rays with energy W through the filter is given by:

$$\beta_{\mathrm{trans}}[W] = \mathrm{e}^{-l/l_{\mathrm{attn}}[W]}. \tag{5.1}$$

The attenuation length, $l_{\mathrm{attn}}[W]$, is typically very small for K_α photons but substantially larger for KLL-Auger $\rightarrow$ K-RR photons, with energies twice that of K_α photons. This difference enables the use of a filter with an appropriate thickness l, which can attenuate the vast majority of K_α photons while still allowing a decent portion of KLL-Auger $\rightarrow$ K-RR photons to pass through. Since the probability of double-photon detection scales quadratically with the probability of single-photon detection, the suppression of double Kα photon hits is even stronger, effectively eliminating this background signal. A similar argument holds for the other channel, L-PI $\rightarrow$ K-RR photons, where the K_α photons and elastically scattered photons are suppressed, while the RR signal remains largely unaffected.

In this experiment, an Al filter was used for attenuation. The attenuation length, l_{attn}, is 32 μm for Mn K_α photons (5.9 keV) but increases significantly to 244 μm for photons with twice the K_α energy (11.8 keV). Based on this, a filter with a thickness of several hundred μm can be anticipated to sufficiently suppress K_α photons while allowing a significant fraction of photons from KLL-Auger $\rightarrow$ K-RR to pass through.

The exact number of photons from both sources cannot be precisely determined prior to the experiment. Therefore, the optimal filter thickness is typically determined during the beamtime. Increasing the filter thickness causes the transmission β_{trans} of both Kα photons and KLL $\rightarrow$ K RR photons to decrease. However, due to the much shorter attenuation length of K_α photons, their suppression is significantly stronger. Combined with the quadratic scaling of double-photon hits with single-photon probabilities, increasing the filter thickness improves the signal-to-noise ratio (SNR) by effectively eliminating double-photon detections.

Nevertheless, a balance must be struck as excessive filter thickness also reduces the signal level of RR emissions from non-thermal electrons themselves. In this experiment, a filter thickness of 650 μm was used. While this thickness likely achieved strong suppression of K_α photons to achieve a high SNR level, it may not have been optimal due to limited beamtime, which restricted the ability to fine-tune the filter thickness.

5.3 Experimental Results

The LCLS's ability to generate ultrashort X-ray pulses, combined with XTCAV diagnostics for temporal characterisation, provides a solid foundation for the success of this experiment. The set-up of the four detectors offers rich information regarding the electron relaxation dynamics in the sample. However, due to the author's limited scope, this thesis will primarily focus on the tSPC results, with the other parts remaining as future work.

Data analysis centred on quantifying the photon counts in the desired energy channels, particularly those associated with K-shell RR. The results reveal a distinct correlation between the emission intensity and the XFEL pulse durations. This focused perspective, afforded by the top-SPC detector, provides valuable information regarding electron relaxation dynamics in warm, dense plasma.

5.3.1 SPC Signal Processing

The signal from the tSPC detector is processed in a manner similar to that described in Chapter 4, with no fundamental differences. The only distinction lies in the readout of the detector itself. As LCLS has improved its data acquisition workflow, the ePix detectors are now capable of reading photon energies in eV rather than ADUs. This improvement is achieved by pre-calibrating the detector, yielding an energy resolution of approximately 100 eV. Therefore, the clustering algorithm (Sec. 4.2.2) works directly with eV readouts and then constructs histograms using an appropriate bin width for the deconvolution algorithm (Sec. 4.2.3). The bin widths are chosen depending on the signal level, ensuring that the spectra are not overly spiky due to noise at low signal levels while still maintaining sufficient resolution.

Apart from the detector improvements, it is worth noting that the number of photons per shot is extremely small due to the use of the thick (650 μm Al) filter and the relatively low pulse energy ($\sim$300 μJ) for the shortest pulse duration ($\sim$ 4 fs). For comparison, normal SASE pulses with durations of $\sim$50 fs typically deliver $\sim$2 mJ of pulse energy.

These experimental conditions result in an average of approximately two photons detected per shot, or equivalently, photon density [1] $\beta_{\mathrm{ph}} \approx 0.004\%$. Despite the low photon count, the spatial resolution and sensitivity of the tSPC detector allow for clear identification of individual photon events. Figure 5.6 shows a typical image from the tSPC detector, in which three photons were detected in a single shot.

The sparse photon distribution simplifies the signal processing, as the probability of overlapping photon signals is negligible. However, the low photon density necessitates extended data acquisition times to accumulate statistically meaningful results. Over the

[1] See Eq. 4.4.

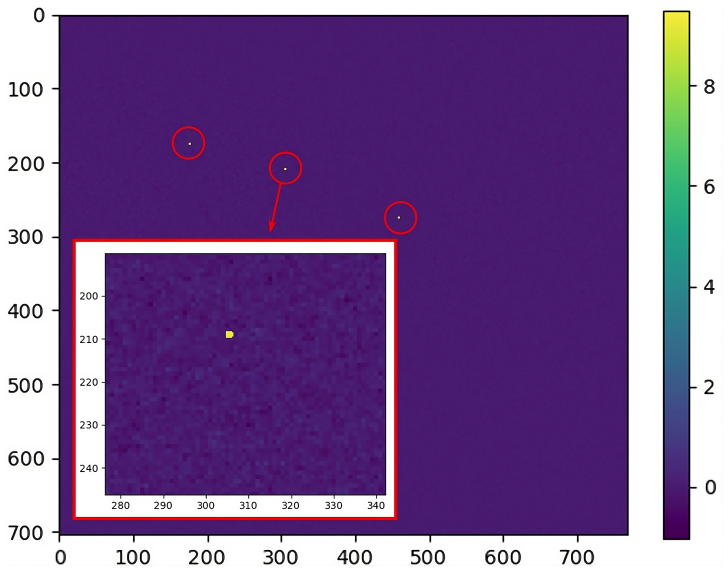


Figure 5.6: A typical image from the tSPC detector, showing three detected photon hits (highlighted with red circles). Each photon event is identified by its spatial position and intensity. The colour bar indicates the energy of the photon in eV. The inset shows a zoomed-in view of one photon hit. The pixels with photons are enlarged for visibility.

course of the experiment, more than one million shots were recorded, ensuring sufficient photon statistics for detailed data analysis.

5.3.2 Non-thermal Electron Emissions

Figure 5.7 shows the SPC spectrum obtained in the experiment by going through the procedure outlined in Chapter 4, integrated over all pulse durations, with a 100 eV bin width chosen to ensure sufficient but still meaningful resolution. On the leftmost side of the spectrum, one can observe the Mn K_α/K_β peaks near 6 keV, as well as the elastic scattering peak near 9.5 keV. The elastic peak may contain contributions from non-thermal electron emission processes, such as K-PI $\rightarrow$ K-RR or L-PI $\rightarrow$ L-RR, in addition to elastic XRTS. This residual XRTS arises due to the finite size of the detector, which cannot entirely eliminate contributions from scattered photons, even when aligned with the polarisation direction. The elastic peak is the strongest in the spectrum and dominates the signal.

Beyond the elastic peak, additional features are observed that provide insight into the non-thermal electron dynamics. The peak near 12 keV corresponds to the recombination of Auger electrons into the K-shell (KLL/KLM/KMM-Auger $\rightarrow$ K-RR), producing photons with energies of $2 \times W_{K_\alpha}, W_{K_\alpha} + W_{K_\beta}, 2 \times W_{K_\beta}$ respectively. Another prominent feature is the peak near 15 keV, which is attributed to L/M-shell photo-ionisation followed by K-shell recombination radiation (L/M-PI $\rightarrow$ K-RR), with energies of $\hbar\omega_0 + W_{K_\alpha}, \hbar\omega_0 + W_{K_\beta}$ respectively. Finally, a significant peak is observed at approximately 19 keV, corresponding

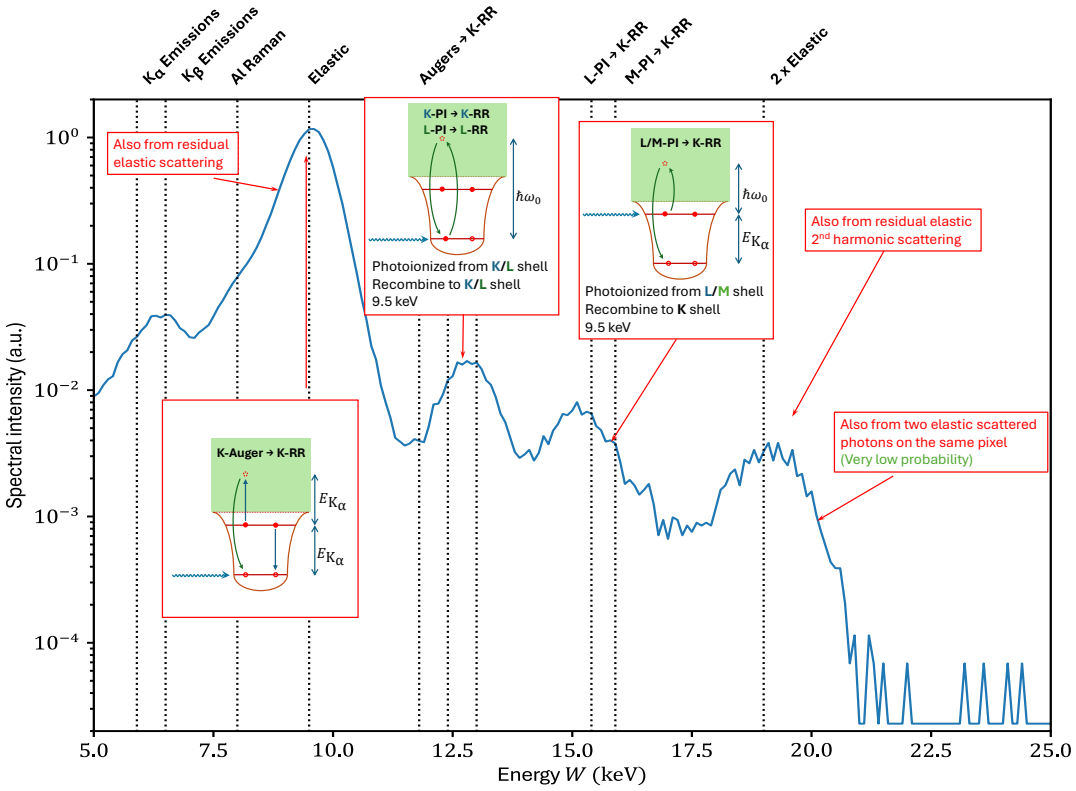


Figure 5.7: Spectrum obtained from the tSPC. The Mn K_α/K_β peaks (5.9 keV / 6.5 keV) and the elastic scattering peak (9.5 keV) are on the leftmost side of the spectrum. The 9.5 keV elastic peak comprises contributions from K/L-PI → K/L-RR and XRTS. Beyond the elastic peak, additional features include the Auger → K-RR, the L/M-PI → K-RR peak, and a peak at 19 keV corresponding to $2\times\hbar\omega_0$, which comes from the elastic XRTS from second harmonics. Insets illustrate the physical processes associated with the various peaks. The dotted lines are corresponding photon energies. Although the channels involve the L-shell-related processes, they were not shown in the insets for clarity.

to twice the incident photon energy ($2\times\hbar\omega$). This peak was not predicted by the initial energy analysis in Sec. 4.3.1. This is due to the FEL having a second harmonic, which was elastically scattered by the bound electrons. The composition of the second harmonic was measured to be about $\sim 0.01\%$ of the fundamental [187, 188] in previous experiments. Though not directly measured here, the result therein is consistent with this experiment after accounting for the difference in filter transmission at 9.5 keV and 19 keV.

Although the deconvolution algorithm has been applied, the possibility of detecting two photons forming one single cluster as a double-photon detection cannot be completely excluded. However, a statistical estimate shows that this scenario is highly unlikely. Assuming an average of two photons per shot, with the majority being elastic, the probability of two photons landing on the same pixel can be estimated as:

$$N_{2\ \mathrm{ph}} \sim \beta_{\mathrm{ph}}^2 \cdot N_{\mathrm{det}}, \tag{5.2}$$

where β_{ph} is the photon density (photons per pixel per shot), and N_{det} is the total number of detector pixels. Given the experimental conditions of $N_{\mathrm{det}} \approx 0.5 \times 10^6$, the expected signal level from this process is approximately 1×10^{-5}, which is several orders of magnitude lower than the observed intensity of the peak at 19 keV.

The other possible process responsible for producing this peak, the two-photon absorption process, where a single electron sequentially or simultaneously absorbs two XFEL photons, happens only at a very low probability at this XFEL intensity due to the extremely low cross-section [189, 190]. This strongly supports the interpretation of the 19 keV peak as arising from elastic XRTS from second harmonics rather than coincidental elastic scattering. On the other hand, the filter transmission (for 650 μm Al foil) at 19 keV is found to be about 50%, whereas that at 9.5 keV is 0.6%. Additionally, the quantum efficiency of the detectors is 90% and 40%, respectively. These figures, together with an estimation of a 0.01% ratio between the second harmonic and the fundamental, suggest a $\sim$ 0.5% ratio between fundamental elastic XRTS and that from the second harmonic, which is consistent with the experimental findings ($\sim$ 0.2%).

Similarly, the observed $2 \times \mathrm{K}_\alpha$ peak is much higher than the expected rate of two K_α photons arriving in coincidence. This is evident from the relative heights of the peaks in the spectrum, and similarly applies to the 15.4 keV peak. These observations further validate the detection of non-thermal electron RR emissions.

It should be noted that as the elastic peak is predominantly contributed by elastic XRTS instead of the non-thermal processes, they will be excluded from further discussion. Processes involving M-shell will not be explicitly discussed either because the energy resolution of the SPC, combined with the broadening of non-thermal peaks, makes it difficult to distinguish between contributions from L and M-shells with only several hundreds of eV difference. As a result, the three peaks beyond the elastic peak are collectively denoted as K-Auger $\rightarrow$ K-RR, L-PI $\rightarrow$ K-RR, and two-photon absorption peaks, respectively. Furthermore, because the first two peaks are both recombinations into the K-shell, the "K-RR" notation will also be omitted.

5.3.3 Pulse-Duration-Grouped Spectra

In the previous analysis, all pulse durations were integrated to achieve an overall spectrum. However, to investigate the dependence of non-thermal electron emissions on pulse duration further, the data should be grouped by pulse duration. The pulse durations used in this analysis are obtained from the XTCAV diagnostic, which provides the power profile for each shot.

XTCAV uses two methods for power measurement: energy loss and energy spread. The power reconstruction of the X-ray pulse is only considered reliable when good agreement

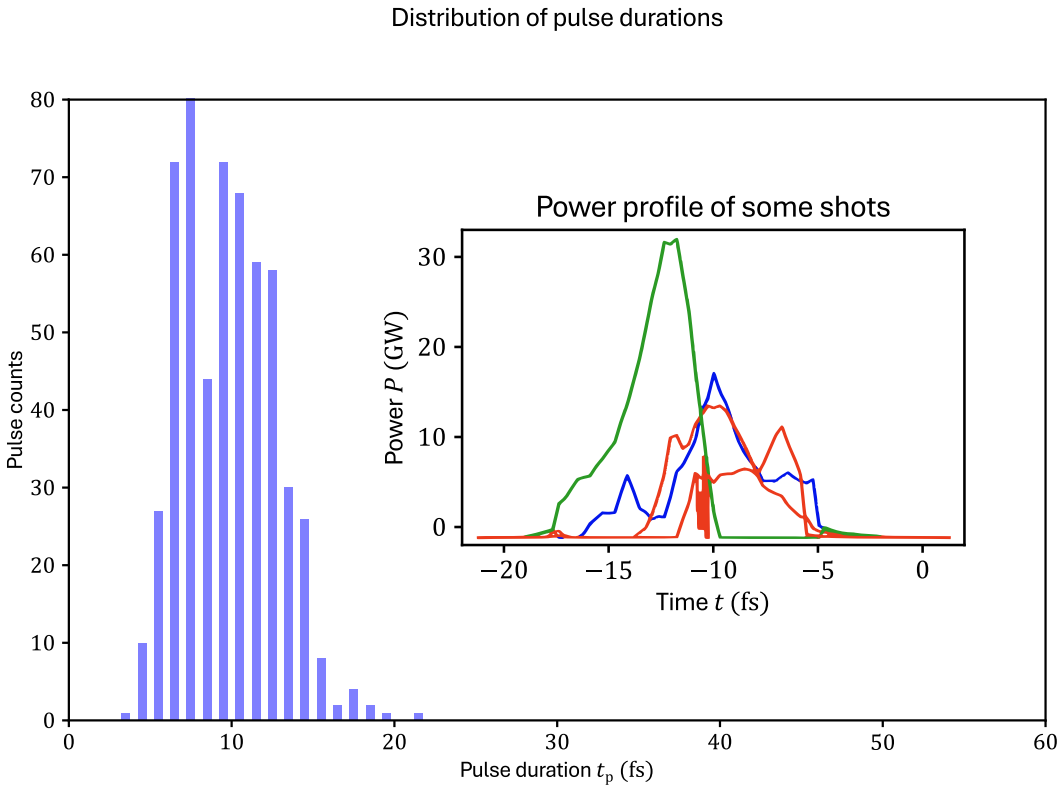


Figure 5.8: Distribution of pulse durations for shots where a nominal "10 fs" pulse duration was requested. The inset shows the power profiles of several individual shots, reconstructed using the energy loss method.

is reached between the two methods. LCLS provides guidelines [191] for evaluating and interpreting this using an agreement score that ranges from -1 to 1; a threshold of agreement score greater than 0.7 is used in this analysis to ensure accurate power-profile data. Only shots meeting this criterion were selected for further analysis. For shots that meet this criterion, the LCLS XTCAV team suggests using the energy loss as a more precise measurement of the power profile [192].

The power profiles obtained from XTCAV (as shown in Fig. 5.8 (inset)) reveal that the pulse does not always exhibit a well-defined shape. Many pulses have irregular or multi-spiked structures, making it challenging to reliably define a single pulse duration. To address this, the pulse duration in this study is defined as the time interval during which 20% to 80% of the total pulse energy is delivered.

Although the experimental set-up allowed requesting specific pulse durations, the actual pulse duration distribution was rather broad due to limited control over the beam. as illustrated in Figure 5.8, which shows the distribution of pulse durations measured by XTCAV for shots where a nominal "10 fs" pulse duration was requested, but the actual pulse

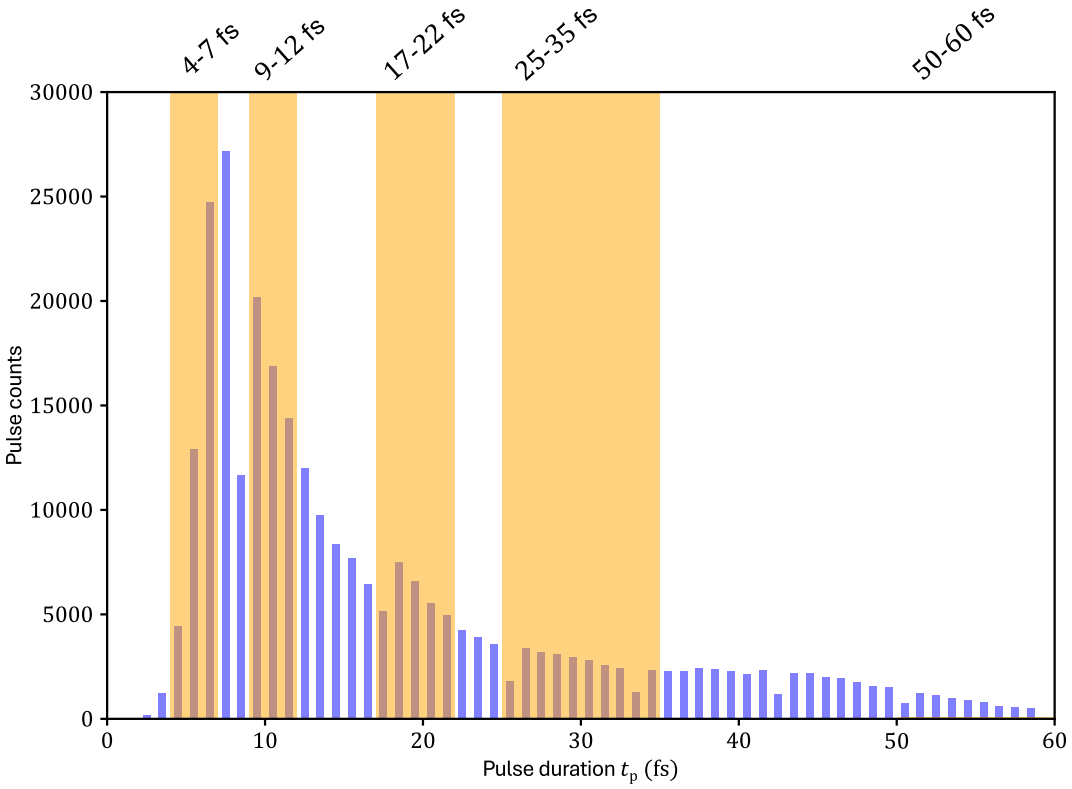


Figure 5.9: Distribution of the pulse durations and the selected groups based on their width and the number of shots.

durations exhibit significant variability, ranging from a few femtoseconds to over 40 fs.

To ensure the data are comparable, only single-spike pulses were selected for further analysis. This selection criterion significantly reduces the overall signal level but ensures that the spectra are not influenced by multi-spike pulse structures, which are hard to model and also bring extra difficulty for interpretation.

In this analysis, the pulse duration groups used in this analysis were selected to balance two considerations. First, the intervals were chosen to be sufficiently narrow so that each group could be reasonably approximated by a single representative pulse duration. Second, the grouping ensures that enough shots are included in each bin to achieve good statistical reliability. This approach allows for a systematic comparison across different pulse duration ranges while minimising noise introduced by inadequate statistics. The distribution of the pulse durations across all different shots is shown in Fig. 5.9. The pulse duration groups used in this study are 4-7 fs, 9-12 fs, 17-22 fs, 23-45 fs, and 50-60 fs. The last group is intentionally set to deviate from all others to provide a long-pulse reference for nearly thermal conditions. The number of shots in each group is 13605, 19084, 4851, 8120, and 4373, respectively.

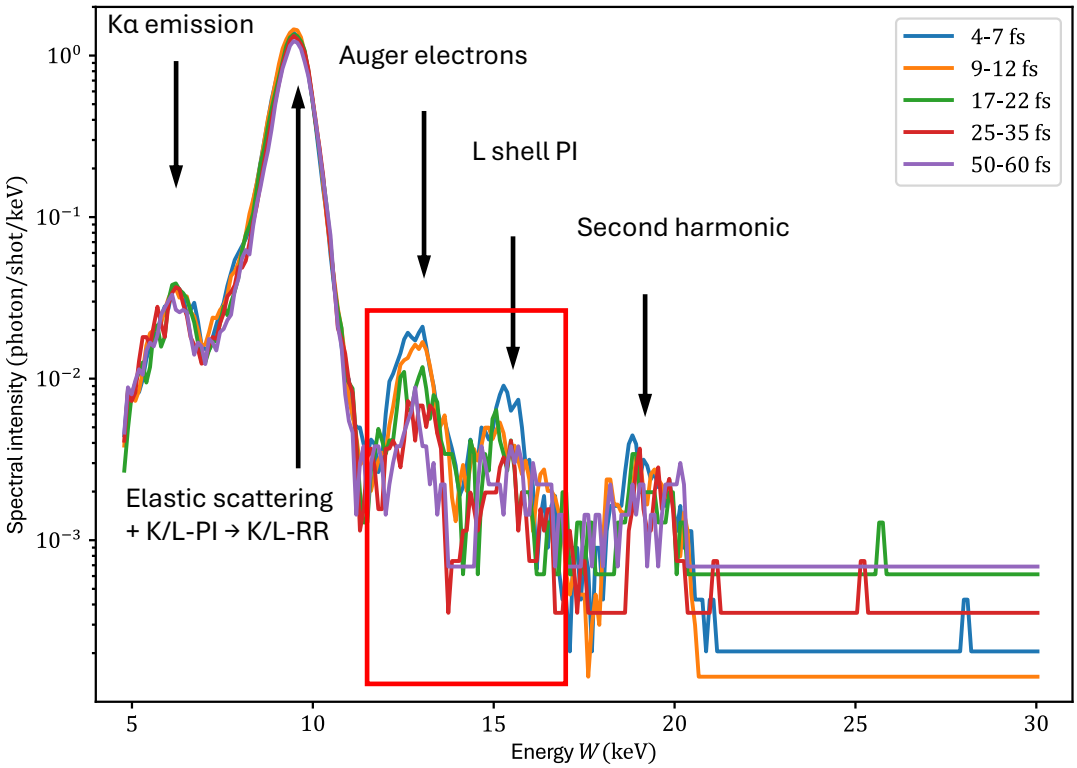


Figure 5.10: Non-thermal emission spectra for different pulse duration ranges, showing the dependence of spectral intensity on pulse duration. For shorter pulses, the non-thermal emission is strongest across all peaks, with a consistent decrease in intensity as the pulse duration increases. The intensity converges for pulse durations exceeding 30 fs. The errors are treated using the method discussed in Sec. 4.2.4, with translucent colours used to indicate the uncertainty in the spectra. These spectra are normalised according to the number of shots within each group.

The spectra grouped by pulse durations are shown in Figure 5.10 with the 1-σ errors estimated using the method discussed in Sec. 4.2.4, where the intensity of the non-thermal emission exhibits a clear dependence on pulse duration. For shorter pulse durations, the non-thermal emission is the strongest across all peaks, including those attributed to two-photon absorption, L-shell PI, and Auger electrons. However, as the pulse duration increases, the intensity of the non-thermal emission consistently decreases. This trend is observed for all peaks, with the most pronounced decay occurring between the shortest pulse durations (4 – 7 fs) and the intermediate range (9 – 12 fs and 17 – 22 fs). For pulse durations exceeding 30 fs, the non-thermal emission intensity appears to converge, with minimal further reduction, indicating that longer pulses do not significantly alter the non-thermal emission processes. The only exception to this trend is observed for the last peak, corresponding to elastic XRTS from the second harmonic, which should in principle not change, and roughly consistent with the experimental observation.

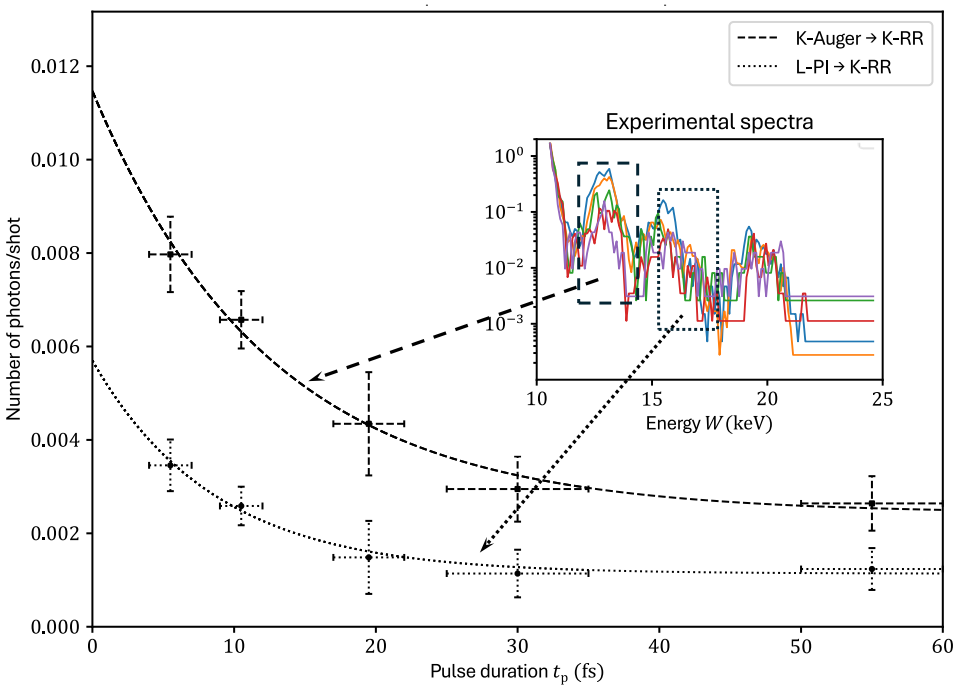


Figure 5.11: Decay of non-thermal emission intensity as a function of pulse duration for Auger electrons, L-shell PI, and second harmonic elastic XRTS peaks. Shorter pulses enhance non-thermal emission, with pronounced decay for Auger and L-shell peaks. The error bars are obtained by adding the error from each energy bin quadratically, as they are independent and obey the same Poisson statistics. It should be noted that the "decay-like" trend of the second harmonic elastic XRTS peak is due to the change of operation mode and does not reflect electron collision dynamics.

To better visualise the trend of non-thermal emission strength as a function of pulse duration, the number of photons in each peak is plotted against pulse duration in Fig. 5.11. This decay plot provides a clearer view of how non-thermal emission intensity diminishes with increasing pulse duration. Both the Auger electron and the L-shell PI peak show a consistent decay trend, while the two-photon absorption peak, on the other hand, exhibits a relatively weaker dependence on pulse duration. However, the overall trend is similar to what has been discussed in chapter 3, validating the general concept of observing the electron thermalisation process directly through a pulse duration scan and offering insights into the underlying electron relaxation dynamics. It should be noted that there seems to be a decay trend for the second harmonic elastic XRTS peak as well, while the XRTS itself should not depend on the pulse duration. This conflict could be explained by noticing that the operation mode of the XFEL has been changed between generating the shortest pulse durations and the longer pulse durations [2]. This likely changes the composition of the XFEL

[2]In this experiment, XFEL pulses shorter than 10 fs were generated using low charge + slotted spoiler, while those longer than 10 fs were generated using half charge.

second harmonic [193]. As the Second harmonic composition has never been measured during the experiment, this assumption could not be validated at this stage.

5.4 Inferred Collision Time

The experimental data collected on the decay of non-thermal emission intensity as a function of XFEL pulse duration exhibit a clear trend that can be captured using a functional form

$$N[t_{\mathrm{p}}] = N_0 e^{-t_{\mathrm{p}}/t_{\mathrm{d}}} + N_1 \ , \tag{5.3}$$

where t_{p} is the pulse duration, and t_{d} represents a characteristic timescale associated with the decay and N_1 is an assumed background indicating any detector noise level. It is important to note that t_{d} can not be directly interpreted as the physical collision time of the electrons. The central challenge lies in relating this decay plot to the electron collision times, which are governed by elastic e-e and inelastic e-i collisions. To establish this connection, simulations must be employed to compare the experimental decay trends with theoretical predictions.

A natural approach for relating the decay plot with electron collision times is to follow the methodology outlined in Chapter 3. In this method, time-dependent non-thermal emission spectra are simulated for a range of XFEL pulse durations, integrated over energy windows of peaks, and analysed in the form of a decay plot similar to the experimental one. By comparing these decay plots from the simulation with the experimental data, the collision rates can be inferred. However, this approach faces two significant challenges.

The first issue is the computational expense associated with using `CCFLY` for simulations. The Al simulations, discussed in Chapter 3, require approximately 400 CPU hours per case. Mn, with its 25 electrons and significantly more complex electron configurations, would require substantially longer simulation times. A test case conducted for Mn indicates that generating a decay plot similar to Fig. 5.11 with a minimum of six different XFEL pulse durations would require at least 30,000 CPU hours. This accounts only for generating one single decay plot, and to match the experimental result, further simulations would be needed to explore the parameter space. Importantly, this process requires treating both e-e and e-i collision rates as parameters. Considering the computational expense for a single parameter scan alone, this approach becomes impractical.

The second issue lies in the extraction of e-e and e-i collision rates (or times), which involves solving a two-dimensional parameter space inverse problem in the presence of noise. This problem is prone to inverse problem instabilities when the parameters are correlated, and small variations in the experimental data can lead to large variations in the inferred

parameters [194]. The correlated nature of the two parameters makes it challenging to reliably quantify uncertainties solely by matching the experimental outcomes to the simulation results.

To overcome these challenges, two alternative strategies are deployed. First, the `CCFLY` simulation is replaced with a stand-alone Fokker-Planck simulation. This is enabled by using the "electron-only" mode offered by `CCFLY`. The "electron-only" mode treats the system as a one-component electron plasma driven by a Fokker-Planck equation (representing electron-electron interactions) along with an inelastic operator and a source operator representing electron-ion interactions. Since no atomic kinetics are involved, the simulation is unaffected by the complexity of Mn's electron configuration, making it significantly faster. Each set of simulations, including six pulse durations, requires approximately 30 CPU hours, which is about a thousand times faster than the original `CCFLY` approach. Second, the Markov Chain Monte Carlo (MCMC) method, as discussed in [194], is adopted. By employing a soft-boundary likelihood function for Bayesian inference, this method infers the posterior distribution of the e-e and e-i rates based on the experimental outcomes, providing a robust framework to quantify the uncertainties and confidence intervals of the e-e and e-i collisional times.

5.4.1 Simulation Set-up

An alternative to the standard `CCFLY`, which takes a substantial amount of time to finish, is the electron-only mode that evaluates only the evolution of the electron distribution function. As the atomic kinetics part is excluded, it runs significantly faster than the standard mode and can be used to interpret the experimental data, as the relaxation of the electrons is not strongly affected by the ion populations to the first order.

In the electron-only mode, the evolution of the electron distribution function is described by the same equation as in Eq. 3.17:

$$\frac{\partial f}{\partial t} = \hat{\mathcal{O}}_{\mathrm{e},f}[f] + \hat{\mathcal{O}}_{\mathrm{i},f}[f] + \hat{\mathcal{O}}_{\mathrm{s},f}[f] \ , \tag{5.4}$$

where $\hat{\mathcal{O}}_{\mathrm{e},f}[f]$ is the elastic collision operator, given by Eqs. 3.8 and 3.9, $\hat{\mathcal{O}}_{\mathrm{i},f}[f]$ and $\hat{\mathcal{O}}_{\mathrm{s},f}[f]$ are the inelastic collision and the source operator, respectively.

Since atomic kinetics are not included in this mode, the inelastic and source operators are evaluated manually. This is achieved by first running a standard `CCFLY` simulation under the desired input conditions as a baseline. Upon completion of the atomic kinetics module, the electron distribution function and ion state populations are recorded in an output file before being sent to the spectra module. The electron distribution is disregarded, while the ion state populations are used to evaluate the operators on the right-hand side of Eq. 5.7. Specifically, for a given process X induced by inelastic electron-ion collisions, the ion state

population $\rho_{N_\mathrm{l}}[t]$ is employed to construct the operators using a cross-section model similar to Eq. 3.12 and Eq. 3.14, resulting in the following operator:

$$\begin{aligned}&\hat{\mathcal{O}}_{\mathrm{X,l\to u}}[f]\\&= \rho_{N_\mathrm{l}}\left(K'_{\mathrm{X,l\to u}}\left[W+W_{\mathrm{l,u}}\right] f\left[W+W_{\mathrm{l,u}}\right] - K'_{\mathrm{X,l\to u}}[W]f[W]\right)\ ,\end{aligned} \tag{5.5}$$

where the rate is given by:

$$K'_{\mathrm{X,l\to u}}[W] = S_{\mathrm{X}}[W]\sqrt{\frac{2W}{m_{\mathbf{e}}}}\ , \tag{5.6}$$

Unlike the standard mode, where the collision operators are evaluated self-consistently while solving the ODE for the distribution function f, the electron-only mode computes the inelastic and source operators only once per time step. These values, multiplied by the time step length, are then added to the distribution function instantaneously at the beginning of that time step. Between two user-defined time steps, only the elastic e-e collision operator is evaluated. This approach can be written compactly as:

$$\begin{aligned}\frac{\partial f}{\partial t} &= \sum_{\bar{i}} \hat{\mathcal{O}}_{\mathrm{e},f}[f] + \left(\hat{\mathcal{O}}_{\mathrm{i},f}[f_0] + \hat{\mathcal{O}}_{\mathrm{s},f}[f_0]\right)\Delta t_{\bar{i}}\delta[t-t_{\bar{i}}]\\&= \begin{cases}\hat{\mathcal{O}}_{\mathrm{e},f}[f] & (\forall \bar{i}:\ t_{\bar{i}-1} < t < t_{\bar{i}})\\ \left(\hat{\mathcal{O}}_{\mathrm{i},f}[f_0] + \hat{\mathcal{O}}_{\mathrm{s},f}[f_0]\right)\Delta t_{\bar{i}}\delta[t-t_{\bar{i}}] & (\exists \bar{i}: t = t_{\bar{i}})\end{cases},\end{aligned} \tag{5.7}$$

where $f_0 = f[t_{\bar{i}} - 0]$ is the distribution function output from the previous time step, and $\Delta t_{\bar{i}} = t_{\bar{i}+1} - t_{\bar{i}}$ is the size of the time step. This approach significantly reduces computational complexity, as it removes the need to evaluate the inelastic and source rates iteratively while solving the ODE, enabling substantial acceleration that would otherwise be unattainable. Because the effects of these operators are only evaluated once per time step, the time step must be set finer than in the baseline simulation to ensure that changes in the distribution function remain small. The solver thus self-consistently solves the Fokker-Planck equation between time steps and updates the value at the timestep until the simulation is completed and the distribution function is recorded at each time step.

Apart from the processes that depend on the electron distribution, there are also processes that depend solely on the temporal profile of the XFEL pulse and the ion populations, including Auger decay (AD) and photo-ionisation (PI). They are computed by altering the electron distribution instantaneously at the beginning of each time step, similar to those that depend on the electron distribution.

For detailed modelling of the system, all the states from the output file should ideally be considered. However, to reduce computational expense, a small subset of only a few states can be selected to represent all states involved. This approximation is valid only when the chosen states dominate the total ion density. Careful consideration is required

as ion populations evolve over time, and usually, a single dominant state does not exist for the entire simulation period.

Once the electron distributions are obtained as a function of time, along with the ion state populations given by the baseline case, the spectra can be computed using the method described in Sec. 3.3.3. Similar to the atomic kinetics, the spectra generation process can be accelerated significantly by reducing the states involved such that only the most populated core-hole states are retained.

For the purpose of this work, only two groups of operators are considered. The first group includes collisional ionisation (CI) and collisional recombination (CR), which account for the electron relaxation through e-i collision. The second includes photon-ionisation (PI) and Auger decay (AD), accounting for the processes that add non-thermal electrons to the system. While other processes are possible, they play a more subtle role in the electron relaxation dynamics. The CI and CR operators are only constructed for the M-shell process because the relevant cross-sections for the K-shell and L-shell will be substantially lower. The PI and Auger operators, on the other hand, consider all shells (K/L/M-shell PI and KLL/KLM Augers). Although they are all referred to as "source operators" in Sec. 3.3.2, as they either add or remove electrons to the distribution, this section will refer to CI and CR as the e-i collision operators and the relevant rates will be referred to as "e-i collision rates". It is worth stressing again that, as the ions have a very low temperature, the elastic e-i collision operator plays no role in this scenario.

Similarly, in generating the spectrum, only recombination processes involving the K-shell core-holes are included. This simplification is legitimate by considering the fact that the K-shell RR cross-section is substantially larger than that of the L/M-shell, and corresponds to the experimental results (Fig. 5.7) as well.

To facilitate comparison with experimental data, a set of pulse durations ranging from 5 fs to 60 fs is selected for baseline references. The pulse energy is kept constant across these durations, corresponding to 100 μJ on the target. This represents the experimental 300 μJ pulse energy after attenuation, accounting for the $\sim$30% beamline transmission [195]. The focal spot diameter is assumed to be approximately 1.5 μm, consistent with experimental conditions [196]. The simulation lasts for 200 fs to allow sufficient thermalisation to happen, and the peak intensity of the X-ray pulse is always assumed to occur at twice the pulse duration (for example, a 5 fs pulse will have a peak at 10 fs.)

It should be noted that the pulse durations defined in `CCFLY` differ from those measured experimentally. In `CCFLY`, the pulse duration is characterised by the full width at half maximum (FWHM) of the intensity profile, whereas experimentally, it is defined as the time

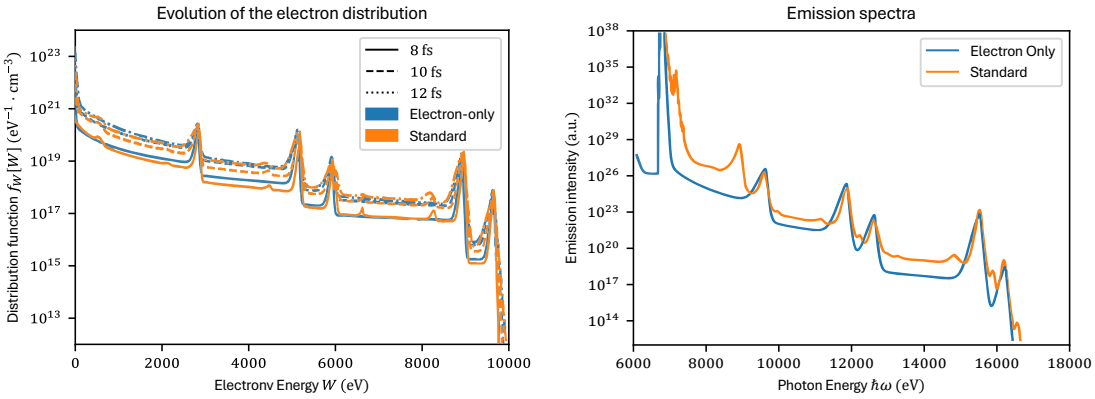


Figure 5.12: Comparison of (a) the electron distribution function and (b) the emission spectra between the electron-only mode and the standard mode for a 5 fs XFEL pulse. The XFEL pulse peaks at 10 fs, and the interval from 8 fs to 12 fs corresponds to the period of major emission. The electron distributions show good agreement, while the emission spectra mostly overlap except for the missing 8.7 keV peak in the electron-only mode. The spectra align with the experimental spectra within the resolution of SPC, indicating that the electron-only mode can be used to interpret the experimental data at a lower computational cost.

interval over which $20 - 80\%$ of the energy is delivered. To ensure consistency between the two, a conversion factor must be applied, which is obtained by integrating over a Gaussian pulse:

$$\beta = \frac{2\sqrt{2}\mathrm{Erf}^{-1}[0.8 - 0.2]}{2\sqrt{2\mathrm{Ln}\,[2]}} \approx 0.72\ , \tag{5.8}$$

where Erf is the error function. Although many of the pulses are not Gaussian, the selection criterion in Sec. 5.3.3 ensures that the pulses have sufficiently good temporal characteristics, and the approximation remains valid.

The effectiveness of the electron-only mode is demonstrated in Fig. 5.12, which compares the electron distribution function (left) and emission spectra (right) for a simulation with a pulse duration of 5 fs. The XFEL pulse is centred at 10 fs, with a full width at FWHM of 5 fs. Consequently, the time interval from 8 fs to 12 fs corresponds to the period during which the majority of emission occurs.

As shown in the left panel, the electron distributions obtained in the electron-only mode closely overlap with those from the standard `CCFLY` mode with only subtle differences with the satellite peaks, which are not resolved in the electron-only mode due to the fact that only a few states are included in constructing the operators for complexity-reduction purposes. These peaks will not significantly affect the analysis due to their relatively low intensity.

The emission spectra, shown in the right panel, also exhibit substantial overlap between the two methods. The only significant difference is the absence of a peak at 8.7 keV in the electron-only mode. This peak corresponds to L-PI followed by M-RR. However, since

this peak overlaps with the elastic scattering signal in experimental measurements, its omission does not affect further analysis.

Apart from this, all peaks in the standard mode simulation are resolved, with only subtle differences in the satellite peaks, and also align with the experimental spectra. Because the satellite peaks are not resolved experimentally, the agreement between the standard calculation and the electron-only mode confirms that this reduced scheme can be used to replace the full `CCFLY` simulation at a significantly lower cost to interpreting the experimental results.

As using this mode requires running a standard `CCFLY` to establish the ion populations beforehand, doing a single simulation is not beneficial. However, to determine the collision time, the e-e and e-i collision rates are scaled, as described in Sec. 3.4.4. This mode thus becomes advantageous, as the same ion population from the baseline can be reused, avoiding the need to rerun the full simulation for each set, significantly reducing the computational cost.

This method relies on the assumption that the ion population remains unchanged when the rates are varied. While this assumption is not generally valid, as states with similar configurations often have comparable cross-sections, it will not have a significant impact on the electron relaxation. For instance, CI from $K^2L^8M^8$ state to $K^2L^8M^7$ state involves two states with similar cross-sections. Changes in population between these two states do not significantly affect the total rates given by the sum of them. This assumption only breaks down when the rates are such that the $K^2L^8M^0$ state dominates because this configuration allows no M-shell CI. Fortunately, the relatively low intensity of the XFEL beam and temperature of the plasma forbid the domination of such a high charge state across various rates, and the assumption of an invariable state population remains valid.

5.4.2 Simulation Results

The ability of `CCFLY` to run efficiently in the electron-only mode allows a large number of spectra to be generated for different pulse durations and collision rates, enabling direct comparison with experimental data. This is achieved by scaling the rates in the Fokker-Planck operator for e-e collisions and the CI and CR operators for e-i collisions. Notably, to maintain the principle of detailed balance, the CR rates are always scaled with the same ratio as the CI rates. Thus, the e-i collision rate can be characterised by the CI rate alone.

Before altering the collision rates, it is necessary to verify that the expected electron relaxation behaviour is reproduced by increasing the pulse duration. Fig. 5.13 shows the distribution at the XFEL peak and the simulated emission spectra for different pulse durations, with the collision rates unaltered. It can be observed that longer pulse durations lead to more relaxed electron distributions, resulting in a weaker non-thermal feature and a lower number of emitted photons. This trend is consistent with the results of the Al simulations

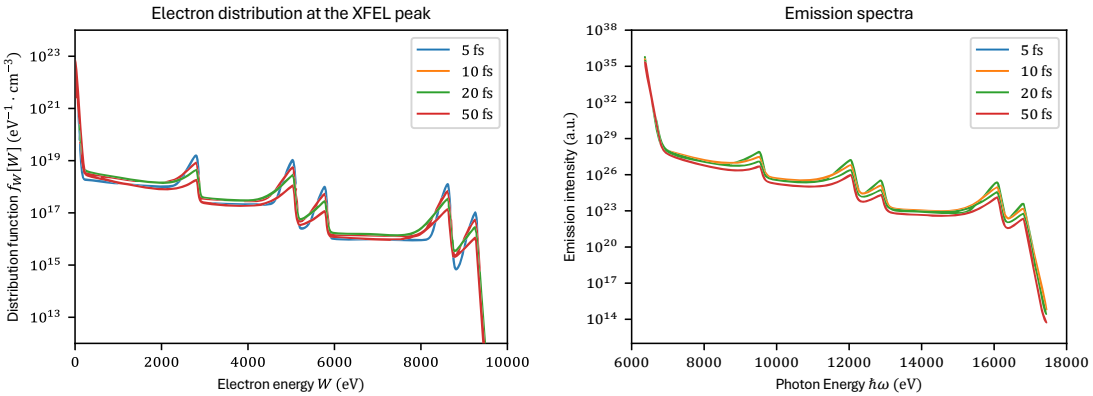


Figure 5.13: (a) Electron distribution function at the XFEL peak and (b) emission spectra for varying XFEL pulse durations. Longer pulse durations result in more relaxed electron distributions. Correspondingly, the emission spectra show a reduction in intensity and broadening of features. These results align with Al simulations (Sec. 3.4.2) and experimental data.

presented in Sec. 3.4.2 and agrees with experimental observations. It is also worth noting that the non-thermal features in the emission spectra are significantly stronger than those observed in the Al simulations, even though the XFEL pulse durations, in this case, are over an order of magnitude longer. This observation validates that non-thermal electrons in Mn take longer to thermalise due to their higher energies, and supports the choice of Mn as a suitable material for this study.

For these simulations, the e-i collision rates were calculated using the Lotz cross-section. To determine the corresponding rate, the operator for CI given in Sec. A.2, which quantifies the rate of removing one electron with energy W [3] is used:

$$\hat{\mathcal{O}}'_{\mathrm{CI}}[f]\big|_W = -\rho_{N_1}\sqrt{\frac{2W}{m_\mathrm{e}}}f[W]S_{\mathrm{CI}}[W]\ , \tag{5.9}$$

The corresponding e-i collision rate can thus be expressed as:

$$\nu_{\text{e-i}}[W] = \rho_{N_1}\sqrt{\frac{2W}{m_\mathrm{e}}}S_{\mathrm{CI}}[W]\ , \tag{5.10}$$

As seen from Fig. 5.14, the rate depends on the electron energy W. For most electron energies, the rate is approximately 0.1 fs^{-1}. To facilitate comparison across simulation sets, the value for Auger electrons near 5.3 keV, $\nu_{\text{e-i}} = 0.15$ fs^{-1} is quoted as the e-i collision rate. For reference, the more accurate BCF model reported recently [49] is also shown in Fig. 5.14. The difference between the two models is mostly constant across the energy region of interest. For the BCF model, the corresponding rate is approximately 0.094 fs^{-1}.

[3] Note that this is not the rate of change in the electron distribution $\frac{\partial f}{\partial t}$ due to CI, as CI creates two new electrons upon removing one. For further details, refer to Sec. A.2.

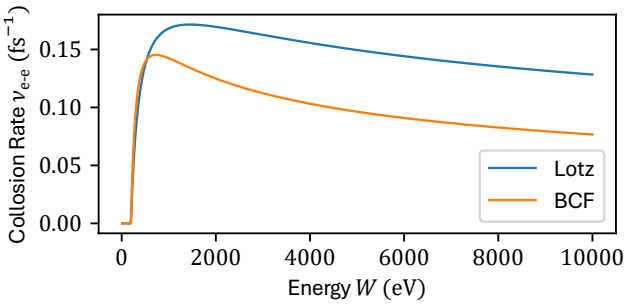


Figure 5.14: Collisional ionisation rates as a function of electron energy, calculated using the Lotz cross-section (blue) and the more accurate BCF model (orange) [49] a model with a form similar to the Clark, Abdallah, and Mann (CAM) model [197] with IPD scaling similar to that proposed in [198], but consistent with the widely used Burgess and Chidichimo (BC) model in the atomic limit. The models have a roughly constant difference at most energies over 1 keV.

The e-e collision rate is computed using the same approach as described in Sec. 3.4.4, with Eq. 3.20. For this simulation, with a temperature of 30 eV extracted from the simulation, the relaxation time is calculated to be approximately 0.27 fs. This value approximated the Al case, as the temperature and density do not differ greatly in the current scenario. Thus, the more prominent non-thermal features in Mn are predominantly attributed to the higher energies of the non-thermal electrons, which persist longer before thermalising. Because the energy of the pulse is kept constant across pulse durations, the temperature when the XFEL peaks is also approximately constant. The e-e collision rate, defined as the inverse of the relaxation time, is therefore approximately 3.7 fs^{-1}. For simplicity purposes, it is also assumed that different collision rates do not change the temperature significantly.

It should be noted that the temperature of the electrons could be better measured using the XRTS spectrometer. However, the relatively low resolution of the detector, combined with the fact that the density of the system is also unknown, makes the precise determination quite difficult [194]. Due to the Author's limited scope, this problem has not yet been addressed and is left as future work. Recent developments in XRTS, such as [199], will also be considered in future experiments. For this study, the temperature is always assumed to be 30 eV across various conditions, such that the scaling of the collision operator is proportional to the collision rate.

With the collision operator scaled, both the e-e and e-i collision rates are adjusted proportionally. Each combination of e-e and e-i collision rates produces a set of spectra similar to Fig. 5.13. These spectra can be analysed in a manner analogous to experimental data by integrating the emission intensity over the non-thermal peaks and plotting it as a function of pulse duration. The results are shown in Fig. 5.15, which includes experimental

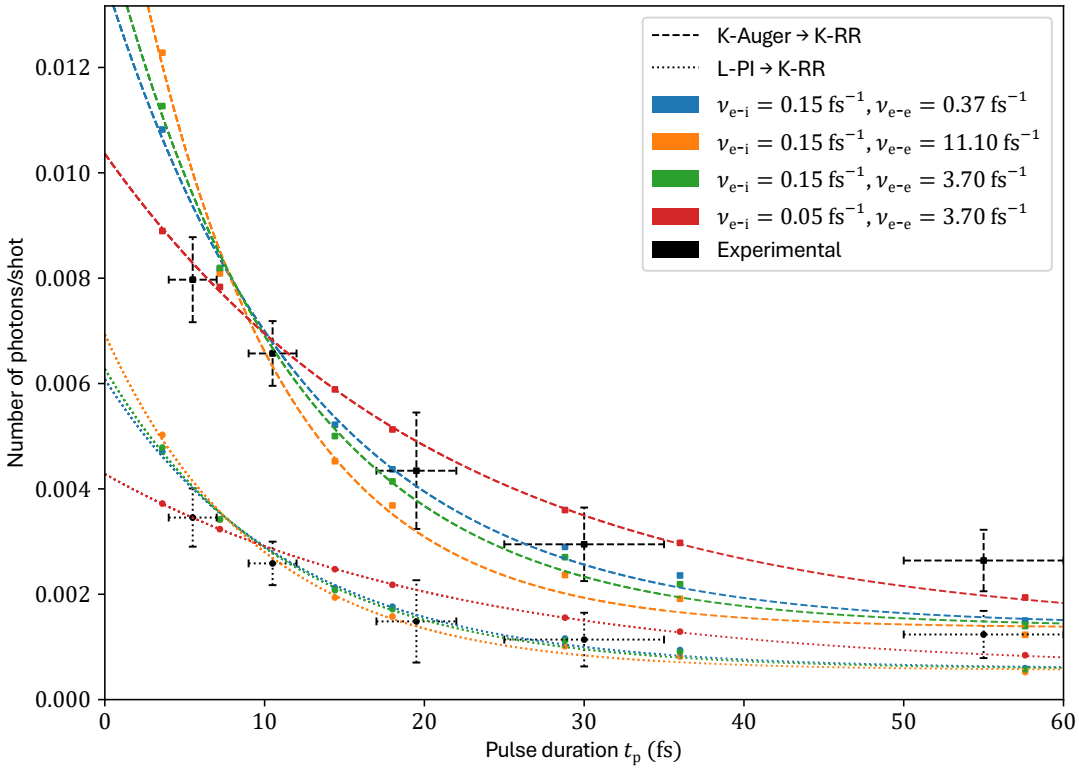


Figure 5.15: Integrated non-thermal emission intensity as a function of pulse duration. The experimental data are shown as black points, while the dashed and dotted lines represent simulations for different combinations of e-e and e-i collision rates. The values of the e-e and e-i collision rates are indicated in the legend.

data and various simulated collision rates. Note that the pulse durations have been converted to align with the experimental definition.

As shown in Fig. 5.15, higher e-e or e-i collision rates result in a steeper decay of the non-thermal emission intensity as a function of pulse duration. This behavior is expected, as higher collision rates accelerate the relaxation of the electron distribution, leading to fewer non-thermal electrons at any given time snapshot. Consequently, the non-thermal emission features become weaker.

Different combinations of e-e and e-i collision rates produce decay curves with distinct shapes. Some combinations match the experimental data quite well, while others deviate significantly. For instance, the combination of $\nu_{e\text{-}i} = 0.15\ fs^{-1}$ and $\nu_{e\text{-}e} = 3.70\ fs^{-1}$ yields a good agreement with the experimental observations for both Auger → K-RR and L-PI → K-RR transitions. In contrast, combinations with lower $\nu_{e\text{-}i}$ or higher $\nu_{e\text{-}e}$ result in decay curves that either underpredict or overpredict the steepness of the experimental data.

While it is possible to perform simulations with finer resolution in collision rates to extract the optimal values for e-e and e-i collision rates, this approach requires substantial repetitions of the simulation, which is infeasible even when operating in electron-only mode.

Additionally, matching the decay curves by visual inspection is unreliable, as no quantitative measure of goodness-of-fit is obtained, and the uncertainty in the inferred collision rates cannot be rigorously evaluated.

To address these limitations, a neural-network-like fitting function is deployed to predict the decay curves. This function is trained on a set of precomputed spectra corresponding to various e-e and e-i collision rate combinations. By employing MCMC sampling, the confidence intervals for the inferred e-e and e-i parameters can be determined based on the experimental data. This approach not only reduces computational overhead but also provides a statistically reliable evaluation of the fitting quality and parameter uncertainties.

5.4.3 Collision Times

The first step in extracting the collision rates is to construct a fitting function capable of producing the decay plot for arbitrary input values of $\nu_{\text{e-i}}$ and $\nu_{\text{e-e}}$. This is achieved by fitting the decay curves with the function $N[t_{\text{p}}] = N_0 e^{-t_{\text{p}}/t_{\text{d}}} + N_1$, where N_0, N_1, and t_{d} are the fitting parameters. When the decay curves are sampled for a range of $\nu_{\text{e-i}}$ and $\nu_{\text{e-e}}$, the corresponding fitting produces sets of parameters N_0, N_1, and t_{d}. These parameters can then be used to construct a mapping from the collision rates $\nu_{\text{e-i}}$ and $\nu_{\text{e-e}}$ to the decay curve.

To construct such a mapping, a cubic spline function ξ is employed to generate the three parameters N_0, N_1, and t_{d}, where separate quadratic functions are defined for each of the decay parameters N_0, N_1, and t_{d}. This results in a set of coefficients (ξ functions) to be optimised for each of the Auger and L-shell PI curves. The fitting process minimises the loss function, which is defined directly on the decay curve instead of the decay parameters, as:

$$[\text{Loss}] = \sum_{t_{\text{p,sim}},\ \nu_{\text{e-i}},\ \nu_{\text{e-e}}} \left(N[t_{\text{p}} = t_{\text{p,sim}}|N_0, N_1, t_{\text{d}}] - N_{\text{sim}}[t_{\text{p,sim}}]\right)^2 \ , \tag{5.11}$$

where $N[t_{\text{p}}]$ is computed using the decay model for a given set of N_0, N_1, and t_{d}. Since these parameters depend on $\nu_{\text{e-e}}$ and $\nu_{\text{e-i}}$, minimising the loss function corresponds to optimising the quadratic mapping coefficients ξ, as shown in Fig. 5.16. This approach ensures an accurate and computationally efficient representation of the relationship between the collision rates and the decay curves.

To achieve the mapping between collision rates and the decay parameters, $120 = 15 \times 8$ sets of simulations were performed. These simulations span 8 e-i collision rates from 0.05 fs^{-1} to 0.2 fs^{-1} and 15 e-e collision rates from 0 fs^{-1} to 11.10 fs^{-1}, with each set containing 6 pulse durations ranging from 3.6 fs to 36 fs [4]. This approach ensures sufficient parameter coverage to compute the mapping efficiently without introducing bias due to limited sampling.

[4] Based on the 20% to 80% energy delivery criterion.

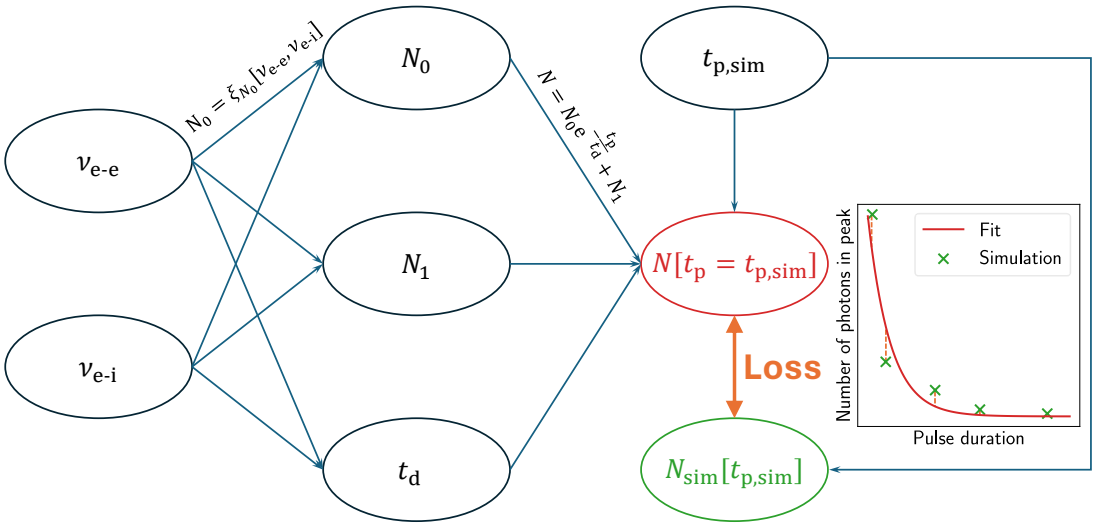


Figure 5.16: Schematic of the fitting process to map collision rates ($\nu_{e\text{-}e}$, $\nu_{e\text{-}i}$) to decay parameters (N_0, N_1, t_d). The predicted decay curve is compared to simulation data, and the loss function is minimised to optimise the mapping. The inset shows a typical fit compared to the simulation results.

The effectiveness of the fitting procedure is demonstrated in Fig. 5.17, which compares the fitted decay curves to the simulation results. As shown, the fitted curves closely follow the simulated data, indicating that the fitting is sufficiently accurate for interpreting the results and analysing the underlying processes. Note that the orange curve corresponds to a parameter value not included in the simulations but derived from the fit. Its position between two adjacent simulation parameters demonstrates the robustness of the fit and its ability to interpolate accurately.

The next step is to determine the confidence intervals of the e-i and e-e collision rates ($\nu_{e\text{-}i}, \nu_{e\text{-}e}$) that match the experimental observables within their associated uncertainties. Statistically, this is equivalent to finding the posterior distribution of the rates given the experimental distribution of the observables. This relationship can be expressed as:

$$\boldsymbol{p}[\{\nu\}|\{N\}] = \frac{\boldsymbol{p}[\{N\}|\{\nu\}]\boldsymbol{p}[\{\nu\}]}{\boldsymbol{p}[\{N\}]} \,, \tag{5.12}$$

where $\{\nu\}$ represents the rates $\nu_{e\text{-}i}$ and $\nu_{e\text{-}e}$, $\{N\}$ represents the number of photons in each peak, $\boldsymbol{p}[\{N\}|\{\nu\}]$ is the likelihood function. The posterior distribution $\boldsymbol{p}[\{\nu\}|\{N\}]$ can be sampled using an MCMC algorithm, as described in [194] and references therein.

To account for potential inaccuracies in the fitting model, a soft-boundary likelihood function is chosen, tolerating deviations between the model predictions and the experimental

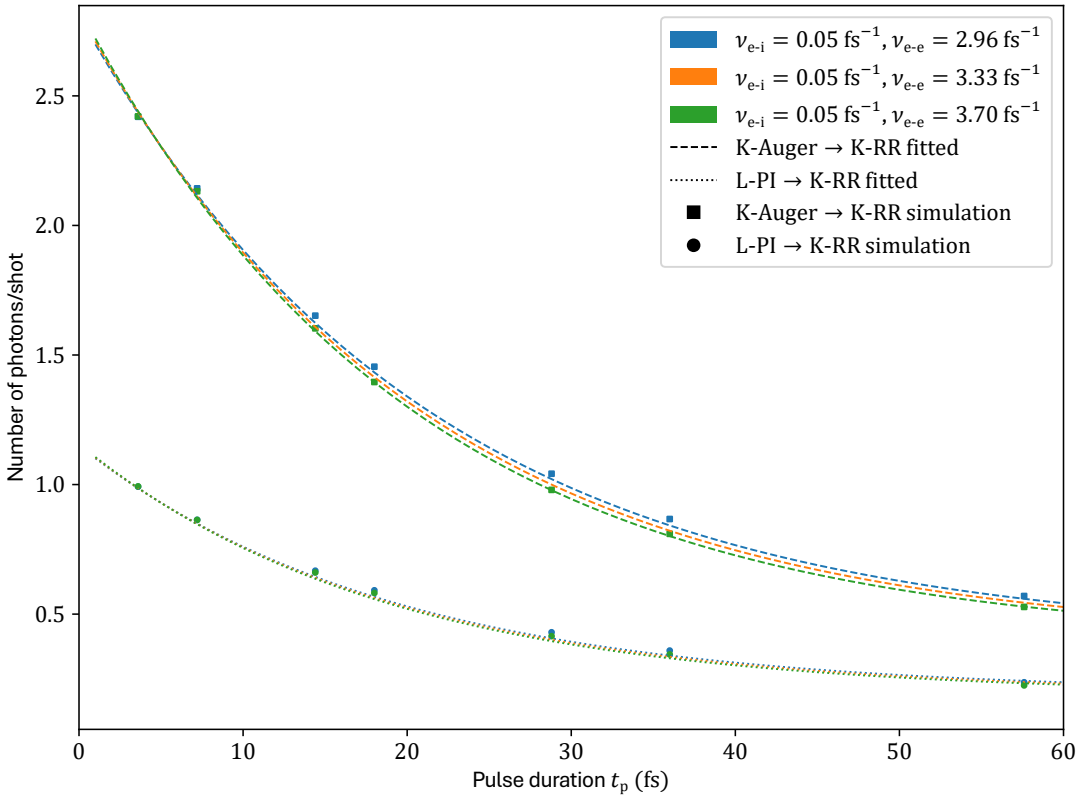


Figure 5.17: Comparison between the fitted decay curves and simulation results for various collision rates. The lines represent the fitted decay curves for K-Auger → K-RR and L-PI → K-RR processes, while the points represent the simulation results. The close agreement between the fitted and simulated data demonstrates that the fitting model accurately captures the decay behaviour for a range of collision rates. Note that the orange curve corresponds to a parameter value not included in the simulations. The fitted result positions between two adjacent simulation parameters, showing the robustness of the fit.

observables. This likelihood function is expressed as:

$$\boldsymbol{p}[\{N\}|\{\nu\}] = \mathrm{Exp}\left[-\underset{\bar{i}}{\mathrm{Max}}\left[\frac{N[t = t_{\mathrm{p}_{\bar{i}}}|\{\nu\}] - N_{\mathrm{exp}_{\bar{i}}}}{u_{\bar{i}}}\right]\right] , \tag{5.13}$$

where $N[t = t_{\mathrm{p}_{\bar{i}}}]$ is the predicted number of photons for a given pulse duration $t_{\mathrm{p}_{\bar{i}}}$, $N_{\mathrm{exp}_{\bar{i}}}$ is the experimentally measured value, and $u_{\bar{i}}$ is the uncertainty associated with the measurement. The likelihood function is penalised based on the maximum deviation between the predictions and experimental data, scaled by the uncertainties. The prior distribution of the rates $\boldsymbol{p}[\{\nu\}]$, is set to be a uniform distribution within the simulation range, and the $\boldsymbol{p}[\{N\}]$, the marginal likelihood of the observed data, is omitted as it only serves as a scaling factor independent of $\{\nu\}$. Importantly, the uncertainty in the pulse duration must also be incorporated into the analysis, as the experimentally obtained decay plot originates from gating the pulse duration within a relatively broad range. To account for this, the pulse

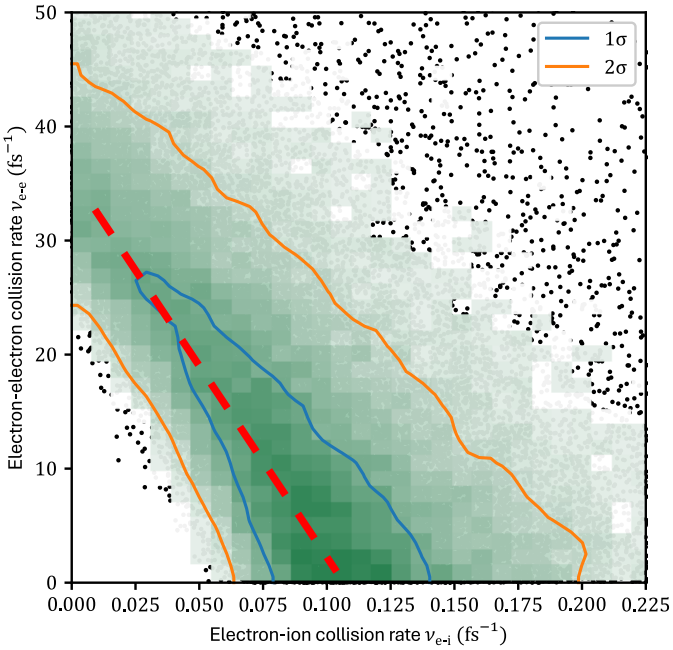


Figure 5.18: Posterior distribution of the electron-ion ($\nu_{e\text{-}i}$) and electron-electron ($\nu_{e\text{-}e}$) collision rates obtained from MCMC sampling. The heatmap represents regions of higher probability, with the 1σ, 2σ, and 3σ confidence intervals shown as contours. The results indicate a strong correlation between the two relaxation rates, as shown by the red dashed line, consistent with their roles in reducing non-thermal emission by thermalising the electron distribution through different mechanisms.

duration is allowed to vary within the error bars shown in Fig. 5.11, with distribution sampled from the XTCAV measured results in Fig. 5.9.

With the fitting function established, large-scale sampling via MCMC becomes feasible. In this work, 100,000 samples were drawn from the parameter space, enabling a thorough exploration of the posterior distribution. The results, shown in Fig. 5.18, clearly highlight regions of higher probability, indicating where the parameter combinations are more consistent with the experimental observables.

Notably, a strong correlation is observed between the $\nu_{e\text{-}e}$ and $\nu_{e\text{-}i}$. This finding is consistent with previous analyses, which suggest that both processes contribute to the relaxation of non-thermal electrons, albeit through distinct mechanisms, and increasing either results in a reduction of non-thermal emission. Even so, their relaxation behaviours remain fundamentally different. As a result, one process does not completely compensate for the other, as revealed by the gradient along the correlation axis.

The contour lines in Fig. 5.18 represent the 1σ, 2σ, and 3σ confidence intervals. The 1σ and 2σ contours enclose regions of high probability and provide reliable constraints on the collision rates. However, the 3σ contour extends far beyond the sampled parameter space and exhibits a strangely shaped edge. This behaviour arises due to limited data gathered

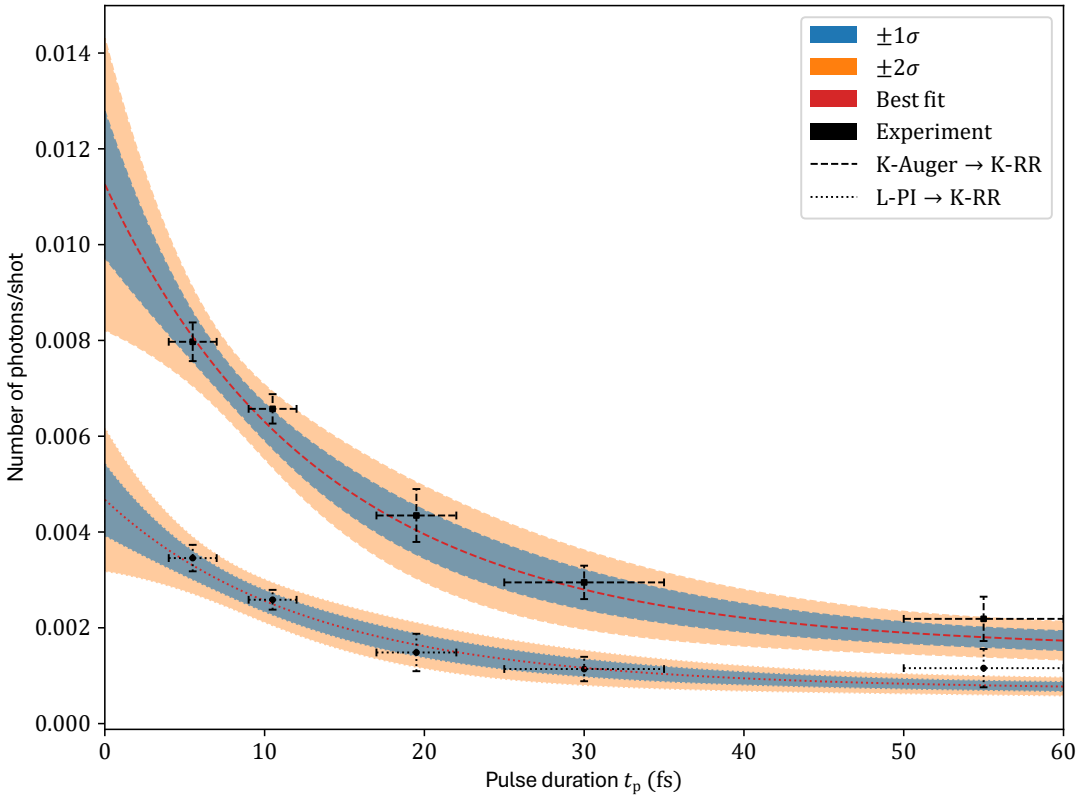


Figure 5.19: Comparison of the decay plot generated using MCMC-derived parameters with the experimental data. The red line represents the best-fit curve, while the blue and orange shaded regions correspond to the $\pm 1\sigma$ and $\pm 2\sigma$ confidence intervals, respectively. The MCMC results lie within the error range of the experimental data, demonstrating the reliability of the MCMC approach in inferring the collision rates.

from non-thermal electrons, which are challenging to detect because of their extremely low signal levels. As a result, the quantification of the 3σ region is unreliable and will not be discussed further in this work.

To further demonstrate the effectiveness of the MCMC approach, the decay plot for parameters within the confidence intervals is compared to the experimental data, as shown in Fig. 5.19. The comparison highlights how the MCMC framework not only identifies the best-fit parameters (red line) but also provides a detailed uncertainty quantification through the confidence intervals (shaded regions). The $\pm 1\sigma$ (blue) and $\pm 2\sigma$ (orange) shaded regions demonstrate the robustness of the method, as the experimental data points largely fall within these intervals. This indicates that the MCMC approach reliably constrains the parameters and accurately reproduces the experimental decay trends.

The structure of the posterior distribution cannot be fully captured by simply quoting the two rates with their confidence intervals. Instead, the rates must be expressed conditionally to account for their correlation properly. Nevertheless, the individual collision rates can

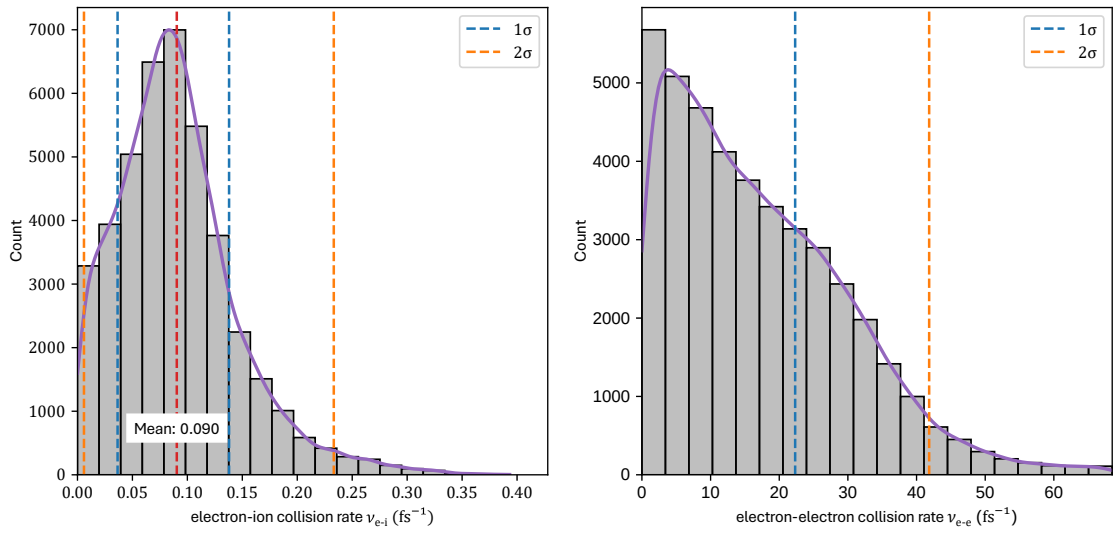


Figure 5.20: Marginalised distributions for the electron-ion ($\nu_{\text{e-i}}$, left panel) and electron-electron ($\nu_{\text{e-e}}$, right panel) collision rates obtained from MCMC sampling. The solid purple line represents the smoothed distribution, while the shaded histograms show the raw counts from the MCMC samples. The dashed vertical lines indicate the 68.3% (blue) and 95.4% (orange) confidence intervals.

be extracted by integrating the other parameters. The resulting marginalised distributions, shown in Fig. 5.20, provide a clearer summary of the e-i and e-e collision rates.

For the e-i collision rate, the 95% confidence interval is $\nu_{\text{e-i}} = 0.1^{+0.1}_{-0.1}$ fs^{-1}. This distribution is well-constrained and centred around a meaningful average value. In contrast, the distribution of the e-e collision rate peaks near zero, indicating that the maximum likelihood for this rate is close to zero. As such, it is more appropriate to quantify only the upper limit for $\nu_{\text{e-e}}$. At a 95% confidence level, the upper limit for the electron-electron collision rate is $\nu_{\text{e-e}} < 42$ fs^{-1}.

When expressed in terms of collision times, the results are as follows:

$$t_{\text{e-i}} > 5 \text{ fs}, \quad t_{\text{e-e}} > 0.02 \text{ fs} \quad (95\% \text{ confidence interval}). \tag{5.14}$$

5.4.4 Discussions

With the rates inferred in this study, it is important to place the results in the context of prior investigations and assess their consistency with established findings. Notably, at the estimated density of 6×10^{23} cm^{-3} and temperature of $\sim$30 eV, the electron-ion collision rate ($\nu_{\text{e-i}}$), centred around 0.1 fs^{-1}, deviates from the initial collision rate inferred from Lotz CI cross-sections, which was approximately 0.15 fs^{-1} (see Sec. 5.4.2). However, it closely aligns with the predictions of the more accurate BCF model [49], which gives 0.094 fs^{-1}. This agreement serves as a cross-validation of the analysis, highlighting the reliability of

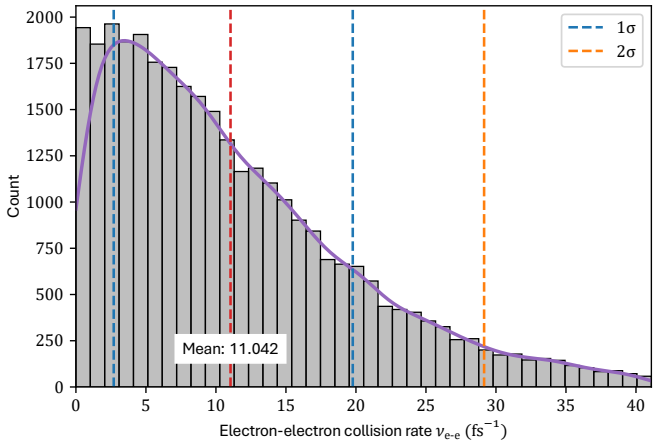


Figure 5.21: Conditional distribution of the electron-electron collision rate ($\nu_{\text{e-e}}$), assuming an electron-ion collision rate of $\nu_{\text{e-i}} = 0.1$ fs^{-1}. The solid purple line represents the smoothed distribution, while the shaded histogram shows the raw counts from the MCMC samples. The red dashed line indicates the mean value of 3.6 fs^{-1}, and the blue and orange dashed lines represent the 68.3% and 95.4% confidence intervals, respectively.

the present results when compared with the more refined measurement with high spectral resolution and dedicated to measuring the collisional ionisation rate.

Given that the distribution of the electron-ion collision rate is consistent with the BCF prediction, this value is taken as a reliable reference. Using this constraint, the electron-electron collision rate is analysed conditionally, setting $\nu_{\text{e-i}} = 0.1$ fs^{-1}. The resulting distribution, shown in Fig. 5.21, exhibits a structure different from previous results, with a notable peak near 2 fs^{-1}. For this conditional distribution, the mean value is 11 fs^{-1}. While the 1σ confidence interval can be quoted, the 2σ lower bound remains close to zero. As a result, it is still most appropriate to characterise the electron-electron collision rate by an upper bound. At the 95% confidence level, this upper bound is found to be about 30 fs^{-1}.

When expressed in terms of collision times, the results are summarised as follows:

$$\begin{aligned} t_{\text{e-i}} &: \ 10 \text{ fs}, \quad \text{(Assumed to be accurate)} \\ t_{\text{e-e}} &: \ \text{mean} \sim \ 0.1 \text{ fs}, \quad \text{max probability} = 0.45 \text{ fs}, \\ t_{\text{e-e}} &> 0.03 \text{ fs}. \quad \text{(95\% confidence interval)}. \end{aligned} \tag{5.15}$$

These results provide a consistent picture of the relaxation dynamics, with electron-ion collisions playing a dominant role, while electron-electron collisions exhibit greater variability and are better constrained by upper limits.

Recent advances in ultrafast laser technology have significantly enhanced the ability to measure relaxation times in various materials under extreme conditions. These techniques have enabled studies of electron dynamics in a wide range of systems. For example, in warm dense gold, ultrafast pump – probe reflectometry was used to extract the electron momentum

damping rate and conduction electron density through a Drude-type model analysis [164]. In fused silica, a two-colour pump-probe imaging method was employed to track the spatio-temporal evolution of plasma, using transmission and phase shifts to infer electron-ion relaxation times [110]. Another approach proposed a dielectric loss function analysis to measure quantum relaxation times, accounting for bound-electron effects and bridging discrepancies between classical Drude theory and experimental data [165]. While these methods have provided valuable insights into relaxation processes, they rely heavily on optical property measurements and transport models, which often require indirect interpretations.

The method used in this study is fundamentally different. Unlike the aforementioned techniques, which employ Drude-type models and are based on reflectivity, transmission, or phase shift measurements, the relaxation process here is directly observed through non-thermal emission. This direct measurement captures the thermalisation process itself, independent of any additional transport models. While the interpretation of the results involves Fokker-Planck and atomic kinetics modelling to extract the collision time, the observed relaxation dynamics are not reliant on these models. This sets the current approach apart as a more direct method for probing ultrafast electron dynamics.

A key limitation of the Drude model lies in its reliance on the relaxation time approximation (RTA), which assumes a single relaxation time for all scattering processes. This assumption is not valid theoretically, as discussed in Sec. 2.2.3. The RTA is often employed for convenience but does not reflect the true complexity of the underlying dynamics. Consequently, the collision times reported here cannot be directly compared to those extracted using Drude-based approaches. However, an evaluation of the transport coefficients themselves, such as [28, 30] suggests that the results are typically of the same order of magnitude. In this sense, the collision time inferred in this study is consistent with the findings of [154], though extrapolation is required to extend the comparison to higher electron temperatures around 30 eV, as the previous study only covered the range up to 5 eV.

5.5 Summary

In this chapter, the first direct measurement of electron collision times in warm dense matter was reported. This experiment, conducted at the LCLS XFEL facility, targeted Mn plasmas pumped by 9.5 keV hard X-rays, providing insight into the electron-electron (e-e) and electron-ion (e-i) collision rates through non-thermal electron emission spectra. The study aims to bridge the gap between theoretical predictions and experimental validation by directly observing the thermalisation process in strongly coupled systems.

The experimental set-up was designed to isolate non-thermal features with high precision. XFEL pulses of durations ranging from 5 to 60 fs were used to ionise solid-density Mn targets,

generating non-thermal electrons alongside a warm dense plasma. Non-thermal electrons' recombination radiation was captured by the SPC detectors, while auxiliary K_α and XRTS detectors monitored the thermal emission and plasma conditions. Mn was selected for its distinct K_α emission at 5.9 keV, which facilitates precise spectroscopic analysis, and its ability to produce energetic non-thermal electrons with extended thermalisation timescales.

The methodology used in this study is fundamentally different from previous investigations. Unlike other works, which employ Drude-type models and rely on optical property measurements such as reflectivity, transmission, or phase shifts, the relaxation process here was directly observed through non-thermal emission. While the interpretation of the results involved Fokker-Planck and atomic kinetics modelling to extract the collision rates, the observed thermalisation process itself remained independent of these models. This approach avoids the limitations of the relaxation time approximation (RTA) inherent in Drude models, providing a more direct and robust understanding of ultrafast electron dynamics.

The results of the study revealed that the electron-ion collision rate ($\nu_{\text{e-i}}$) is centred around 0.1 fs^{-1}, closely aligning with the predictions of the BCF model (0.094 fs^{-1}) but deviating slightly from values inferred using Lotz CI cross-sections (0.15 fs^{-1}). For the electron-electron collision rate ($\nu_{\text{e-e}}$), the mean value was found to be 11 fs^{-1} with a maximum probability at 2 fs^{-1} and an upper bound of 30 fs^{-1} at the 95% confidence level. The corresponding collision times were determined to be 10 fs for electron-ion interactions and greater than 0.03 fs for electron-electron interactions (95% confidence).

These findings were compared with previous studies, such as [110, 164, 165], which rely heavily on optical property measurements and transport models. The current study stands apart by directly probing the relaxation process through non-thermal emissions and avoiding the dependence on RTA assumptions. Although the collision times reported here cannot be directly compared with those extracted using Drude-based approaches, evaluations of transport coefficients suggest that the results are typically of the same order of magnitude. Thus, the collision time inferred in this study is consistent with results from [154].

It should be noted that this analysis used a constant Coulomb logarithm (CL) for all electrons, depending only on the electron temperature. As discussed in Sec. 2.2.3, this approach is not strictly valid, as higher-energy electrons experience a larger effective CL due to their higher velocities. Non-thermal electrons, therefore, would have a higher CL compared to the thermal component. This effect was omitted in this study due to computational constraints. As a result, the effective CL for thermal electrons would be lower than the value used here. However, since the results provide an upper bound on the collision rates, this simplification does not introduce a fundamental issue, though it results in a slightly less restrictive upper boundary. Future work will incorporate a velocity-dependent CL to refine the analysis further and provide a more accurate representation of the collisional dynamics.

Additionally, the analysis showed that there is some degree of "degeneracy" in the effects of e-e and e-i collisions, as different combinations of e-e and e-i rates can produce similar decay behaviour. This degeneracy is not intrinsic but is introduced by integrating over the non-thermal emission peaks, which results in the loss of information about the peak width. As discussed in Sec. 3.4.3, e-e collisions predominantly broaden the peaks, while e-i collisions depopulate them. Therefore, more precise measurements of the peak width and height could distinguish between the effects of e-e and e-i collisions. However, due to the limited signal and resolution of SPC detectors, this approach is currently infeasible. Future developments in detection technology could enable such measurements, providing a more detailed understanding of the relative roles of e-e and e-i collisions.

Overall, this chapter provides a comprehensive framework for understanding electron relaxation dynamics in WDM, offering direct insight into both e-e and e-i collision processes. By addressing the limitations of previous methodologies and advancing experimental techniques, the results contribute significantly to the understanding of ultrafast electron dynamics in strongly coupled systems.

The Roman pages, like the Roman Empire, must come to its inevitable end.

`\end{romanpages}`

— *Oxford Thesis Template*

6 Conclusions

Contents

6.1 Summary **139**
6.2 Future Work **141**

6.1 Summary

The study presented in this thesis has explored the relaxation dynamics of non-thermal electrons in warm dense plasmas, a unique regime where quantum effects and strong coupling coexist, bridging the gap between classical plasmas and condensed matter physics. This regime is critical for understanding fundamental processes in inertial confinement fusion, planetary interiors, and laser-matter interactions. However, the ultrafast timescales of electron relaxation, combined with the strong coupling nature and quantum effects, present significant challenges for experimental investigation. By addressing these challenges, this research has developed and demonstrated a novel approach to directly measure electron collision times in warm dense plasmas. Through experimental validation and theoretical modelling, this work provides new insights into the relaxation processes that govern transport properties in extreme conditions, focusing on measuring collision times and understanding the role of electron-electron and electron-ion interactions.

The research develops a novel method to measure electron collision times by leveraging XFEL-driven plasmas and pulse-duration-dependent emission spectra. Non-thermal electrons in warm dense plasmas are created through photon-ionisation and Auger decay processes during XFEL irradiation, producing distinct emission features through radiative recombination. The duration of the XFEL pulse plays a critical role in shaping the emission spectra. Shorter pulse durations limit the time available for electron collisions, allowing the emission spectra to retain distinct features associated with non-thermal electron populations. In contrast, as the XFEL pulse duration increases, the non-thermal electrons have more time to undergo collisions, leading to the gradual broadening and eventual disappearance of non-thermal features. By varying the duration of XFEL pulses, the thermalisation of non-thermal electrons is observed, offering a direct means to study their relaxation dynamics.

Computational simulations using the `CCFLY` collisional-radiative code further illustrate how these dynamics unfold. The simulations support that shorter XFEL pulses enhance non-thermal electron features in the emission spectra. They also reveal the distinct roles of electron-electron and electron-ion collisions: the former broadens non-thermal peaks, while the latter depopulates them. These insights provide a detailed understanding of the relaxation process and the relative contributions of different collisional mechanisms, validating the experimental approach of probing ultrafast electron dynamics in extreme conditions.

The experimental techniques developed and employed in this research were critical to isolating and detecting the weak signals associated with non-thermal electron dynamics in warm dense plasmas. Single-photon counting (SPC) detectors were utilised to capture the broad and weak energy distributions of non-thermal electrons. The SPC technique enabled direct detection of radiative recombination (RR) and inverse Compton scattering (ICS) emissions, both of which serve as key diagnostics of electron relaxation. Advanced clustering and deconvolution algorithms were employed to address challenges such as charge spread and multi-photon detection, ensuring accurate reconstruction of photon energy distributions under experimental conditions. To distinguish between isotropic RR emissions and anisotropic ICS signals, an optimised dual-detector configuration was implemented, with one detector aligned along the XFEL polarisation direction to suppress elastic scattering and the other positioned at a backscattering angle to maximise ICS signal collection. The experimental setup also incorporated precise filtering to eliminate background signals from thermal RR and K_α emissions, further enhancing the signal-to-noise ratio.

Experimental validation was conducted at the LCLS XFEL facility using Mn plasmas irradiated by 9.5 keV hard X-rays. The experimental setup, including single-photon counting detectors and XTCAV temporal diagnostics, enabled the capture of weak non-thermal electron emission with high precision. Non-thermal electron relaxation was directly observed through the decay of emission intensity as XFEL pulse durations were increased. The

experimental results revealed that electron-ion collisions dominate the thermalisation process, with a collision rate of approximately 0.1 fs^{-1} (collision time of 10.5 fs), consistent with predictions based on the BCF cross-section model. The electron-electron collision rate was less constrained, with an upper limit of 8.3 fs^{-1} (collision time >0.12 fs) and a mean value of 3.6 fs^{-1}. These findings provide the first direct measurement of electron collision times in warm dense matter, offering robust experimental validation of theoretical models.

The results highlight that the developed method effectively bridges the gap between theoretical predictions and experimental observations of collision dynamics in warm dense matter. By enabling the direct observation of the relaxation process rather than relying on transport properties, this approach provides a model-independent framework for studying ultrafast electron dynamics. Furthermore, for electron-ion collisions in strongly coupled systems, these findings suggest BCF being a more preferable model compared with Lotz up to 1 σ confidence level, and establish a benchmark for electron-electron collision models, whether they lie within or beyond the Coulomb logarithm framework.

In conclusion, this work establishes a comprehensive methodology for probing ultrafast electron dynamics and thermalisation processes in warm dense matter, addressing critical gaps in the understanding of relaxation and transport phenomena under extreme conditions.

6.2 Future Work

While this study has provided a novel method of investigating the electron relaxation dynamics in warm, dense plasma, several open questions and limitations remain, offering opportunities for further development in both experimental and theoretical aspects. On the experimental side, advancing ultrafast diagnostic capabilities, improving data analysis methods, and optimising spectroscopy techniques could significantly enhance the precision and scope of future studies. Theoretical developments, such as implementing advanced collision models, incorporating quantum effects, and improving simulation frameworks, are equally critical for refining the understanding of electron relaxation processes. This section outlines key directions for future work, focusing on both experimental and theoretical advancements.

Going to attosecond pulses: Recent advancements at facilities like the European XFEL have demonstrated the generation of 180 μJ pulses with durations as short as 180 as [185], offering comparable pulse energies to the current study. These attosecond pulses provide an opportunity to directly complement the existing dataset without requiring a complete re-execution of the experiments, allowing for the investigation of even earlier stages of non-thermal electron relaxation. Although current attosecond systems lack shot-to-shot

temporal diagnostics, such as XTCAV, the pulse duration (180 as) is orders of magnitude shorter than the shortest pulses in the current study (4 fs), making variations in duration a minor concern. Furthermore, ongoing advancements in attosecond XFEL technology are paving the way for reliable pulse duration measurements at the attosecond scale, which would further enhance experimental precision. Incorporating attosecond pulses into future experiments promises to revolutionise the study of ultrafast dynamics in warm dense matter.

Higher repetition rate: The current experiment operates at a repetition rate of 60 Hz, while facilities like LCLS-II are capable of reaching rates up to 1 MHz. Higher repetition rates would allow the collection of significantly more data, enabling better statistics and reducing uncertainties in the experimental results. Faster detectors are under development to accommodate these capabilities. However, achieving such rates introduces challenges, particularly the need for rastering the target, which involves significant mechanical complexities. Addressing these issues lies beyond the scope of this work, but future advancements in target delivery systems could make full use of high-repetition-rate capabilities.

Controlling target density and temperature: Future experiments should explore the dependence of the results on target density and temperature. This could be achieved by employing techniques such as controlled focusing, pump-probe setups, or dynamic compression. These approaches would allow precise manipulation of the target conditions, enabling a deeper understanding of how density and temperature affect the relaxation rates, providing valuable benchmarks for theoretical models and simulations.

Precise measurement of target conditions: In the current experiment, the target temperature was estimated to be around 30 eV, but this estimate is subject to significant inaccuracy. The XRTS spectrometer, while effective for higher temperatures, is limited by its energy resolution and is not particularly useful for precise measurements in the O[10 eV] range. Accurate determination of temperature and density remains a major challenge in this regime. However, recent advancements [199] have demonstrated the ability to measure temperatures down to 1 eV, which could pave the way for more precise characterisation of target conditions in future studies. Implementing such techniques would greatly enhance the reliability of experimental data and improve comparisons with theoretical models.

Inverse Compton scattering: Inverse Compton scattering (ICS) was theoretically developed and included in the experimental setup, but the data remain unanalysed due to time limitations. ICS has the potential to directly probe the electron distribution function, providing valuable insights into non-thermal and thermal populations. A careful analysis of the existing ICS data is essential to extract detailed information on electron relaxation. Future work should prioritise this analysis to fully leverage the capabilities of ICS as a diagnostic tool.

Better choice of material: The current experiment used Mn as the target material due to its characteristic emission lines, which maximise the signal-to-noise ratio. However, the resultant decay plot behaviour was dominated by electron-ion relaxation, leading to high uncertainty in determining the electron-electron collision rate. Since e-e and e-i relaxation rates have different dependencies on electron energy, future experiments could benefit from selecting target materials where e-e collisions dominate based on energy levels. Such a choice would allow a more precise and direct investigation of the e-e collision dynamics, reducing uncertainties and enhancing the understanding of non-thermal electron relaxation.

Higher resolution spectrometer: With e-e collisions primarily broadening the peak, while e-i collisions shift electrons out of the peak, the analysis in Chapter 5 can be augmented by measuring the broadening of the non-thermal emission peak in addition to integrating over it. The resolution of the current spectrometer (SPC) is insufficient to measure peak width accurately. To the best of the author's knowledge, no existing spectrometer can achieve the required resolution for such low-emission signals. However, future advancements in spectrometer technology may make this achievable, enabling more precise measurements of spectral features and a clearer distinction between e-e and e-i relaxation processes.

Use of machine learning data analysis: Higher repetition rate experiments would generate large-scale datasets, which could make the current SPC data analysis methods computationally infeasible. Machine learning (ML) techniques, as discussed in [200], could provide an efficient and scalable approach to analyse such large datasets. By leveraging ML, it may be possible to extract key features and trends from the data more effectively, enabling faster and more accurate analysis in future high-repetition-rate experiments.

Velocity-dependent Coulomb logarithm and alternative models: The Coulomb logarithm (CL) depends on velocity, which introduces computational challenges and was therefore omitted in the current implementation. Future work should incorporate this velocity dependence into the Fokker-Planck framework to improve modelling accuracy. Additionally, other CL models should also be implemented within the Fokker-Planck framework to allow

benchmarking against experimental outcomes. Such comparisons could help identify the most accurate and physically consistent model for describing collision dynamics.

Quantum Landau-Fokker-Planck collision operators: At low temperatures, where Fermi-Dirac statistics become significant, the classical Fokker-Planck collision operator may no longer provide accurate results. In such cases, the quantum Landau-Fokker-Planck (qLFP) collision operator should be used to account for quantum effects. This is particularly important for plasmas with temperatures of a few eV or in high-density regimes, such as those discussed in [134], which, to date, remains extremely challenging. Incorporating the qLFP operator into simulations would enable more accurate modelling of relaxation processes under these conditions.

Inhomogeneous (3D) `CCFLY` modelling: The current version of `CCFLY` is a 0-dimensional (0-D) code that assumes an isotropic electron distribution in the velocity space and a homogeneous distribution of ions and electrons in the real space. While this assumption simplifies the computational framework, it limits the ability to model anisotropic electron distributions and spatial gradients, which are critical for understanding more complex plasma systems. Future work should extend `CCFLY` to incorporate anisotropic distributions using spherical harmonic expansions [57], enabling a more accurate description of electron velocity space. Additionally, implementing a 3-dimensional (3-D) spatial model, as suggested in [111], would allow the investigation of inhomogeneous systems, such as those with significant density or temperature gradients. These advancements would provide a more comprehensive understanding of electron relaxation and transport phenomena in warm dense plasmas.

Improvements to `CCFLY`: The current implementation of `CCFLY` runs very slowly, presenting a significant bottleneck for large-scale and high-resolution simulations. The author acknowledges a limited background in large-scale scientific computing, which has constrained the optimisation of the code. `CCFLY` originates from its predecessor `FLYCHK`, which was designed for small-scale computing (for example, running on personal computers within minutes). Therefore, the engineering of `CCFLY` is far from optimal for modern high-performance computing environments. Future work should focus on re-engineering the code to leverage parallel computing, optimised algorithms, and scalable frameworks to improve performance and applicability to large datasets.

Utilizing machine learning for simulations: The current methodology involves running a large number of simulations and fitting an exponential model with parameters derived from a quadratic fit. While effective, this approach is computationally expensive and could be replaced by machine learning-based emulators. These emulators can learn the simulation outputs and predict results for given parameters with significantly reduced computational cost, as demonstrated in [201]. Implementing such machine learning techniques would streamline the workflow, enable faster exploration of parameter spaces, and make the process more efficient for large-scale studies.

With the framework established in this work and the proposed improvements, there are numerous opportunities to deepen the understanding of relaxation processes, warm dense matter, and the foundations of statistical physics and kinetic theory. Nevertheless, while this work primarily considers two-body or three-body interactions, many-body physics, which is notoriously difficult to model, has not yet been fully accounted for. Addressing these challenges remains an open question, awaiting future developments.

Appendices

A

Transition Rates and Collision Operators

Contents

A.1 Transition Rates in Atomic Kinetics 147
A.2 Electron Source Operators 148
A.3 Inelastic Collision Operators 149

A.1 Transition Rates in Atomic Kinetics

This table summarises the rates from the lower state $|\mathrm{l}\rangle$ to the upper state $|\mathrm{u}\rangle$ (or vice versa). The transition rate is the sum of all rates listed here. For any process X, S_X represents the corresponding cross-section (if applicable), and $\hbar\omega$ represents the energy of the photon (in photon-induced processes) while W represents that of an electron (in collision-induced processes). $f[W]$ represents the electron distribution function in collision-induced processes, and $\Psi[\hbar\omega]$ is the XFEL intensity profile (indicating the number of photons per unit energy) in a photon-induced process. For excitation and de-excitation, $\mathcal{N}$ is the degeneracy of the states, f is the oscillator strength. Note that "lower" always refers to the state with lower energy, regardless of the ionisation stage (therefore, in Auger decay, the upper state ion has one more electron, while in photo-ionisation, the lower state has one more electron).

Table A.1: Transition rates for various processes

Processes	**Rates**	**Notes**
Spontaneous Decay $\mathrm{u} \to \mathrm{l}$	$\frac{2q_\mathrm{e}^2 W_{\mathrm{u,l}}^2}{m_\mathrm{e}\hbar^2 v_\mathrm{c}^3}\frac{\mathcal{N}_\mathrm{l}}{\mathcal{N}_\mathrm{u}}\mathscr{f}_{\mathrm{l}\to\mathrm{u}}$	
Photon Excitation $\mathrm{l} \to \mathrm{u}$	$4\pi\beta_\mathrm{esc}\int_0^\infty S_\mathrm{PE}[\hbar\omega]\Psi[\hbar\omega]\mathrm{d}(\hbar\omega)$	See further notes [1]
Stimulated Decay $\mathrm{u} \to \mathrm{l}$	$4\pi\beta_\mathrm{esc}\int_0^\infty S_\mathrm{StD}[\hbar\omega]\Psi[\hbar\omega]\mathrm{d}(\hbar\omega)$	See further notes [2]
Collisional Excitation $\mathrm{l} \to \mathrm{u}$	$\int_{W_\mathrm{trans}}^\infty \sqrt{\frac{2W}{m_\mathrm{e}}} S_\mathrm{CE}[W] f[W]\mathrm{d}W$	$W_\mathrm{trans} = W_\mathrm{u} - W_\mathrm{l}$ is the transition energy
Collisional De-excitation $\mathrm{u} \to \mathrm{l}$	$\int_0^\infty \sqrt{\frac{2W}{m_\mathrm{e}}} S_\mathrm{CD}\left[W + W_\mathrm{trans}\right] f[W]\mathrm{d}W$	See further notes [3]
Auger Decay $\mathrm{u} \to \mathrm{l}$	k_AD	Treated as constant [78]
Dielectric Recombination $\mathrm{l} \to \mathrm{u}$	$\frac{\sqrt{2}}{16\pi}\frac{\mathcal{N}_\mathrm{u}}{\mathcal{N}_\mathrm{l}}\frac{h^3}{m_\mathrm{e}^3}\sqrt{\frac{2W_\mathrm{res}}{m_\mathrm{e}}}\frac{k_\mathrm{AD}}{W} f[W_\mathrm{R}]$	$W_\mathrm{R} = W_\mathrm{AD} - W_\mathrm{i}$ [4]
Photo-ionisation $\mathrm{l} \to \mathrm{u}$	$4\pi\int_0^\infty \Psi[\hbar\omega] S_\mathrm{PI}[\hbar\omega]\mathrm{d}(\hbar\omega)$	The ionized electron has energy $\hbar\omega - W_\mathrm{i}$
Radiative Recombination $\mathrm{u} \to \mathrm{l}$	$\int_0^\infty \sqrt{\frac{2W}{m_\mathbf{e}}} S_\mathrm{RR}[W] f[W]\mathrm{d}W$	See further notes[5]
Collisional Ionisation $\mathrm{l} \to \mathrm{u}$	$\int_{W_\mathrm{I}}^\infty \sqrt{\frac{2W}{m_\mathrm{e}}} S_\mathrm{CI}[W] f[W]\mathrm{d}W$	
Collisional Recombination $\mathrm{u} \to \mathrm{l}$	$\iint_0^\infty \frac{2\sqrt{W_1 W_2}}{m_\mathbf{e}} f[W_2]\, f[W_\mathrm{l}]\, \varkappa_\mathrm{CR}\left[W_\mathrm{l}, W_2\right] \mathrm{d}W_\mathrm{l}\mathrm{d}W_2$	See further notes [6]

A.2 Electron Source Operators

Each of the later six terms in Table A.1 either creates or absorbs electrons in the free electron distribution. These act as sources of electrons. The corresponding source operators are summarised here. Note that these are only transitions for individual transition $\mathrm{l} \to \mathrm{u}$, or vice versa. The overall source operator should be summed over all possible contributions.

[1] $S_{\mathrm{PE},l\to\mathrm{u}}[\hbar\omega] = \pi\left(\frac{q_\mathrm{e}^2}{mc}\right)\mathscr{f}_{1\to\mathrm{u}}\mathrm{V}[\omega]$, where $\mathrm{V}[\omega]$ is the Voigt function. β_esc is the escape factor.

[2] From detailed balance: $\mathcal{N}_\mathrm{l} S_{\mathrm{PE,l}\to\mathrm{u}} = \mathcal{N}_\mathrm{u} S_{\mathrm{StD,u}\to\mathrm{l}}$.

[3] $\mathcal{N}_\mathrm{l} S_{\mathrm{CD,u}\to\mathrm{l}} = \mathcal{N}_\mathrm{u} S_{\mathrm{CE,l}\to\mathrm{u}}$

[4] W_R is the residual energy of the Auger electron from the corresponding inverse process (Auger decay), where W_AD is the Auger decay transition energy, and W_i the ionisation energy of the Auger electron before being ionised.

[5] Similar to excitation and de-excitation this radiative process also has a stimulated component. This is absorbed in the cross-section: $S_\mathrm{RR} = S_\mathrm{RR,Sp} + S_\mathrm{RR,St}$, where $S_\mathrm{RR,St} = \frac{v_\mathrm{c}^2\hbar}{8\pi^2\omega^2}\Psi[\hbar\omega] S_\mathrm{RR,Sp}$ and $\hbar\omega = W + W_\mathrm{I}$(conservation of energy). $S_\mathrm{RR,Sp}$ is related to S_PI via Einstein-Milne relation: $S_{\mathrm{RR,sp,u}\to\mathrm{l}}[W] = S_{\mathrm{PI,l}\to\mathrm{u}}[\hbar\omega]\frac{\mathcal{N}_\mathrm{l}}{2\mathcal{N}_\mathrm{u}}\frac{(\hbar\omega)^2}{m_\mathrm{e}v_\mathrm{c}^2 W}$.

[6] W_1, W_2 denotes the energies of two incoming electrons, $\varkappa$ is the CR coefficient computed through the detailed balance: $\varkappa[W_1, W_2] = \frac{(2\pi\hbar)^3}{16\pi m_\mathrm{e}}\frac{\mathcal{N}_\mathrm{l}}{\mathcal{N}_\mathrm{u}}\frac{W_1+W_2+W_\mathrm{I}}{W_1 W_2}\varkappa_\mathrm{CI}[W_1+W_2+W_\mathrm{I}, W_1+W_\mathrm{I}]$. $\varkappa_\mathrm{CI}[W, W']$ is the differential cross-section of energy transfer W' in CI event from an electron with energy W[116].

Table A.2: Electron Source Operators

Processes	Source Operators	Notes
Auger Decay $\mathrm{u} \to \mathrm{l}$	$\rho_{N_\mathrm{u}} k_\mathrm{AD} \delta[W - W_\mathrm{res}]$	Treated as constant [78]
Dielectric Recombination $\mathrm{l} \to \mathrm{u}$	$-\rho_{N_\mathrm{l}} \sqrt{\frac{2W}{m_\mathrm{e}}} f[W] S_\mathrm{DR}[W] \cdot \delta[W - W_\mathrm{res}]$	
Photo-ionisation $\mathrm{l} \to \mathrm{u}$	$\rho_{N_\mathrm{l}} k_\mathrm{PI} \cdot \delta[W - (\hbar\omega - W_\mathrm{I})]$	
Radiative Recombination $\mathrm{u} \to \mathrm{l}$	$-\rho_{N_\mathrm{u}} \sqrt{\frac{2W}{m_\mathrm{e}}} f[W] S_\mathrm{RR}[W]$	
Collisional Ionisation $\mathrm{l} \to \mathrm{u}$	$\widehat{\mathcal{O}}'_\mathrm{CI} + \widehat{\mathcal{O}}''_\mathrm{CI}$	See further notes [7]
Collisional Recombination $\mathrm{u} \to \mathrm{l}$	$\widehat{\mathcal{O}}'_\mathrm{CR} + \widehat{\mathcal{O}}''_\mathrm{CR}$	See further notes [8]

A.3 Inelastic Collision Operators

Similarly, Collisional excitation and de-excitation will redistribute the electrons. These are captured by the following inelastic collision operators:

Table A.3: Inelastic Collision Operators

Processes	Source Operators	Notes
Collisional Excitation $\mathrm{l} \to \mathrm{u}$	$-\rho_{N_\mathrm{l}} \left(\sqrt{\frac{2W}{m_\mathrm{e}}} S_\mathrm{CE}[W] f[W] + \sqrt{\frac{2(W+W_\mathrm{T})}{m_\mathrm{e}}} S_\mathrm{CE}[W + W_\mathrm{T}] f[W + W_\mathrm{T}] \right)$	
Collisional De-excitation $\mathrm{u} \to \mathrm{l}$	$-\rho_{N_\mathrm{u}} \left(\sqrt{\frac{2W}{m_\mathrm{e}}} S_\mathrm{CD}[W] f[W] + \sqrt{\frac{2(W+W_\mathrm{T})}{m_\mathrm{e}}} S_\mathrm{CD}[W - W_\mathrm{T}] f[W - W_\mathrm{T}] \right)$	

[7] $\hat{\mathcal{O}}'_\mathrm{CI} = -\rho_{N_\mathrm{l}} \sqrt{\frac{2W}{m_\mathrm{e}}} f[W] S_\mathrm{CI}[W]$, $\hat{\mathcal{O}}''_\mathrm{CI} = \rho_{N_\mathrm{l}} \int \sqrt{\frac{2(W+W')}{m_\mathrm{e}}} f[W + W'] \varkappa_\mathrm{CI}[W + W', W'] \mathrm{d}W' + \rho_{N_\mathrm{l}} \int \sqrt{\frac{2(W+W')}{m_\mathrm{e}}} f[W + W'] \varkappa_\mathrm{CI}[W + W', W' + W_\mathrm{i}] \mathrm{d}W'$. This represents removing one electron with energy W and creating two electrons both with energy W.

[8] $\hat{\mathcal{O}}'_\mathrm{CR} = -\rho_{N_\mathrm{l}} \left(\int \varkappa_\mathrm{CR}[W_1, W] \sqrt{\frac{2W_1}{m_\mathrm{e}}} f[W_1] \mathrm{d}W_1 + \int \varkappa_\mathrm{CR}[W, W_2] \sqrt{\frac{2W_2}{m_\mathrm{e}}} f[W_2] \mathrm{d}W_2 \right) \sqrt{\frac{2W}{m_\mathrm{e}}} f[W]$,
$\hat{\mathcal{O}}'_\mathrm{CR} = \rho_{N_\mathrm{l}} \int \varkappa_\mathrm{CR}[W' - W_\mathrm{I}, W - W'] \sqrt{\frac{2(W-W')}{m_\mathrm{e}}} f[W - W'] \sqrt{\frac{2(W'-W_\mathrm{I})}{m_\mathrm{e}}} f[W' - W_\mathrm{I}] \mathrm{d}W'$

References

[1] Forrest J. Rogers and Carlos A. Iglesias. “Astrophysical Opacity”. In: *Science* 263.5143 (1994), pp. 50–55.

[2] Gilles Chabrier. “Plasma physics and planetary astrophysics”. In: *Plasma Physics and Controlled Fusion* 51.12 (2009), p. 124014.

[3] Tristan Guillot. “Interiors of Giant Planets Inside and Outside the Solar System”. In: *Science* 286.5437 (1999), pp. 72–77.

[4] Francis F. Chen. *Introduction to plasma physics and controlled fusion*. Dec. 2015.

[5] John D. Lindl et al. “The physics basis for ignition using indirect-drive targets on the National Ignition Facility”. In: *Physics of Plasmas* 11.2 (2004), pp. 339–491.

[6] S. X. Hu et al. “Strong coupling and degeneracy effects in inertial confinement fusion implosions”. In: *Physical Review Letters* 104.23 (June 2010).

[7] O. A. Hurricane et al. “Fuel gain exceeding unity in an inertially confined fusion implosion”. In: *Nature* 506.7488 (Feb. 2014), pp. 343–348.

[8] A. B. Zylstra et al. “Burning plasma achieved in inertial fusion”. In: *Nature* 601.7894 (Jan. 2022), pp. 542–548.

[9] Bruce A. Remington, R. Paul Drake, and Dmitri D. Ryutov. “Experimental astrophysics with high power lasers andZpinches”. In: *Reviews of Modern Physics* 78.3 (Aug. 2006), pp. 755–807.

[10] D. Kraus et al. “Formation of diamonds in laser-compressed hydrocarbons at planetary interior conditions”. In: *Nature Astronomy* 1.9 (Aug. 2017), pp. 606–611.

[11] B. Militzer et al. “A Massive Core in Jupiter Predicted from First-Principles Simulations”. In: *The Astrophysical Journal* 688.1 (Oct. 2008), pp. L45–L48.

[12] National Research and Sciences Council, Division on Engineering and Physical and Astronomy, Board on Physics and Committee, Plasma Science and Physics, Committee on High Energy Density Plasma. *Frontiers in High Energy Density Physics: The X-Games of Contemporary Science*. National Academies Press, May 2003.

[13] T. E. Faber and John Ziman. “A theory of the electrical properties of liquid metals”. In: *The philosophical magazine* 11.109 (Jan. 1965), pp. 153–173.

[14] S Toleikis et al. “Probing near-solid density plasmas using soft x-ray scattering”. In: *Journal of Physics B: Atomic, Molecular and Optical Physics* 43.19 (Sept. 2010), p. 194017.

[15] S. M. Vinko et al. “Creation and diagnosis of a solid-density plasma with an X-ray free-electron laser”. In: *Nature* 482.7383 (2012), pp. 59–62.

[16] A. Lévy et al. “The creation of large-volume, gradient-free warm dense matter with an x-ray free-electron laser”. In: *Physics of Plasmas* 22.3 (Mar. 2015), p. 030703.

[17] O. Ciricosta et al. “Detailed model for hot-dense aluminum plasmas generated by an x-ray free electron laser”. In: *Physics of Plasmas* 23.2 (2016), p. 022707.

[18] M. G. Gorman et al. “Direct observation of melting in Shock-Compressed bismuth with femtosecond x-ray diffraction”. In: *Physical Review Letters* 115.9 (Aug. 2015).

[19] Justin S. Wark, Malcolm I. McMahon, and Jon H. Eggert. “Femtosecond diffraction and dynamic high pressure science”. In: *Journal of Applied Physics* 132.8 (Aug. 2022).

[20] A. Amouretti et al. *Phase transitions of Fe_2O_3 under laser shock compression*. 2024. arXiv: 2402.18432 [cond-mat.mtrl-sci].

[21] M. Sliwa et al. “Femtosecond X-Ray Diffraction Studies of the Reversal of the Microstructural Effects of Plastic Deformation during Shock Release of Tantalum”. In: *Physical Review Letters* 120.26 (June 2018).

[22] Céline Crépisson et al. *Shock-driven amorphization and melt in Fe_2O_3*. 2024. arXiv: 2408.17204 [cond-mat.mtrl-sci].

[23] James M. Glownia et al. “Time-resolved pump-probe experiments at the LCLS”. In: *Optics Express* 18.17 (Aug. 2010), p. 17620.

[24] Siegfried H. Glenzer and Ronald Redmer. “X-ray Thomson scattering in high energy density plasmas”. In: *Reviews of Modern Physics* 81.4 (Dec. 2009), pp. 1625–1663.

[25] L. B. Fletcher et al. “Ultrabright X-ray laser scattering for dynamic warm dense matter physics”. In: *Nature Photonics* 9.4 (Mar. 2015), pp. 274–279.

[26] L. B. Fletcher et al. “X-ray Thomson scattering measurements of temperature and density from multi-shocked CH capsules”. In: *Physics of Plasmas* 20.5 (May 2013).

[27] B. I. Cho et al. “Resonant K_α Spectroscopy of Solid-Density Aluminum Plasmas”. In: *Physical Review Letters* 109.24 (2012).

[28] Robert S. Cohen, Lyman Spitzer, and Paul McR. Routly. “The Electrical Conductivity of an Ionized Gas”. In: *Physical Review* 80.2 (1950), pp. 230–238.

[29] H Brysk. “Electron-ion equilibration in a partially degenerate plasma”. In: *Plasma Physics* 16.10 (Oct. 1974), pp. 927–932.

[30] Lyman Spitzer and Richard Härm. “Transport phenomena in a completely ionized gas”. In: *Physical Review* 89.5 (Mar. 1953), pp. 977–981.

[31] Setsuo Ichimaru. *Statistical Physics of dense plasmas*. Jan. 2019.

[32] E. Wigner. “On the Interaction of Electrons in Metals”. In: *Physical Review* 46.11 (Dec. 1934), pp. 1002–1011.

[33] H. Thomas et al. “Plasma Crystal: Coulomb Crystallization in a Dusty Plasma”. In: *Physical Review Letters* 73.5 (Aug. 1994), pp. 652–655.

[34] Setsuo Ichimaru. “Strongly coupled plasmas: high-density classical plasmas and degenerate electron liquids”. In: *Reviews of Modern Physics* 54.4 (Oct. 1982), pp. 1017–1059.

[35] Einar Hinnov and Joseph G. Hirschberg. “Electron-Ion Recombination in Dense Plasmas”. In: *Physical Review* 125.3 (Feb. 1962), pp. 795–801.

[36] J C Weisheit. “Recombination in dense plasmas”. In: *Journal of Physics B Atomic and Molecular Physics* 8.15 (Oct. 1975), pp. 2556–2564.

[37] Thomas Gawne et al. “Investigating mechanisms of state localization in highly ionized dense plasmas”. In: *Physical review. E* 108.3 (Sept. 2023).

[38] P. Hohenberg and W. Kohn. “Inhomogeneous Electron Gas”. In: *Physical Review* 136.3B (Nov. 1964), B864–B871.

[39] Erich Runge and E. K. U. Gross. “Density-Functional Theory for Time-Dependent Systems”. In: *Physical Review Letters* 52.12 (Mar. 1984), pp. 997–1000.

[40] H. Reinholz et al. “Conductivity of warm dense matter including electron-electron collisions”. In: *Physical Review E* 91.4 (Apr. 2015).

[41] K. P. Driver and B. Militzer. “All-Electron Path Integral Monte Carlo Simulations of Warm Dense Matter: Application to Water and Carbon Plasmas”. In: *Physical Review Letters* 108.11 (Mar. 2012).

[42] Bradley W. Carroll and Dale A. Ostlie. *An introduction to modern astrophysics*. Sept. 2017.

[43] Hae Ja Lee et al. “Driving Iron plasmas to stellar core conditions using extreme x-ray radiation”. In: *Research Square (Research Square)* (July 2023).

[44] John M. J. Madey. “Stimulated emission of Bremsstrahlung in a periodic magnetic field”. In: *Journal of Applied Physics* 42.5 (Apr. 1971), pp. 1906–1913.

[45] Luis R. Elias et al. “Observation of stimulated emission of radiation by relativistic electrons in a spatially periodic transverse magnetic field”. In: *Physical Review Letters* 36.13 (Mar. 1976), pp. 717–720.

[46] A. Nilsson et al. “Catalysis in real time using X-ray lasers”. In: *Chemical Physics Letters* 675 (Feb. 2017), pp. 145–173.

[47] Walter Bambynek et al. “X-Ray fluorescence yields, Auger, and Coster-Kronig transition probabilities”. In: *Reviews of Modern Physics* 44.4 (Oct. 1972), pp. 716–813.

[48] S. M. Vinko et al. “Investigation of femtosecond collisional ionization rates in a solid-density aluminium plasma”. In: *Nature Communications* 6.1 (2015).

[49] Q. Y. Van Den Berg et al. “Clocking Femtosecond Collisional Dynamics via Resonant X-Ray Spectroscopy”. In: *Physical Review Letters* 120.5 (Feb. 2018).

[50] Kittel. *Introduction to Solid State Physics, 7th Ed.* John Wiley & Sons, Jan. 2007.

[51] P. L. Bhatnagar, E. P. Gross, and M. Krook. “A model for collision processes in gases. i. Small amplitude processes in charged and neutral One-Component systems”. In: *Physical Review* 94.3 (May 1954), pp. 511–525.

[52] E. P. Gross and M. Krook. “Model for collision processes in gases: Small-Amplitude oscillations of charged Two-Component systems”. In: *Physical Review* 102.3 (May 1956), pp. 593–604.

[53] David Tong. *Kinetic theory*. Graduate Course, University of Cambridge, Cambridge, UK, 2012.

[54] Joachim Appel. “Electron-Electron scattering and transport phenomena in nonpolar semiconductors”. In: *Physical Review* 122.6 (June 1961), pp. 1760–1772.

[55] H. Reinholz and G. Röpke. “Dielectric function beyond the random-phase approximation: Kinetic theory versus linear response theory”. In: *Physical Review E* 85.3 (Mar. 2012).

[56] J. D. Huba. *NRL Plasma Formulary*. Naval Research Laboratory, Washington, 2013.

[57] M. Tzoufras et al. “A Vlasov – Fokker – Planck code for high energy density physics”. In: *Journal of Computational Physics* 230.17 (2011), pp. 6475–6494.

[58] P. Mulser, G. Alber, and M. Murakami. “Revision of the Coulomb logarithm in the ideal plasma”. In: *Physics of Plasmas* 21.4 (2014), p. 042103.

[59] C. E. Starrett. “Coulomb log for conductivity of dense plasmas”. In: *Physics of Plasmas* 25.9 (Sept. 2018).

[60] P. Mora. “Coulomb logarithm accuracy in a Yukawa potential”. In: *Phys. Rev. E* 102 (3 Sept. 2020), p. 033206.

[61] F. J. Blatt. *Theory of mobility of electrons in solids*. Jan. 1957, pp. 199–366.

[62] G. Röpke. “Quantum-statistical approach to the electrical conductivity of dense, high-temperature plasmas”. In: *Physical review* 38.6 (Sept. 1988), pp. 3001–3016.

[63] R. Redmer. “Physical properties of dense, low-temperature plasmas”. In: *Physics Reports* 282.2-3 (Apr. 1997), pp. 35–157.

[64] S.K. Kodanova et al. “Relaxation of non-isothermal hot dense plasma parameters”. In: *Matter and Radiation at Extremes* 3.1 (2018), pp. 40–49.

[65] Setsuo Ichimaru and Shigenori Tanaka. “Theory of interparticle correlations in dense, high-temperature plasmas. V. Electric and thermal conductivities”. In: *Physical Review A* 32.3 (1985), pp. 1790–1798.

[66] S. X. Hu et al. “First-principles thermal conductivity of warm-dense deuterium plasmas for inertial confinement fusion applications”. In: *Physical Review E* 89.4 (2014).

[67] D. O. Gericke, M. S. Murillo, and M. Schlanges. “Dense plasma temperature equilibration in the binary collision approximation”. In: *Physical Review E* 65.3 (2002).

[68] H.-K. Chung et al. “FLYCHK: Generalized population kinetics and spectral model for rapid spectroscopic analysis for all elements”. In: *High Energy Density Physics* 1.1 (2005), pp. 3–12.

[69] Shenyuan Ren et al. “Non-thermal evolution of dense plasmas driven by intense x-ray fields”. In: *Communications Physics* 6.1 (2023), p. 99.

[70] H.-K. Chung et al. “Atomic processes modeling of X-ray free electron laser produced plasmas using SCFLY code”. In: *AIP Conference Proceedings* (2017).

[71] Josef Krása et al. “Ion emission from warm dense matter produced by irradiation with a soft x-ray free-electron laser”. In: *Matter and Radiation at Extremes* 9.1 (Nov. 2023).

[72] Y.-F. Shi et al. “Exploring relaxation dynamics in warm dense plasmas by tailoring non-thermal electron distributions with a free electron laser”. In: *Physics of Plasmas* 31.8 (Aug. 2024).

[73] Alessandro Forte et al. “Resonant inelastic x-ray scattering in warm-dense Fe compounds beyond the SASE FEL resolution limit”. In: *Communications Physics* 7.1 (Aug. 2024).

[74] Alessandro Forte et al. *Methods for energy dispersive x-ray spectroscopy with photon-counting and deconvolution techniques*. 2024. arXiv: `2411.16581 [physics.app-ph]`.

[75] Braginski S. I. *Transport processes in a plasma*. Jan. 1965.

[76] Thomas Peter and Jürgen Meyer-Ter-Vehn. “Energy loss of heavy ions in dense plasma. I. Linear and nonlinear Vlasov theory for the stopping power”. In: *Physical Review A* 43.4 (Feb. 1991), pp. 1998–2014.

[77] L. P. Pitaevskii and E.M. Lifshitz. *Physical kinetics*. Butterworth-Heinemann, Dec. 2012.

[78] Mau Hsuing Chen, Bernd Crasemann, and Hans Mark. "Relativistic K-shell Auger rates, level widths, and fluorescence yields". In: *Physical Review A* 21.2 (1980), pp. 436–441.

[79] Richard Fitzpatrick. *Plasma Physics*. CRC Press, Aug. 2014.

[80] Sydney Chapman and T. G. Cowling. *The Mathematical Theory of non-uniform gases*. Cambridge University Press, Jan. 1990.

[81] Andrew Lenard. "On Bogoliubov's kinetic equation for a spatially homogeneous plasma". In: *Annals of Physics* 10.3 (July 1960), pp. 390–400.

[82] R. Balescu. "Irreversible Processes in Ionized Gases". In: *The Physics of Fluids* 3.1 (Jan. 1960), pp. 52–63.

[83] R. Balescu. "Approach to equilibrium of a quantum plasma". In: *The Physics of Fluids* 4.1 (Jan. 1961), pp. 94–99.

[84] Setsuo Ichimaru. "Theory of Strong Turbulence in Plasmas". In: *The Physics of Fluids* 13.6 (June 1970), pp. 1560–1572.

[85] M. Nambu. "Collision terms for plasmas with strong correlation". In: *Physics Letters A* 39.4 (May 1972), pp. 303–304.

[86] Uwe Czarnetzki and Luís Lemos Alves. "Describing local and non-local electron heating by the Fokker–Planck equation". In: *Reviews of Modern Plasma Physics* 6.1 (2022), p. 31.

[87] Chi-Kang Li and Richard D. Petrasso. "Fokker-Planck equation for moderately coupled plasmas". In: *Phys. Rev. Lett.* 70 (20 May 1993), pp. 3063–3066.

[88] Keiichi Nishimura. "Velocity Dependence of the Coulomb Logarithm and the Temperature Equalization of Electrons and Ions in a Plasma". In: *Physical Review* 152.1 (1966), pp. 177–181.

[89] Kip S. Thorne and Roger D. Blandford. *Modern Classical Physics: optics, fluids, plasmas, elasticity, relativity, and statistical Physics*. Sept. 2017.

[90] R.L. Liboff. *Kinetic theory*. Springer Science & Business Media, Sept. 2003.

[91] Felix I Parra. *The Linearized Fokker-Planck Collision Operator and the Spitzer-H¨arm Problem*.

[92] Jérôme Daligault. "On the quantum Landau collision operator and electron collisions in dense plasmas". In: *Physics of Plasmas* 23.3 (Mar. 2016).

[93] J. A. Krommes. "An introduction to the physics of the Coulomb logarithm, with emphasis on quantum-mechanical effects". In: *Journal of Plasma Physics* 85.1 (2019).

[94] Jérôme Daligault. "Collisional transport coefficients of dense high-temperature plasmas within the quantum Landau-Fokker-Planck framework". In: *Physics of Plasmas* 25.8 (Aug. 2018).

[95] Hai P. Le. "Quantum Fokker-Planck modeling of degenerate electrons". In: *Journal of Computational Physics* 434 (Feb. 2021), p. 110230.

[96] R. J. DiPerna and P. L. Lions. "On the Cauchy Problem for Boltzmann Equations: Global Existence and Weak Stability". In: *Annals of Mathematics* 130.2 (Sept. 1989), p. 321.

[97] Cédric Villani. "On a new class of weak solutions to the spatially homogeneous Boltzmann and Landau equations". In: *Archive for Rational Mechanics and Analysis* 143.3 (Sept. 1998), pp. 273–307.

[98] A. V. Bobylev. "Exact solutions of the Boltzmann equation". In: *Sov. Phys. - Dokl. (Engl. Transl.); (United States)* 225.12 (Dec. 1975), pp. 1296–1299.

[99] A.V. Bobylev and V.A. Chuyanov. "On the numerical solution of Landau's kinetic equation". In: *USSR Computational Mathematics and Mathematical Physics* 16.2 (1976), pp. 121–130.

[100] Max Krook and Tai Tsun Wu. "Exact solutions of the Boltzmann equation". In: *The Physics of Fluids* 20.10 (Oct. 1977), pp. 1589–1595.

[101] Hai P. Le and Jean-Luc Cambier. "Conservative algorithms for non-Maxwellian plasma kinetics". In: *Physics of Plasmas* 24.12 (2017), p. 122105.

[102] Alberto G. De La Varga et al. "Non-Maxwellian electron distributions in time-dependent simulations of low-Z materials illuminated by a high-intensity X-ray laser". In: *High Energy Density Physics* 9.3 (May 2013), pp. 542–547.

[103] M. S. Cho et al. "Numerical investigation of nonequilibrium electron effects on the collisional ionization rate in the collisional-radiative model". In: *Phys. Rev. E* 109 (4 Apr. 2024), p. 045207.

[104] Sergei Nayakshin and Fulvio Melia. "Self-consistent Fokker-Planck Treatment of Particle Distributions in Astrophysical Plasmas". In: *The Astrophysical Journal Supplement Series* 114.2 (Feb. 1998), p. 269.

[105] Klaus Morawetz. *Interacting Systems far from Equilibrium*. Dec. 2017.

[106] Yoshimasa Hidaka et al. "Foundations and applications of quantum kinetic theory". In: *Progress in Particle and Nuclear Physics* 127 (Aug. 2022), p. 103989.

[107] D. Kremp et al. "Quantum kinetic theory of plasmas in strong laser fields". In: *Physical review. E, Statistical physics, plasmas, fluids, and related interdisciplinary topics* 60.4 (Oct. 1999), pp. 4725–4732.

[108] Gert Brodin and Jens Zamanian. "Quantum kinetic theory of plasmas". In: *Reviews of Modern Plasma Physics* 6.1 (Feb. 2022).

[109] Quan Sun et al. "Measurement of the collision time of dense electronic plasma induced by a femtosecond laser in fused silica". In: *Optics Letters* 30.3 (Feb. 2005), p. 320.

[110] Changji Pan et al. "Temporal-spatial measurement of electron relaxation time in femtosecond laser induced plasma using two-color pump-probe imaging technique". In: *Applied Physics Letters* 112.19 (May 2018), p. 191101.

[111] T. R. Preston et al. "Measurements of the K-Shell Opacity of a Solid-Density Magnesium Plasma Heated by an X-Ray Free-Electron Laser". In: *Phys. Rev. Lett.* 119 (8 Aug. 2017), p. 085001.

[112] S. M. Vinko et al. "Time-Resolved XUV Opacity Measurements of Warm Dense Aluminum". In: *Phys. Rev. Lett.* 124 (22 June 2020), p. 225002.

[113] S.M. Vinko et al. "Free – free opacity in warm dense aluminum". In: *High Energy Density Physics* 5.3 (2009), pp. 124–131.

[114] P. Hollebon et al. "Ab initio simulations and measurements of the free-free opacity in aluminum". In: *Phys. Rev. E* 100 (4 Oct. 2019), p. 043207.

[115] B.J.B. Crowley. "Continuum lowering – A new perspective". In: *High Energy Density Physics* 13 (2014), pp. 84–102.

[116] Q. Y. van den Berg. "Femtosecond electron dynamics in hot solid-density plasmas". PhD thesis. University of Oxford, 2021.

[117] Marshall N. Rosenbluth, William M. MacDonald, and David L. Judd. "Fokker-Planck Equation for an Inverse-Square Force". In: *Physical Review* 107.1 (1957), pp. 1–6.

[118] W. Lotz. "An empirical formula for the electron-impact ionization cross-section". In: *The European Physical Journal A* 206.2 (Apr. 1967), pp. 205–211.

[119] H. Van Regemorter. "Rate of collisional excitation in stellar atmospheres". In: *The Astrophysical Journal* 136 (Nov. 1962), p. 906.

[120] Wm.J. Veigele. "Photon cross sections from 0.1 keV to 1 MeV for elements Z = 1 to Z = 94". In: *Atomic Data and Nuclear Data Tables* 5.1 (Jan. 1973), pp. 51–111.

[121] *LCLS FEL Parameters* . Jan. 2022.

[122] S. Matsuyama et al. "Nanofocusing of X-ray free-electron laser using wavefront-corrected multilayer focusing mirrors". In: *Scientific reports* 8.1 (Nov. 2018).

[123] G. Gregori et al. "Electronic structure measurements of dense plasmas". In: *Physics of Plasmas* 11.5 (Apr. 2004), pp. 2754–2762.

[124] M. J. MacDonald et al. "Measurement of high-dynamic range x-ray Thomson scattering spectra for the characterization of nano-plasmas at LCLS". In: *Review of Scientific Instruments* 87.11 (Aug. 2016).

[125] J. Lu et al. "Development of spatially resolved high resolution x-ray spectroscopy for fusion and light-source research". In: *Proceedings of SPIE, the International Society for Optical Engineering/Proceedings of SPIE* (Sept. 2014).

[126] J. Lu et al. "Characterization of x-ray imaging crystal spectrometer for high-resolution spatially-resolved x-ray Thomson scattering measurements in shock-compressed experiments". In: *Journal of Quantitative Spectroscopy and Radiative Transfer* 187 (Oct. 2016), pp. 247–254.

[127] H. Poole et al. "A case study of using x-ray Thomson scattering to diagnose the in-flight plasma conditions of DT cryogenic implosions". In: *Physics of Plasmas* 29.7 (July 2022).

[128] Satoshi Tanaka and Shaul Mukamel. "Coherent X-Ray Raman Spectroscopy: A Nonlinear Local Probe for Electronic Excitations". In: *Physical Review Letters* 89.4 (July 2002).

[129] K. Voigt et al. "Demonstration of an x-ray Raman spectroscopy setup to study warm dense carbon at the high energy density instrument of European XFEL". In: *Physics of Plasmas* 28.8 (Aug. 2021).

[130] Nobuya Iwamoto, Norimasa Umesaki, and Shigeki Endo. "Characterization of plasma-sprayed zirconia coatings by X-ray diffraction and Raman spectroscopy". In: *Thin Solid Films* 127.1-2 (May 1985), pp. 129–138.

[131] O. S. Humphries et al. "Probing the Electronic Structure of Warm Dense Nickel via Resonant Inelastic X-Ray Scattering". In: *Physical Review Letters* 125.19 (Nov. 2020).

[132] V. K. Unnikrishnan et al. "Measurements of plasma temperature and electron density in laser-induced copper plasma by time-resolved spectroscopy of neutral atom and ion emissions". In: *Pramana* 74.6 (June 2010), pp. 983–993.

[133] S. S. Harilal et al. "Electron density and temperature measurements in a laser produced carbon plasma". In: *Journal of Applied Physics* 82.5 (Sept. 1997), pp. 2140–2146.

[134] H. J. Lee et al. "X-Ray Thomson-Scattering measurements of density and temperature in Shock-Compressed beryllium". In: *Physical Review Letters* 102.11 (Mar. 2009).

[135] E. García Saiz et al. “Probing warm dense lithium by inelastic X-ray scattering”. In: *Nature Physics* 4.12 (Oct. 2008), pp. 940–944.

[136] Shu-Xing Wang and Lin-Fan Zhu. “Non-resonant inelastic X-ray scattering spectroscopy: A momentum probe to detect the electronic structures of atoms and molecules”. In: *Matter and Radiation at Extremes* 5.5 (July 2020).

[137] O. Ciricosta et al. “Direct Measurements of the Ionization Potential Depression in a Dense Plasma”. In: *Physical Review Letters* 109.6 (2012).

[138] G. Pérez-Callejo et al. “Dielectronic satellite emission from a solid-density Mg plasma: Relationship to models of ionization potential depression”. In: *Physical review. E* 109.4 (Apr. 2024).

[139] Max Born and Emil Wolf. *Principles of optics: electromagnetic theory of propagation, interference and diffraction of light*. Elsevier, 2013.

[140] William Lawrence Bragg. “The analysis of crystals by the X-ray spectrometer”. In: *Proceedings of the Royal Society of London Series A Containing Papers of a Mathematical and Physical Character* 89.613 (Feb. 1914), pp. 468–489.

[141] K. Ramakanth Hebbar. *Basics of X-Ray diffraction and its applications*. I. K. International Pvt Ltd, Jan. 2007.

[142] R R Fäustlin et al. “A compact soft X-ray spectrograph combining high efficiency and resolution”. In: *Journal of Instrumentation* 5.02 (Feb. 2010), P02004.

[143] C. Stoeckl et al. “Operation of a single-photon – counting x-ray charge-coupled device camera spectrometer in a petawatt environment”. In: *Review of Scientific Instruments* 75.10 (Oct. 2004), pp. 3705–3707.

[144] James R. Janesick. *Scientific Charge-Coupled devices*. Jan. 2001.

[145] Christian Brönnimann and Peter Trüb. *Hybrid Pixel Photon Counting X-Ray Detectors for Synchrotron Radiation*. Jan. 2016, pp. 995–1027.

[146] Glenn F. Knoll. *Radiation detection and measurement*. John Wiley & Sons, Jan. 1979.

[147] F Scholze and G Ulm. “Characterization of a windowless Si(Li) detector in the photon energy range 0.1 – 5 keV”. In: *Nuclear Instruments and Methods in Physics Research Section A Accelerators Spectrometers Detectors and Associated Equipment* 339.1-2 (Jan. 1994), pp. 49–54.

[148] Sol M. Gruner, Mark W. Tate, and Eric F. Eikenberry. “Charge-coupled device area x-ray detectors”. In: *Review of Scientific Instruments* 73.8 (July 2002), pp. 2815–2842.

[149] Neil J. Murray et al. “The X-ray quantum efficiency measurement of high resistivity CCDs”. In: *Nuclear Instruments and Methods in Physics Research Section A Accelerators Spectrometers Detectors and Associated Equipment* 604.1-2 (Jan. 2009), pp. 180–182.

[150] Hong Du and Kenneth J. Voss. “Effects of point-spread function on calibration and radiometric accuracy of CCD camera”. In: *Applied Optics* 43.3 (Jan. 2004), p. 665.

[151] Panagiotis F. Liaparinos et al. “Monte Carlo study on the imaging performance of powder phosphor screens under x-ray excitation: Comparison with screens”. In: *Medical Physics* 34.5 (Apr. 2007), pp. 1724–1733.

[152] George G. Pavlov and John A. Nousek. “Charge diffusion in CCD X-ray detectors”. In: *Nuclear Instruments and Methods in Physics Research Section A Accelerators Spectrometers Detectors and Associated Equipment* 428.2-3 (June 1999), pp. 348–366.

[153] Ian S. McLean. *Electronic imaging in astronomy*. Springer Science & Business Media, Aug. 2008.

[154] C. Fourment et al. "Broadband, high dynamics and high resolution charge coupled device-based spectrometer in dynamic mode for multi-keV repetitive x-ray sources". In: *Review of Scientific Instruments* 80.8 (Aug. 2009).

[155] *Excellence in X-Ray Detection: Advanced X-Ray Cameras for Scientific and Industrial Applications*. eprint: `PrincetonInstruments`.

[156] Michael Bruce Swift. "Comparison of confidence intervals for a poisson mean – further considerations". In: *Communication in Statistics- Theory and Methods* 38.5 (Feb. 2009), pp. 748–759.

[157] F. Garwood. "(i) Fiducial Limits for the Poisson Distribution". In: *Biometrika* 28.3-4 (Dec. 1936), pp. 437–442.

[158] Steven A. Rodney and John L. Tonry. "Characterizing Charge Diffusion in CCDs with X-Rays". In: *Publications of the Astronomical Society of the Pacific* 118.844 (June 2006), pp. 866–873.

[159] E. Lefa, S. R. Kelner, and F. A. Aharonian. "On the Spectral Shape of Radiation Due to Inverse Compton Scattering Close to the Maximum Cutoff". In: *The Astrophysical Journal* 753.2 (June 2012), p. 176.

[160] Rafał Moderski et al. "Klein-Nishina effects in the spectra of non-thermal sources immersed in external radiation fields". In: *Monthly Notices of the Royal Astronomical Society* 363.3 (Sept. 2005), pp. 954–966.

[161] H. Krawczynski. "The Polarization Properties of Inverse Compton Emission and Implications for Blazar Observations with Thegemsx-Ray Polarimeter". In: *The Astrophysical Journal* 744.1 (Dec. 2011), p. 30.

[162] C. Curatolo, L. Lanz, and V. Petrillo. "Inverse Compton cross section revisited". In: *Physics Procedia* 52 (Jan. 2014), pp. 46–51.

[163] O. Klein and Y. Nishina. *On the Scattering of Radiation by Free Electrons According to Dirac's New Relativistic Quantum Dynamics*. Mar. 2014, pp. 253–272.

[164] C. Fourment et al. "Experimental determination of temperature-dependent electron-electron collision frequency in isochorically heated warm dense gold". In: *Physical Review B* 89.16 (Apr. 2014).

[165] Peng Zhang et al. "A direct measurement method of quantum relaxation time". In: *National Science Review* 8.4 (Sept. 2020).

[166] Y. Ding et al. "Measurements and simulations of ultralow emittance and ultrashort electron beams in the LINAC Coherent light source". In: *Physical Review Letters* 102.25 (June 2009).

[167] A. Marinelli et al. "Experimental demonstration of a single-spike hard-X-ray free-electron laser starting from noise". In: *Applied Physics Letters* 111.15 (Oct. 2017).

[168] P. Emma et al. "Femtosecond and Subfemtosecond X-Ray Pulses from a Self-Amplified Spontaneous-Emission – Based Free-Electron Laser". In: *Physical Review Letters* 92.7 (Feb. 2004).

[169] V Wacker et al. "Sub-femtosecond hard x-ray pulse from very low charge beam at LCLS". In: *THPD31, Proceedings of FEL* (Jan. 2012), pp. 606–609.

[170] S. Huang et al. “Generating Single-Spike Hard X-Ray Pulses with Nonlinear Bunch Compression in Free-Electron Lasers”. In: *Physical Review Letters* 119.15 (Oct. 2017).

[171] Y. Ding et al. “Generation of attosecond x-ray pulses with a multicycle two-color enhanced self-amplified spontaneous emission scheme”. In: *Physical Review Special Topics - Accelerators and Beams* 12.6 (June 2009).

[172] Alexander A. Zholents. “Method of an enhanced self-amplified spontaneous emission for x-ray free electron lasers”. In: *Physical Review Special Topics - Accelerators and Beams* 8.4 (Apr. 2005).

[173] E. L. Saldin, E. A. Schneidmiller, and M. V. Yurkov. “Self-amplified spontaneous emission FEL with energy-chirped electron beam and its application for generation of attosecond x-ray pulses”. In: *Physical Review Special Topics - Accelerators and Beams* 9.5 (May 2006).

[174] James P. Cryan et al. *The development of attosecond XFELs for understanding ultrafast electron motion*. Jan. 2022, pp. 1–64.

[175] Joseph Duris et al. “Tunable isolated attosecond X-ray pulses with gigawatt peak power from a free-electron laser”. In: *Nature Photonics* 14.1 (Dec. 2019), pp. 30–36.

[176] D. Xiang et al. “Evidence of High Harmonics from Echo-Enabled Harmonic Generation for Seeding X-Ray Free Electron Lasers”. In: *Physical Review Letters* 108.2 (Jan. 2012).

[177] Chao Feng et al. “Coherent and ultrashort soft x-ray pulses from echo-enabled harmonic cascade free-electron lasers”. In: *Optica* 9.7 (June 2022), p. 785.

[178] Yaozong Xiao, Chao Feng, and Bo Liu. “Generating isolated attosecond X-Ray pulses by wavefront control in a seeded Free-Electron laser”. In: *Ultrafast Science* 2022 (Jan. 2022).

[179] David Gauthier et al. “Chirped pulse amplification in an extreme-ultraviolet free-electron laser”. In: *Nature Communications* 7.1 (Dec. 2016).

[180] Haoyuan Li et al. “Femtosecond-Terawatt Hard X-Ray Pulse Generation with Chirped Pulse Amplification on a Free Electron Laser”. In: *Physical Review Letters* 129.21 (Nov. 2022).

[181] Y. Ding et al. “Femtosecond x-ray pulse temporal characterization in free-electron lasers using a transverse deflector”. In: *Physical Review Special Topics - Accelerators and Beams* 14.12 (Dec. 2011).

[182] C. Behrens et al. “Few-femtosecond time-resolved measurements of X-ray free-electron lasers”. In: *Nature Communications* 5.1 (Apr. 2014).

[183] Florian Christie et al. “Temporal X-ray Reconstruction using Temporal and Spectral Measurements at LCLS”. In: *Scientific Reports* 10.1 (June 2020).

[184] Kristina Dingel et al. “Artificial intelligence for online characterization of ultrashort X-ray free-electron laser pulses”. In: *Scientific Reports* 12.1 (Oct. 2022).

[185] Jiawei Yan et al. “Terawatt-attosecond hard X-ray free-electron laser at high repetition rate”. In: *Nature Photonics* (Nov. 2024).

[186] LCLS Detector Department. *LCLS Detector Department | Linac Coherent Light Source*.

[187] Sanghoon Song et al. “Measurement of the Absolute Number of Photons of the Hard X-ray Beamline at the Linac Coherent Light Source”. In: *Journal of Synchrotron Radiation* 26.2 (Mar. 2019), pp. 320–327.

[188] D. Ratner et al. “Second and Third Harmonic Measurements at the Linac Coherent Light Source”. In: *Physical Review Special Topics - Accelerators and Beams* 14.6 (June 2011), p. 060701.

[189] Hari R. Varma et al. “Above-Threshold Ionization in the x-Ray Regime”. In: *Physical Review A* 80.5 (Nov. 2009), p. 053424.

[190] Kenji Tamasaku et al. “Nonlinear Spectroscopy with X-Ray Two-Photon Absorption in Metallic Copper”. In: *Physical Review Letters* 121.8 (Aug. 2018), p. 083901.

[191] LCLS XTCAV team. *XTCAV Documentation - LCLS Data Analysis - SLAC Confluence*. Mar. 18, 2024.

[192] LCLS XTCAV team. personal communication. Dec. 12, 2022.

[193] Dimitri Khaghani. personal communication. Apr. 12, 2025.

[194] M. F. Kasim et al. “Inverse problem instabilities in large-scale modeling of matter in extreme conditions”. In: *Physics of Plasmas* 26.11 (Nov. 2019), p. 112706.

[195] Hae Ja Lee. personal communication. Mar. 16, 2022.

[196] Dimitri Khaghani. personal communication. Feb. 10, 2023.

[197] R E H Clark and D H Sampson. “Ionisation from the sublevels nl with n=5 and 6 in highly charged ions”. In: *Journal of Physics B Atomic and Molecular Physics* 17.16 (Aug. 1984), pp. 3311–3320.

[198] Christopher J. Fontes, Douglas H. Sampson, and Hong Lin Zhang. “Method for calculating the electron-impact ionization of ions of any complexity”. In: *Physical Review A* 48.3 (Sept. 1993), pp. 1975–1982.

[199] Thomas Gawne et al. “Ultrahigh resolution x-ray Thomson scattering measurements at the European X-ray Free Electron Laser”. In: *Physical review. B./Physical review. B* 109.24 (June 2024).

[200] Giuseppe Carleo et al. “Machine learning and the physical sciences”. In: *Reviews of Modern Physics* 91.4 (Dec. 2019).

[201] M F Kasim et al. “Building high accuracy emulators for scientific simulations with deep neural architecture search”. In: *Machine Learning Science and Technology* 3.1 (Dec. 2021), p. 015013.